

**Design and Evaluation of Next-Generation Cellular Networks through
Digital and Physical Open and Programmable Platforms**

A Dissertation Presented
by

Davide Villa

to

The Department of Electrical and Computer Engineering

in partial fulfillment of the requirements
for the degree of

Doctor of Philosophy

in

Electrical and Computer Engineering

**Northeastern University
Boston, Massachusetts**

December 2025

To my family.

*"There are only two ways to live your life. One is as though nothing is a miracle.
The other is as though everything is a miracle."*

— Attributed to Albert Einstein

Contents

List of Figures	v
List of Tables	xi
List of Acronyms	xii
Abstract of the Dissertation	xvii
1 Introduction	1
1.1 Motivation and Context	1
1.1.1 The Evolution of Cellular Networks	1
1.1.2 Open RAN and AI-RAN: Opening the Network	2
1.1.3 Complexity and the Need for Testbeds	3
1.2 Research Questions and Challenges	4
1.3 The Journey of an Experimental Idea	4
1.4 Contributions and Dissertation Structure	5
2 Large-Scale Wireless Network Emulation with Digital Twins	7
2.1 Introduction	7
2.2 Digital Twins	8
2.3 Digital Twin Platforms	10
2.3.1 Large-scale Emulation: Colosseum	10
2.3.2 Over-the-Air Experimentation: Arena	13
2.4 Digitizing Real-world Environments	13
2.4.1 RF Scenario Twinning	14
2.4.2 Protocol Stack Twinning	17
2.5 Experimental Evaluation	19
2.5.1 CaST Tuning	19
2.5.2 Validation of Colosseum Scenarios through CaST	22
2.5.3 A V2X Use-Case Scenario in Tampa, FL	24
2.5.4 Arena Digital Twin Scenario	27
2.5.5 Arena Digital Twin Experimental Use Cases	28
2.6 Related Work	35
2.7 Conclusions	36

3	Spectrum Sharing and AI-Driven Modeling on Digital Platforms	37
3.1	Introduction	37
3.2	Spectrum Sharing and Incumbent Signal Detection	37
3.2.1	Waveform Twinning and Radar Characterization	39
3.2.2	Spectrum-Sharing Waikiki Beach Scenario	41
3.2.3	Intelligent Radar Detection	44
3.2.4	Performance Evaluation	45
3.2.5	Conclusions	49
3.3	AI-Driven Radio Map Generation	49
3.3.1	Framework Overview	50
3.3.2	Training the Model: Data Collection	51
3.3.3	Deep Learning-Based Propagation Model	55
3.3.4	Performance Results	56
3.3.5	Integration with the Colosseum Emulator	57
3.3.6	Conclusions	59
3.4	Generative Models for Synthetic RF Data	60
3.4.1	Gen-TWIN Platform	60
3.4.2	Data Augmentation with <i>soft</i> -GAN	62
3.4.3	Data Collection	64
3.4.4	Experiment Evaluation	65
3.4.5	Conclusions	69
3.5	Summary and Discussion	70
4	Design and Deployment of a Private 5G O-RAN Testbed	72
4.1	Introduction	72
4.2	X5G Software	75
4.2.1	Full-stack Programmable RAN with NVIDIA Aerial and OpenAirInterface	75
4.2.2	Integration with the OSC Near-RT RIC	78
4.2.3	X5G Software Licensing and Tutorials	79
4.3	X5G Infrastructure	81
4.4	RF Planning with Ray-tracing	83
4.5	Experiment Results	86
4.5.1	Setup Overview	87
4.5.2	Static Experiments	88
4.5.3	Mobile Experiments	92
4.5.4	Video Streaming Experiments	94
4.5.5	Peak Performance Experiments	95
4.5.6	Long-running Experiments	96
4.6	GPU-Accelerated dApp Framework	97
4.6.1	dApp Background and Motivation	98
4.6.2	GPU-accelerated dApp Framework Design	99
4.6.3	High-Level Architecture	99
4.6.4	Profiling dApp Framework Performance	103
4.6.5	ARC-OTA Experimental Setup	104

4.6.6	Framework Benchmarks	104
4.7	Related Work	106
4.8	Conclusions and Discussion	109
5	Intelligent RAN Control and Security on Physical Platforms	110
5.1	Introduction	110
5.2	cuSense: Uplink CSI-based ISAC dApp for Person Detection	111
5.2.1	Overview and Goals	111
5.2.2	Uplink CSI Processing Pipeline	112
5.2.3	Experimental Evaluation	115
5.2.4	Related Work	119
5.2.5	Summary	119
5.3	InterfO-RAN: In-band Uplink Interference Detection	120
5.3.1	Introduction	120
5.3.2	System Architecture	122
5.3.3	GPU-Accelerated Physical Layer Processing	123
5.3.4	InterfO-RAN Design and Implementation	125
5.3.5	Data and Evaluation Framework	129
5.3.6	Performance Evaluation and Experimental Results	132
5.3.7	Related Work	136
5.3.8	Summary	137
5.4	ORANSlice: Dynamic Resource Management	137
5.4.1	Introduction	137
5.4.2	Network Slicing Background	138
5.4.3	ORANSlice Implementation	140
5.4.4	Testbeds and Experiment Results	142
5.4.5	Related Work	145
5.4.6	Conclusions	146
5.5	TIMESAFE: Security of Open Interfaces	146
5.5.1	Introduction	146
5.5.2	Background	148
5.5.3	Threat model	149
5.5.4	Experimental Setup	151
5.5.5	Impact of the Attacks	151
5.5.6	ML-Based Attack Detection	153
5.5.7	Related Work	155
5.5.8	Conclusion	155
5.6	Summary and Discussion	156
6	Conclusions	158
Bibliography		160
Acknowledgments		180

List of Figures

1.1	Evolution of cellular networks from 1G to 6G, showing the progression in data rates, capabilities, and the increasing demands on next-generation systems.	2
1.2	The Open RAN architecture, illustrating the transition from traditional closed-box base stations to disaggregated, software-defined, and intelligent network components connected through open interfaces [1].	3
1.3	Continuous growth in complexity, where modern cellular networks can be seen as a puzzle of interoperable hardware, software, and AI components.	4
1.4	The journey of an experimental idea: from initial concept through design and simulation, to emulation at scale, to real-world OTA testing, and finally to production deployment.	5
2.1	High-level representation of digital twin components.	9
2.2	Main components of our high-level representation of a DT.	9
2.3	Colosseum architecture, adapted from [2].	11
2.4	FPGA-based RF scenario emulation in Colosseum, from [2].	11
2.5	Arena architecture.	13
2.6	CaST scenario creation workflow.	14
2.7	CaST channel sounding workflow.	16
2.8	Protocol stack twinning workflow across a digital environment, i.e., Colosseum, and two physical environments, i.e., Arena and a generic over-the-air testbed.	18
2.9	Controlled laboratory environment used for the <i>CaST</i> tuning process.	20
2.10	Correlation of different code sequences in the controlled laboratory environment.	22
2.11	Received path gains in the controlled laboratory environment with 0 and 30 dB total transmit and receive gains use cases (15 dB at both transmitter and receiver sides).	23
2.12	Path loss heatmap as measured by <i>CaST</i> in a 0 dB Colosseum RF scenario with 10 SRNs.	23
2.13	Comparison between emulated and modeled path gains in Colosseum for a single time frame.	24
2.14	Tampa, FL, V2X scenario simulation environment in WI.	25
2.15	Comparison between original and received path gains for OBU#3 (node 4) against RSU (node 1) and OBU#2 (node 3).	26
2.16	Results comparison for the mobile use case scenario.	26

2.17	The conversion from a real-world location, into a digital medium scenario used to create the digital twin representation.	27
2.18	Location of the nodes in an Arena DT scenario.	27
2.19	Heat map of the path loss among the nodes of Figure 2.18, with a line separator between antenna, static, and mobile. The mobile nodes are considered in the starting position on the left.	28
2.20	Location of the nodes in the cellular experiment.	29
2.21	UDP downlink throughput of the cellular use case on the Arena and Colosseum testbeds.	30
2.22	TCP downlink throughput of the cellular use case on the Arena and Colosseum testbeds.	30
2.23	TCP SINR of the cellular use case on the Arena and Colosseum testbeds.	30
2.24	Location of the nodes in the multiple BSs cellular use-case, consisting of 2 BSs (BS 1, BS 2), and 6 static UEs, equally assigned to each BS: UE 1, UE 2, and UE 3 for BS 1; UE 4, UE 5, and UE 6 for BS 2.	31
2.25	Downlink throughput average results and 95% confidence interval of the second cellular networking use-case with 2 BSs and 6 UEs.	32
2.26	Location of the nodes in the jamming experiment, consisting of three static (1, 8, 9) and one mobile (41).	33
2.27	Throughput and SINR results on the Arena and Colosseum testbeds of the jamming experiments for the narrowband and wideband use cases. The spectrogram is shown for both forms of jamming, showing the wideband and narrowband signals over a channel.	34
2.28	Impact of a moving jammer for narrowband (a) and wideband (b) use cases on the throughput and SINR of Wi-Fi nodes on Arena and Colosseum testbed.	35
3.1	Waveform twinning on Colosseum.	39
3.2	Radar characterization with PSD and constellation plots.	40
3.3	Block diagram of the operations needed to integrate the radar signal in Colosseum.	40
3.4	Results of a radar transmission through <i>CaST</i>	41
3.5	<i>CaST</i> scenario creation toolchain blocks diagram. Figure adapted from [3].	42
3.6	Location of the nodes in the Waikiki Beach scenario.	42
3.7	Layout of the scenario loaded in the MATLAB ray-tracer and visualized with Site Viewer.	43
3.8	Heat map of the path loss among the nodes of the Waikiki scenario in Figure 3.7. The mobile ship node is considered in its starting position at the top.	44
3.9	CNN model used to train the radar detector.	45
3.10	CNN radar detection accuracy with varying SNR of the radar signal, and varying SINR where the cellular signal is considered to be interference.	46
3.11	Moving average of cellular network downlink throughput and CQI. A radar transmission is ongoing from second 150 to second 190, highlighted with a blue shade.	47
3.12	(top) Downlink cellular spectrogram; (bottom) radar detection system. The BS is shut down when a radar transmission is detected and resumes normal operations after no radar is detected.	48

3.13	Computation time required for a radar classification, with different batch sizes, run on CPU on a Colosseum SRN with 48-cores Intel Xeon processor and 126 GB of RAM.	48
3.14	Training process, data calibration, and model validation.	51
3.15	Northeastern University, Boston Campus, used for generating the main dataset consisting of 61 TX and 7,569 RX. Location: 42°20'22"N, 71°05'14"W.	53
3.16	A comparison of the model's output (Figure 3.16c) with the ground truth heatmap generated by Wireless InSite (Figure 3.16d), showing its superior performance compared to (Figure 3.16b).	53
3.17	Measurement campaign at Northeastern University Campus in collaboration with VIAVI to gather real-world data for model validation and refinement.	54
3.18	U-Net architecture adapted from PMNet [4]. We use elevation maps and propagation estimates as inputs to achieve an accurate propagation model.	56
3.19	Model performance comparison at Northeastern University and Fenway Park.	57
3.20	eCDF of error w/ and w/o calibration using the measurement data (10% of the dataset).	58
3.21	Real-time channel emulation pipeline on Colosseum. User-selected locations trigger U-Net inference, with predicted taps sent via MQTT to MCHEM for emulation.	58
3.22	Comparison of RSRP reports from OAI on Colosseum (10 runs per experiment). The Calibrated U-Net closely matches measurements, while Ray Tracing and Uncalibrated U-Net failed to establish a connection in this setup.	59
3.23	Left: O-RAN Digital Twin Layer; Colosseum—the world's largest wireless network emulator with hardware in the loop [2] to create a comprehensive twin of the O-RAN network. Right: Generative AI Layer; Proposed <i>soft</i> -GAN Model — soft-attention-LSTM based Generative Adversarial Network.	61
3.24	Data collection scenarios for the real world (POWDER, left picture) and digital world (Colosseum, right picture). The red circles indicate the actual nodes used for data collection. Colosseum node 6 is a remnant of the now-decommissioned POWDER Medical Tower Rooftop node.	65
3.25	<i>soft</i> -GAN training and validation loss over epochs (left picture). Generator and discriminator loss over epochs (right picture).	66
3.26	Components of real and generated samples in the PCA subspace; Generated samples (marked as “x”) exhibit a substantial overlap with the real samples (marked as “+”).	68
3.27	Spectrogram of <i>soft</i> -GAN generated synthetic RF (25 dB gain) Signals	69
4.1	X5G end-to-end programmable testbed overview.	74
4.2	Architecture of the lower layers of the X5G RAN following O-RAN specifications and consisting of: (i) a Foxconn O-RU; (ii) an O-DU-low based on NVIDIA Aerial SDK; (iii) an O-DU-high based on OpenAirInterface with their corresponding interfaces.	76
4.3	Integration of the OSC Near-RT RIC in the OpenShift cluster with the X5G RAN.	79
4.4	KPM xApp example architecture including an X5G gNB with four connected UEs, each performing a different operation (ping, video streaming, DL test, and DL/UL tests), and a KPM xApp that pushes UE metrics into an Influx database, which are then visualized in a Grafana dashboard.	80

4.5	Slicing xApp example showing: (a) DL throughput for two different slices, each with a single UE connected and pushing 50 Mbps of UDP traffic; (b) the network policy applied by the slicing xApp, switching between no-priority (0), prioritize slice 1 (1), and prioritize slice 2 (2).	81
4.6	Hardware architecture infrastructure of the X5G deployment at Northeastern University.	82
4.7	Site viewer with RU (red squares) and UE (blue icons) locations.	84
4.8	Heatmap results of the normalized average SINR $\Phi(\Gamma)$ with 2 RUs.	87
4.9	Node locations considered in our experiments: RUs (red circles in 6 and 23); possible static UEs (blue squares); and mobile UEs (green dashed line).	87
4.10	Performance profiling with one UE and single RU for the static iPerf use case during DL (blue bars) and UL (orange bars) data transmissions.	89
4.11	Performance profiling for one RU and two static UEs for the static iPerf use case.	90
4.12	Performance profiling with multiple UEs at fixed location 4 for the static iPerf use case using a DDDSU TDD pattern, a 2x2 MIMO configuration, 2 layers DL and 1 layer UL.	91
4.13	Performance profiling for two RUs in the static iPerf use case, each with one assigned UE: UE1 to RU1 and UE2 to RU2.	91
4.14	MAC KPIs in the two RUs iPerf use case, each with one static UE (UE1 assigned to RU1 and UE2 to RU2): (a) averages and confidence intervals for DL MCS (solid lines) during DL data transmissions, and UL MCS (dashed lines) during UL transmissions, for UE1 (blue) and UE2 (orange); (b) averages and confidence intervals of RSRP reported by UE1 (blue) and UE2 (orange) during DL (solid lines) and UL (dashed lines) transmissions.	92
4.15	Performance profiling with one RU and one mobile UE in the iPerf use case: (a) CDF of DL and UL throughputs with averages (solid lines) and SD (shaded areas); (b) averages (solid lines) and SD (shaded areas) of the DL MCS during DL transmissions (blue) and of the UL MCS during UL transmissions (orange); (c) averages (solid lines) and SD (shaded areas) of the RSRP reported by the UE during DL (blue) and UL (orange) data transmissions.	93
4.16	Video streaming performance with one UE and single RU across both static (8—close, 12—mid, 16—far) and mobile use cases.	94
4.17	Performance profiling to achieve peak network throughput, leveraging: one (<i>1-ota</i>) and two (<i>2-ota</i>) OTA UEs at a fixed location using iPerf and a DDDDDDSUUU TDD pattern; one (<i>1-sim</i>) and two (<i>2-sim</i>) emulated UEs using Keysight RuSIM and CoreSIM with a DDDDDDSUUU TDD pattern; and two (<i>2-simdl</i> , <i>2-simul</i>) and twenty-five (<i>25-simdl</i> , <i>25-simul</i>) emulated UEs with Keysight RuSIM and CoreSIM, a reduced number of guard symbols, a DDDDDDDSUU TDD pattern for DL cases, and a DDDSU TDD pattern for UL cases.	95
4.18	Long-running stability experiment involving one UE randomly cycling for over 180 hours among three operations, repeated every 10 minutes: (blue) DL iPerf for 1 minute; (orange) UL iPerf for 1 minute; and (green) disconnection from the network for the remainder of the 10-minute cycle window.	96

4.19 GPU utilization (blue) and power draw (orange) of the NVIDIA Grace Hopper server node during a one-hour window of the long-running stability experiment. The results show the behavior of the system when the UE cycles through three operations: disconnecting for 10 minutes, performing a DL iPerf test for 1 minute, followed by 10 minutes of idling, and performing a UL iPerf test for 1 minute, followed by 10 minutes of idling.	97
4.20 NVIDIA ARC-OTA dApp Integration Architecture.	99
4.21 Aerial Data Lake ping-pong mechanism and shared memory structure.	100
4.22 Data path integration between Aerial L1, Real-time ADL, shared-memory, and the E3 Agent. The steps (Op. 1–4) match the operations in Table 4.4.	101
4.23 Support for multiple RAN nodes, E3 Agents, and dApps in the same gNB.	102
4.24 dApp container reference architecture with E3 Manager, NVIDIA Triton Inference Server, and dApp Client.	103
4.25 Client latency (Operations 5–8 of Table 4.4) and inference latency (δ) for the iq-processor model across different backends.	105
5.1 Overview of the cuSense UL DMRS-based ISAC dApp for person localization. . .	111
5.2 cuSense dApp processing pipeline overview.	112
5.3 Proposed NN architecture of cuSense dApp for CSI-based location estimation. . .	114
5.4 cuSense experimental environment.	115
5.5 Temporal-random split strategy with example of contiguous validation/test blocks within training runs and fully unseen runs.	117
5.6 cuSense localization accuracy on test set (a, b) and unseen runs (c, d): 3GPP wireless sensing service category distributions and CDF of peak distance error.	118
5.7 Trajectory tracking comparison of an unseen run segment for the X and Y axis. .	118
5.8 In-band UL interference overview (dashed lines).	121
5.9 System Architecture.	123
5.10 InterfO-RAN as a post-processing component following the PUSCH CUDA graph, where each node represents a CUDA kernel.	124
5.11 The workflow diagram for the OrtCtx class for performing inference.	126
5.12 InterfO-RAN’s CNN architecture showing inputs (I/Q and scalar features), layer specifications, and the binary interference detection output.	129
5.13 Indoor experiment layout maps of Northeastern University EXP (a) and ISEC (b) buildings, showing: the designated regions for the two cell sites, where the corresponding UEs can be located; RU locations for each respective cell site; and primary UE locations, where most of the data is collected.	130
5.14 UL throughput, TB size, and CB count across different scenarios, demonstrating their close correlation.	131
5.15 Confusion matrix of the model tested on synthetic data with 13800 samples per class.	133
5.16 Model performance (accuracy, specificity, and recall) for Transfer Learning: (a) familiar RF environment and (b) unseen RF environment to evaluate generalization.	134

5.17	Classification accuracy (percentage, sample count) with and without TL across different RF environments: (a) no TL in a familiar environment, (b) TL tested in a familiar environment, and (c) TL tested in an unseen environment, using the same color bar as Figure 5.15.	135
5.18	Inference time from first iteration: (a) temporal variation with a 5-instance moving average with No (before 24 s) and High Traffic (after 24 s), (b) inference time CDF.	135
5.19	GPU utilization (blue) and power draw (orange) comparison with and without InterfO-RAN dApp.	136
5.20	End-to-end network slicing in O-RAN.	139
5.21	Illustration of RRM Policy Ratio Message	141
5.22	Average number of DL PRBs allocated to each slice in the first experiment.	144
5.23	DL Throughput for each slice in the first experiment.	144
5.24	DL throughput for each slice and UE in the second experiment.	145
5.25	The Open Fronthaul employs PTP to synchronize the master clock with distributed base station components over a switched network. In this scenario, an attacker compromises a device on the network and, at time A , initiates a Spoofing Attack. This leads to gradual synchronization drift (B), first degrading performance (C) and then causing the base station to crash at time D	147
5.26	The Fronthaul connects the Distributed Unit (DU) to the Radio Unit (RU). There are four Synchronization Plane topologies based on the location of the clock source and switched network. LLS-C2 and LLS-C3 present the greatest risk to PTP because the switched network is used to transport the timing messages.	148
5.27	The black (solid/dotted) lines represent normal traffic, while the red (dashed) lines on the left side illustrate the flow of messages during a Spoofing Attack, where an attacker manipulates the BMCA to become the master. The red (dashed) on the right side illustrates the flow of messages during a Replay Attack, showing the re-transmission of Sync and FollowUp messages.	150
5.28	Downlink throughput to a User Equipment (UE) during a spoofing attack with the switch port set to Precision Timing Protocol (PTP) master. Approximately 60 seconds into the experiment, the spoofing attack is initiated. Around second 440 there is a 50% drop in throughput, progressing to a 75% drop by second 510, and ultimately causing the base station to crash at around second 580.	152
5.29	Downlink throughput to a UE during a spoofing attack with switch ports set to PTP dynamic role. Throughput remains stable at around 350 Mbps initially. About 40 seconds in, the spoofing attack begins, causing the 5G cell to drop and the UE to lose connectivity.	153
5.30	The final TIMESAFE transformer model uses 2 transformer layers, a fully connected linear layer with ReLU activation function, a dropout layer, and a second linear layer with a sigmoid activation function. The output is a single binary classification for the entire sequence.	154
5.31	Confusion matrix for production environment attack detection. The Transformer model achieves over 99% accuracy in detecting PTP attacks on the X5G platform.	155

List of Tables

2.1	Configuration parameters used in the controlled laboratory setup.	20
2.2	Wireless parameters for the Tampa simulation scenario.	25
2.3	Normalized cross-correlation results, and their averages, considering the maximum values between 10 lags for the single BS cellular experiment.	32
2.4	Normalized cross-correlation results, and their averages, considering the maximum values between 10 lags for each jamming experiment.	35
3.1	Parameters of the Waikiki Beach scenario.	43
3.2	Parameters of the experiments.	46
3.3	Measurement Setup and Equipment	55
3.4	Data collection parameters summary between the two testbeds: POWDER for OTA data, and Colosseum for emulated data.	64
3.5	Hyper-parameter tuning stage of <i>soft</i> -GAN	65
3.6	NRMSE and Context FID-Scores (Lower values in these metrics indicate better model performance)	67
3.7	Discriminative and Predictive Score Results (Lower values in these metrics indicate better model performance)	67
3.8	Comparison of classification performance of baseline models	67
4.1	X5G ARC deployment main features.	77
4.2	Parameters of the MATLAB ray-tracing study to determine RU locations.	85
4.3	Best RUs and average SINR $\Phi(\Gamma)$ range values.	86
4.4	Data messaging path and cumulative latency for a single dApp end-to-end control-loop iteration.	105
5.1	cuSense localization accuracy on unseen runs.	117
5.2	cuSense inference latency breakdown.	119
5.3	Inference time between different execution providers for standalone ORT.	126
5.4	Lookup Table for gNB UL Traffic and Labels	132
5.5	Average inference times across different models.	136

List of Acronyms

- $\hat{\mathbf{H}}$** Channel Estimates
- CaST*** Channel emulation generator and Sounder Toolchain
- 1G** First Generation
- 2G** Second Generation
- 3G** Third Generation
- 3GPP** 3rd Generation Partnership Project
- 4G** Fourth Generation
- 5G** Fifth Generation
- 6G** Sixth Generation
- ABR** Adaptive Bitrate Streaming
- ADC** Analog to Digital Converter
- ADL** Aerial Data Lake
- AI** Artificial Intelligence
- AMF** Access and Mobility Management Function
- AoA** Angle of Arrival
- API** Application Programming Interface
- ARC** Aerial RAN CoLab
- ARC-OTA** Aerial RAN CoLab Over-the-Air
- AWGN** Additive White Gaussian Noise
- BBU** Base Band Unit
- BLER** Block Error Rate
- BMCA** Best Master Clock Algorithm
- BPSK** Binary Phase-shift keying
- BS** Base Station
- CB** Code Block
- CBRS** Citizen Broadband Radio Service
- CD** Continuous Delivery
- CDF** Cumulative Distribution Function
- CDMA** Code-Division Multiple Access
- CFO** Carrier Frequency Offset
- CFR** Code of Federal Regulations
- CI** Continuous Integration
- CI/CD** Continuous Integration/Continuous Delivery
- CIR** Channel Impulse Response
- CN** Core Network
- CNN** Convolutional Neural Network
- COTS** Commercial Off-the-Shelf
- CP** Control Plane
- CPRI** Common Public Radio Interface
- CPU** Central Processing Unit
- CQI** Channel Quality Information

CRC Cyclic Redundancy Check
CSI Channel State Information
CU Central Unit
cuBB CUDA Baseband
cuBLAS CUDA Basic Linear Algebra Subroutines
CUDA Compute Unified Device Architecture
cuDNN CUDA Deep Neural Network library
cuPHY CUDA Physical layer
dApp distributed Application
DCI Downlink Control Information
DL Downlink
DMRS DeModulation Reference Signal
DPU Data Processing Unit
DSP Digital Signal Processing
DT Digital Twin
DT-RAN Digital Twin for Radio Access Network
DTMN Digital Twins for Mobile Networks
DTN Digital Twin Network
DU Distributed Unit
E2AP E2 Application Protocol
E2E end-to-end
E2SM E2 Service Model
E3AP E3 Application Protocol
eCDF Empirical Cumulative Distribution Function
eCPRI enhanced CPRI
EM Electro-Magnetic
eMBB Enhanced Mobile Broadband
FAPI Functional Application Platform Interface
FCC Federal Communications Commission
FH Fronthaul
FID Fréchet Inception Distance
FIR Finite Impulse Response
FL Federated Learning
FP16 Float16
FP32 Float32
FPGA Field Programmable Gate Array
FPS Frames per second
FR1 Frequency Range 1
FRAND Fair, Reasonable, And Non-Discriminatory
GAN Generative Adversarial Network
Gen-TWIN GenerativeAI-enabled Digital Twin
GenAI Generative Artificial Intelligence
GH Grace Hopper
GLFSR Galois Linear Feedback Shift Register
gNB Next Generation Node Base
GPU Graphics Processing Unit
gRPC gRPC Remote Procedure Calls
GUI Graphical User Interface
HDF5 Hierarchical Data Format version 5
HDR High Dynamic Range
HTTP HyperText Transfer Protocol
I/Q In-phase and Quadrature
IFW Interference Free Window
IoT Internet of Things

IP Internet Protocol
IRC Interference Rejection Combining
ISAC Integrated Sensing and Communication
IW Interference Whitening
KL Kullback–Leibler
KPI Key Performance Indicator
KPM Key Performance Measurement
LDPC Low Density Parity-Check
LEO Low Earth Orbit
LFSR Linear Feedback Shift Register
LOS Line-of-Sight
LS Loosely Synchronised
LSTM Long Short Term Memory
LTE Long Term Evolution
LXC Linux Container
MAC Medium Access Control
MCHEM Massive Channel Emulator
MCS Modulation and Coding Scheme
MGEN Multi-Generator
MIG Multi-Instance GPU
MIMO Multiple Input, Multiple Output
ML Machine Learning
MLP Multilayer Perceptron
MMSE Minimum Mean Square Error
mMTC Massive Machine-Type Communications
MPS Multi-Process Service
NAS Network Attached Storage
NextG Next Generation
NF Network Function
NFV Network Function Virtualization
NIC Network Interface Card
NLB Non-local Block
NLOS Non-Line-of-Sight
NN Neural Network
NRMSE Normalized Root Mean Squared Error
NTP Network Time Protocol
NVIPC NVIDIA Inter-Process Communication
OAI OpenAirInterface
OAIC Open AI Cellular
OBU Onboard Unit
ODC ORAN Development Company
OFDM Orthogonal Frequency Division Multiplexing
ONNX Open Neural Network Exchange
Open RAN Open Radio Access Network (RAN)
ORT ONNX Runtime
OSC O-RAN Software Community
OSM OpenStreetMap
OTA Over-the-Air
OTC Over-the-Cable
P5G Private 5G
PAWR Platforms for Advanced Wireless Research
PCA Principal Component Analysis
PCI Peripheral Component Interconnect
PDCCH Physical Downlink Control Channel

PDU Packet Data Unit
PH Power Headroom
PHY Physical
PL Path Loss
PRACH Physical Random Access Channel
PRB Physical Resource Block
PRTC Primary Reference Time Clocks
PSD Power Spectral Density
PTP Precision Timing Protocol
PUCCH Physical Uplink Control Channel
PUSCH Physical Uplink Shared Channel
QAM Quadrature Amplitude Modulation
QoS Quality of Service
QSFP28 Quad Small Form-factor Pluggable 28
RACH Random Access Channel
RAN Radio Access Network
RDMA Remote Direct Memory Access
RE Resource Element
RF Radio Frequency
RIC RAN Intelligent Controller
RLC Radio Link Control
RMSE Root Mean Squared Error
RNTI Radio Network Temporary Identifier
RRM Radio Resource Management
RSRP Reference Signal Received Power
RSSI Received Signal Strength Indicator
RSU Road-Side Unit
RU Radio Unit
RX Receiver
S-NSSAI Single Network Slice Selection Assistance Information
S-plane Synchronization Plane
SAS Spectrum Access System
SCF Small Cell Forum
SCTP Stream Control Transmission Protocol
SD Standard Deviation
SDK Software Development Kit
SDN Software-defined Networking
SDR Software-defined Radio
SFP+ Small Form-factor Pluggable Plus
SHM Shared Memory
SINR Signal to Interference plus Noise Ratio
SIR Signal to Interference Ratio
SM Service Model
SMF Session Management Function
SNR Signal-to-Noise-Ratio
SoC System-on-Chip
SRN Standard Radio Node
SRS Sounding Reference Signal
SST Slice/Service Type
STFT Short-Time Fourier Transform
SyncE Synchronous Ethernet
TA Timing Advance
TAI International Atomic Time
TB Transport Block

TCP Transmission Control Protocol
TDD Time Division Duplexing
TDL Tapped Delay Line
TF Tensorflow
TGEN Traffic Generator
TL Transfer Learning
ToA Time of Arrival
TRT Tensor RealTime
TTI Transmission Time Interval
TX Transmitter
UAV Unmanned Aerial Vehicle
UCI Uplink Control Indication
UDP User Datagram Protocol
UE User Equipment
UL Uplink
UP User Plane
UPF User Plane Function
URLLC Ultra Reliable and Low Latency Communication
USRP Universal Software Radio Peripheral
UTC Coordinated Universal Time
V2X Vehicle-to-everything
VLAN Virtual Local Area Network
WI Wireless InSite
WSN Wireless Sensor Network
ZMQ ZeroMQ

Abstract of the Dissertation

Design and Evaluation of Next-Generation Cellular Networks through
Digital and Physical Open and Programmable Platforms

by

Davide Villa

Doctor of Philosophy in Electrical and Computer Engineering

Northeastern University, December 2025

Prof. Tommaso Melodia, Advisor

The evolution of the Radio Access Network (RAN) in 5G and 6G technologies marks a shift toward open, programmable, and softwarized architectures, driven by the Open RAN paradigm. This approach emphasizes open interfaces for RAN telemetry sharing, intelligent data-driven control loops for network optimization and control, and the virtualization and disaggregation of multi-vendor RAN components. While promising, this transition introduces significant challenges, including the need to design interoperable solutions, acquire datasets to train and test Artificial Intelligence (AI)/Machine Learning (ML) algorithms for network inference, forecasting, and control, and develop comprehensive testbeds to benchmark and validate these solutions. To this end, experimental wireless platforms and private 5G deployments play a key role, providing architectures comparable to real-world systems and enabling the design, prototyping, and testing of a wide variety of solutions in realistic environments.

This Ph.D. dissertation focuses on the development and evaluation of complementary experimental platforms: Colosseum—the world's largest Open RAN digital twin—and X5G—an open, programmable, multi-vendor, end-to-end private 5G O-RAN testbed with GPU acceleration. It further discusses how these platforms can be leveraged to advance use cases in spectrum sharing, AI-driven modeling, security, network slicing, and Integrated Sensing and Communication (ISAC) for next-generation cellular research. The main contributions of this dissertation include: (i) the development of CaST (Channel emulation Scenario generator and Sounder Toolchain), enabling the automated creation and validation of digital twin wireless scenarios for Colosseum through 3D modeling, ray-tracing, and channel sounding; (ii) the validation of Colosseum digital twins at scale, demonstrating that emulated environments can closely reproduce real-world setups and providing

RAN emulation blueprints for the research community; (iii) the design and deployment of X5G, an open, programmable, multi-vendor private 5G O-RAN testbed that integrates NVIDIA Aerial GPU-accelerated PHY layer processing with OpenAirInterface higher layers; (iv) the integration of a GPU-accelerated dApp framework for real-time inference and control within the RAN, exposing PHY/MAC telemetry and enabling sub-millisecond control loops for AI-native applications, including ISAC; and (v) the realization of intelligent RAN applications and pipelines spanning spectrum sharing, interference detection, network slicing, security assessment, and CSI-based sensing.

Overall, this dissertation provides an end-to-end methodology and set of platforms that bridge digital and physical experimentation, offering a practical blueprint for designing, validating, and operating next-generation open and programmable cellular networks.

Chapter 1

Introduction

The ever-growing wireless industry is driving an ongoing demand for systems that deliver higher key performance metrics, including increased throughput, reduced latency, and the ability to connect a greater number of UEs simultaneously. Over the past few decades, each cellular generation has reshaped how people, devices, and services connect. This evolution is not only bringing higher data rates and lower latency, but also increasing the scope of what wireless networks can support, from traditional Enhanced Mobile Broadband (eMBB), Massive Machine-Type Communications (mMTC), and Ultra Reliable and Low Latency Communication (URLLC) to sensing, localization, and Artificial Intelligence (AI)-native applications [5, 6]. At the same time, the way in which these networks are built is changing. Earlier generations were mainly developed on vertically integrated hardware platforms in a closed-box approach, while modern RANs are becoming more open, programmable, and softwarized. Open interfaces, virtualized network functions, and AI-enabled control loops are turning the RAN into a platform on which new services and intelligent applications can be developed and deployed [7]. This transition, while promising, also makes the network substantially more complex to design, test, and operate.

This dissertation sits at this intersection and focuses on how experimental platforms can be leveraged to ease the design, deployment, and evaluation of next-generation, open, programmable, and AI-native cellular networks. Throughout the thesis, we embark on an experimental journey that starts with large-scale wireless digital emulators and continues through Over-the-Air (OTA) testing on a physical private Fifth Generation (5G) network, including the development and testing of various intelligent applications for monitoring, control, sensing, and security.

1.1 Motivation and Context

1.1.1 The Evolution of Cellular Networks

Cellular networks have historically experienced a generational update cycle of approximately ten years, with each generation bringing advances in capabilities and services. As shown in Figure 1.1, this progression started with First Generation (1G) in the 1980s, offering voice-only services at approximately 2.4 kbps. The 1990s introduced Second Generation (2G) with text messaging capabilities at 64 kbps. The new millennium brought Third Generation (3G) and the advent of mobile Internet

CHAPTER 1. INTRODUCTION

access at 2 Mbps, fundamentally changing how people retrieved and accessed information. The 2010s delivered Fourth Generation (4G)/Long Term Evolution (LTE) and the Internet of applications at 1 Gbps, coinciding with the smartphone revolution that put powerful computing devices in the pockets of billions worldwide [8, 9]. The current decade is characterized by 5G, with data rates approaching 10 Gbps, enabling the Internet of Things (IoT), real-time augmented and virtual reality, smart devices, and connected vehicles, and leveraging new frequency bands and advanced spectrum-sharing techniques. Looking ahead, Sixth Generation (6G) development is already underway and is expected to push toward 1 Tbps, with ubiquitous connectivity, adaptive systems powered by Digital Twins (DTs), and AI/Machine Learning (ML)-driven network intelligence [10, 11]. This progression reflects an ever-growing demand for higher data rates, more connected devices, and richer services, all with lower latency, energy consumption, and operational costs. This raises the challenge of how to drive this innovation and generational evolution efficiently.

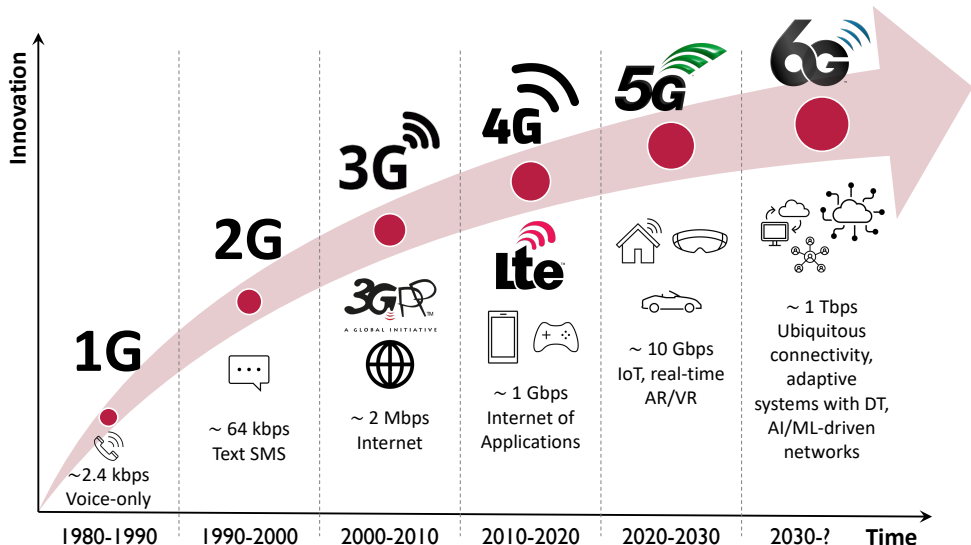


Figure 1.1: Evolution of cellular networks from 1G to 6G, showing the progression in data rates, capabilities, and the increasing demands on next-generation systems.

1.1.2 Open RAN and AI-RAN: Opening the Network

In recent years, the Open RAN paradigm has emerged as a key answer to this question, reshaping how next-generation networks are designed, deployed, and operated. As shown in Figure 1.2, Open RAN is built on a few key pillars [1]. *Disaggregation* splits the traditional monolithic base station into atomic functional units, Central Unit (CU), Distributed Unit (DU), and Radio Unit (RU), each dedicated to running a specific part of the RAN. *Open interfaces* enable these units to communicate via standardized protocols, enabling a multi-vendor ecosystem in which equipment from different manufacturers can interoperate seamlessly. *Softwareization* delivers network functions as software running on general-purpose or accelerated hardware, enabling high scalability, rapid updates, and virtualized deployments. Finally, *intelligence and virtualization* introduce data-driven optimization

CHAPTER 1. INTRODUCTION

by deploying intelligent applications in the RAN Intelligent Controllers (RICs) (rApps, xApps) or colocating them with the Next Generation Node Base (gNB) (dApps) at various closed-loop control timescales [12]. This introduces the notion of *AI-RAN*, in which a programmable RAN exposes telemetry, and AI/ML models can be used to enhance network efficiency and enable new use cases, such as Integrated Sensing and Communication (ISAC). However, this shift toward open and programmable networks also introduces greater complexity in properly designing, building, and operating a wireless system.

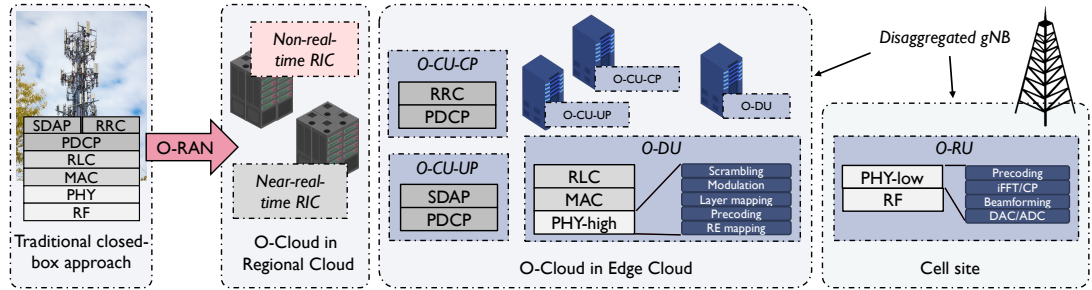


Figure 1.2: The Open RAN architecture, illustrating the transition from traditional closed-box base stations to disaggregated, software-defined, and intelligent network components connected through open interfaces [1].

1.1.3 Complexity and the Need for Testbeds

A useful way to visualize the increasing complexity of current networks is through the puzzle metaphor shown in Figure 1.3. Modern cellular systems require many components to work seamlessly together to provide connectivity to end users: antennas and radio hardware, signal processing chains, protocol stacks, computing infrastructure, AI/ML components, edge services, and diverse user devices. Each of these elements must integrate correctly with the others, much like pieces of a puzzle that must fit together precisely to form a complete picture. Completing such a puzzle takes time and resources, and the increasing number of pieces, particularly with the addition of intelligent components and multi-vendor interoperability requirements, and the possibility of swapping existing ones, opens the floor to new challenges in how to connect all these pieces effectively while allowing the system to still function correctly.

To tackle these problems, this dissertation proposes the answer of *testbeds*. Testbeds are experimental platforms that can support wireless research in numerous areas, from IoT and Wireless Sensor Network (WSN) [13] to satellite communications, and address these challenges in three fundamental ways. First, they provide an open and programmable environment where researchers can design and develop new solutions with complete control over each component of the network stack. Second, they can serve as data factories capable of generating large volumes of realistic Radio Frequency (RF) data under diverse conditions, data that is essential for training and testing AI/ML algorithms. Third, they offer a controlled playground where solutions can be evaluated and validated before deployment, allowing researchers to test bold ideas, break things, and recover without risking commercial infrastructure or end-user services.

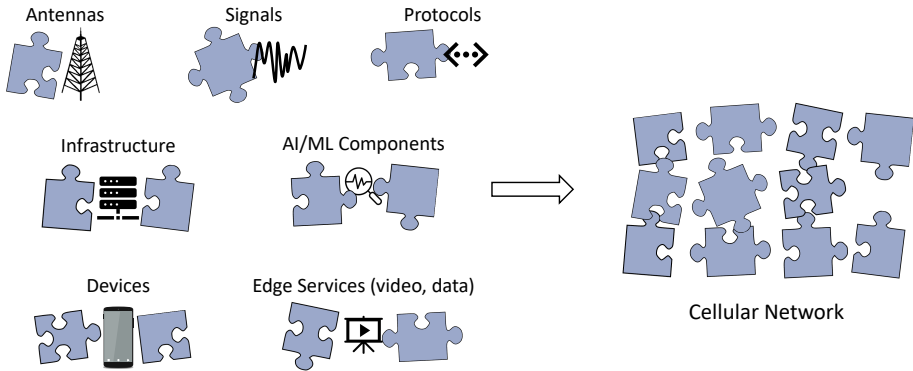


Figure 1.3: Continuous growth in complexity, where modern cellular networks can be seen as a puzzle of interoperable hardware, software, and AI components.

1.2 Research Questions and Challenges

While testbeds offer potential for advancing wireless research, fundamental questions must be addressed to use these systems effectively. Throughout this dissertation, four key research dimensions have guided the work.

Deployment. Given the complexity of modern cellular systems, how can we design and deploy experimental platforms that are realistic, reproducible, and scalable? This includes questions on the architecture, orchestration, and automation of the platforms, as well as challenges related to hardware and software integration.

Realism. Do testbeds accurately reflect real-world conditions? Even the most sophisticated emulator is ultimately an approximation of reality, and physical testbeds are deployed in specific locations with their own constraints. The value of experimental results depends critically on how well the testbed environment matches the characteristics of production deployments, such as channel propagation, protocol behavior, and device interactions.

Usability. How can we ensure interoperability and accessibility for the broader research community? The Open RAN ecosystem presents challenges related to the end-to-end (E2E) integration of components from multiple vendors. Beyond building capable testbeds, it is essential to provide tools, documentation, and interfaces that lower the entry barrier for researchers.

Use Cases. How can experimental platforms help address key challenges and advance research? Ultimately, testbeds should demonstrate their value by enabling concrete research contributions that would be difficult or impossible to achieve solely through simulation, and by supporting the transfer of these contributions toward commercialization.

1.3 The Journey of an Experimental Idea

To address these challenges, this dissertation develops complementary platforms that together support the lifecycle of wireless research, as illustrated in Figure 1.4. A researcher can follow the journey of an experimental idea through progressive stages of increasing fidelity and realism. An

CHAPTER 1. INTRODUCTION

initial concept moves from design and simulation using tools such as MATLAB, Sionna, or ns-3, to large-scale emulation and DTs on platforms like Colosseum, where hardware-in-the-loop experiments can be conducted at scale, and finally to real-world OTA validation on physical testbeds like X5G before potential production deployment. Each stage offers different trade-offs between control, scale, realism, and risk, and the ability to move ideas smoothly through this pipeline accelerates the path from concept to deployment.

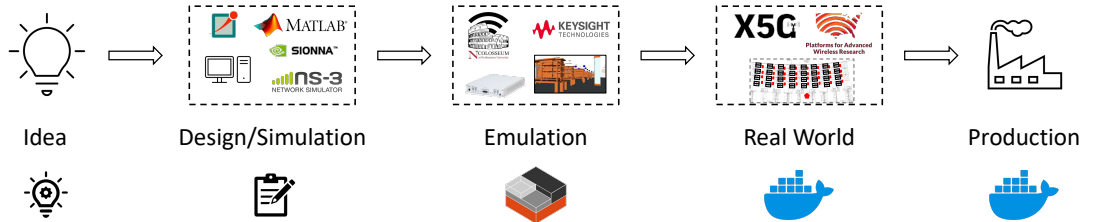


Figure 1.4: The journey of an experimental idea: from initial concept through design and simulation, to emulation at scale, to real-world OTA testing, and finally to production deployment.

1.4 Contributions and Dissertation Structure

The main contributions of this dissertation align directly with the experimental journey outlined above and address research questions related to both emulation and real-world validation. In particular, this work:

- Develops CaST, a toolchain to enable the automated creation and validation of DT wireless scenarios for large-scale wireless emulators through 3D modeling, ray-tracing, and channel sounding.
- Validates DTs on emulation platforms like Colosseum at scale, demonstrating that emulated environments can closely reproduce real-world setups and providing RAN emulation blueprints for the research community.
- Designs and deploys X5G, a Graphics Processing Unit (GPU)-accelerated private 5G O-RAN platform for OTA experimentation with commercial devices and multi-vendor components.
- Integrates a GPU-based dApp framework for real-time inference and control within the RAN, enabling sub-millisecond control loops and AI-native applications.
- Realizes intelligent RAN applications and pipelines for monitoring and control, spectrum sensing, ISAC, network slicing, and security assessment, showcasing the capabilities of the proposed platforms to advance the development of next-generation wireless networks.

The remainder of this dissertation is organized as follows. Chapter 2 (based on [2, 14, 3, 15]) introduces DTs for wireless networking and presents the CaST toolchain and the Colosseum testbed as core systems for large-scale emulation. Chapter 3 (based on [16, 17, 18, 19]) explores use cases enabled by Colosseum, including spectrum sharing with incumbent radar systems, AI-driven radio

CHAPTER 1. INTRODUCTION

map generation, and generative models for synthetic RF data augmentation. Chapter 4 (based on [20, 21, 22]) describes the design, deployment, and evaluation of X5G, an open, programmable, and multi-vendor private 5G testbed, as well as the development of a GPU-accelerated dApp framework for real-time applications. Chapter 5 (based on [22, 23, 24, 25]) presents intelligent RAN applications realized on X5G, including cuSense for Channel State Information (CSI)-based ISAC, InterfO-RAN for real-time interference detection, ORANSlice for dynamic resource management, and TIMESAFE for fronthaul security assessment. Finally, Chapter 6 summarizes the contributions, revisits the research questions, and discusses the broader implications of this work for next-generation wireless research.

Chapter 2

Large-Scale Wireless Network Emulation with Digital Twins

2.1 Introduction

Powerful experimental wireless platforms have recently been developed to provide an ecosystem for advanced wireless research through repeatable, reproducible experimentation and the creation of large datasets. These platforms are becoming the nexus of AI-enabled wireless research, where researchers can design, develop, train, and test new solutions for Next Generation (NextG) wireless systems. Examples include the US NSF Platforms for Advanced Wireless Research (PAWR) program with its four at-scale, outdoor programmable platforms [26], and indoor testbeds including the Drexel Grid [27], ORBIT [28], and Arena [29]. While these testbeds expose realistic indoor and outdoor wireless propagation environments, their physical scope is inherently tied to a specific deployment, and scaling them to capture the dynamics of real-world topologies, traffic conditions, and radio environments can be costly, time-consuming, and sometimes infeasible.

To complement these OTA platforms, large-scale wireless emulation systems have been proposed to support site-independent experimentation. By emulating a virtually unlimited variety of scenarios, these instruments are becoming a key resource for designing, developing, and validating networking solutions in quasi-realistic environments, at scale, and with a diverse set of fully customizable RF channel conditions, traffic scenarios, and network topologies [2, 30, 27]. Solution development and testing for NextG networks are, in fact, evolving toward the integration of actual networked systems with a digital model that provides a replica of the physical network for continuous prototyping, testing, and self-optimization of the living network. These *DTs* [31] are at the forefront of wireless research testing and prototyping [32]. However, the reliability of the solutions developed and tested on DT platforms depends critically on the precision of the emulation process and the underlying channel models, as well as on the ability to validate the emulated environment against real measurements. The realization of high-fidelity emulation-based DTs for wireless systems as a whole, namely a Digital Twins for Mobile Networks (DTMN) [33, 34], remains a challenge that has not been fully addressed.

To this end, this chapter centers on Channel emulation generator and Sounder Toolchain (*CAST*) [14], a complete toolchain for creating and validating wireless DTs on large-scale emulation

testbeds, such as Colosseum—the world’s largest wireless network emulator with hardware-in-the-loop and Open RAN Digital Twin [2, 35]. We leverage *CaST* together with Colosseum to realize DTMNs of representative OTA platforms and environments, and we run experiments on both systems to assess how faithfully the DT reproduces the behavior of a physical system. This chapter primarily targets three of the four key challenges introduced in Chapter 1: the *deployment* of a scalable DT platform, the *realism* of its emulated environments, and the *usability* of a reusable toolchain. The fourth challenge, namely the *use cases*, is the focus of Chapter 3. The main contributions of this chapter are the following:

- We present *CaST*, a streamlined framework for creating and validating realistic wireless scenarios with mobility support, based on precise ray-tracing methods for emulation platforms such as Colosseum [2].
- We leverage the *CaST* toolchain to generate a variety of DT emulation scenarios, both indoor and outdoor, including a DT of the OTA physical platform Arena [29].
- We develop a Continuous Integration/Continuous Delivery (CI/CD) pipeline for real-time twinning of selected protocol stacks, e.g., cellular and Wi-Fi, enabling researchers to automatically test new releases of open-source stacks.
- We validate the fidelity of the twinning process by comparing representative Key Performance Measurements (KPMs), such as throughput and Signal to Interference plus Noise Ratio (SINR), across experiments on digital and physical platforms.

Results show that the twinning process can faithfully reproduce real-world RF environments. The remainder of this chapter is organized as follows. Section 2.2 provides a brief primer on DTs in the context of wireless network emulators. Section 2.3 presents the platforms used to implement our DTMNs. Section 2.4 describes the *CaST* workflow, while Section 2.5 presents our experimental setup and validation results. Section 2.6 surveys related work, and Section 2.7 summarizes the main findings.

2.2 Digital Twins

The DT concept is finding increasing momentum as a means of enhancing the performance of physical systems by using their virtual counterparts [36]. The origin of this name is universally credited to Grieves and Vickers [37], who define a DT as a system consisting of three primary elements (Figure 2.1): (i) a physical product in the real world; (ii) a virtual representation of the product in the virtual world; and (iii) a connection of data and information tying the two.

Over the years, the DT idea has extended into new domains, starting from its description and adding different flavors to this concept. For example, some works consider DT as an enabler for Industry 4.0 applications, as detailed in [38], while others suggest its use in areas such as product design, assembly, or production planning [39]. Moreover, the continuous evolution of DTs and their applications ushered the concept of Digital Twin Networks (DTNs), as systems interconnect multiple DTs [40]. Finally, DTs have been adopted in the context of the wireless communications ecosystem and cellular networks.

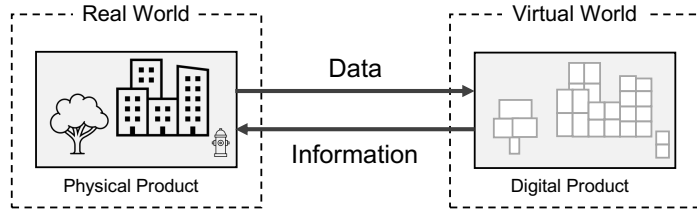


Figure 2.1: High-level representation of digital twin components.

In this work, we apply the concept of DT to experimental wireless research, and, to the best of our knowledge, in what is the *first example of DTMN for real-world applications*. Figure 2.2 shows a high-level diagram of all main components of our DT representation. Specifically, we develop a set of tools to create and validate a comprehensive digital representation of a particular real-world system inside a virtual environment. This would enable researchers to run wireless experiments inside a DT of virtually any type of physical environment; develop and test new algorithms; and derive results as accurately and as close as possible to the behavior that they would obtain in the real-world environment.

To this aim, we propose Colosseum, the world's largest wireless network emulator [2], as a DT for real-world wireless experimental testbeds and environments. Thanks to its large-scale emulation capabilities, Colosseum twins both the real and digital worlds by capturing conditions of real environments and reproducing them in a high-fidelity emulation. This is done through so-called RF scenarios that model the characteristics of the physical world (e.g., channel effects, propagation environment, mobility, etc.) and convert them into digital emulation terrains to be used for wireless experimentation. Colosseum can also twin the protocol stack itself, i.e., it allows the deployment of the same generic software-defined stacks that can replicate the functionalities of real-world wireless networks, e.g., O-RAN managed cellular protocol stacks [12, 41], orchestrators [42], and different Transmission Control Protocol (TCP) congestion control algorithms [43].

Colosseum is not limited to Software-defined Radio (SDR) devices, but it also supports the integration of Commercial Off-the-Shelf (COTS) devices—as long as they expose RF connectors compatible with those of the Massive Channel Emulator (MCHEM) Universal Software Radio Peripherals (USRP)s, e.g., SMA connectors or equivalent ones—as demonstrated in [44], where System-on-Chip (SoC) boards running OpenWiFi are used. Additionally, custom equipment and

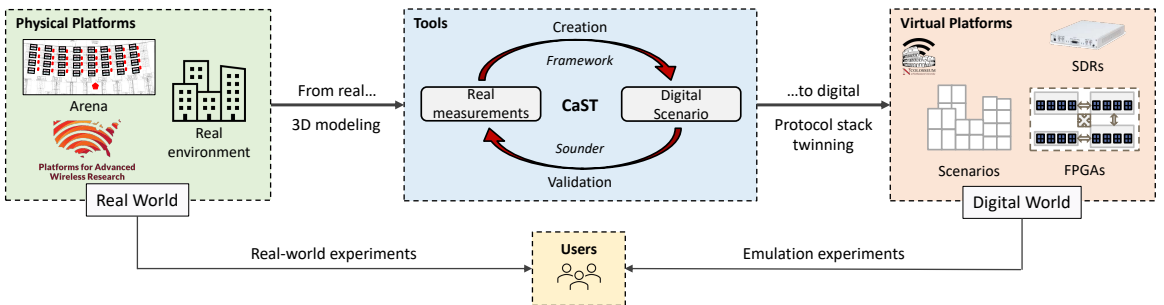


Figure 2.2: Main components of our high-level representation of a DT.

waveforms can be integrated within Colosseum, as demonstrated in prior work where we integrated a proprietary jammer [45], and a radar waveform [16], within the system.

Through the utilization of these scenarios and the twinning of protocol stacks and generic waveforms, users can collect data and test solutions in many different environments representative of real-world deployments, and fine-tune their solutions before deploying them in production networks to ensure they perform as expected. An example of this is provided by [46], where data-driven solutions for cellular networking were prototyped and tested on Colosseum before moving them to other platforms. Overall, this allows users to retain full control over the digitized virtual world, to reproduce all—and solely—the desired channel effects, and to repeat and reproduce experiments at scale. This is particularly important for AI/ML applications [46], where: (i) access to a large amount of data is key to designing solutions as general as possible; and (ii) AI agents need to be thoroughly tested and validated in different conditions to be sure they do not cause harm to the commercial infrastructure.

To enable RF twinning between physical and digital worlds in Colosseum, we utilize our recently developed tool *CaST*, an end-to-end toolchain to create and characterize realistic wireless network scenarios with a high degree of fidelity and accuracy [14]. *CaST* is composed of two main parts: (i) a streamlined framework to create realistic mobile wireless scenarios from real-world environments (thus digitizing them); and (ii) a SDR-based channel sounder to characterize emulated RF channels. The protocol stack twinning is enabled by a Continuous Integration (CI) and Continuous Delivery (CD) platform that can deploy in the Colosseum system the latest, or a specifically desired, version of a wireless protocol stack. We support any software-defined stack that has been designed for real-world experiments and have implemented a specific version of a CI/CD framework for the OpenAirInterface 5G cellular implementation [47].

As proof of concept, we use *CaST* to create the DT of a publicly available over-the-air indoor testbed for sub-6 GHz research, namely Arena [29]. This allows us to showcase the capabilities of Colosseum as a DT platform, as well as the level of fidelity that can be achieved by the twinning process and operations.

2.3 Digital Twin Platforms

In this section, we describe the two platforms that are part of our DT ecosystem: (i) Colosseum, for large-scale emulation/digitization of physical environments, is described in Section 2.3.1; and (ii) Arena, for over-the-air real-world experimentation, in Section 2.3.2.

2.3.1 Large-scale Emulation: Colosseum

Colosseum is the world’s largest publicly available wireless network emulator with hardware-in-the-loop. At a high level, Colosseum consists of five main components, depicted in Figure 2.3 [2]: (i) 128 Standard Radio Nodes (SRNs); (ii) the Massive Channel Emulator (MCHEM); (iii) the Traffic Generator (TGEN); (iv) the GPU nodes; and (v) the management infrastructure.

The Standard Radio Nodes (SRNs), which are divided into four quadrants, comprise 128 high-performance Dell PowerEdge R730 compute servers, each driving a dedicated USRP X310 SDR—able to operate in the [10 MHz, 6 GHz] frequency range—through a 10 Gbps fiber cable. These

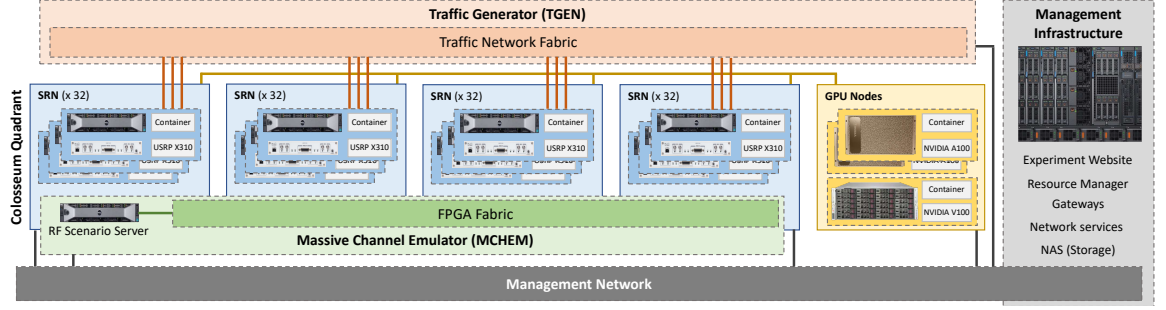


Figure 2.3: Colosseum architecture, adapted from [2].

servers are equipped with Intel Xeon E5-2650 CPUs with 48 cores, as well as NVIDIA Tesla K40m GPUs, to support heavy computational loads (e.g., AI/ML applications) and be able to properly drive their dedicated SDR. Users of the testbed can reserve SRNs for their experiments through a web-based Graphical User Interface (GUI), as well as specify the date/time, and amount of time they need these resources for. At the specified reservation time, Colosseum exclusively allocates the requested resources to the users and instantiates on them a softwarized protocol stack—also specified by the user when reserving resources—in the form of a Linux Container (LXC). After these operations have been carried out, users of the testbed can access via SSH to the allocated SRNs, and use the softwarized protocol stack instantiated on them (e.g., cellular, Wi-Fi, etc.) to drive the SDRs and test solutions for wireless networking in a set of diverse environments emulated by Colosseum.

These environments—called RF scenarios in the Colosseum jargon—are emulated by Colosseum MCHEM. MCHEM is formed of 16 NI ATCA 3671 Field Programmable Gate Array (FPGA) distributed across the four quadrants of Colosseum. Each ATCA module includes 4 Virtex-7 690T FPGAs that process through Finite Impulse Response (FIR) filters the signals from/to an array of USRPs X310 (32 USRPs per MCHEM quadrant, for a total of 128 USRPs across the four quadrants of Colosseum) connected one-to-one, through SMA cables, to the USRPs driven by the SRNs controlled by the users (see Figure 2.4).

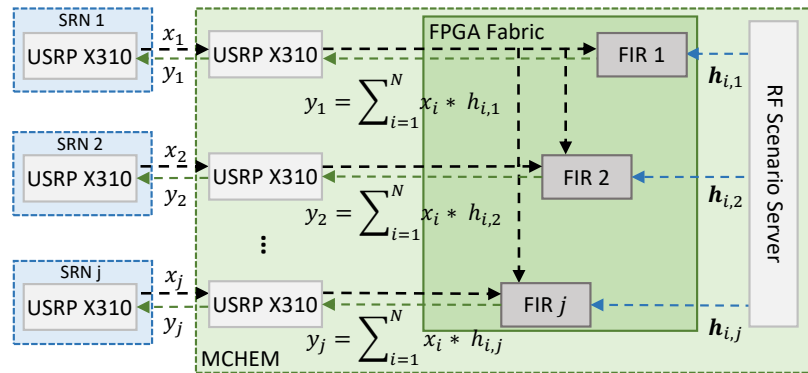


Figure 2.4: FPGA-based RF scenario emulation in Colosseum, from [2].

Instead of being transmitted over the air, signals generated by the SRN USRPs are sent to the

corresponding USRP on the MCHEM side. From there, they are converted in baseband and to the digital domain, and processed by the FIR filters of the MCHEM FPGAs that apply the Channel Impulse Response (CIR) corresponding to the RF scenario chosen by the user of the testbed (see Figure 2.4).

Specifically, these FIR filters comprise 512 complex-valued taps that are set to reproduce the conditions and characteristics of wireless channels in real-world environments, i.e., the CIR among each pair of SRN. As an example, and as depicted in Figure 2.4, signal x_i generated by one of the SRNs is received by the USRP of MCHEM and transmitted to its FPGAs. Here, the FIR filters load the vector $h_{i,j}$ corresponding to the 512-tap CIR between nodes i and j (with $i, j \in \{1, \dots, N\}$ set of SRNs active in the user experiment) from the RF scenario server, which contains a catalog of the scenario available on Colosseum. Then, they apply these taps to x_i through a convolution operation. The signal $y_j = \sum_{i=1}^N x_i * h_{i,j}$ resulting from this operation, i.e., the originally transmitted x_i signal with the CIR of the emulated channel, is finally sent to SRN j . Analogous operations also allow Colosseum to perform superimposition of signals from different transmitters, and to consider interfering signals (besides the intended ones), as it would happen in a real-world wireless environment [48]. In this way, thus, Colosseum can emulate effects typical of real and diverse wireless environments, including fading, multi-path, and path loss, in terrains up to 1 km² of emulated area, and with up to 80 MHz bandwidth, and can support the simultaneous emulation of different scenarios from multiple users. Furthermore, Colosseum is capable of emulating node mobility discretely. Every millisecond, the RF Scenario Server loads different pre-defined channel taps into the Colosseum FPGAs, effectively mimicking changes in channel conditions resulting from node position changes.

Similarly to the emulation of RF environments, the Traffic Generator (TGEN) allows users of the testbed to emulate different IP traffic flows among the reserved nodes. This tool, which is based on the U.S. Naval Research Laboratory's Multi-Generator (MGEN) [49], enables the creation of flows with specific packet arrival distributions (e.g., Poisson, uniform, etc.), packet size, and rate. These traffic flows, namely *traffic scenarios*, are sent to the SRNs of the user experiment that, then, handles them through the specific protocol stack instantiated on the SRNs (e.g., Wi-Fi, cellular, etc.).

Recently, Colosseum added various GPU nodes to the pool of resources that can be reserved by users. These include two NVIDIA DGX servers, state-of-the-art computing solutions with 8 NVIDIA A100 GPUs each and interconnected through a Tbps internal NVlink switching interface, and one large memory node (Supermicro SuperServer 8049U-E1CR4T) with 6 NVIDIA V100 GPUs, 128-core Intel Xeon Gold 6242 CPUs, and 3 TB of RAM. These resources, which can be reserved from the same web-based GUI used for the SRNs, can stream data in real-time from/to the SRNs through high-speed links and have the capability of powering computational-intensive workloads, such as those typical of AI/ML applications.

Finally, Colosseum includes a management infrastructure—not accessible by the users—that is used to maintain the rest of the system operational (see Figure 2.3). Some of the services offered by this include: (i) servers that run the website used to reserve resources on the testbed; (ii) resource managers to schedule and assign SRNs and GPU nodes to users; (iii) multiple Network Attached Storage (NAS) systems to store experiment data and container images; (iv) gateways and firewalls to enable user access and isolation throughout experiments; and (v) precise timing servers and components to synchronize the SRNs, the GPU nodes, and the SDRs.

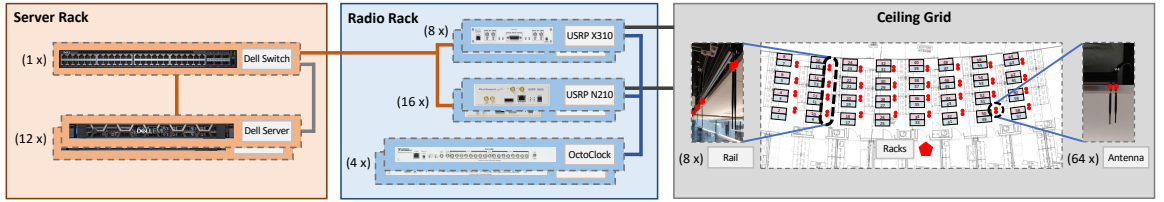


Figure 2.5: Arena architecture.

2.3.2 Over-the-Air Experimentation: Arena

Arena is an over-the-air wireless testbed deployed on the ceiling of an indoor laboratory space [29]. The architecture of Arena is depicted at a high level in Figure 2.5. Its main building blocks are: (i) the ceiling grid; (ii) the radio rack; and (iii) the server rack.

The ceiling grid concerns 64 VERT2450 omnidirectional antennas hung off a 2450 ft² indoor office space. These are deployed on sliding rails and arranged in an 8 × 8 configuration to support Multiple Input, Multiple Output (MIMO) applications. The antennas of the ceiling grid are cabled through 100 ft low-attenuation coaxial cables to the radio rack. This is composed of 24 USRP SDRs (16 USRP N210 and 8 USRP X310) synchronized in phase and frequency through four OctoClock clock distributors. Similarly to the USRPs on Colosseum, these SDRs can be controlled through softwarized protocol stacks (e.g., cellular, Wi-Fi, etc.) deployed on the compute nodes of the server rack, to which they are connected through a Dell S4048T-ON Software-defined Networking (SDN) programmable switch. The server rack includes 12 Dell PowerEdge R340 compute nodes that are powerful enough to drive the SDRs of the radio rack and use them for wireless networking experimentation in a real wireless propagation environment.

Because of the similarities offered by these two testbeds, software containers can be seamlessly transferred between the Colosseum and Arena testbeds with minimal modifications (e.g., specifying the network interface used to communicate with the SDRs), as discussed in Section 2.4.2.) As we will show in Section 2.5, this allows users to design and prototype solutions in the controlled environment provided by the Colosseum *digital twin*, to transfer them on Arena, and to validate these solutions in a real and dynamic wireless ecosystem.

2.4 Digitizing Real-world Environments

The process of digitizing real-world environments into their DT representation is composed of different steps: (i) RF scenario twinning, in which the physical environment is represented into a virtual scenario and validated thereafter; and (ii) protocol stack twinning, in which softwarized protocol stacks are swiftly transferred from the real world to the DT, thus allowing users to evaluate their performance in the designed virtual scenarios. We will describe these steps in the remainder of this section.

2.4.1 RF Scenario Twinning

The RF scenario twinning operations are performed by our Channel emulation generator and Sounder Toolchain (*CaST*) [14], which we made publicly available to the research community.¹ This tool allows users to characterize a physical real-world RF environment and to convert it into its digital representation, to be used in a digital twin, such as the Colosseum wireless network emulator. *CaST* is based on an open SDR-based implementation that enables: (i) the creation of virtual scenarios from physical terrains; and (ii) their validation through channel sounding operations to ensure that the characteristics of the designed RF scenarios closely mirror the behavior of the real-world wireless environment.

2.4.1.1 Scenario Creation

The scenario creation framework consists of several steps that capture the characteristics of a real-world propagation environment and model it into an RF emulation scenario to install on Colosseum. These steps, which are shown in Figure 2.6, concern: (i) identifying the wireless environment to emulate; (ii) obtaining a 3D model of the environment; (iii) loading the 3D model in a ray-tracing software; (iv) modeling nodes and defining their trajectories; (v) sampling the channels between each pair of nodes; (vi) parsing the ray-tracing output of the channel samples; (vii) approximating the obtained channels in a format suitable for the emulation platform (e.g., Colosseum MCHEM FPGAs); and, finally, (viii) installing the scenario on Colosseum.

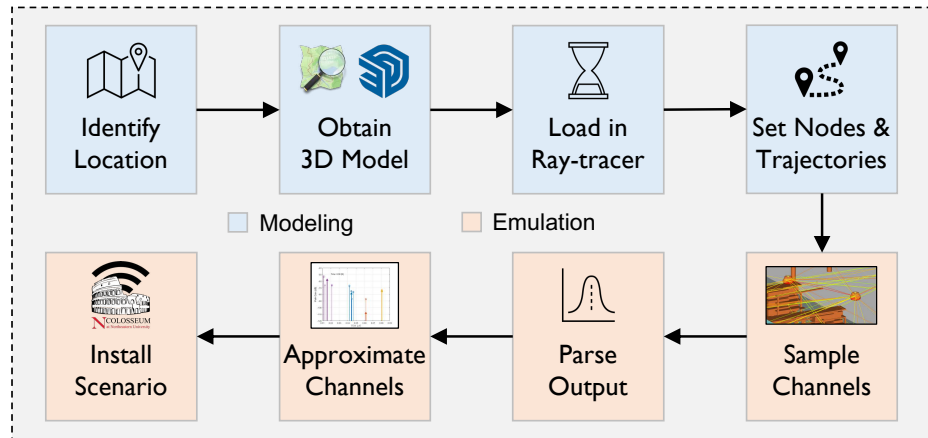


Figure 2.6: CaST scenario creation workflow.

Identify the Wireless Environment. The first step consists of identifying the wireless environment, i.e., the physical location to twin in the channel emulator. The area to model can be of different sizes, and representative of different environments, e.g., indoor (see Section 2.5.4), outdoor (as shown in [14]), urban, or rural.

Obtain the 3D Model. The second step concerns obtaining the 3D model of the area to digitize. This can be obtained from various databases, e.g., OpenStreetMap (OSM), which is publicly available for outdoor environments or it needs to be designed using 3D modeling software, e.g., SketchUp.

¹<https://github.com/wineslab/cast>

Load the Model in the Ray-tracer and Assign Material Properties. The 3D model obtained in the previous step needs to be converted into a file format (e.g., STL) suitable to be loaded into a ray-tracing software, e.g., the MATLAB ray-tracer or Wireless InSite (WI), a commercial suite of ray-tracing models and high-fidelity Electro-Magnetic (EM) solvers developed by Remcom [50]. Each object in the 3D model imported by the ray-tracing software consists of surfaces, and the material properties of these surfaces should be set to have reasonable ray-tracing results. The level of granularity in this step may depend on the ray-tracer platform, e.g., in the WI, the material properties can be assigned to each surface. In the current version of MATLAB ray-tracer, this assignment is limited to the terrain and the buildings. The flexibility in assigning materials with a high level of detail leads to complex structures in the environment objects and accurate ray-tracing results.

Model Nodes and Define Trajectories. Once the 3D model of the environment has been loaded in the ray-tracing software and the material properties are assigned, the radio nodes need to be modeled, which includes setting the nodes' radio parameters, modeling the antenna pattern, and defining locations of the nodes in the physical environment. These nodes can be either static or mobile, in which case their trajectories and movement speeds need to also be defined. The radio parameters of the nodes, e.g., carrier frequency, bandwidth, transmit power, receiver noise figure, ambient noise density, and antenna characteristics, need to be set as well.

Sample the Channels. At this point, the channel is sampled through the ray-tracing software with a predefined sampling time interval T_s , which allows for capturing the mobility of the nodes in a discrete way. To this aim, the node trajectories are spatially sampled with a spacing $D_i = V_i \cdot T_s$, where V_i is the speed of node i . Since spatial consistency plays a key role in providing a consistent correlated scattering environment in the presence of mobile nodes, we follow the 3rd Generation Partnership Project (3GPP) recommendations and consider a coherence distance of 15 m to guarantee an apt spatial consistency [51].

Parse the Output. The next step consists of parsing the ray-tracer output to extract a synchronized channel between each pair of nodes in the scenario for each discrete time instant t spaced at least 1 ms. The temporal characteristic of the wireless channels is considered as a FIR filter, where the CIR is time-variant and expressed by:

$$h(t, \tau) = \sum_{i=1}^{N_t} \tilde{c}_i(t) \cdot \delta(t - \tau_i(t)), \quad (2.1)$$

where N_t is the number of paths at time t , and τ_i and c_i are the Time of Arrival (ToA) and the path gain coefficient of the i -th path, respectively. The latter is a complex number with magnitude a_i and phase φ_i

$$\tilde{c}_i(t) = a_i(t) \cdot e^{j\varphi_i(t)} \quad (2.2)$$

Approximate the Channels. The CIR characterized in the previous steps needs to be converted in a format suitable for MCHEM FPGAs, e.g., 512 channel taps, 4 of which assume non-zero values, spaced with steps of 10 ns and with a maximum excess delay of 5.12 μ s. To do this, we leverage a ML-based clustering technique to reduce the taps found by the ray-tracing software, align the tap delays, and finalize their dynamic range, whilst ensuring the accuracy of the emulated scenario [52].

Install the Scenario. Finally, the channel taps resulting from the previous steps are fed to Colosseum scenario generation toolchain, which converts them in FPGA-friendly format and installs the resulting RF scenario on the DT, ready to be loaded on-demand by the RF Scenario Server.

2.4.1.2 Scenario Validation

Now that the scenario has been created and installed in the DT, we validate its correct functioning through the channel sounder embedded in *CaST* [14]. In doing this, we also ensure that the scenario installed in the DT closely follows the behavior experienced in the real-world environment.

The main steps of *CaST* channel sounder, shown in blue shades in Figure 2.7, are: (i) the transmission of a known code sequence used as a reference for the channel sounding operations; (ii) the reception of the transmitted code sequence, processed by MCHEM through the channel taps of the emulated RF scenario; (iii) the post-processing of the received data and its correlation with the originally transmitted code sequence; and (iv) the validation of the results with the modeled channel taps.

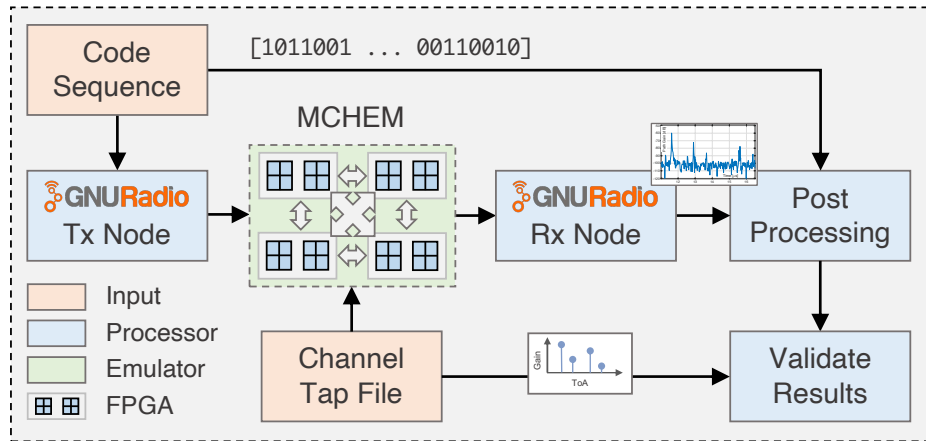


Figure 2.7: CaST channel sounding workflow.

The *CaST* sounder uses a transmitter and a receiver node implemented through the GNU Radio open-source SDR development toolkit [53]. This software toolkit allows implementing and programming SDRs through provided signal processing blocks that can be interconnected to one another.

In our sounding application, the transmitter takes as input a known code sequence—how to derive the specific code sequence is described in Section 2.5.1—and transmits it to the receiver node through the wireless channel emulated by the Colosseum DT through the RF scenario to evaluate. The transmitted signal is composed of sequential repetitions of the code sequence encoded through a Binary Phase-shift keying (BPSK) modulation. While other modulation types are not restricted, we leverage BPSK because it offers sufficient channel information for the sounding in Colosseum. Additionally, it allows for simple data computations that are less susceptible to errors and approximations, resulting in a cleaner and less disrupted signal. Data is streamed to the USRP controlled by the SRN that transmits it to the receiving node through MCHEM. For increased

flexibility of the channel sounder, *CaST* allows users to set various USRP parameters, such as clock source, sample rate, and frequency.

At the receiver side, the SRN USRP samples the signal sent by MCHEM, i.e., the transmitted signal processed with the channel taps of the emulated scenario. This signal is cross-correlated with the originally transmitted known code sequence to extract the CIR $h(t)$ of the emulated scenario, and the Path Loss (PL) $p(t)$. The CIR is then used to obtain the ToA of each multi-tap component of the transmitted signal, which allows measuring the distance between taps, while the PL allows measuring the intensity and attenuation of such components as a function of the time delay. To perform the above post-processing operations, let $c(t)$ be the N -bit known code sequence, and $s^{IQ}(t)$ and $r^{IQ}(t)$ the In-phase and Quadrature (I/Q) components of the transmitted ($s(t)$) and received ($r(t)$) signals, respectively. The I/Q components of the CIR are computed by separately correlating $r^I(t)$ and $r^Q(t)$ (i.e., the I and Q components of $r^{IQ}(t)$) with the I and Q components of $s(t)$ divided by the inner product of the transmitted known sequence with its transpose:

$$h^I(t) = \frac{r^I(t) \otimes s^I(t)}{s^{IT}(t) \times s^I(t)}, \quad (2.3)$$

$$h^Q(t) = \frac{r^Q(t) \otimes s^Q(t)}{s^{QT}(t) \times s^Q(t)}, \quad (2.4)$$

where \otimes is the cross-correlation operation [54] between two discrete-time sequences x and y , which measures the similarity between x and shifted (i.e., lagged) repeated copies of y as a function of the lag k following:

$$\chi(k) = \sum_{n=1}^N x(n) \cdot y(n+k), \quad (2.5)$$

with χ denoting the cross-correlation and N the length of the x sequence. It is worth noticing that if the considered modulation is a BPSK, the denominator is equal to the length N of $c(t)$. The amplitude of the CIR can be computed as:

$$|h(t)| = \sqrt{(h^I(t))^2 + (h^Q(t))^2} \quad (2.6)$$

and the path gains as:

$$G_p(t)[dB] = 20\log_{10}(|h(t)|) - P_t - G_t - G_r, \quad (2.7)$$

where P_t is the power of the transmitted signal, and G_t and G_r are the transmitter and receiver antenna gains expressed in dB.

2.4.2 Protocol Stack Twinning

The twinning of protocol stacks from real to virtual environments (and back) is key in the DT ecosystem, as it allows users to swiftly transfer and evaluate real-world solutions in a controlled setup through automated tools. Twinning at the protocol stack level, combined with the RF scenario twinning discussed in Section 2.4.1, makes it possible to seamlessly prototype, test, and transition

end-to-end, full-stack solutions for wireless networks to and from digital and physical worlds. After validation in the controlled environment of the DT—to make sure whatever is tested works as expected—the protocol stack solutions can be transitioned back to real-world deployments where they are ultimately used on a production network. As an example, in our prior works [46, 41], we have shown how AI solutions for 5G cellular networks trained and tested on the digital twin environment—Colosseum—can be effective and also work on real-world environments—Arena and the PAWR platforms [26].

At a high level, the twinning of the protocol stack involves: (i) tracking one or multiple remote, centralized version control systems that host the code of the protocol stack; and (ii) providing pipelines that can automatically replicate the same software build in the digital and physical domains. In addition, it is possible to embed automated steps for the performance validation (i.e., profiling of relevant performance metrics), similar to the scenario validation step of *CaST*.

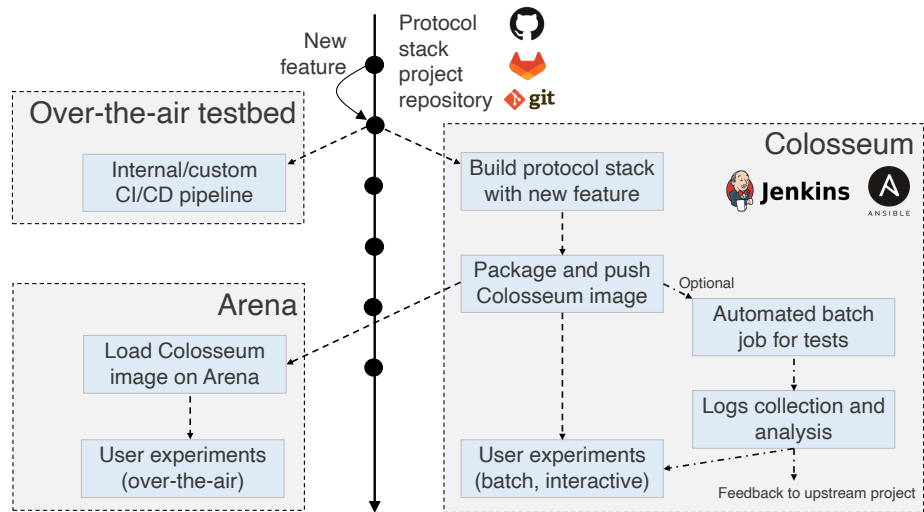


Figure 2.8: Protocol stack twinning workflow across a digital environment, i.e., Colosseum, and two physical environments, i.e., Arena and a generic over-the-air testbed.

Figure 2.8 illustrates how the protocol stack twinning is implemented in Colosseum (right), with extensions to a generic over-the-air testbed (top left) and the specific integration with Arena (bottom left). The figure refers to a project repository for a sample protocol stack, hosted on a versioning platform that supports the `git` version control system (e.g., GitHub, GitLab, among others). In Colosseum, we implemented this pipeline for the OpenAirInterface reference stack for 5G base stations and UEs, and are working toward the integration of additional components for O-RAN testing [46].

Whenever a new feature (i.e., a commit on selected branches, or a pull request) is pushed to the target project repository, a CI/CD framework implemented with Jenkins and Ansible triggers the automated process in the digital Colosseum domain. Specifically, Jenkins monitors the remote repository and orchestrates the kickoff of the build job, and Ansible applies the relevant configuration parameters to the machine that actually executes the build job (e.g., a Colosseum SRN or a dedicated virtual machine on AWS). Once the build is successful, the Jenkins job packages the output of the

process into an LXC image which is stored on the Colosseum NAS.

Once this is done, Colosseum can be further used to perform automated testing, e.g., to automatically test solutions and algorithms on the DT and collect relevant metrics from such experiments. These can be shared with the relevant stakeholders, e.g., the developers of the protocol stack framework being deployed and tested. Moreover, since no over-the-air transmissions happen in Colosseum, as the channels are emulated through MCHEM (see Section 2.3.1), this DT environment enables users to test networking solutions over frequencies and bandwidths that would normally require compliance with the Federal Communications Commission (FCC) regulations.

Finally, the image with the relevant components can be used by experimenters in Colosseum or moved to the physical domain, e.g., Arena, for validation on a real-world infrastructure. In addition, the protocol stack can be twinned in other over-the-air testbeds following their internal and custom CI/CD pipelines, as long as the centralized repository that the different testbeds track provides shared specifications for the build environment (e.g., operating system, compiler versions, packages, etc.). As an example, the Colosseum protocol stack twinning process already replicates internal CI/CD pipelines used in the Eurecom/OpenAirInterface facilities [55].

2.5 Experimental Evaluation

This section discusses the capabilities of our DT system through experimental evaluations, and it is organized as follows: (i) we showcase *CaST* tuning process (Section 2.5.1); (ii) we leverage *CaST* to validate Colosseum scenarios, both with single and multiple taps (Section 2.5.2); (iii) we present a ray-tracing V2X use-case scenario in Tampa, FL and validate its emulated channels on Colosseum (Section 2.5.3); (iv) we describe the Arena scenario designed as part of this work (Section 2.5.4); (v) we compare some experimental use cases (e.g., for cellular networking and Wi-Fi applications) both in the Arena testbed and in its DT representation (Section 2.5.5).

2.5.1 CaST Tuning

As a first step, we tune *CaST* parameters and configurations (see Section 2.4.1) outside the Colosseum channel emulator to identify a code sequence with high auto-correlation and low cross-correlation between transmitted code sequence and received signal which functions well within our combination of software and hardware. It is worth noting that the tuning of *CaST* is a one-time operation, and it would need to be repeated only upon changes in the Colosseum hardware (e.g., radio devices and channel emulation system). This step, which is key for *CaST* to be able to derive taps from arbitrary CIRs, is performed in the controlled environment shown in Figure 2.9.

This consists of two USRP X310 SDRs equipped with a UBX-160 daughterboard and synchronized in phase and frequency through an OctoClock clock distributor to mirror the same deployment used in Colosseum. Differently from the Colosseum deployment, however, the two USRPs are connected through a 12 inches SMA cable, and 30 dB attenuators (to shield the circuitry of the daughterboard from direct power inputs, as indicated in their datasheet). This is done to derive the above-mentioned code sequences in a baseline and controlled setup without additional effects introduced by over-the-air wireless channels, or channel emulators. The USRPs are connected through a network switch to a Dell XPS laptop, used to drive them. The sounding parameters used

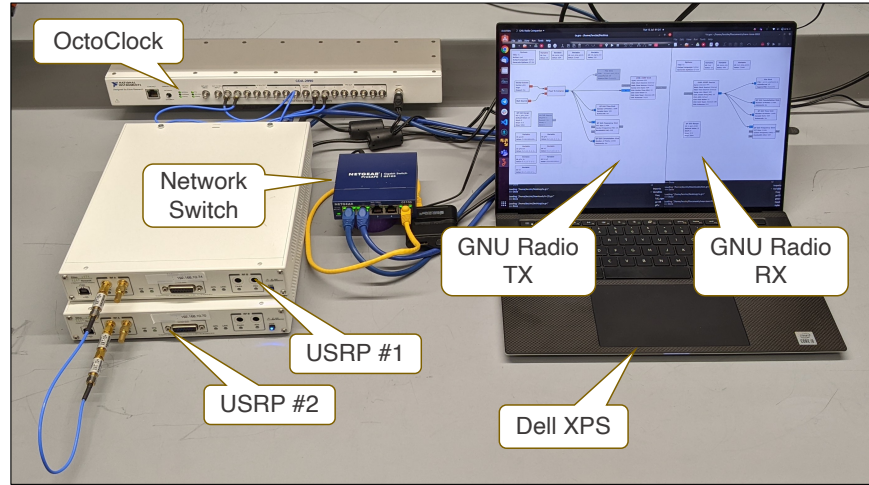


Figure 2.9: Controlled laboratory environment used for the *CaST* tuning process.

in this setup are summarized in Table 2.1. We consider different values for the gains of the USRPs (i.e., in $[0, 15]$ dB) to evaluate their effect on the sounding results. The receiving period time and data acquisition are set to 3 s.

Table 2.1: Configuration parameters used in the controlled laboratory setup.

Parameter	Value
Center frequency	1 GHz
Sample rate	$[1, 50]$ MS/s
USRP transmit gain	$[0, 15]$ dB
USRP receive gain	$[0, 15]$ dB

Finding the Code Sequence. Code sequences have been widely investigated in the literature because of their role in many different fields [56, 57]. Good code sequences achieve a high auto-correlation (i.e., the correlation between two copies of the same sequence), and a low cross-correlation (i.e., the correlation between two different sequences). For our channel-sounding characterization, we consider and test four different code sequences by leveraging the laboratory environment shown in Figure 2.9:

- *Gold sequence.* These sequences are created by leveraging the XOR operator in various creation phases applied to a pair of codes, u , and v , which are called a preferred pair. This pair of sequences must satisfy specific requirements to qualify as suitable for a gold sequence, as detailed in [58]. Gold sequences have small cross-correlation within a set, making them useful when more nodes are transmitting in the same frequency range. They are mainly used in telecommunication (e.g., in Code-Division Multiple Access (CDMA)) and in satellite navigation systems (e.g., in GPS). In this work, we use a Gold sequence of 255 bits generated with the MATLAB Gold sequence generator system object with its default first and second

polynomials, namely $z^6 + z + 1$ and $z^6 + z^5 + z^2 + z + 1$, for the generation of the preferred pair sequences.

- *Golay complementary sequence.* Being complementary, these sequences have the property that the sum of their out-of-phase aperiodic auto-correlation coefficients is equal to 0 [59]. Their applications range from multi-slit spectrometry and acoustic measurements to Wi-Fi networking and Orthogonal Frequency Division Multiplexing (OFDM) systems. In our tests, we use a 128-bit type A Golay Sequence (Ga_{128}) as defined in the IEEE 802.11ad-2012 Standard [60].
- *Loosely Synchronised (LS) sequence.* These sequences exhibit the property of reaching very low auto-correlation and cross-correlation values in a certain portion of time, based on the maximum delay dispersion of the channel, called Interference Free Window (IFW). This allows the mitigation of the interference if the maximum transmission delay is smaller than the IFW length. In our experiments, we use an LS sequence generated following the directions in [61], and only leveraging the first codeset of $\{-1, 1\}$ without including the IFW.
- *Galois Linear Feedback Shift Register (GLFSR) sequence.* These sequences add time offsets to Linear Feedback Shift Register (LFSR) codes by leveraging extra XOR gates at the output of the LFSR. This allows to achieve a higher degree of randomness if compared to the classic LFSR, making them more efficient and fast in detecting potential faults with increased auto-correlation results [62]. In this work, we leverage GNU Radio to generate a 255-bits sequence with the following parameters: shift register degree 8, bit mask 0, and seed 1.

Each of these sequences has been separately used by the transmitter node to construct the sending signal and to send it to the receiver node with a sample rate of 1 MHz. After that, the receiver node performs the post-processing operations. Results of $800 \mu s$ CIR for each code sequence are shown in Figure 2.10. We can notice that all code sequences are able to correctly identify the starting position of the transmitted signal, as shown by the peak values. The distance D_{peak} of each peak can be written as a function of the code length N and the sampling rate SR .

$$D_{peak} = \frac{N}{SR} \quad (2.8)$$

Therefore, D_{peak} is equal to $255 \mu s$ for the Gold, LS, and GLFSR codes, each showing 3 transmitted sequences in Figure 2.10, and to $128 \mu s$ for the Ga_{128} code, which displays 6 sequences instead. We notice that GLFSR shows the highest auto-correlation and lowest cross-correlation among the four considered code sequences. This results in an overall cleaner CIR. For these reasons, we adopt the GLFSR code sequence in our experimental evaluation through *CaST*.

CaST Validation in a Laboratory Environment. After identifying the code sequence for our application, we evaluate *CaST* in the laboratory setup shown in Figure 2.9. To this aim, we test our sounder with a GLFSR code sequence and various configuration parameters, e.g., sample rate, center frequency, and antenna gains, to study its behavior and gather reference information to be leveraged in the Colosseum experiments. Figure 2.11 shows a time frame of the received path gains for the case with 0 dB (blue line in the figure), and 30 dB total transmit and receive gains (15 dB at both transmitter and receiver sides, orange line).

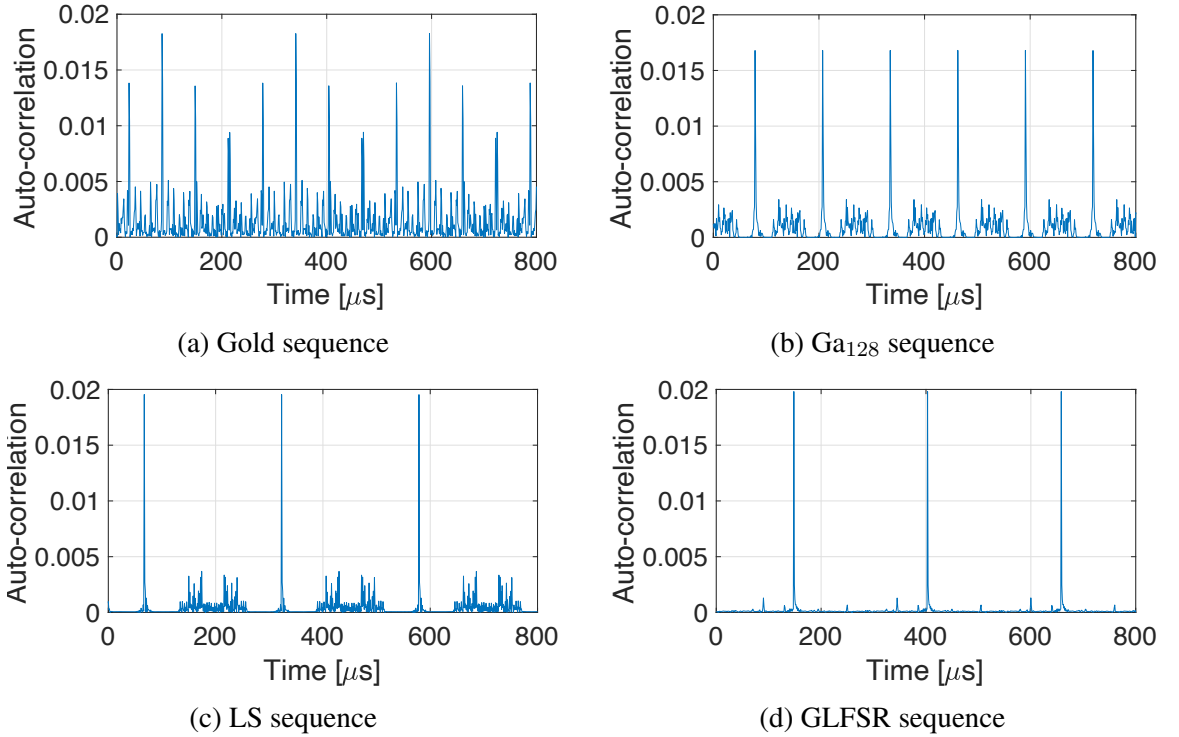


Figure 2.10: Correlation of different code sequences in the controlled laboratory environment.

The figure shows signals that repeat based on the length of the transmitted code sequence, i.e., every 255 sample points (or equivalently every 255 μ s, since one point equals to $1/\text{sample_rate} = 1 \mu\text{s}$). The peaks represent the path loss of the single tap of this experiment, which are equal to 34.06 dB for the 0 dB case, and 5.24 dB for the 30 dB case. Since we have 30 dB attenuation in this validation setup, these results are in line with our expectations (with some extra loss due to the physical components of the setup, e.g., cable attenuation and noise). We also notice that in the 30 dB case, the measured loss is slightly more severe due to imperfections in the power amplifiers of the USRPs. We use these results as a reference for our channel-sounding operations.

2.5.2 Validation of Colosseum Scenarios through CaST

After the tuning and validation in the controller laboratory environment, we can leverage *CaST* to validate the behavior of Colosseum MCHEM. We deploy the *CaST* sounder on the Colosseum wireless network emulator by creating an LXC container from the open-source *CaST* source code. This container, which has been made publicly available on Colosseum, contains all the required libraries and software to perform channel-sounding operations, as well as for the post-processing of the obtained results. This enables the re-usability of the sounder with different SRNs and scenarios, as well as portability to different testbeds (e.g., to the Arena testbed described in Section 2.3.2). It also allows the automation of the channel sounding operations through automatic runs supported by Colosseum, namely *batch jobs*.

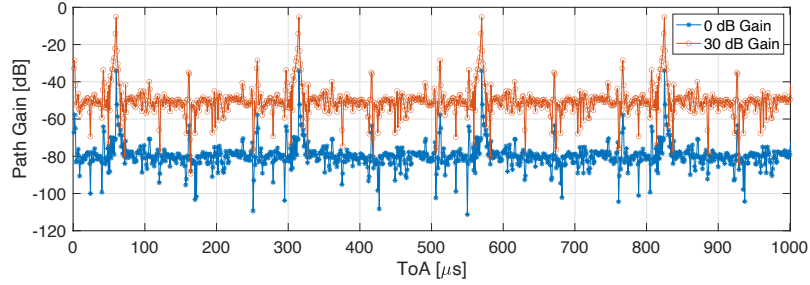


Figure 2.11: Received path gains in the controlled laboratory environment with 0 and 30 dB total transmit and receive gains use cases (15 dB at both transmitter and receiver sides).

To achieve our goal of characterizing MCHEM, we test a set of synthetic RF scenarios (i.e., single- and multi-tap RF scenarios) on Colosseum, i.e., scenarios created specifically for the purpose of channel sounding. These scenarios have been manually generated with specific channel characteristics to validate the behavior of MCHEM, and have been made publicly available for all Colosseum users. The parameters used in this evaluation are the same as the ones in Table 2.1 with the only exception of the sample rate that is set at 50 MS/s to have a 20 ns resolution (thus being able to properly retrieve tap delays and gains), and the GLFSR code sequence found above.

Single-tap Scenario. The first synthetic RF scenario that we consider is a single-tap scenario with nominal 0 dB path loss (i.e., 0 dB of path loss added to the inherent loss of the hardware components of the testbed). To find the base loss of MCHEM, i.e., the loss due to Colosseum hardware-in-the-loop, we instantiate *CaST* on 10 SRNs, and sound the channels among them, measuring the path loss of each link, shown in Figure 2.12.

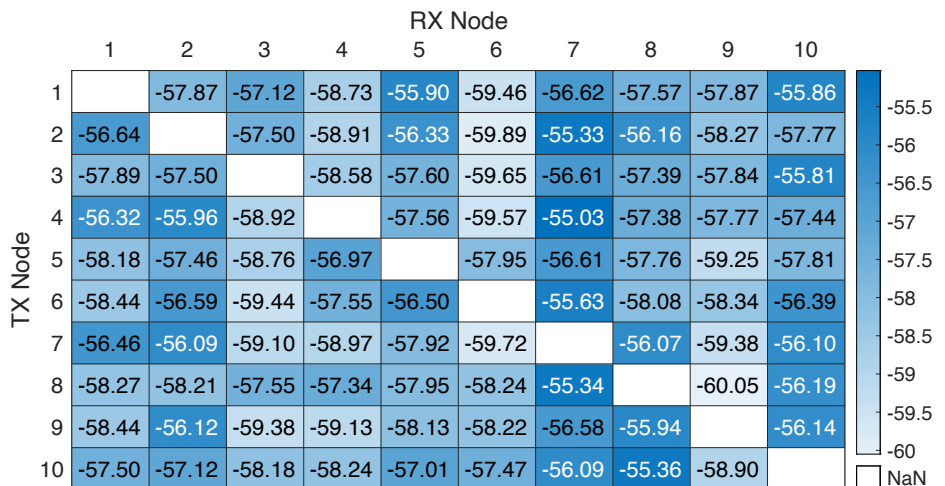


Figure 2.12: Path loss heatmap as measured by *CaST* in a 0 dB Colosseum RF scenario with 10 SRNs.

Each cell in the figure represents the average path loss for 2 s of reception time between transmitter (row) and receiver (column) nodes. Results show an average Colosseum base loss of 57.55 dB with a

Standard Deviation (SD) of 1.23 dB. We also observe that the current dynamic range of Colosseum is approximately 43 dB, i.e., between the 57.55 dB base loss at 1 GHz and the noise floor of -100 dB.

Multi-tap Scenario. The second synthetic RF scenario that we consider is a four-tap scenario in which taps have different delays and path gains. We characterize such a scenario on Colosseum through *CaST* channel sounding operations. Results for the emulated and modeled path gains for a single time frame are shown in Figure 2.13 in blue and orange, respectively.

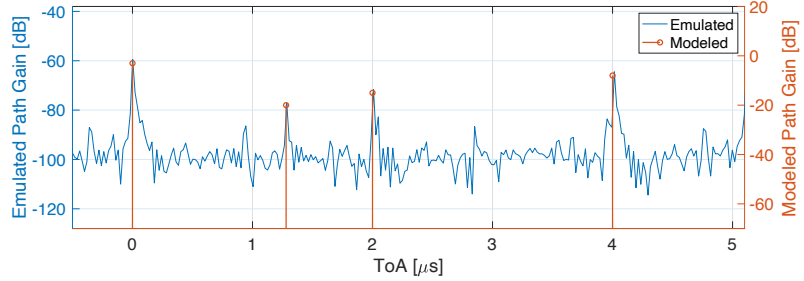


Figure 2.13: Comparison between emulated and modeled path gains in Colosseum for a single time frame.

We notice that the ToAs match between the modeled CIR and the taps emulated by the Colosseum RF scenario, namely they occur at 0, 1.28, 2, and $4\ \mu\text{s}$. We also notice that the received powers are in line with our expectations. Indeed, by adding the Colosseum base loss computed in the previous step to the power measured by *CaST* (in blue in the figure), we obtain the modeled taps (corresponding to -3 , -20 , -15 , and -8 dB, shown in orange in the figure).

We now analyze the accuracy of the measurements performed with *CaST* by computing the relative difference between the emulated taps over time. We do so by considering 1,500 time frames. Results show that the average difference between the strongest tap of each time frame is in the order of 10^{-6} dB, with a SD of 0.03 dB. Analogous results occur for the second tap—which is the weakest tap in our modeled CIR—with a SD of 0.17 dB, and for the third and fourth taps. Finally, differences between the first and second taps of each time frame (i.e., between strongest and weakest taps in our modeled CIR) amount to 0.52 dB with a SD of 0.18 dB. These results are a direct consequence of the channel noise, which impacts weaker taps more severely.

Overall, results demonstrate MCHEM accuracy in emulating wireless RF scenarios in terms of received signal, tap delays, and gains. This also shows *CaST* effectiveness in achieving a 20 ns resolution, thus sustaining a 50 MS/s sample rate, and a tap gain accuracy of 0.5 dB, which allows *CaST* to capture even small differences between the modeled and emulated CIR.

2.5.3 A V2X Use-Case Scenario in Tampa, FL

2.5.3.1 V2X Scenario Description

We consider a scenario around the Tampa Hillsborough Expressway in Tampa, FL. In order to simulate the scenario in WI, we need a 3D model of the wireless environment. We obtained such a model from OSM in XML format and converted it to an STL file, which is supported by WI. The resulting scenario is depicted in Figure 2.14.

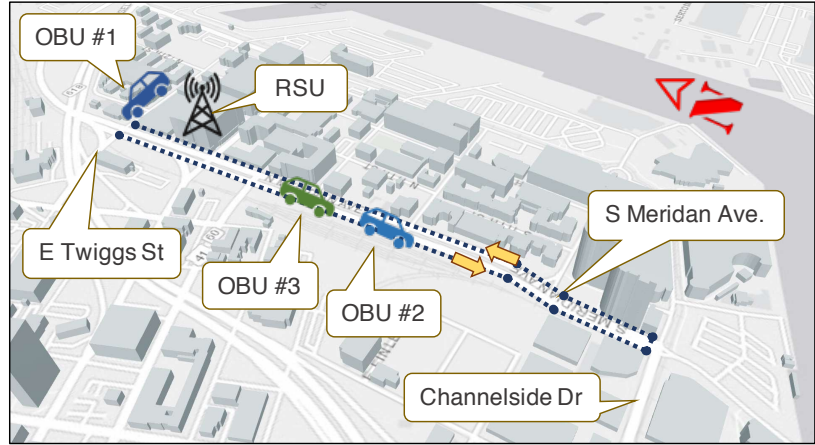


Figure 2.14: Tampa, FL, V2X scenario simulation environment in WI.

In this scenario, we consider a Vehicle-to-everything (V2X) model with four nodes. One is a Road-Side Unit (RSU) mounted on the traffic light at the intersection of E. Twiggs St. and N. Meridan Ave. The other three nodes are Onboard Units (OBUs) installed on three vehicles: one is stationary and parked in the parking lot of the Tampa Expressway Authority; the other two vehicles are following each other at a constant speed of 25 Mph on Meridan Avenue, from E. Twiggs St. to Channelside Dr., and then back to E. Twiggs St. (Figure 2.14). The radio parameters of the nodes are listed in Table 2.2.

Table 2.2: Wireless parameters for the Tampa simulation scenario.

Parameters	Values for V2X
Carrier frequency	5.915 [GHz]
Signal bandwidth	20 [MHz]
Transmit power	20 [dBm]
Antenna pattern	Omnidirectional
Antenna gain	5 [dBi]
Antenna Height	RSU: 16 [ft], OBUs: 5 [ft]
Ambient noise density	-172.8 [dBm/Hz]

2.5.3.2 V2X Mobile Scenario Validation

In this set of experiments, we test the V2X mobile use-case DT in Tampa, FL. This scenario has been installed in Colosseum, with an increase of 60 dB across all taps, to fall within the Colosseum dynamic range. The parameters for the sounding process are the same as those listed in Table 2.1 with 15 dB gains and 10 MS/s sample rate. Since the total scenario time is 175 s and processing all the data together would require extreme memory, the rx time is divided into three chunks of around 60 s each. In this way, each chunk is around 5 GB in size, and it takes about 30 minutes to be processed. The results from each chunk are cleaned and merged to produce the final outcome. The

received path gains have been adjusted by removing the Colosseum base loss and adding the original 60 dB increase. Figure 2.16b shows how the received path gains (xy-axis) vary over the scenario time (z-axis). We can notice that the strongest tap resembles the same ‘V-shape’ behavior seen in the original tap representation (Figure 2.16a) as a direct consequence of the movement to and from the static RSU node. Moreover, Figure 2.15 shows the link path loss of node 1 (RSU) and mobile node 3 (OBU#2) against the mobile node 4 (OBU#3).

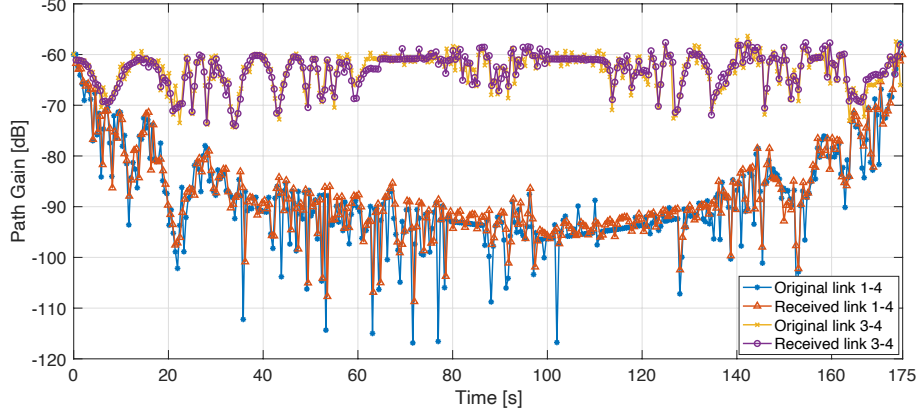


Figure 2.15: Comparison between original and received path gains for OBU#3 (node 4) against RSU (node 1) and OBU#2 (node 3).

The original and received results are fluctuating due to multi-path fading, but they align almost perfectly. In this case, for links 1-4, a very similar received-power trend with a convex ‘U-shape’ is noticeable. The mobile node first moves away from the RSU, heading south, decreasing the gains and increasing the ToA. Then the pattern reverses as the vehicle turns around and travels back to the intersection and the RSU. On the other hand, links 3-4 exhibit a more stable trend because the two vehicle nodes travel together. These results confirm that Colosseum emulates the channel correctly even in a mobile scenario and validate the twinning capabilities of *CaST* of creating DTs even when the metrics change over time.

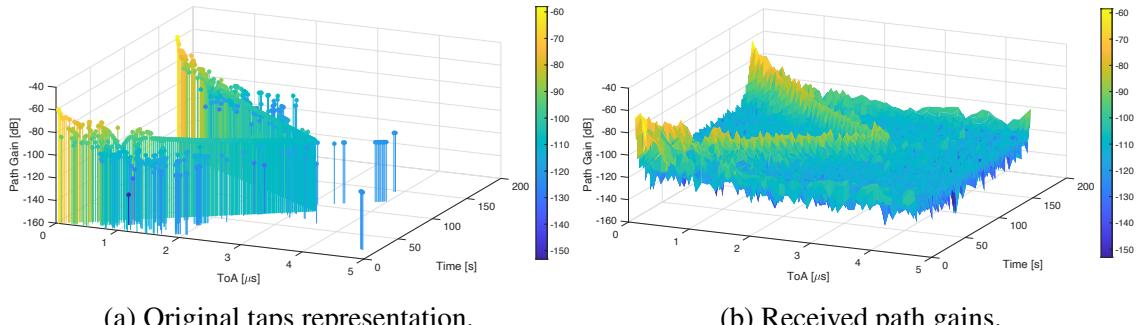


Figure 2.16: Results comparison for the mobile use case scenario.

2.5.4 Arena Digital Twin Scenario

We use Sketchup [63] software to create a 3D representation of the Arena testbed. This software allows users to model a broad range of environments starting from an architectural layout (e.g., of the Arena testbed, a picture of which is shown in Figure 2.17a), and with different surface renderings, e.g., glass walls and windows, wooden walls, carpeted floors [63]. The resulting 3D model (shown in Figure 2.17b) is then fed to the ray-tracing software, Wireless inSite [50] in this case, to create a DT scenario on Colosseum following the steps described in Section 2.4.1.

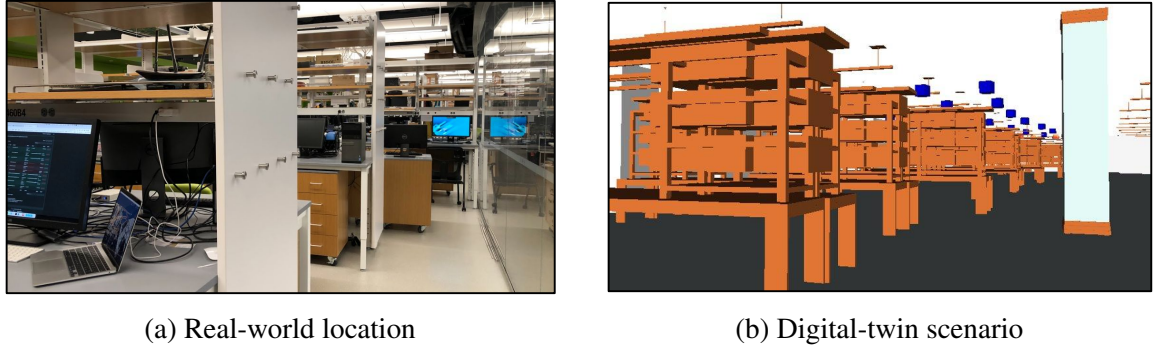


Figure 2.17: The conversion from a real-world location, into a digital medium scenario used to create the digital twin representation.

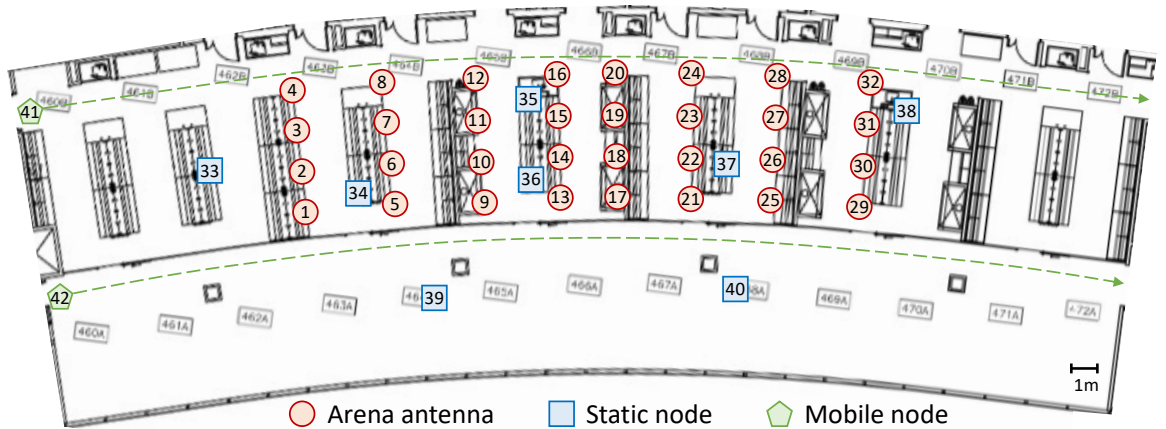


Figure 2.18: Location of the nodes in an Arena DT scenario.

For the developed Arena scenario, we model the antenna points of the Arena testbed in 32 locations (one for each antenna pair), as well as 8 static nodes distributed in their surroundings, and 2 mobile nodes traversing the laboratory space at a constant speed of 1.2 m/s. The height of the nodes (both static and mobile) is set to 1 m, e.g., to emulate handheld devices, or devices lying on table surfaces. The modeled locations and nodes are shown in Figure 2.18, where the red circles represent the antenna pairs of Arena, while the blue squares and green pentagons identify the static and mobile nodes, respectively. The dashed green arrows denote the movement direction of the

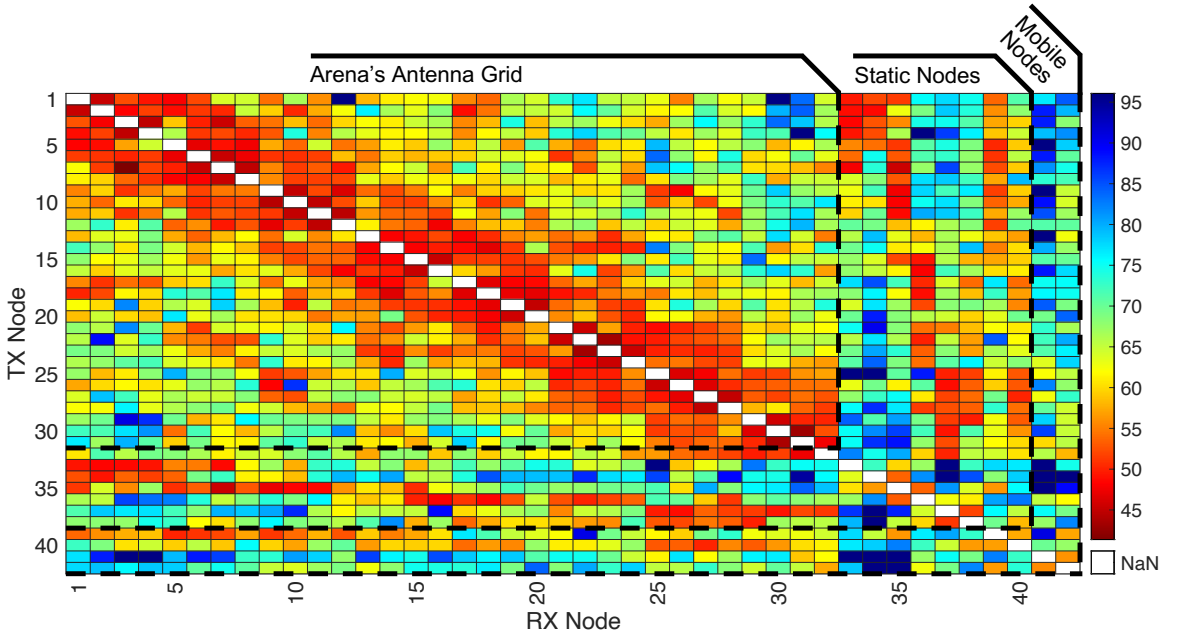


Figure 2.19: Heat map of the path loss among the nodes of Figure 2.18, with a line separator between antenna, static, and mobile. The mobile nodes are considered in the starting position on the left.

mobile nodes. By using a Dell T630 machine with 2 Xeon E52660 14 cores CPU, 128 GB RAM, and Tesla K40 GPU, the ray-tracing operations of this scenario took 14 h and 21 m, while the channel approximation process 2 h and 33 m. Additionally, the installation process in Colosseum required around 19 h and 30 m by leveraging a virtual machine hosted on a Dell PowerEdge M630 Server with 24 CPU cores and 96 GB of RAM. It is worth noting that these are one-time operations, and the scenario is played on demand right away afterward.

Figure 2.19 shows the heat map of the path loss among the transmit-receive node pairs (the mobile nodes are considered in the starting position on the left). As expected, closer nodes experience a lower path loss, which increases with the distance between the nodes. A similar trend is also visible for the static nodes, even though this is less noticeable due to their scattered locations. On the other hand, due to their remote starting locations on the side of the room, the mobile nodes exhibit a very high path loss against all nodes, as depicted in Figure 2.19. These path losses decrease as they get closer to each node on their path, and increase again while reaching their end locations on the other side of the room.

2.5.5 Arena Digital Twin Experimental Use Cases

In this section, we show outcomes of relevant experimental use cases run on both the Arena testbed, as well as on its DT representation. The first use case involves the deployment of a cellular networking system using the srsRAN software suite, while the second one encompasses a Wi-Fi adversarial jamming use case built on GNU Radio.

2.5.5.1 Cellular Networking

Single BS. In the first cellular networking use case, we leverage SCOPE [64]—an open-source framework based on srsRAN [65] for experimentation of cellular networking technologies—to deploy a twinned RAN protocol stack with one Base Station (BS) and three UEs in the Arena over-the-air testbed and in the Colosseum emulation system. The same node positions, shown in Figure 2.20, are used in the two platforms: the BS, which transmits over a 10 MHz spectrum, is located on node 12, two static UEs on nodes 34 and 37, and one mobile UE on node 41. In Arena, UEs are implemented through commercial smartphones (Xiaomi Redmi Go), while on Colosseum, they are deployed on the SDRs of the testbed.

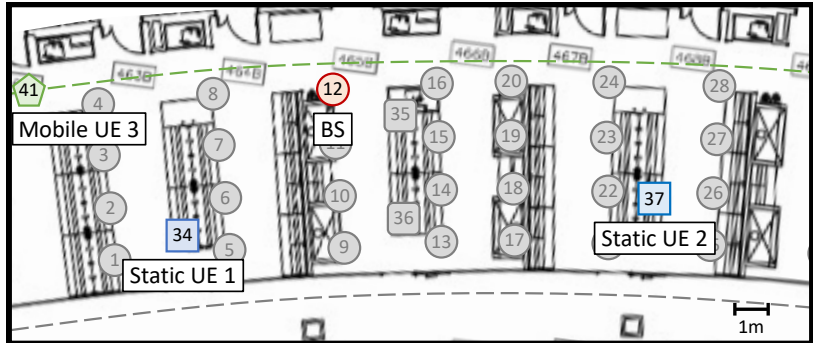


Figure 2.20: Location of the nodes in the cellular experiment.

We conduct two experiments on each system: the first one involves a downlink User Datagram Protocol (UDP) traffic sent at a 5 Mbps rate; the second one TCP downlink traffic. The traffic generation for each experiment is achieved using iPerf, a benchmarking tool designed for assessing the performance of IP networks [66]. The following results show the average of at least 5 separate experiment realizations.

Figure 2.21 shows the UDP downlink throughput for static (blue and orange lines), and mobile (yellow line) nodes on the Arena (Figure 2.21a) and Colosseum (Figure 2.21b) testbeds. We can notice similar trends and patterns exhibited on both testbeds. Specifically, the throughput of the static nodes remains stable around 5 Mbps in both Colosseum and Arena, where we notice a less stable behavior due to the use of over-the-air communications, and potential external interference. As expected, the throughput of the mobile node—that starts from the top-left location shown in Figure 2.20 and travels to the right along the trajectory depicted with the green line in the figure—increases as the node gets closer to the BS (where it reaches a 5 Mbps peak), and then decreases as the node gets farther away.

Figure 2.22 and Figure 2.23 plot the TCP downlink throughput and SINR results of the second experiment for static (blue and orange) and mobile (yellow) nodes on Arena (Figure 2.22a and Figure 2.23a) and Colosseum (Figure 2.22b and Figure 2.23b). Also in this use case, a similar pattern is clearly noticeable. In particular, the two static nodes maintain a relatively stable throughput of the nominal 5 Mbps TCP traffic on both testbeds with no apparent impact during the passage of the mobile UE close to the static UEs, which in the Arena case is moved manually. This behavior is visible in the SINR results, which show a decrease due to the created interference when the mobile

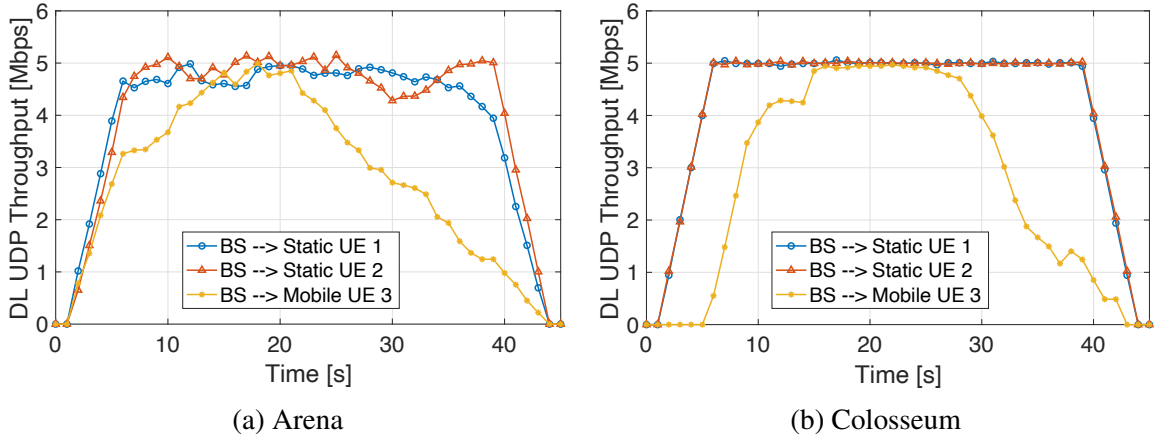


Figure 2.21: UDP downlink throughput of the cellular use case on the Arena and Colosseum testbeds.

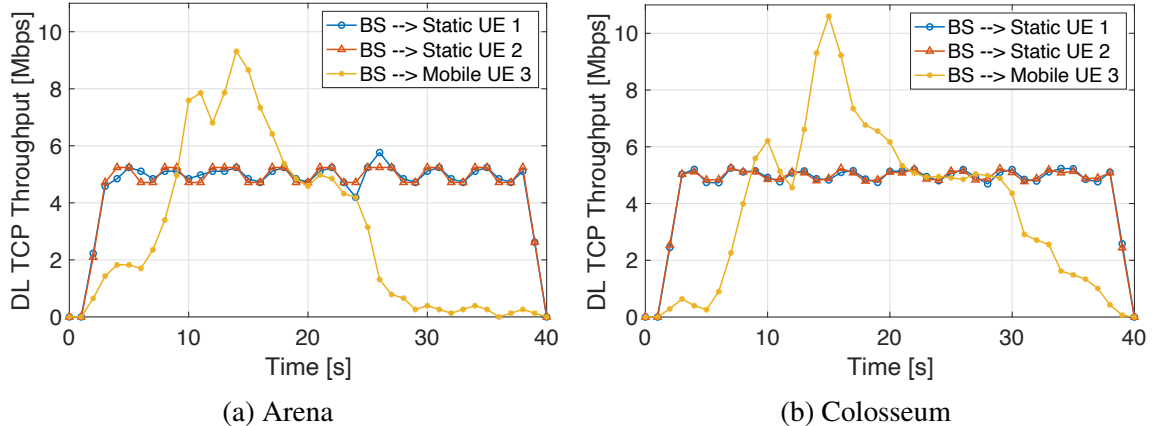


Figure 2.22: TCP downlink throughput of the cellular use case on the Arena and Colosseum testbeds.

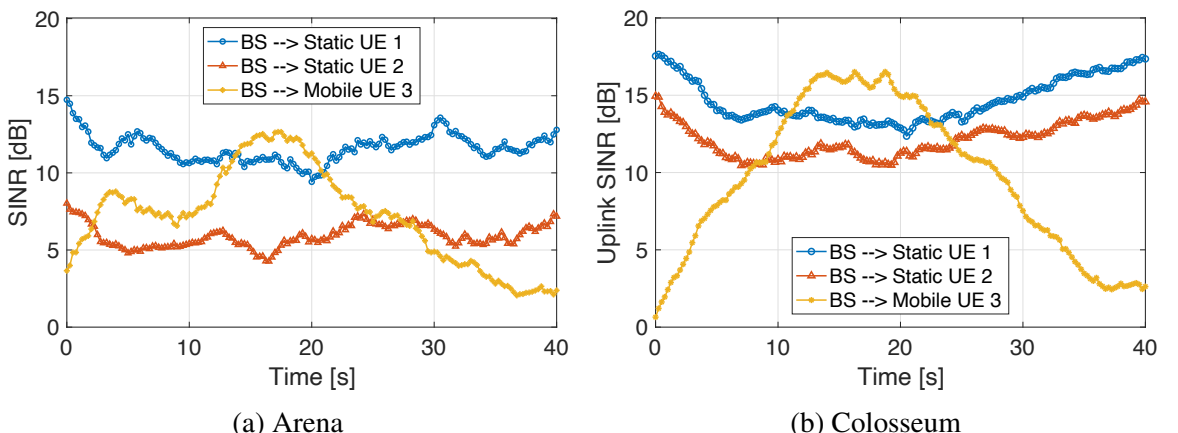


Figure 2.23: TCP SINR of the cellular use case on the Arena and Colosseum testbeds.

node approaches each of the static UEs. The mobile node exhibits a similar trend with two high peaks in throughput on both systems. These peaks can be attributed to the TCP protocol, which retransmits data to ensure delivery in case of packet failures as soon as the signal improves, resulting in higher application throughput values compared to the nominal 5 Mbps. Specifically, each peak corresponds to the time right after the mobile device transitions close to static node 1 (around time 10 s), and then to static node 2 (around time 15 s). Due to the increased interference, the mobile node loses more packets, which will eventually be retransmitted.

Multiple BSs. In the second cellular networking use case, we use a similar setup as for the first experiment by leveraging SCOPE and Xiaomi Redmi Go phones to deploy a twinned srsRAN protocol stack with two BSs located in positions 10 (BS 1) and 25 (BS 2), as shown in Figure 2.24. We assign three UEs to each BS, for a total of 6 UEs (i.e., the number of smartphones currently at our disposal). Specifically, UE 1, UE 2, and UE 3 are assigned to BS 1, while UE 4, UE 5, and UE 6 are assigned to BS 2.

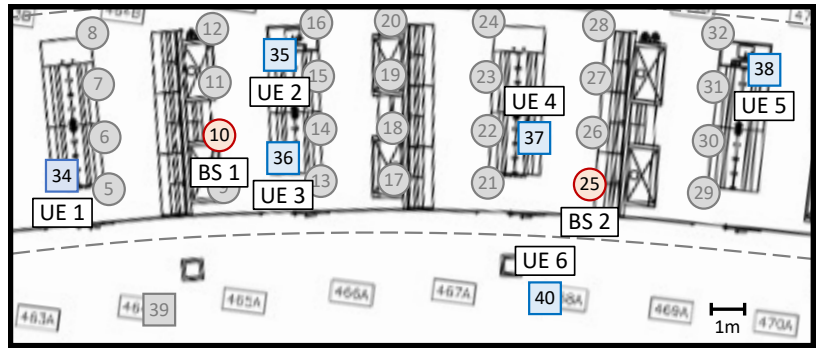


Figure 2.24: Location of the nodes in the multiple BSs cellular use-case, consisting of 2 BSs (BS 1, BS 2), and 6 static UEs, equally assigned to each BS: UE 1, UE 2, and UE 3 for BS 1; UE 4, UE 5, and UE 6 for BS 2.

Once each UE has completed the attachment procedures, we initiate a continuous 5 Mbps UDP downlink traffic stream from each smartphone using iPerf towards its corresponding BS. Figure 2.25 shows the average downlink throughput results over a period of more than 30 minutes of data collection, along with 95% confidence intervals. These metrics are collected at the data-link layer at the BS level through the SCOPE framework. We observe that all UEs are able to consistently ensure the 5 Mbps throughput with a very low 95% confidence interval showing an average margin of error of 0.02 Mbps. This demonstrates the accuracy of the digital twin representation, even in the presence of multiple BSs and UEs, showcasing the scalability of our DTMN.

Comparison. By analyzing the results after the UEs have completed the attachment procedures, we can assess the similarity between the two testbeds by following

$$\rho(k) = \frac{\sum_{n=1}^N (x(n) - \bar{x})(y(n+k) - \bar{y})}{\sqrt{\sum_{n=1}^N (x(n) - \bar{x})^2 \sum_{n=1}^N (y(n) - \bar{y})^2}}, \quad (2.9)$$

which measures the normalized cross-correlation $\rho(k)$ between the Arena data sequence, denoted as $x(n)$, and shifted lagged copies of the Colosseum data sequence, denoted as $y(n)$, as a function of

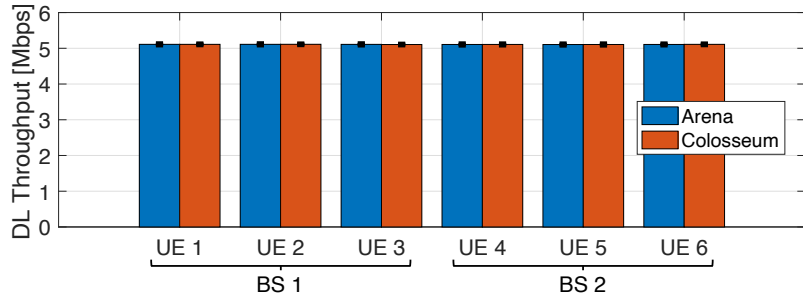


Figure 2.25: Downlink throughput average results and 95% confidence interval of the second cellular networking use-case with 2 BSs and 6 UEs.

the lag k . In this context, \bar{x} and \bar{y} represent the means of the input sequences and N is their length. If $x(n)$ and $y(n)$ have different lengths, zeros are appended to the end of the shorter vector to ensure both sequences have the same length N .

Table 2.3 presents the normalized cross-correlation results and their averages for throughput and SINR of each UE, considering the maximum values between 10 lags, of the UDP and TCP single BS use-case experiments. The multiple BSs experiments would yield similar comparison results.

Table 2.3: Normalized cross-correlation results, and their averages, considering the maximum values between 10 lags for the single BS cellular experiment.

Metric	Static UE 1	Static UE 2	Mobile UE 3	Average
UDP Throughput	0.986	0.998	0.999	0.994
TCP Throughput	0.937	0.998	0.998	0.978
TCP SINR	0.997	0.994	0.982	0.991

We can observe a very high similarity between the two testbeds in all use-case experiments, with individual UE values consistently above 0.93 and an average exceeding 0.97 for each use-case metric. It is worth noting, as observed in Figure 2.23, that the SINR results in Arena are quite similar from UE 1 and UE 3, and they present a fixed difference of about 5 dB compared to Colosseum for UE 2. This difference can mainly be attributed to the additional and uncontrolled interference and impairments of a real-world RF environment, as well as the different power levels between a simulated UE and a real smartphone. However, these variances can be compensated for in the DT by adjusting factors such as the node gains at the transmitter and receiver, as well as by adding stochastically representative interference models to the channel that represents the real-world behavior more closely. These findings confirm the capabilities of the DT to perform emulated cellular experiments that closely replicate the behavior of real-world setups and environments, even in the presence of mobile nodes.

2.5.5.2 Wi-Fi Jamming

Adversarial jamming has continuously plagued the wireless spectrum over the years with the ability to disrupt, or fully halt, communications between parties. While there are potential solutions to specific types of jamming, due to the open nature of wireless communication, this kind of attack

continues to find ways to be effective. However, the development of new techniques to counter this attack is not always straightforward, as even experimenting with possible solutions requires complying with strict FCC regulations [67]. Even though some environments allow for jamming research, e.g., anechoic chambers or Faraday cages, these setups can hardly capture the characteristics and scale of real-world network deployments. To bridge this gap, a DT environment—such as the Colosseum wireless network emulator—could be fundamental in further developing techniques for jamming mitigation research as shown in our previous work in [45] where we implement jamming software within Colosseum to test the impact that jamming signals have within a cellular scenario as well as compare real-world and DT throughput results.

Here, we leverage the GNU Radio-based IEEE 802.11 implementation [68] to deploy two Wi-Fi nodes (Transmitter (TX) and Receiver (RX)) communicating over a 20 MHz spectrum on the Arena testbed [29]. Additionally, we leverage GNU Radio to deploy a jammer (both stationary and mobile) that transmits Gaussian noise signals to hamper the correct functioning of our Wi-Fi network. Our setup can be seen in Figure 2.26. For the sake of fairness in the transmitted signals, in the stationary case, we deployed our nodes so that the Wi-Fi transmitter and jammer are at the same distance from the Wi-Fi receiver. We consider two common forms of static jamming: (i) jamming through narrowband signals (shown in Figure 2.27a); and (ii) jamming through wideband signals (Figure 2.27b).

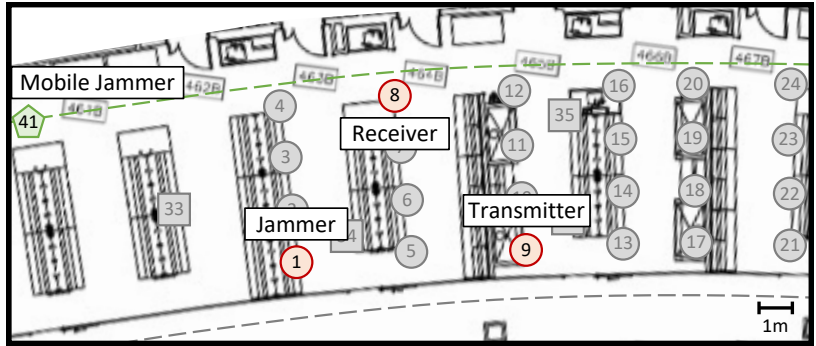


Figure 2.26: Location of the nodes in the jamming experiment, consisting of three static (1, 8, 9) and one mobile (41).

The first type of jamming only occupies a small portion of the Wi-Fi bandwidth (i.e., ~ 156 kHz), resulting in a minimal displacement of the Wi-Fi signals. On the contrary, the latter covers half of the spectrum used by the Wi-Fi nodes (i.e., 10 MHz), causing larger disruptions in the network.

Static Jamming. Figure 2.27 evaluates how narrowband and wideband stationary jammers impact the throughput and SINR of a Wi-Fi network in the real and DT-based scenarios. In this experiment, the Wi-Fi nodes communicate for 60 seconds, and the jammer starts transmitting at second 20 for a duration of 20 seconds. Specifically, Figure 2.27a shows Wi-Fi throughput and SINR for the narrowband jamming experiment in both the real-world and DT, while the wideband jamming experiment throughput and SINR results as perceived by the Wi-Fi nodes are shown in Figure 2.27b.

By looking at the narrowband jamming case, we notice that in the real-world experiment, the Wi-Fi throughput achieves between 5 and 6 Mbit/s when there is no jammer (Figure 2.27a). Once the jammer starts (at second 20), we notice a rapid decrease in the throughput (i.e., between 37%

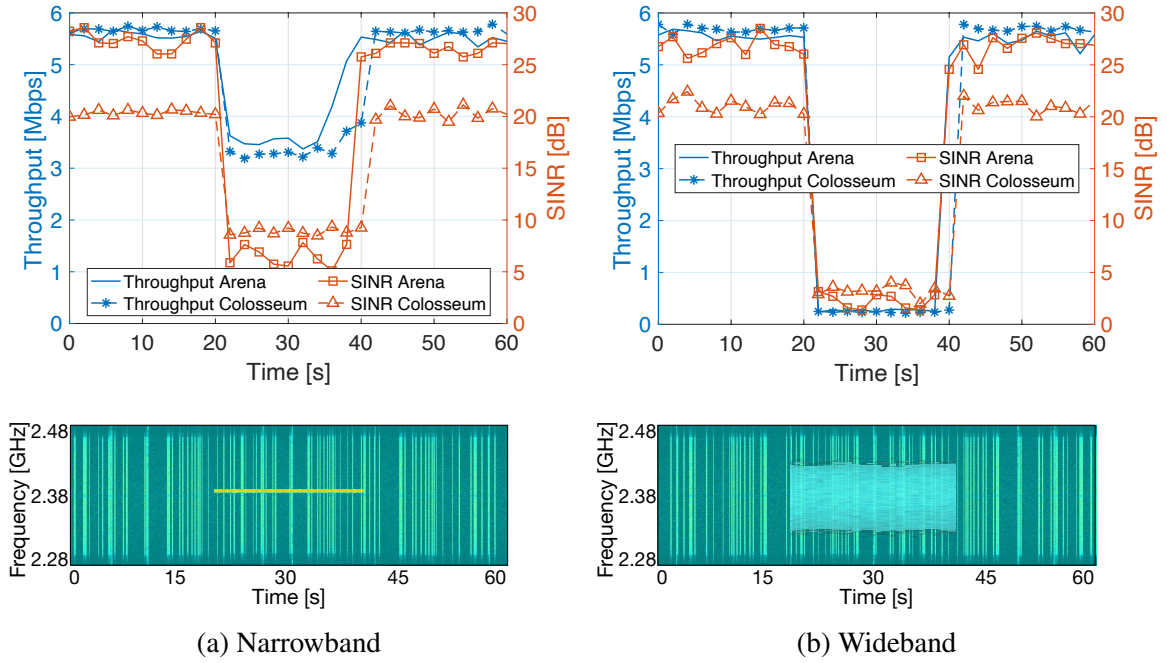


Figure 2.27: Throughput and SINR results on the Arena and Colosseum testbeds of the jamming experiments for the narrowband and wideband use cases. The spectrogram is shown for both forms of jamming, showing the wideband and narrowband signals over a channel.

and 43% decrease). The wideband jammer (Figure 2.27b), instead, has a more severe impact on the Wi-Fi throughput, causing a performance drop between 94% and 96% (with the throughput achieving values between 220 and 290 kbit/s). In both narrowband and wideband cases, we notice that the behavior obtained in the DT is consistent with that of the real-world scenario. Analogous trends can be seen for the SINR of both signal types, where the narrowband jammer causes an SINR decrease of approximately 20 dB (i.e., $\sim 77\%$ decrease), while the wideband jammer of approximately 25 dB (i.e., $\sim 92\%$ decrease) in the real-world scenario. Similarly to the previous case, results are consistent with those of the DT.

Mobile Jamming. Now, we evaluate the impact that a narrowband and wideband mobile jammer (node 41 in Figure 2.26) moving at pedestrian speed has on the Wi-Fi throughput. Wi-Fi nodes are located as in the previous case, i.e., nodes 8 and 9 in the figure. Results are shown in Figure 2.28. As expected, the impact of the jamming signal on the Wi-Fi throughput varies as the jammer moves closer or farther from the Wi-Fi receiver, and it also depends on the type of jamming, i.e., narrowband vs. wideband. Specifically, as the jammer gets closer to the Wi-Fi nodes (i.e., seconds 5 to 30) in the narrowband case, we observe a $\sim 90\%$ decrease in the Wi-Fi throughput in both real-world and DT scenarios (see Figure 2.28a). A comparable decrease can be observed in the SINR as well, where we notice a clear drop in both the over-the-air Arena case and the DT of about $\sim 65\%$ in a lookalike trend. Following a similar pattern, in the wideband case, we observe a more pronounced drop as the jammer approaches (i.e., seconds 5 to 30), reaching peaks near 100% drops in throughput and SINR in the closest locations with the nodes at around second 15.

Comparison. As for the cellular experiment, Table 2.4 shows the normalized cross-correlation

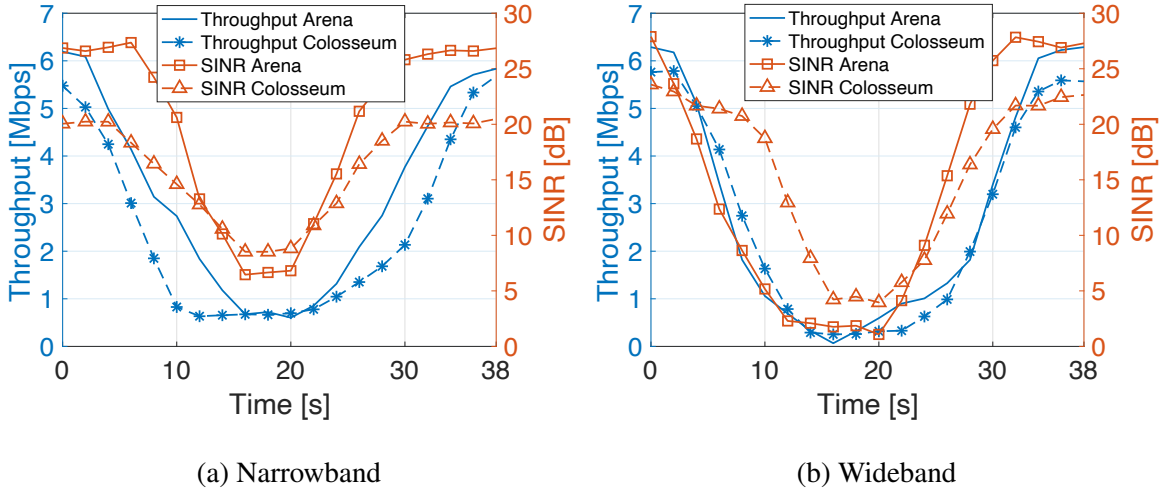


Figure 2.28: Impact of a moving jammer for narrowband (a) and wideband (b) use cases on the throughput and SINR of Wi-Fi nodes on Arena and Colosseum testbed.

results and their averages, considering the maximum values between 10 lags, for each jamming experiment. We observe a strong similarity between the two testbeds in both static and mobile experiments, with individual values consistently above 0.93.

Table 2.4: Normalized cross-correlation results, and their averages, considering the maximum values between 10 lags for each jamming experiment.

Metric	Narrowband	Wideband	Average
Static Throughput	0.996	0.982	0.989
Static SINR	0.986	0.984	0.985
Mobile Throughput	0.982	0.993	0.988
Mobile SINR	0.993	0.935	0.964

Overall, considering all sample experiments in this work, our DTMN is able to achieve an average similarity of 0.987 in throughput and 0.982 in SINR. These results prove the ability of our system to properly emulate various use case experiments with different protocol stacks and scenarios.

2.6 Related Work

The concept of DT is rapidly gaining momentum in both industry and academia. Initial approaches showcase the use of DTs for industry 4.0 [38], and to assist design, assembly, and production operations in the manufacturing process [39]. A comprehensive literature review on DT-related applications in manufacturing is provided by Kritzinger et al. in [69].

Recently, researchers and practitioners have started to apply the concept of DT to the wireless ecosystem due to the potential of digitalization processes, and easier integration and monitoring of interconnected intelligent components, as Zeb et al. discuss in [70]. Nguyen et al. theoretically

discuss how DTs can enable swift testing and validation on real-time digital replicas of real-world 5G cellular networks [71], while Khan et al. provide the architectural requirements for 5G-oriented DTs, mentioning them as key components for the development of 6G networks [72]. He et al. leverage the DTs and mobile edge computing in cellular networks to enhance the creation of digital models affected by the straggler effect of user devices in a Federated Learning (FL) process [73]. Lu et al. incorporate DTs into wireless networks to mitigate long and unreliable communications among users and BS and define a permissioned blockchain-based FL framework for edge computing [74]. Zhao et al. combine DTs with software-defined vehicular networks to learn, update, and verify physical environments to foresee future states of the system while improving the network performance [75].

Overall, the above works agree on the potential of DTs in: (i) assessing the network performance; (ii) creating realistic and accurate system models; (iii) predicting the impact of changes in the deployment environment; and (iv) reacting and optimizing the performance of the network.

The works most similar to our *CaST* toolchain in modeling and simulating channel characteristics are those of Patnaik et al. [76], Ju and Rappaport [77], Bilibashi et al. [78], and Oliveira et al. [79]. Specifically, Patnaik et al. compare the response of FIR filters with their simulated counterpart [76], while Ju and Rappaport devise a technique to improve the representation of channel impairments and variations for adaptive antenna algorithms in a mmWave channel simulator [77]. Bilibashi et al., and Oliveira et al., instead, leverage ray-tracing approaches to include mobility in the emulated channels in [78] and [79], respectively. However, these works only target specific use cases, and they cannot model generic scenarios and deployments, as our *CaST* toolchain does.

Finally, to the best of our knowledge, there are no practical works that encompass all the various building blocks of a DT system, from channel characterization and modeling to large-scale experimentation on a DT, to real-world validation on an OTA testbed, as we carry out in this work.

2.7 Conclusions

In this chapter, we applied the concept of DTs to wireless communication systems, presented Colosseum—the world’s largest wireless network emulator—as an ideal candidate for realizing DTNs, and introduced *CaST*, an open toolchain to create and validate realistic channel scenarios. We validated *CaST* through experiments on a lab setup and on Colosseum, showing that it achieves up to 20 ns accuracy in sounding the CIR tap delays and 0.5 dB accuracy in measuring the tap gains. We then used *CaST* to digitize and characterize a variety of emulation scenarios, including a ray-tracing-based V2X deployment and the Arena testbed, and validated the twinning process through cellular, Wi-Fi, and jamming experiments, achieving up to 0.987 similarity in throughput and 0.982 in SINR between emulated and real-world results. This proves that DTs can closely reproduce real-world setups, enabling users to run meaningful experiments in a highly realistic environment.

Connecting to the four key research challenges outlined in Chapter 1, this chapter: (i) demonstrated automated scenario creation and validation through the *CaST* toolchain (*deployment*); (ii) validated DTs that closely reproduce real setups via paired experiments between physical and digital platforms (*realism*); and (iii) released open-source tools (e.g., *CaST*), methodologies, and scenarios to ease experimentation by other researchers (*usability*). The fourth challenge, namely *use cases*, is addressed in Chapter 3, where we show how Colosseum and DTs enable research across various areas, such as spectrum sharing, AI-driven modeling, and synthetic data generation.

Chapter 3

Spectrum Sharing and AI-Driven Modeling on Digital Platforms

3.1 Introduction

Chapter 2 has established DTs and large-scale wireless emulation platforms, such as Colosseum, together with *CaST* for the creation and validation of these DTs, as valuable tools for the research community. They provide a controlled, repeatable, and reproducible environment for wireless experimentation in which to explore complex behaviors that would otherwise be impractical, expensive, unsafe, or constrained by regulatory requirements for OTA testing in real-world settings. This chapter demonstrates the *use case* dimension of DT platforms, addressing the fourth research challenge introduced in Chapter 1 and presenting three classes of problems enabled by Colosseum, building on [16, 80, 17, 18, 19]: (i) spectrum sharing and incumbent signal detection; (ii) AI-driven radio-map generation; and (iii) generative models for synthetic RF data.

Section 3.2 presents a framework for spectrum sharing between cellular networks and radar systems in the Citizen Broadband Radio Service (CBRS) band, showing how commercial waveforms can be twinned on Colosseum and how data can be collected on the emulator to train a Convolutional Neural Network (CNN)-based detector for incumbent radar transmissions. Section 3.3 addresses the challenge of real-time channel modeling for DT-based applications, presenting AIRMap, a deep-learning framework for ultra-fast radio-map estimation, and demonstrating its integration with Colosseum for validation. Section 3.4 explores the use of generative AI to augment RF datasets for O-RAN applications, describing Gen-TWIN and its dataset generation methodology using Colosseum and another testbed to enable model training that generalizes across diverse channel conditions. Finally, Section 3.5 summarizes the research impact enabled by DT platforms and discusses their limitations, motivating the transition to OTA testing in the following chapters.

3.2 Spectrum Sharing and Incumbent Signal Detection

The increasing demand for wireless spectrum is driving the adoption of spectrum-sharing techniques, in which multiple wireless systems from different vendors and with different objectives coexist in the same frequency bands. This presents significant challenges, particularly when commercial

networks must share the spectrum with incumbent systems operating mission-critical communication links, such as nautical and aerial fleet radars [81]. One prominent example is the potential interference of 5G RANs on incumbent radar communications in the CBRS band, ranging from 3.55 GHz to 3.7 GHz, where U.S. military radar systems operate along coastal areas. According to federal regulations, dynamic access to the CBRS spectrum is permitted, but it requires thorough study, research, and the development of mitigation strategies to ensure the reliable operation of both systems, i.e., seamless communication in cellular networks while avoiding harmful interference to incumbent radar systems [82].

AI/ML-based solutions have emerged as promising tools to address this challenge, thanks to their ability to learn complex patterns, generalize across diverse channel conditions, and make real-time decisions [44]. In the context of Open RAN, these AI/ML agents can be deployed in the RICs proposed by O-RAN [1], i.e., as xApps and rApps, or at the BS directly as dApps [83]. However, these methods require abundant high-quality data to train effective ML models. Gathering diverse, representative datasets that capture real-world scenarios can be time-consuming and resource-intensive, but it is crucial for achieving accurate, robust performance of AI algorithms. Prior work generates datasets that are not always able to capture high-fidelity, diverse environments or leverage synthetic waveforms that are not representative of commercial radios, resulting in impractical AI models whose performance substantially degrades when deployed in the real world [84, 85, 86]. In the context of incumbent radios and communication links, such as nautical and aerial fleets, safety is of paramount importance, and non-carefully planned real-world experiments can endanger critical operations. As discussed in Chapter 2, high-fidelity emulation platforms and DTs, such as Colosseum, allow researchers to simulate interference scenarios realistically and evaluate their impact without posing any actual risk to operational systems.

In this section, we develop a framework to emulate a spectrum-sharing scenario with cellular and radar nodes implemented in a high-fidelity DT system on Colosseum [2]. We create a scenario emulating the coastal environment of Waikiki Beach in Honolulu, Hawaii, where a BS operating in the CBRS band must detect radar transmissions from a ship moving in the North Pacific Ocean. We collect I/Q samples from radar and cellular communications and train a CNN that can be deployed as a dApp to detect the presence of radar signals and notify the RAN to vacate the bandwidth and eliminate interference with the incumbent radar communications. Our experimental results show an average accuracy of 88%, with accuracy above 90% in Signal-to-Noise-Ratio (SNR) regimes above 0 dB and in SINR regimes above -20 dB. Through timing experiments, we also observe an average detection time of 137 ms. This demonstrates the effectiveness of our system in detecting in-band interference in the CBRS band, as it complies with both maximum timing requirements (60 s) and accuracy (99% within the 60 s time window) [87].

The remainder of this section is organized as follows. Section 3.2.1 details the waveform twinning methodology and radar characterization. Section 3.2.2 describes the spectrum-sharing scenario for the coexistence of cellular and radar signals. Section 3.2.3 presents the intelligent radar detection approach, while Section 3.2.4 discusses the experimental results.

3.2.1 Waveform Twinning and Radar Characterization

3.2.1.1 Waveform Twinning

As introduced in Chapter 2, Colosseum enables the deployment of softwarized protocol stacks through LXC containers. This capability extends to twinning arbitrary waveforms, including commercial radar signals, allowing researchers to experiment with spectrum-sharing scenarios in a controlled environment. This process is shown at a high level in Figure 3.1. First, the waveform is either recorded from a real-world transmission (e.g., radar, Wi-Fi, or cellular transmission) or synthetically generated. The waveform is imported on Colosseum and interfaced with the softwarized LXC container running on Colosseum SRN. It is then transmitted by the SRN USRP to the other nodes of the experiment through MCHEM. At the end of the experiment, data is collected and analyzed for post-processing purposes. Finally, it is worth noting that this procedure can be repeated on the Colosseum for fine-tuning designed user solutions and their validation, thus allowing reproducible experiments to be carried out on the testbed.

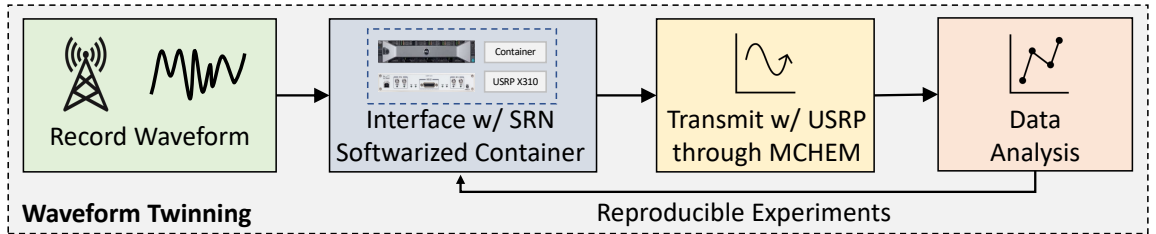


Figure 3.1: Waveform twinning on Colosseum.

3.2.1.2 Radar Characterization

Radar systems leverage reflections of RF electromagnetic signals from a target to infer information on such a target [88]. Typical information may include detection, tracking, localization, recognition, and composition of the target, which may include aircraft, ships, spacecraft, vehicles, astronomical bodies, animals, and weather phenomena. Even though radar's primary uses were mainly related to military applications, nowadays this technology is commonly used in other areas, such as weather forecasting and automotive applications.

In this work, we leverage a weather radar that combines techniques typical of continuous-wave radars, e.g., pulse-timing to compute the distance of the target, and of pulse radars, like the Doppler effect of the returned signal to establish the velocity of the moving target [89]. Note that similar considerations can be applied to any other radar or waveform type, and the radar signal considered in this work is a use-case study (without loss of generality) to showcase Colosseum capabilities. Our radar operates in the S-Band, typically located within the [3.0, 3.8] GHz frequency range. The signal has been synthetically generated as a collection of I/Q samples and timestamps, with a sampling rate of 6 MS/s and 106657 sampling points for a total duration of 17.8 ms. Figure 3.2 shows some characterization of the radar signal. Figure 3.2a depicts the Power Spectral Density (PSD) of the radar. Figure 3.2b displays the constellation diagram of the transmitted signal. We notice that the signal lies only in the first quadrant of the I/Q-plane, which is typical of some radars.

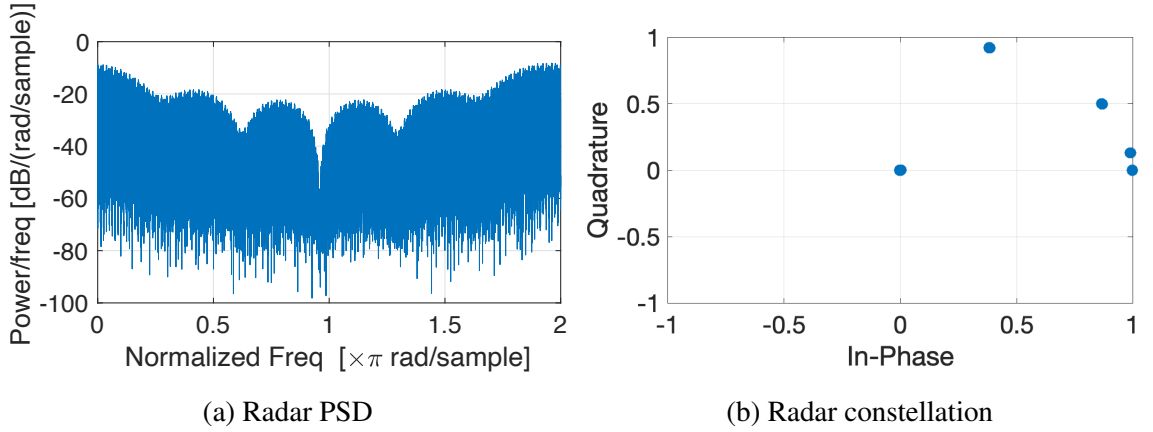


Figure 3.2: Radar characterization with PSD and constellation plots.

Figure 3.3 shows the various operations that we developed to integrate an arbitrary waveform (radar in this case) into the Colosseum environment. In the first step, the radar signal is generated

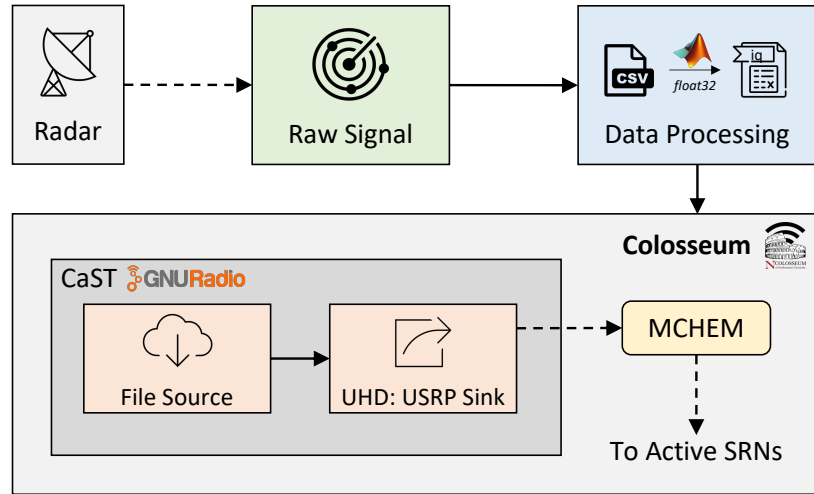


Figure 3.3: Block diagram of the operations needed to integrate the radar signal in Colosseum.

either through a hardware device or in a synthetic manner. The output of this step is a raw signal formed of I/Q samples for given time instances, which in our case is stored in a `.csv` file. The raw data is then processed to convert it into a format that can be interpreted by Colosseum. We use MATLAB to read the `.csv` raw signal and generate a `.iq` file with the array of I/Q values sequentially saved in a `float32` format. Finally, the newly created `.iq` file is transmitted in the Colosseum environment by leveraging the open-source *CaST* framework, which is based on GNU Radio [3, 53]. For the purpose of this work, *CaST* has been modified to include a *File Source* block that allows us to load the `.iq` file on the Colosseum system. The signal is then passed through an *UHD: USRP Sink* block, which connects to the USRP SDR in Colosseum, and transmits the signal over MCHEM to the other SRNs.

Figure 3.4 shows the radar signal transmitted on the Colosseum wireless network emulator through *CaST* and received by another SRN. Figure 3.4a displays real and imaginary parts of the raw

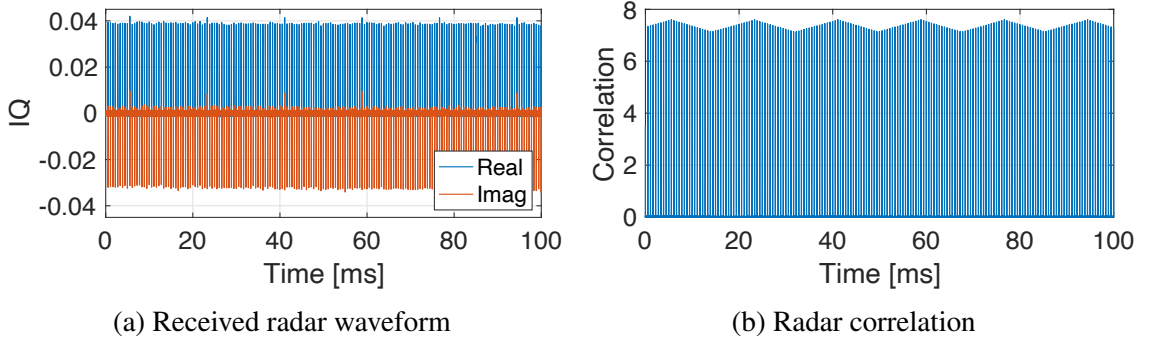


Figure 3.4: Results of a radar transmission through *CaST*.

radar waveform at the receiver node, while Figure 3.4b displays the correlation between the original radar signal and the received waveform. We notice that the correlation values are clearly visible, meaning that the radar signal is correctly transmitted and detected at the receiver side. We also notice a periodic jigsaw trend in the correlation results. This behavior is due to the large length of the transmitted radar I/Q sequence (106657 complex points). Upon performing the correlation operation, the length of the sequence causes peaks at the beginning of the sequence, as well as valleys, because of leftover samples from the correlation.

3.2.2 Spectrum-Sharing Waikiki Beach Scenario

To evaluate the coexistence of cellular and radar technologies, we consider a 4G/5G RAN operating in the CBRS band that must vacate the spectrum upon detection of an incumbent radar transmission.

CBRS regulations allow commercial broadband access to the RF spectrum ranging from 3.55 GHz to 3.7 GHz, as depicted in the Code of Federal Regulations (CFR) [90]. This spectrum is shared with various incumbents, including the U.S. military, which operates radar systems in this frequency range, e.g., shipborne radars along the U.S. coasts. According to the regulations, dynamic access to the spectrum is permitted as long as the network can detect the presence of the radar and activate interference mitigation measures when necessary [82]. Once detected, BSs can either move to an unused bandwidth, if any, or terminate any ongoing communication to give priority to the radar.

To effectively study this use case on Colosseum, we created a novel RF scenario that emulates the propagation environment of Waikiki Beach in Honolulu, Hawaii. This scenario involves a BS—whose location was taken from the OpenCellID database [91] of real-world cellular deployments—that serves 6 UEs, and a radar-equipped ship that moves in the North Pacific Ocean. This scenario was created with the *CaST* toolchain [3] following the steps of Figure 3.5.

In the first step, we identify the scenario location. Since we are considering a ship node for the radar, we chose the coastal area of Waikiki Beach in Honolulu, Hawaii. Next, we obtain the 3D model of the selected location through the OSM tool [92]. We generate an `.osm` file of a rectangular area of about $700 \times 800 \text{ m}^2$, which includes Waikiki Beach, nearby buildings, and skyscrapers, as

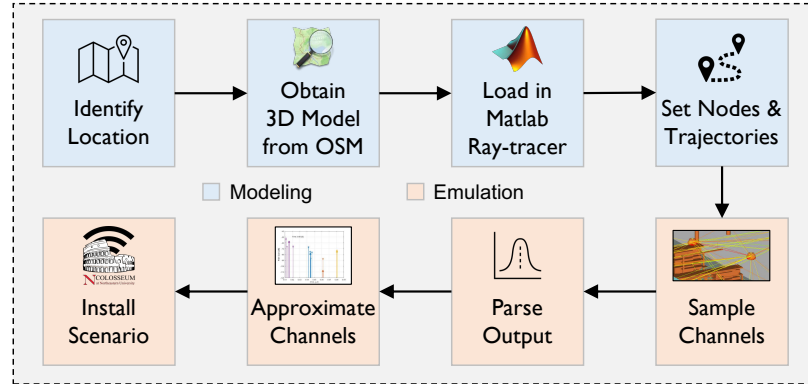


Figure 3.5: *CaST* scenario creation toolchain blocks diagram. Figure adapted from [3].

well as a portion of the ocean. We then load the 3D model into the MATLAB ray-tracer, and define the nodes of our scenario (shown in Figure 3.6) as well as their trajectories.

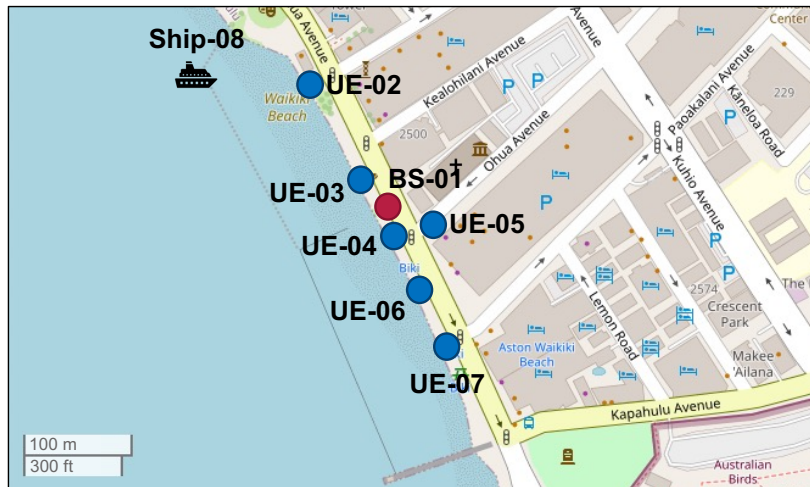


Figure 3.6: Location of the nodes in the Waikiki Beach scenario.

Our nodes are as follows.

- One cellular BS (red circle in Figure 3.6), whose antennas are located at 3 m from the ground.
- Six static UEs (blue circles in Figure 3.6) uniformly distributed in the surroundings of the BS. UEs are located at 1 m from the ground level to emulate hand-held devices.
- One ship (shown in black in Figure 3.6) equipped with a radar, whose antennas are located at a height of 3 m. The ship moves following a North-South linear trajectory along Waikiki beach at a constant speed of 20 knots (~ 10 m/s). This speed was derived as the average between the speed typical of civilian container ships—which travel at around 10 knots (~ 5 m/s)—and that of aircraft carriers—which reach speeds of around 30 knots (~ 15 m/s) [93].

Table 3.1: Parameters of the Waikiki Beach scenario.

Parameter	Value
Signal bandwidth	20 MHz
Transmit power (BS and ship)	30 dBm
Transmit power (UEs)	20 dBm
Antenna height (BS and ship)	3 m
Antenna height (UEs)	1 m
Building material	Concrete
Max number of reflections	3
Sampling time	1 second
Ship speed	10 m/s
Emulation area	700x800 m ²

Table 3.1 summarizes the wireless parameters defined for the designed Colosseum RF emulation scenario. Figure 3.7 shows the layout of the scenario loaded in the MATLAB ray-tracer. We notice the 3D model of the environment (white building blocks in the figure), together with the radio node locations (red icons), and the trajectory of the ship (green dots). In this step, we perform ray-tracing to characterize the environment of interest and derive the channel taps between each pair of the nodes of our scenario.



Figure 3.7: Layout of the scenario loaded in the MATLAB ray-tracer and visualized with Site Viewer.

After these operations are completed, the next step involves approximating the channel taps returned by the ray-tracer. This step is required to install the scenario in Colosseum, since MCHEM supports a maximum of 4 non-zero channel taps, with a maximum delay spread of $5.12 \mu\text{s}$. This is performed through a k-means clustering algorithm that we previously developed [52]. The heat map of the path loss among each pair of nodes after this channel approximation step is depicted in Figure 3.8. (The ship node is considered to be in the top position at the beginning of the scenario.) As expected, closer

nodes experience lower path loss values.

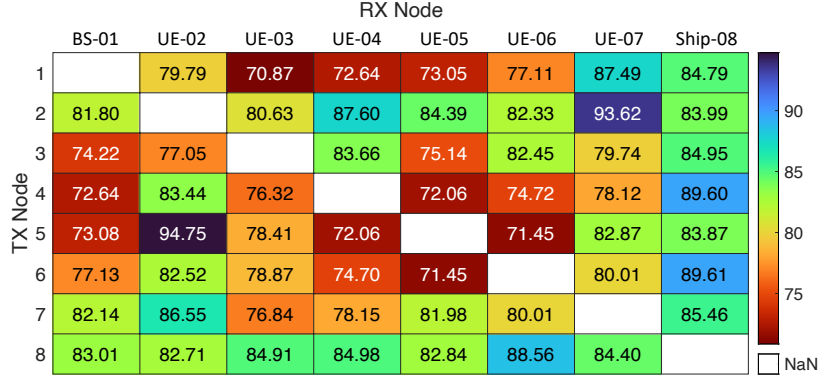


Figure 3.8: Heat map of the path loss among the nodes of the Waikiki scenario in Figure 3.7. The mobile ship node is considered in its starting position at the top.

As a final step, the channel taps are converted into FPGA-readable format, and the scenario is installed in Colosseum. Generating the channel taps with the ray-tracing software, and approximating them to the four non-zero taps required around 7 hours by using a 2021 MacBook Pro M1 with 10 cores and 16 GB of RAM. Installing the scenario on the Colosseum system required around 50 minutes by leveraging a virtual machine hosted on a Dell PowerEdge M630 Server with 24 CPU cores and 96 GB of RAM.

3.2.3 Intelligent Radar Detection

The BS leverages an AI model to detect radar signals during or before cellular communications. This section explains how we collect and pre-process the data before feeding it into our model, as well as the structure of the model itself.

3.2.3.1 Data Collection

By using the scenario of Section 3.2.2, radar and cellular signals are transmitted in different combinations and varying reception gain. Specifically, we collect I/Q samples when only the radar is present, only the cellular signal is present, both are present, and neither is present (empty channel). These combinations encompass all the possible real scenarios that the intelligent radar detector might come across.

We pre-process these recordings by first breaking them into smaller samples of 1024 I/Qs, as this is the input size to the ML agent. This input size was chosen as we have found it to be the smallest size that still offers high classification performance. We then convert each sample to its frequency domain representation. Finally, we offer a binary label to each sample: 1 if radar exists in the sample, and 0 otherwise. In this way, the model groups empty channels and un-interfered cellular transmissions as 0 and therefore is free to communicate in the given band.

3.2.3.2 Model Design and Training

We use a lightweight, modified CNN for radar detection. Specifically, we use a smaller version of VGG16 [94]. We chose this structure as it is commonly used in wireless applications and can adequately show the capabilities of our framework.¹ The model architecture can be seen in Figure 3.9.

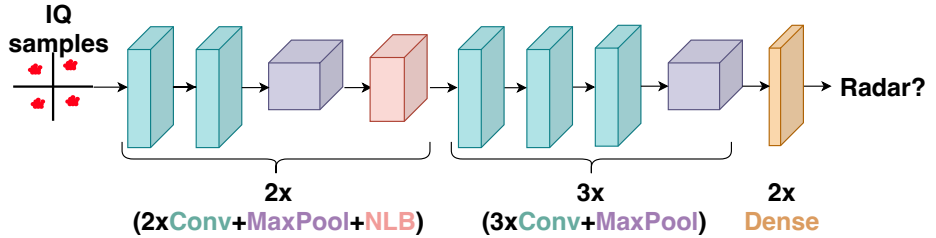


Figure 3.9: CNN model used to train the radar detector.

For the first two convolutional blocks, we append a Non-local Block (NLB). These blocks help the CNN achieve self-attention and focus on spatially distant information. More on these blocks can be read in [95]. This is a desirable trait as it can help identify long-range dependencies that may be present in the wireless signal rather than only focusing on adjacent I/Qs. The model takes as input I/Qs in the shape of $(batch_size, 1024, 2)$ where the last dimension is the real and complex part of the I/Q separated into two distinct channels.

3.2.4 Performance Evaluation

In this section, we present results on the effect of a radar signal on a cellular network deployed on the Colosseum wireless network emulator by showing: (i) the performance and accuracy of the ML intelligent detector model; and (ii) the Key Performance Indicators (KPIs), e.g., throughput, Channel Quality Information (CQI), and computation time of real-time experiments with and without radar transmissions and the intelligent detector.

3.2.4.1 Intelligent Detector Results

We test our radar detector on data withheld during training and observe an accuracy of 88%, a precision of 94%, and a recall of 79%. This tells us that our model is not susceptible to false positives (misclassifying empty channels or cellular signals as radar), but is susceptible to false negatives (misclassifying radar as an empty channel or a cellular signal).

To delve deeper into these results, we plot the accuracy as a function of SNR in Figure 3.10a. For this plot, we keep the cellular nodes static in the scenario and only vary the radar gain. Here we can see that through varying SNRs we have very high and consistent performance in detecting radar signals, above 90%. However, when we add cellular signals into the channel, this makes the detection of radar more difficult, as can be seen in Figure 3.10b, where we plot accuracy as a function

¹More complex AI algorithms can be used for this task. However, this is out of the scope of this work.

of SINR. The cellular signal is considered interference in this plot. Indeed, with high cellular signal gain and low radar gain, we see that our classification accuracy decreases to about 75%.

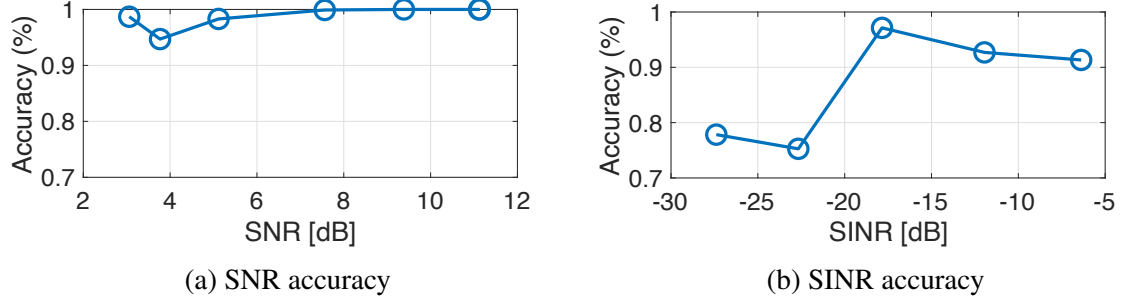


Figure 3.10: CNN radar detection accuracy with varying SNR of the radar signal, and varying SINR where the cellular signal is considered to be interference.

3.2.4.2 Experimental Results

To properly study the network performance with and without the presence of radar transmissions, we leverage Colosseum and the newly created scenario described in Section 3.2.2 to deploy a cellular network and run traffic analysis. The parameters of the experiments are summarized in Table 3.2.

Table 3.2: Parameters of the experiments.

Parameter	Value
Center frequency	3.6 GHz
Signal bandwidth (radar)	20 MHz
Signal bandwidth (cellular)	10 MHz
Number of BSs	1
Number of UEs	6
USRP BS gains (Tx and Rx)	[10, 30] dB
USRP UE gains (Tx and Rx)	20 dB
USRP radar Tx gain	20 dB
Scenario Duration	40 s
Traffic type	UDP Downlink
Traffic rate	10 Mbps
Scheduling policy	Round-robin

The center frequency is set to 3.6 GHz in the newly opened CBRS band, which is also used by S-Band-type radars. It is worth noticing that, even though characterized at 3.6 GHz, the scenario has been installed in Colosseum at a center frequency of 1 GHz, at which MCHEM is optimized to work. The scenario duration is set to 40 s, which is the time needed by the ship to travel the planned 400 m trajectory at the constant speed of 10 m/s. Then, the scenario repeats cyclically from the beginning indefinitely.

We leverage the open-source SCOPE framework to deploy a twinned srsRAN protocol stack with one BS and six UEs [64, 65]. Additionally, the radar signal is transmitted through the use of

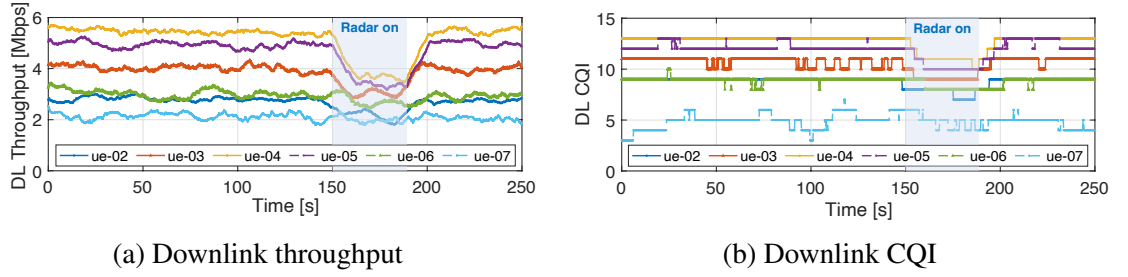


Figure 3.11: Moving average of cellular network downlink throughput and CQI. A radar transmission is ongoing from second 150 to second 190, highlighted with a blue shade.

the *CaST* transmit node [14], which has been modified to support custom radio waveforms. In the following subsections, we show the results for three main cellular network use cases: (i) no radar transmission; (ii) with radar signal interference; and (iii) with radar and an intelligent detector. In all experiments, a UDP downlink traffic of 10 Mbps among BS and UEs is generated through iPerf, a tool to benchmark the performance of Internet Protocol (IP) networks.

No Radar The performance of the cellular network, in terms of downlink throughput and CQI, without radar transmissions is shown in Figure 3.11, from second 0 to 150. The gains of the BS USRP are set to 25 dB. As expected, the throughput, shown in Figure 3.11a, decreases with the increase of the distance between UEs and BS. The best performance is achieved by UE-04, with values between 5.22 and 5.71 Mbps, while the other UEs achieve between 1.82 and 5.25 Mbps. UE-07 achieves the worst throughput due to its large distance from the BS, environmental conditions, and interference with the other nodes. The CQI, shown in Figure 3.11b, follows a similar trend. Best values are reported by UE-04, with a stable CQI of 13. The other UEs show CQI values between 2 and 13, with UE-07 reporting the lowest CQI values (between 2 and 7).

Radar The impact of radar transmissions on the cellular performance is shown in Figure 3.11, from seconds 150 to 190. As expected, we notice a drop in the throughput (Figure 3.11a) and CQI values reported by the UEs (Figure 3.11b). This is more visible for the nodes closer to the BS, e.g., UE-03, UE-04, and UE-05, since they get more affected by the radar transmission. When the radar stops transmitting, i.e., at around second 190, the performance of the UEs goes back to the initial values, i.e., to the values in the $[0, 150]$ s window.

Intelligent Radar Detection In this last use case, we evaluate the effectiveness of our intelligent detector in understanding the presence of the radar signal, as shown in Figure 3.12. The top portion of the figure shows the downlink cellular spectrogram centered at 980 MHz (i.e., the downlink center frequency we use for srsRAN in Colosseum) with a 6 MHz span; the bottom one displays the results of the radar detection system. At the beginning of the experiment—from second 0 to second 50—the BS is serving the UEs through UDP downlink traffic (Figure 3.12, top), as we notice from the orange and yellow stripes. Then, at second 50, a radar transmission is detected by the intelligent detector (Figure 3.12, bottom) described in Section 3.2.3, and the BS is shut down accordingly. After the radar transmission ends, i.e., at second 90, the BS receives the command to power back on and, after around 10 seconds, it resumes its operations (second 100). Finally, at second 110, the UEs reconnect to the BS, and the downlink transmissions are restarted. Overall, this demonstrates the effectiveness of our intelligent detector in identifying radar signals and vacating the cellular bandwidth. Note

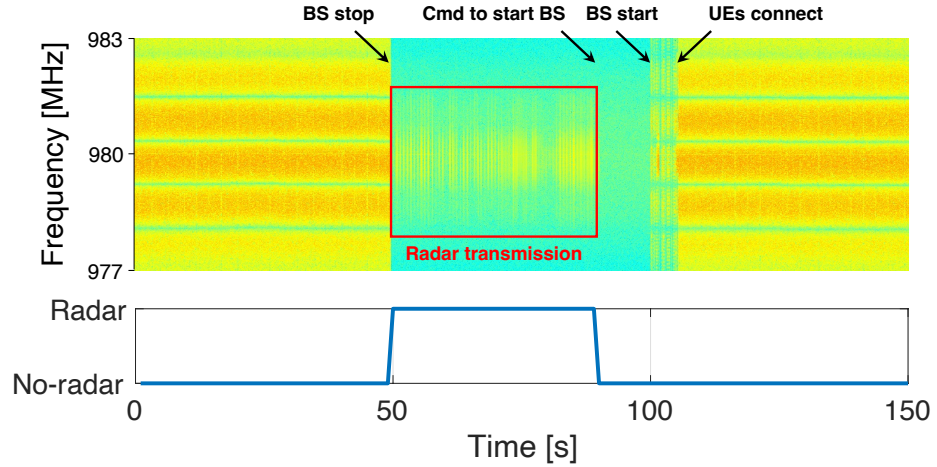


Figure 3.12: (top) Downlink cellular spectrogram; (bottom) radar detection system. The BS is shut down when a radar transmission is detected and resumes normal operations after no radar is detected.

that even if we have not tested our ML agent with different radar signal types, changes in the radar waveform that impact its frequency domain representation might require a re-training of the model to achieve similar performance.

Figure 3.13 shows the required computation time for the classification, performed on CPU, with different batch sizes in a Colosseum SRN. We notice that values grow linearly with the batch size, e.g., 6 ms for a batch size of 1 sample, 27.4 ms for 10, 239 ms for 100. This can be traced back to the fact that these operations run on a CPU, so there is not much parallelization of the processes as there would be in a GPU. However, even in the case of a batch size of 100 samples, the maximum time of 60 seconds required for the detection of commercial transmissions in the CBRS band is satisfied [87]. To avoid false positives and false negatives, we leverage a voting system of 100 samples, in which the signal to shut down the BS is sent only when more than 50% of the outputs are detecting a radar. Moreover, we use a batch size of 10 samples, which gives us a good tradeoff between computation time and granularity of the output samples needed for the voting system. In

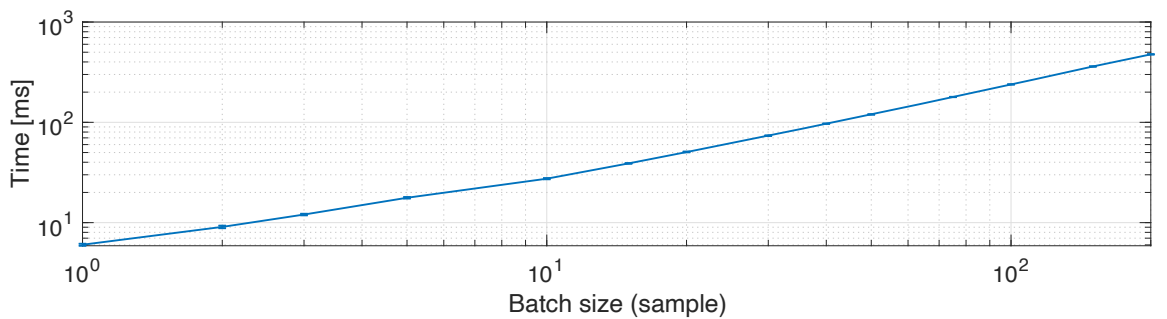


Figure 3.13: Computation time required for a radar classification, with different batch sizes, run on CPU on a Colosseum SRN with 48-cores Intel Xeon processor and 126 GB of RAM.

these conditions, our intelligent detector is able to detect an incumbent radar transmission and vacate the cellular bandwidth within 137 ms—which is the average time for the ML model to generate 50 new outputs with a batch size of 10 samples—and with an accuracy of 88%.

3.2.5 Conclusions

In this section, we developed a framework for high-fidelity emulation-based spectrum-sharing scenarios with cellular and radar nodes implemented as a DT system on the Colosseum wireless network emulator. First, we twinned the radar waveform on Colosseum, then we collected I/Q samples of radar and cellular communications in different conditions. Finally, we trained a CNN network—that can run as a dApp—to detect the presence of the radar signal and halt the cellular network to eliminate the undesired interference on the incumbent radar communications. Our experimental results show that our detector obtains an average accuracy of 88% (above 90% when SNR and SINR are greater than 0 dB and -20 dB respectively), and requires an average time of 137 ms to detect ongoing radar transmissions. This work demonstrates how DT platforms like Colosseum enable the study of spectrum-sharing scenarios that would be difficult or unsafe to conduct in real-world environments, thereby showcasing the platform use-case key challenge dimension for AI-driven wireless research.

3.3 AI-Driven Radio Map Generation

Accurate, low-latency channel modeling is essential for effective real-time wireless network simulation and DT applications to precisely and swiftly characterize the radio signal propagation through a dynamic environment. Channel modeling for RF scenarios traditionally falls into three main categories: measurement-based models, statistical models, and deterministic methods (e.g., ray-tracing). Measurement-based approaches capture site-specific phenomena with high accuracy but are costly, labor-intensive, and quickly outdated in dynamic environments [96]. Statistical channel models employ stochastic or deterministic mathematical equations to characterize wireless propagation [97]. However, these models often fail to represent all scenarios or capture environmental intricacies. Their reliance on simplified environmental assumptions leads to prediction inaccuracies, particularly in site-specific scenarios [98]. Ray tracing provides a deterministic means of modeling wireless channels by launching rays and simulating their interactions—reflection, diffraction, and transmission—with environmental geometries using material-specific parameters [99]. Although it achieves higher site-specific accuracy than empirical models—especially in architecturally complex settings—it remains impractical for real-time use. Even with GPU-accelerated implementations, the computational burden of dynamic mobility modeling and scenario adaptation is prohibitive, and the exhaustive pre-computation generally demands extensive storage. Furthermore, its fidelity depends on highly detailed 3D maps with accurate material assignments and accurate antenna patterns, since electromagnetic responses vary noticeably across surfaces. In a trade-off against computational burden, ray tracing remains an approximation—constrained by finite ray sampling and often incomplete modeling of propagation phenomena like diffraction, scattering, and reflection for all possible points. These factors limit ray tracing’s suitability for high-fidelity channel modeling in DTs.

To address these limitations, advanced AI-based techniques have been proposed. These methods leverage ground truth data from measurements or simulations to train data-driven models, enabling rapid and precise predictions of channel properties. By establishing a mapping function between the wireless environment and channel parameters, AI tools facilitate proactive network design. They effectively tackle challenges such as resource allocation, user mobility analysis, localization, and radio propagation modeling. AI-based techniques offer greater flexibility, scalability, and reduced computational complexity, thus enabling real-time propagation modeling in complex urban environments.

Radio (environment) maps provide a two-dimensional representation of averaged statistics of channel characteristics (e.g., received signal power, interference power, power spectral density, delay spread, and channel gain) over a geographic region [100]. Unlike individual point-wise channel estimates, radio maps capture spatial relationships and large-scale propagation patterns, reflecting how neighboring locations influence one another. This inherent spatial structure makes radio maps a natural and effective output format for Downlink (DL) models, which can leverage locality and spatial dependencies. For instance, CNN architectures can process environmental inputs such as terrain and building layouts to generate channel predictions for an entire area in a single inference step, rather than predicting each point independently. This structured approach not only improves scalability and inference speed but also provides the spatial context essential for real-time digital twin applications.

This section presents work on DL-based frameworks for real-time, high-fidelity radio map estimation, developed in collaboration with the authors of [17, 18]. We first describe the initial approach introduced in [17], which demonstrated real-time path gain prediction using a U-Net architecture with elevation maps and rough propagation estimates as inputs, achieving inference times of 46 ms on GPU. We then mention its extension, AIRMap [18], which simplifies the input to a single-channel elevation map and further reduces inference time to under 4 ms, enabling integration with the Colosseum emulator for real-time channel emulation.

The remainder of this section is organized as follows. Section 3.3.1 provides a general overview of the framework. Section 3.3.2 describes the data collection process, including ray-tracing simulations and the measurement campaign. Section 3.3.3 details the DL-based propagation model. Section 3.3.4 presents the performance results. Section 3.3.5 demonstrates the integration with the Colosseum emulator. Finally, Section 3.3.6 concludes this section.

3.3.1 Framework Overview

The overall training process, data calibration, and model validation pipeline is illustrated in Figure 3.14. To achieve this, we employ a U-Net structure inspired by Lee and Molish [4], which allows the model to cover an entire area with a single inference while capturing spatial features effectively. We leverage two key inputs: an elevation map to accurately convey 3D geographical information to the model, and a rough estimation of the propagation model to maintain generalizability. This rough estimation is subsequently upsampled and refined into a high-fidelity propagation model. Unlike other approaches, we place the TX at the center to reduce the model’s complexity. This improves model performance compared to using an additional channel for the TX location. By implementing these changes, we address the generalizability issues of previous works, enabling real-time propagation modeling for any environment with available 3D geographical data. Our approach significantly

improves both accuracy and computational efficiency. Specifically, we achieve a normalized Root Mean Squared Error (RMSE) of less than 0.035 dB over a 37,210 square meter area, with processing times of just 46 ms on a GPU. These results demonstrate the model's ability to rapidly provide high-fidelity propagation predictions, surpassing traditional ray tracing methods that require over 387.6 seconds. Additionally, refining the model with a small amount of measurement data shows an RMSE of 0.0113, demonstrating its adaptability to real-world data. The remarkable performance and efficiency of AI-driven techniques underscore their potential to revolutionize wireless network design and optimization, enabling real-time adaptation to dynamic and complex telecommunication environments.

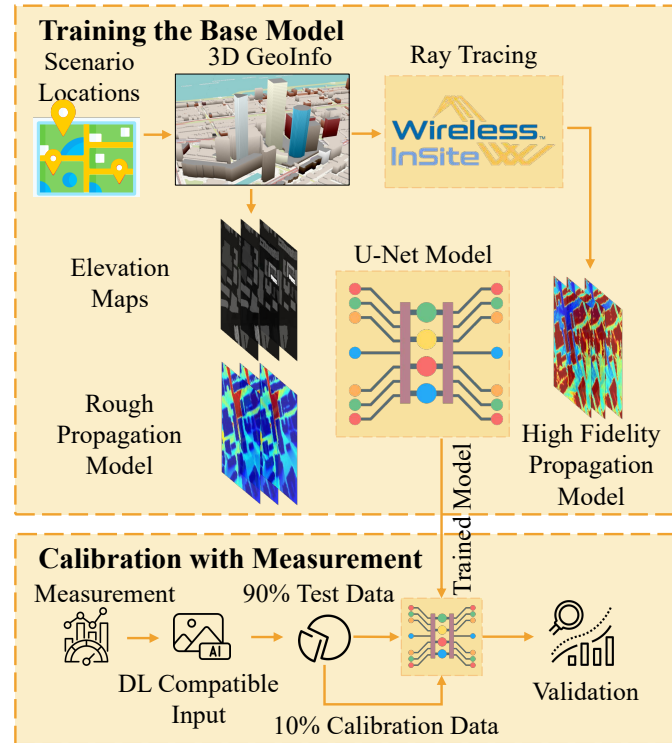


Figure 3.14: Training process, data calibration, and model validation.

3.3.2 Training the Model: Data Collection

To construct a comprehensive and precise dataset for predicting path gain (expressed in dB throughout this study), we use both ray tracing simulations and empirical measurements. Our objective is to forecast the Path Gain (PG), as delineated in equation (3.1), by leveraging the received power at the receiver (P_{RX}) and the transmitted power (P_{TX}).

$$PG(t) = P_{RX}(t) - P_{TX}(t), \quad (3.1)$$

The CIR can be defined as:

$$h(t, \tau) = \sum_{i=1}^N \alpha_i(t) \delta(\tau - \tau_i(t)), \quad (3.2)$$

where $\alpha_i(t)$ is the time-varying complex amplitude of the i -th path and $\tau_i(t)$ is the time-varying delay of the i -th path. To extract the received power from the channel, we use the CIR as shown in (3.3)

$$\begin{aligned} P_{\text{RX}}(t) &= 10 \log_{10} \left(\int_{-\infty}^{\infty} |h(t, \tau)|^2 d\tau \right) \\ &= 10 \log_{10} \left(\sum_i |\alpha_i(t)|^2 \right). \end{aligned} \quad (3.3)$$

In a stationary environment with a mobile receiver, $PG(t)$ and $PG(q_{\text{RX}})$, where q_{RX} is the location of RX can be considered equivalent since the position q_{RX} of the receiver varies with time t . Thus, modeling $PG(q_{\text{RX}})$ effectively captures the time-varying nature of the path gain $PG(t)$ as the receiver moves through different locations q_{RX} .

3.3.2.1 Ray Tracing

Urban environments pose challenges for conventional channel models, which often fail to accurately characterize channel properties. Ray tracing methods offer a potential solution for these complex scenarios. To build a comprehensive dataset, we employed Wireless InSite Ray Tracing software [101] by RemCom to collect high-fidelity data. The ray tracing model is configured by one diffraction and four reflections. In the scenario described below, simulating one transmitter takes 1:25:12 using CPU or 0:03:16 using GPU on a machine with two Intel Xeon E5-2660 processors with 28 cores and one Nvidia Tesla K40c GPU with 2880 CUDA cores.

In this study, we focus on the Northeastern University campus in Boston, shown in Figure 3.15, as an urban use case scenario to train and test the model. We consider a grid of potential RX locations, comprising 7,569 points (red points) spread over a 435×435 square meters area, and 61 TX locations (green points) situated at the corners of building rooftops for potential BS. Additionally, we examine Fenway Park ($42^{\circ}20'26''\text{N}$ $71^{\circ}05'38''\text{W}$), as a separate location with a lower density of buildings (and not seen in the DL training phase) with another 16 TXs to evaluate the model's generalization capabilities. To ensure accuracy, we import a precise 3D model of the area using data gathered by Boston Planning and Development Agency [102].

To prepare the input data for the model, we simulate ray tracing for all transmitter locations in the Northeastern University scenario, as shown in Figure 3.15, to obtain path gain heat maps. These heat maps serve as the ground truth for training the model, with Figure 3.16 presenting an example. We convert these maps into gray-scale single-channel images to reduce the data requirements and mitigate overfitting. Since DL models require fixed input sizes, we crop the images to ensure uniform input sizes across different scenarios. Each image in our dataset measures 100×100 pixels, representing approximately a 1.929×1.929 meter area per pixel. Generating data for numerous scenarios is impractical, so we employ data augmentation techniques to create an augmented dataset from a limited synthetic dataset. Specifically, we use random rotations to incorporate the transmitter

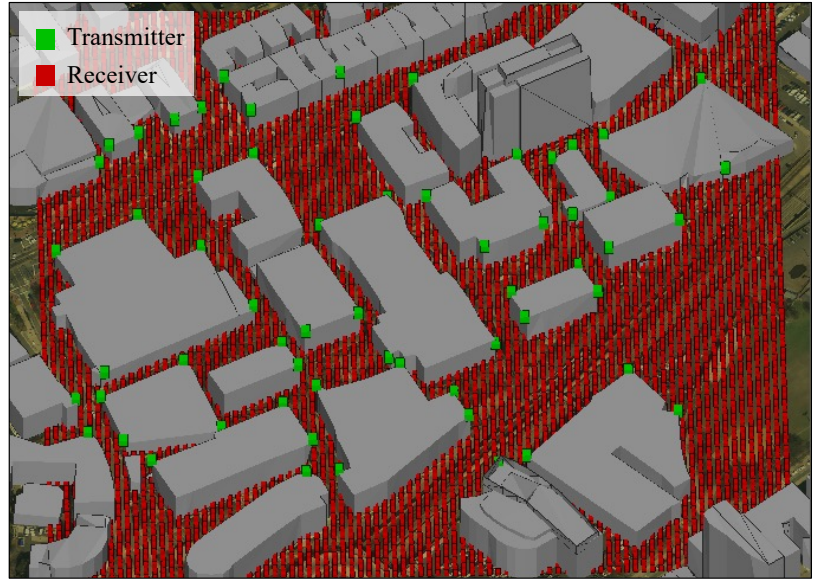
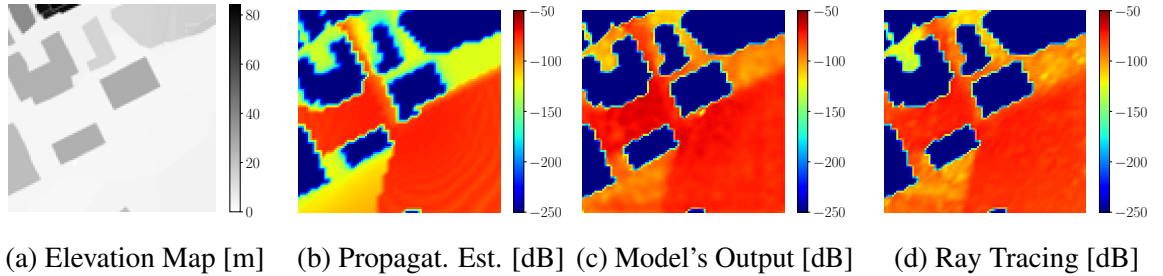


Figure 3.15: Northeastern University, Boston Campus, used for generating the main dataset consisting of 61 TX and 7,569 RX. Location: $42^{\circ}20'22''\text{N}$, $71^{\circ}05'14''\text{W}$.

location into various input configurations, ensuring a substantial and diverse training dataset to enhance the model's robustness and accuracy.



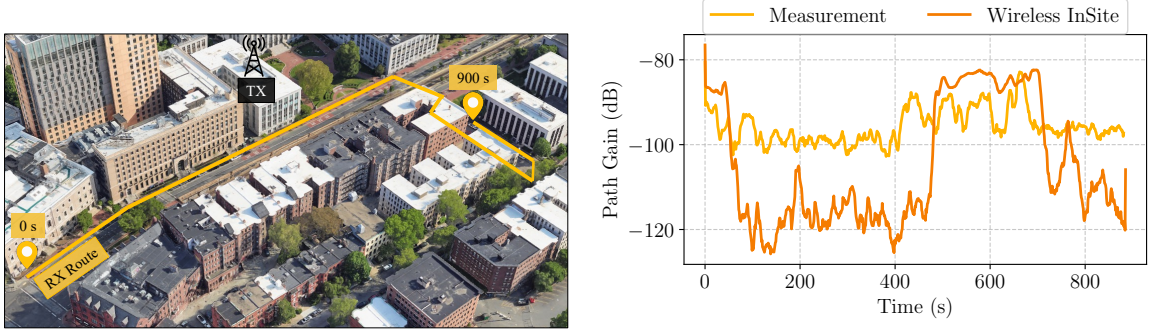
(a) Elevation Map [m] (b) Propagat. Est. [dB] (c) Model's Output [dB] (d) Ray Tracing [dB]

Figure 3.16: A comparison of the model's output (Figure 3.16c) with the ground truth heatmap generated by Wireless InSite (Figure 3.16d), showing its superior performance compared to (Figure 3.16b).

3.3.2.2 Measurement Campaign

Although ray tracing is a powerful tool for modeling channels, real-world scenarios present unique variations that can significantly alter the channel characteristics (see Figure 3.17b). Three main factors contribute to these variations: (1) environmental dynamics, such as moving vehicles, constantly change the channel conditions; (2) the precise shapes and materials of buildings, which 3D models may not accurately capture, can affect channel behavior, as materials are often not modeled with exact fidelity; (3) interference from other users and background noise introduce additional environment noise into the channel, complicating accurate modeling.

To refine, calibrate, and validate the DL model in a real-world scenario, we conducted a measurement campaign in collaboration with VIAVI Solutions around the Northeastern University campus, as depicted in Figure 3.17a. The details of the measurements are provided in Table 3.3.



(a) Path followed during the measurement campaign. (b) The path gain derived from the measurement campaign with moving average applied.

Figure 3.17: Measurement campaign at Northeastern University Campus in collaboration with VIAVI to gather real-world data for model validation and refinement.

For channel sounding, the VIAVI Solutions Ranger, an RF waveform generator and capture platform, was used. It supports two full-duplex channels with 200 MHz bandwidth up to 6 GHz and captures three and one-half hours of recordings. Analysis and waveform modifications are done using the Signal Workshop application, which can be run locally or remotely.

The recorded I/Q samples by the Ranger were processed in two steps: (1) extracting CIR ($h(\tau, t)$) from the raw I/Q samples ($R(\tau, t)$); and (2) calibration to determine the actual Path Gain ($PG(\mathbf{q}_{RX})$). For the first step, we utilized a Galois Linear Feedback Shift Register 14 (GLFSR-14) codeword, modulated it using BPSK, resampled it to match the RX sampling frequency ($s(t)$), and then correlated it with the received data. This process was repeated for each second of the data. Thus, CIR at the receiver $h[\tau, t = n]$ at the n -th second at location \mathbf{q}_{RX} using GPS logs is

$$h(\tau, t) = R(\tau, t) * s(t). \quad (3.4)$$

To remove background noise from the channel, we identified the significant peaks in the channel for every length of the codeword:

$$\alpha = h(\tau, t) \cdot \mathbf{1}_{\{\text{peaks}(h(\tau, t))\}}. \quad (3.5)$$

The indicator function $\mathbf{1}_{\{\text{peaks}(h(\tau, t))\}}$ is defined as

$$\mathbf{1}_{\{\text{peaks}(h(\tau, t))\}} = \begin{cases} 1 & \text{peaks of } h(\tau, t) \\ 0 & \text{otherwise.} \end{cases} \quad (3.6)$$

This function is 1 at the peak (threshold of $+3dB$ of the neighboring points) positions of $h(\tau, t)$ and 0 elsewhere, effectively isolating the peak values of the CIR. After extracting the sparse channel, we sum the values like in (3.3).

Table 3.3: Measurement Setup and Equipment

TX	
RU	Ettus USRP X410
Amplifier	Minicircuits ZHL-1000-3W+ (38 dB)
Antenna	Pasternack PE510M1014 (6 dBi)
Location	42°20'25"N 71°05'16"W
RX	
RU	Ranger provided by VIAVI Solutions
Antenna	Waveform directional antenna (10 dBi)
Location	Mobile (see Figure 3.17a)
Measurement Details	
Frequency	910 MHz
Bandwidth	122.88 MHz
Codeword	GLFSR-14
Synchronization	GPS clock for both TX and RX

To accurately determine the path gain, a conducted calibration test Over-the-Cable (OTC) was performed with all equipment in the loop except for the antennas. Instead of antennas, 60 dB attenuators (L_{ATT}) were placed between RX and TX to prevent Analog to Digital Converters (ADCs) saturation, and the cable loss (L_c) was measured.

$$P_{RX}^{OTC} = P_{TX} + G_{AMP} - L_c - L_{ATT} \quad (3.7)$$

After field measurements, the average received power from the calibration data (P_{RX}^{OTC}) was subtracted from the received power in the actual measurement (P_{RX}^{OTA}) to compensate for amplifiers (G_{AMP}), cable losses (L_c), and TX power (P_{TX}).

$$P_{RX}^{OTA} = P_{TX} + G_{AMP} + G_{ANT} + PG^{OTA} \quad (3.8)$$

The nominal gain of the antennas (G_{ANT}) was also considered in PG^{OTA} :

$$PG^{OTA} = P_{RX}^{OTA} - P_{RX}^{OTC} - L_c - L_{ATT} - G_{ANT} \quad (3.9)$$

3.3.3 Deep Learning-Based Propagation Model

We propose a novel model shown in Figure 3.18 inspired by PMNet [4], which originally takes two inputs: (1) a building map, indicating building locations with binary values (ones and zeros); and (2) a one-hot encoded TX location. We have modified these inputs for improved performance. Instead of using a binary building map, we now input an elevation map (\mathbf{I}_{el}) that shows building

heights (Figure 3.16a). Additionally, rather than a one-hot encoded TX location, we use a rough estimation of the propagation model derived from real-time ray tracing by Wireless InSite (\mathbf{I}_{est}), which runs in approximately 30 ms, as illustrated in Figure 3.16b. The TX location is always at the center of the image, so there is no need to include the TX location in another channel. These modifications to the input enable our model to deliver high-fidelity propagation predictions in real time for different scenarios.

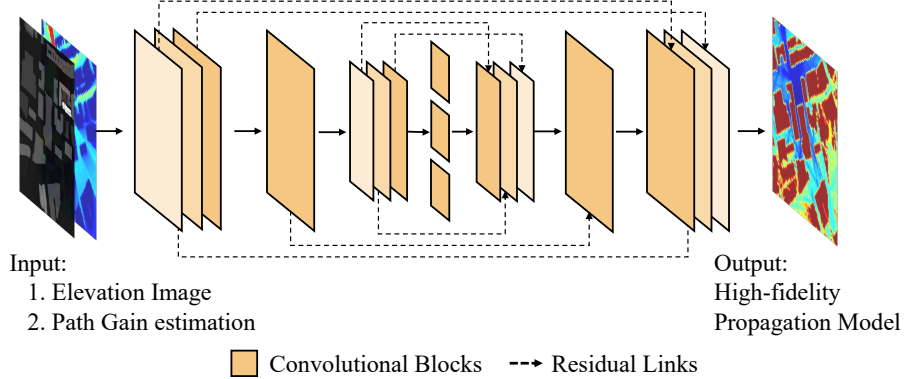


Figure 3.18: U-Net architecture adapted from PMNet [4]. We use elevation maps and propagation estimates as inputs to achieve an accurate propagation model.

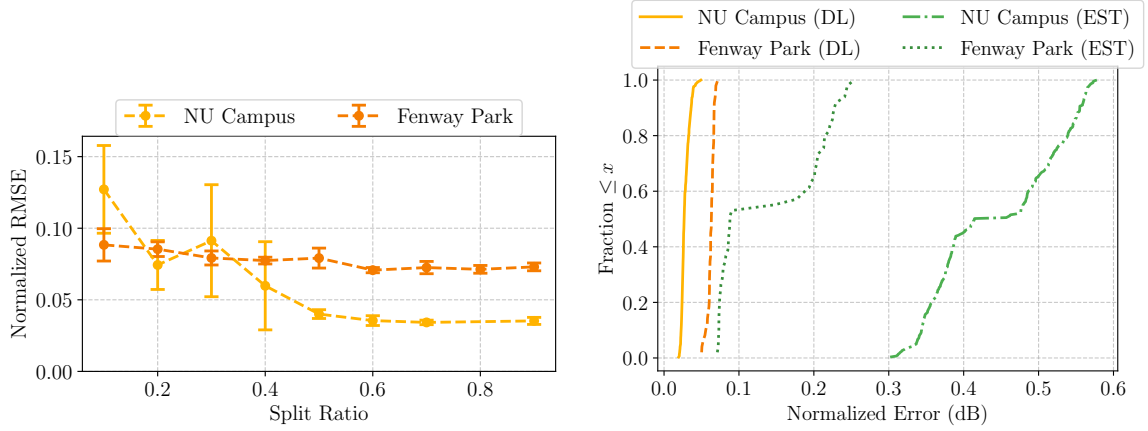
The DL model is designed to predict the path gain ($PG_{dB}(q_{RX})$) given the input \mathbf{x} and the model parameters θ (weights and biases). However, the model's output is not limited to the path gain for a specific location, i.e., pixels, but rather it provides the path gain for an entire area, i.e., a heatmap. Mathematically, this can be represented as $P(PG_{dB}(q_{RX})|\mathbf{x}, \theta)$, where \mathbf{x} is the concatenated input $[\mathbf{I}_{el}, \mathbf{I}_{est}]$, and θ encompasses all the parameters of the model. The objective is to learn the distribution of path gain conditioned on the input data and model parameters. This is achieved by optimizing the model parameters θ during training to minimize the prediction error.

As mentioned in Section 3.3.2, the main dataset consists of 61 different scenarios (TX locations), each with 100 augmented scenarios, resulting in a total of 6,100 images. To validate the robustness and ensure a fair comparison of the model, we randomly split the data into different ratios ten times. This approach helps to: (1) ensure there is no bias towards specific scenarios; and (2) evaluate the model's generalization across various test ratios. Additionally, the trained model is tested in a different type of environment at Fenway Park with 16 TXs to further assess its performance. Besides ray tracing, measurement data is also used to validate the model. The entire process is illustrated in the diagram in Figure 3.14.

3.3.4 Performance Results

As described in Section 3.3.2, the model is trained and tested with different split ratios using 10-fold cross-validation to find the optimal configuration. The results are shown in Figure 3.19a. As observed, the model stabilizes after a 0.6 split ratio, indicating that no further training is required for effective inference. The error has been normalized across all plots, with the path gain range spanning from -50 to -250 dB.

Also, the Empirical Cumulative Distribution Function (eCDF) of error for the best-performing model across 10-fold cross-validation has been plotted using two different test datasets (unseen by the model): (1) the same area at Northeastern; and (2) a different area at Fenway Park ($42^{\circ}20'26''N$, $71^{\circ}05'38''W$), where the environment is more open compared to the dense structure of the Northeastern Campus.



(a) RMSE versus split ratio to evaluate the model's generalizability. (b) eCDF for the DL model compared to real-time propagation modeling from the WI model (EST).

Figure 3.19: Model performance comparison at Northeastern University and Fenway Park.

Results in Figure 3.19b show that the model outperform traditional propagation estimation. Specifically, the median error for DL at Northeastern Campus is 0.0268, and at Fenway Park it is 0.0484. However, for the traditional model, the median error at Northeastern Campus is 0.4146, and at Fenway Park it is 0.0778. These results highlight the model's robustness and adaptability to different environments, maintaining superior performance in both familiar and new scenarios.

In addition to ray tracing, we evaluate the model's performance after adding measurement data in the training phase (Figure 3.20). For this, we use 90% of the points for testing. Initially, the error is relatively high (median of 0.0569 dB), but after refining the model with a small amount of measurement data, the performance improves significantly, reducing the median error to 0.0113 dB. This demonstrates that the DL model can be calibrated with measurement data, unlike common ray tracing software.

Besides the low overall error of the propagation model, using DL models enables near real-time accurate propagation modeling. From our test benches, real-time ray tracing by Wireless Insite takes approximately 30 ms to run, while high-fidelity ray tracing takes over 387.6 s to complete. However, our model requires only 46 ms on a GPU and 183 ms on a CPU to run with minimal error.

3.3.5 Integration with the Colosseum Emulator

To enable real-time channel emulation as well as simulation using our U-Net model, we integrated it into the Colosseum platform. We followed the approach introduced in ColosSUMO [103], which extends Colosseum with real-time scenario generation capabilities. As shown in Fig. 3.21, when a

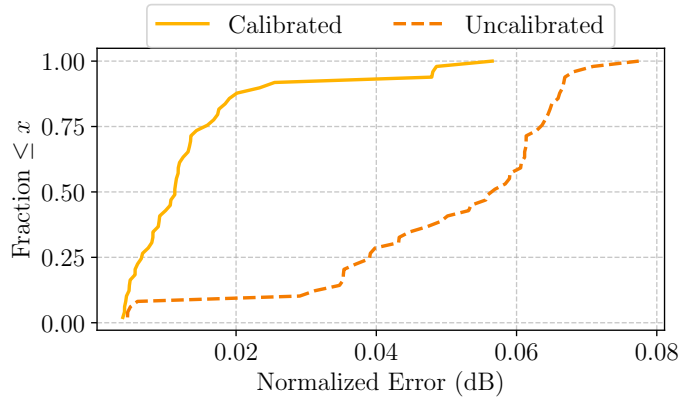


Figure 3.20: eCDF of error w/ and w/o calibration using the measurement data (10% of the dataset).

user selects or updates a location, the corresponding building elevation map is loaded, transformed into the appropriate input shape and format within 20 ms, and passed to our U-Net model. The model performs inference in approximately 4 ms, producing a path gain prediction. This result is then sent to an MQTT broker, which forwards it to Colosseum’s MCHEM, the FPGA-based Massive Channel Emulator. MCHEM then uses these taps to emulate the corresponding wireless channel in real time.

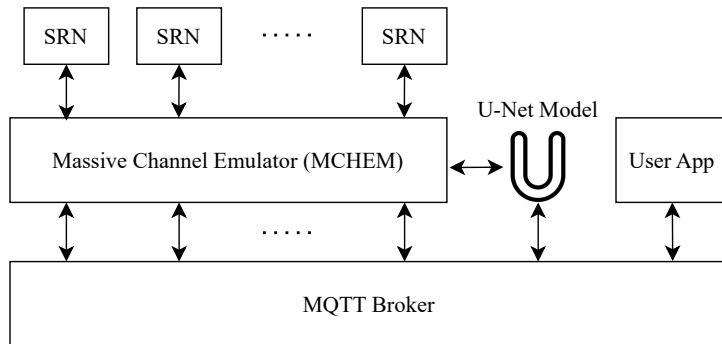


Figure 3.21: Real-time channel emulation pipeline on Colosseum. User-selected locations trigger U-Net inference, with predicted taps sent via MQTT to MCHEM for emulation.

In Figure 3.22, we show results from running OpenAirInterface (OAI) on the Colosseum testbed using single-tap time-domain channels with simple propagation delays to simulate mobile scenarios across four channel models: Ray Tracing, Calibrated U-Net, Uncalibrated U-Net, and actual measurements. Each experiment was repeated 10 times. Both the Ray Tracing and Uncalibrated U-Net models failed to establish a connection under the same configuration, resulting in no Reference Signal Received Power (RSRP) data. In contrast, the Calibrated U-Net model successfully produced RSRP patterns closely matching empirical measurements, with an RMSE of 8.86 dBm.

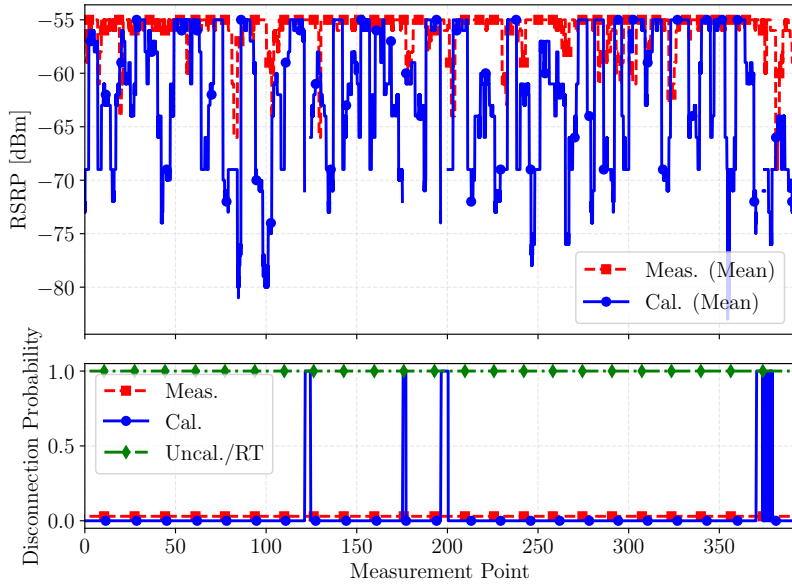


Figure 3.22: Comparison of RSRP reports from OAI on Colosseum (10 runs per experiment). The Calibrated U-Net closely matches measurements, while Ray Tracing and Uncalibrated U-Net failed to establish a connection in this setup.

3.3.6 Conclusions

This section presented a real-time path gain estimator leveraging advanced DL techniques for radio map creation. The initial approach [17] integrates elevation maps and rough propagation model estimations as inputs to a U-Net architecture, achieving a normalized RMSE of less than 0.035 dB across a 37,210 square meter area with inference times of 46 ms on GPU and 183 ms on CPU—a significant advancement over traditional high-fidelity ray tracing methods, which typically require over 387.6 seconds. The measurement campaign conducted at Northeastern University enabled model calibration through transfer learning, reducing the median error to 0.0113 dB with only 10% of the data used for calibration.

The extended framework, AIRMap [18], further simplifies the approach by relying solely on a single-channel elevation map as input, reducing inference time to under 4 ms while maintaining sub-5 dB RMSE. This resolution-adaptive design supports radio-map estimation across physical areas ranging from 500 m to 3 km per side without altering the architecture. Integration into the Colosseum emulator demonstrated the practical feasibility of AI-driven channel models for real-time wireless network emulation, with the calibrated model successfully producing RSRP patterns matching empirical measurements (RMSE of 8.86 dBm) while ray tracing and uncalibrated models failed to establish connections.

This work demonstrates how DT platforms like Colosseum can serve both as data collection environments for training AI models and as deployment systems for real-time channel emulation. The ability to generate accurate radio maps in milliseconds—rather than minutes or hours—enables new use cases such as dynamic scenario adaptation, real-time mobility modeling, and closed-loop

network optimization that were previously impractical with traditional ray-tracing methods.

3.4 Generative Models for Synthetic RF Data

The realization of efficient AI solutions for the optimization of next-generation RAN relies on the availability of expansive, high-quality datasets that accurately capture nuanced, site-specific conditions. However, obtaining such abundant, domain-specific measurements poses a significant challenge, especially as network complexity and energy efficiency demand surge toward 6G. As discussed in Section 3.3, creating accurate DT representations requires substantial data, and field measurements are costly, time-consuming, and quickly become outdated in dynamic environments.

To address these challenges, this section presents GenerativeAI-enabled Digital Twin (Gen-TWIN), a Generative Artificial Intelligence (GenAI)-enabled DT platform that leverages a novel *soft*-Generative Adversarial Network (GAN) based on Long Short Term Memory (LSTM) layers (soft-GAN). This model is designed to generate synthetic Digital Twin for Radio Access Network (DT-RAN) RF data for both transmitter and receiver ends, augmenting the limited datasets collected through field measurements by synthetically replicating key features of RF signals. Building upon the Colosseum DT platform described in Chapter 2, Gen-TWIN demonstrates how testbeds can serve not only as testing environments but also as data sources for training generative models.

The key contributions of this section include:

- The Gen-TWIN platform, integrating Digital Twin and Generative Artificial Intelligence layers.
- A soft-attention LSTM-based time-series GAN model, named *soft*-GAN, specifically for DT-RANs.
- Performance evaluation comparing *soft*-GAN against various baseline generative models, demonstrating up to 19% improvement in accuracy.

The remainder of this section is organized as follows. Section 3.4.1 presents the Gen-TWIN platform architecture, describing both the DT layer built on Colosseum and the GenAI layer. Section 3.4.2 and 3.4.3 detail the soft-GAN model and the data collection methodology, respectively. Section 3.4.4 presents the experimental evaluation, comparing soft-GAN against baseline generative models. Finally, Section 3.4.5 concludes this section.

3.4.1 Gen-TWIN Platform

Our proposed platform comprises two integral components, DT and GenAI layers, as shown in Figure 3.23.

Digital Twin Layer: The DT layer leverages Colosseum, as the O-RAN DT for the network emulator part, and *CaST* [14] for data collection, both described in Chapter 2.

Generative AI Layer: Our GAN framework can be described by the following minmax game:

$$\min_G \max_D \mathbb{E}_{\mathbf{x} \sim p_{\text{data}}(\mathbf{x})} [\log D(\mathbf{x})] + \mathbb{E}_{\mathbf{z} \sim p_{\mathbf{z}}(\mathbf{z})} [\log(1 - D(G(\mathbf{z})))], \quad (3.10)$$

where:

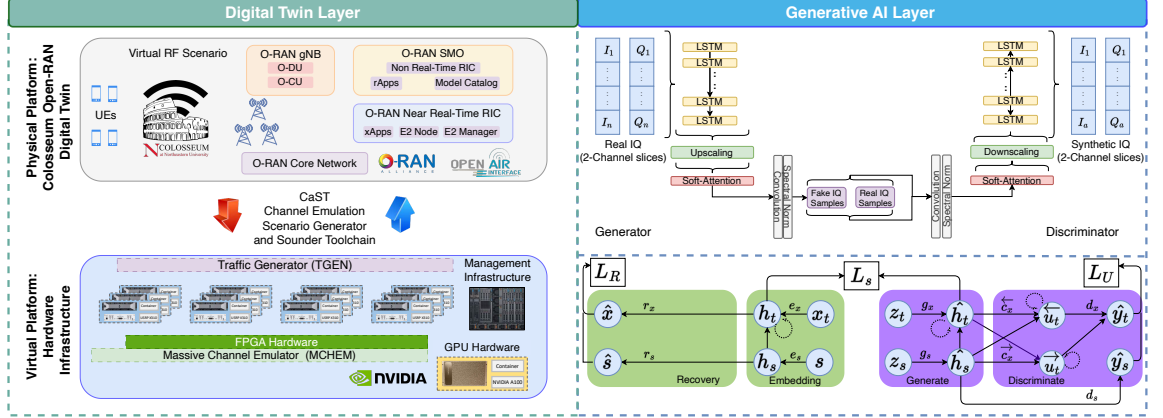


Figure 3.23: Left: O-RAN Digital Twin Layer; Colosseum—the world’s largest wireless network emulator with hardware in the loop [2] to create a comprehensive twin of the O-RAN network. Right: Generative AI Layer; Proposed *soft*-GAN Model — soft-attention-LSTM based Generative Adversarial Network.

- \mathbf{x} represents real I/Q data samples from DT layer.
- $p_{\text{data}}(\mathbf{x})$ denotes the distribution of real time series data.
- \mathbf{z} represents random noise vectors sampled from a prior distribution $p_{\mathbf{z}}(\mathbf{z})$ (e.g., a Gaussian distribution).
- $G(\mathbf{z})$ generates synthetic I/Q data samples from the noise vector \mathbf{z} .
- $D(\mathbf{x})$ represents the probability that \mathbf{x} originates from the real data distribution rather than from G .

In the context of I/Q data augmentation, the generator G learns to produce realistic I/Q data sequences, while the discriminator D tries to distinguish between real and synthetic I/Q data.

The training process iteratively updates the parameters of G and D using gradient-based optimization. Specifically, the discriminator is trained to maximize the likelihood of correctly distinguishing between real and synthetic samples:

$$\mathcal{L}_D = -\mathbb{E}_{x \sim p_{\text{data}}(x)}[\log D(x)] - \mathbb{E}_{z \sim p_z(z)}[\log(1 - D(G(z)))] \quad (3.11)$$

The generator is trained to minimize the likelihood of the discriminator correctly distinguishing synthetic from real samples:

$$\mathcal{L}_G = -\mathbb{E}_{z \sim p_z(z)}[\log D(G(z))] \quad (3.12)$$

These loss functions are alternately optimized at each iteration, leading to gradual improvement in both networks. Once trained, the generator can produce synthetic univariate time series that augment the original dataset. Given a noise vector z , the generator produces a synthetic time series $\hat{x} = G(z)$. These synthetic samples can be used to expand the training dataset, thereby improving the performance and generalization of machine learning models. The augmented dataset \mathbf{X}' can

be represented as $\mathbf{X}' = \mathbf{X} \cup \{G(z_i)\}_{i=1}^N$ where \mathbf{X} is the original dataset and N is the number of synthetic generated samples.

3.4.2 Data Augmentation with *soft-GAN*

3.4.2.1 Fundamentals of *soft-GAN* Model

The values of the time series data are denoted as $m_{i,t} \in \mathbb{R}$, where $i \in \{1, 2, 3, \dots, N\}$ represents the index of individual samples and $t \in \{1, 2, 3, \dots, T\}$ indicates the time points. The associated matrix of time feature vectors is $X_{1,T} = (x_1, \dots, x_T)$ in $\mathbb{R}^{D \times T}$, where D represents the number of time features. Consequently, we take the time series to have a fixed length ζ , denoted as $\hat{M}_{i,t,\zeta} = (\hat{m}_{i,t}, \dots, \hat{m}_{i,t,\zeta})$. Then, using a generator function G and a fixed time sequence t , we can model $\hat{M}_{i,t,\zeta} = G(n, \phi(i), X_{t:t+\zeta})$, where n is a noise vector and ϕ is an embedding function that maps the index of the time series to a vector representation. In the generator G and discriminator D , we use a soft attention mechanism along with convolutional spectral normalization SN as described in [104].

For a sequence of length l , we can write:

$$p : \mathbb{R}^{n_f \times l} \rightarrow \mathbb{R}^{n'_f \times l} \quad (3.13)$$

$$x \mapsto \gamma \text{softA}(f(x) + f(x))$$

$$f(x) = SN(\text{LeakyReLU}(c(x))), \quad (3.14)$$

where n'_f is the number of output features, c is the convolution operator, and softA is the soft-attention mechanism. We use *LeakyReLU* [105] to avoid the well-known dying ReLU problem, where neurons can become inactive and always output zero for any input. On the generator side, we add a spectral normalization layer to further stabilize the training process and prevent sudden escalation of the gradient magnitude [106]. ϕ is a learnable parameter that, when indexed to 0, influences the network's ability to learn local features through the function p .

soft-GAN Generator: The first layer of the generator, $G1$, uses the main function block p :

$$G1 : \mathbb{R}^{n'_f \times 2^3} \rightarrow \mathbb{R}^{n_f \times 2^3} \quad (3.15)$$

$$\hat{M}_0 \mapsto \hat{M}_1 = p(\hat{M}_0),$$

where $i \in [2, L]$. $G1$ maps two channel-separated I/Q sequences \hat{M}_{i-1} to an output \hat{M}_i , then applies an upscale to the function block p :

$$G_i : \mathbb{R}^{n_f \times 2^{i+2}} \rightarrow \mathbb{R}^{n_f \times 2^{i+3}} \quad (3.16)$$

$$\hat{M}_{i-1} \mapsto \hat{M}_i = p(\text{UP}(\hat{M}_{i-1})).$$

In the last layer of the generator, a multivariate sequence is obtained univariately as $\hat{M}_{i,t,\zeta}$ through a one-dimensional convolution operation.

soft-GAN Discriminator: The discriminator design is the same as the generator. The discriminator maps the generator's output $\hat{M}_{i,t,\zeta}$ and $X_{t:t+\zeta}$ to a discriminator score d . The *LeakyReLU* activation function is then used as follows:

$$d_{L+1} : \mathbb{R}^{1+D,\zeta} \rightarrow \mathbb{R}^{n_f,\zeta} \quad (3.17)$$

Algorithm 1 soft-GAN Generator

Input: Noise vector $z \in \mathbb{R}^{(batch_size, seq_len, input_dim)}$

- 1: **Input:** Real IQ Samples
- 2: **First LSTM Layer:** Process IQ and z with an LSTM layer having 256 units, return sequences, dropout of 0.3, and recurrent dropout of 0.3.
- 3: $h_1 = \text{LSTM}_{256}(z)$
- 4: **Batch Normalization:** Normalize the output.
- 5: $h_1 = \text{BatchNorm}(h_1)$
- 6: **Second LSTM Layer:** Process the output with another LSTM layer having 256 units, return sequences, dropout of 0.3, and recurrent dropout of 0.3.
- 7: $h_2 = \text{LSTM}_{256}(h_1)$
- 8: **Batch Normalization:** Normalize the output.
- 9: $h_2 = \text{BatchNorm}(h_2)$
- 10: **Third LSTM Layer:** Process the output with another LSTM layer having 128 units, return sequences, dropout of 0.3, and recurrent dropout of 0.3.
- 11: $h_3 = \text{LSTM}_{128}(h_2)$
- 12: **Spectral Normalization:** Normalize the output.
- 13: $h_3 = \text{SpectNorm}(h_3)$
- 14: **Attention Mechanism:** Apply soft-attention to the output and concatenate it with the LSTM output.
- 15: $\text{attention_out} = \text{Attention}(h_3, h_3)$
- 16: $\text{context_vector} = \text{Concat}(h_3, \text{attention_out})$
- 17: **Fully Connected Layer:** Apply a dense layer with 128 units and LeakyReLU activation.
- 18: $d_1 = \text{Dense}_{128}(\text{context_vector}, \text{activation}=\text{LeakyReLU})$
- 19: **Dropout:** Apply dropout with a rate of 0.3.
- 20: $d_1 = \text{Dropout}_{0.3}(d_1)$
- 21: **Output:** Apply a final dense layer with 2 units to produce the synthetic IQ data.
- 22: $\text{output} = \text{Dense}_2(d_1)$
- 23: **Return:** Samples

$$(\hat{M}_{L+1}, X_{t:t+\zeta}) \longmapsto \hat{M}_L = \text{LR}(c_1(\hat{M}_{L+1}, X_{t:t+\zeta})), \quad (3.18)$$

where $i \in [2, L]$. Downscaling is then applied to the main function block:

$$\begin{aligned} d_i : \mathbb{R}^{n_f \times 2^{i+3}} &\rightarrow \mathbb{R}^{n_f \times 2^{i+2}} \\ Y_i &\longmapsto Y_{i-1} = \text{DOWN}(m(Y_i)). \end{aligned} \quad (3.19)$$

The final operation is handled by a fully connected layer:

$$\begin{aligned} d_1 : \mathbb{R}^{n_f} &\rightarrow \mathbb{R} \\ Y_i &\longmapsto Y_0 = \text{SN}(\text{FC}(\text{LeakyReLU}(\text{softA}(c(Y_1))))) \end{aligned} \quad (3.20)$$

Table 3.4: Data collection parameters summary between the two testbeds: POWDER for OTA data, and Colosseum for emulated data.

Parameter	POWDER	Colosseum
SDR	USRP X310	USRP X310
Nodes	Honors and USTAR Rooftop BS	Digitized Honors and USTAR Nodes
Frequency	3.46-3.465 GHz	1 GHz
Bandwidth	1-10 MHz	80 MHz
Time Capture	30 seconds	30 seconds
Capture Size	2.57 GB	2.96 GB
Sample Time	10 MS/s	10 MS/s
Tx gain	25 dB	15-25 dB
Rx gain	25 dB	15 dB

3.4.3 Data Collection

The data collection operation aims to collect I/Q samples that can serve as a baseline for the data augmentation step. We collect I/Q samples through two different testbeds: (i) POWDER for real-world data, and (ii) Colosseum for emulated data. A summary of the parameters for the data collection is shown in Table 3.4. Additionally, Figure 3.24 depicts the data collection scenarios for the real world (POWDER) and the digital world (Colosseum). The POWDER testbed [107] is a city-scale facility located at the University of Utah in Salt Lake City, UT. The platform supports a wide range of hardware and software configurations, enabling experimentation with real-world OTA scenarios and the development of new wireless technologies. It provides various types of end-to-end software-defined nodes with different capabilities, deployed across the university campus.

In our real-world OTA data collection, we leverage two of its rooftop base station nodes, as shown by the red circles in Figure 3.24: Honors and USTAR. For the emulation data, we utilize Colosseum’s capabilities for digitizing the real world [3]. We use a DT representation of the POWDER platform to recreate a similar real-world environment in an emulated one. Thus, we use the POWDER scenario described in [64] to collect data between the same digitized nodes for Honors and USTAR rooftop base stations, digitized as nodes 1 and 5, respectively.

As shown in Table 3.4, in both cases, we leverage USRP X310 as SDR hardware. The frequencies used for POWDER fall in the CBRS band between 3.46 and 3.465 GHz with bandwidths of 1 MHz and 10 MHz, respectively. In contrast, Colosseum uses its typical emulation of the baseband signal with a frequency of 1 GHz and a bandwidth of 80 MHz. The data capture duration for both platforms is 30 seconds per use case, with a sampling frequency of 10 megasamples per second. The transmission and reception gains of each SDR vary between 15 and 25 dB to compensate for the long distance of about 800 meters between the two nodes.

In each scenario, we leverage CaST [14], which is based on the GNU Radio software development toolkit, to send a BPSK-modulated GLFSR code sequence from the sender node (Honors) and to store the raw received I/Q samples without any processing or equalization on the receiver side (USTAR).

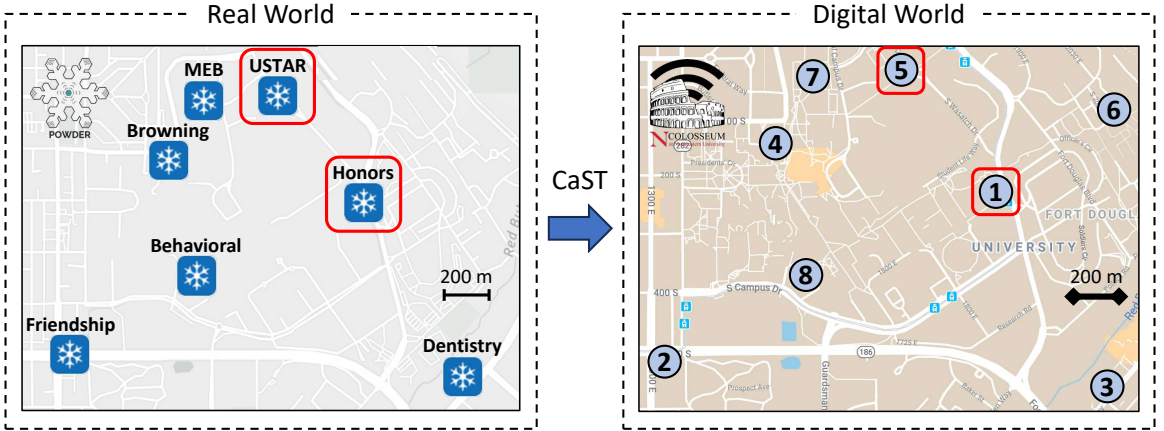


Figure 3.24: Data collection scenarios for the real world (POWDER, left picture) and digital world (Colosseum, right picture). The red circles indicate the actual nodes used for data collection. Colosseum node 6 is a remnant of the now-decommissioned POWDER Medical Tower Rooftop node.

3.4.4 Experiment Evaluation

3.4.4.1 Hyper-parameter Tuning and Training

In our training stage, the initial step in handling the dataset involves splitting it into three distinct parts: 80% training set, 10% validation set, and 10% test set. This division ensures that the model has adequate data for training, tuning, and evaluation, ultimately leading to better performance and generalization. Preprocessing is a critical step in preparing the data for training. The main goal is to normalize the I/Q data to ensure consistency and stability during training. Normalization involves scaling the data so that its values fall within a specific range, -1 to 1. We achieve this by computing the mean (μ) and standard deviation (σ) of the training data and then normalizing each data point accordingly.

Table 3.5: Hyper-parameter tuning stage of *soft-GAN*

Hyper-param.	Search Space	Selected Parameter
Input size	[2, 4, 8, 16, 32]	8
Hidden layers	[1, 2, 3]	3
Hidden layers	[0.5, 1.5, 2.0, 3.0, 5.0]	2.0 \times Input Size
Learning rate	[0.0001, 0.0005, 0.001, 0.005, 0.01]	0.005
Batch size	[64, 128, 256, 512, 1024]	256
Loss Function	[MAE, MSE, sMAPE]	MAE
Training steps	[1000, 5000, 10,000, 20,000, 40,000]	20,000
Optimizer	[RMSprop, SGD, Adam]	Adam

Table 3.5 shows our parameter space. During the hyperparameter tuning stage, an input size of 8 achieves a balance between model complexity and performance. Larger input sizes increase

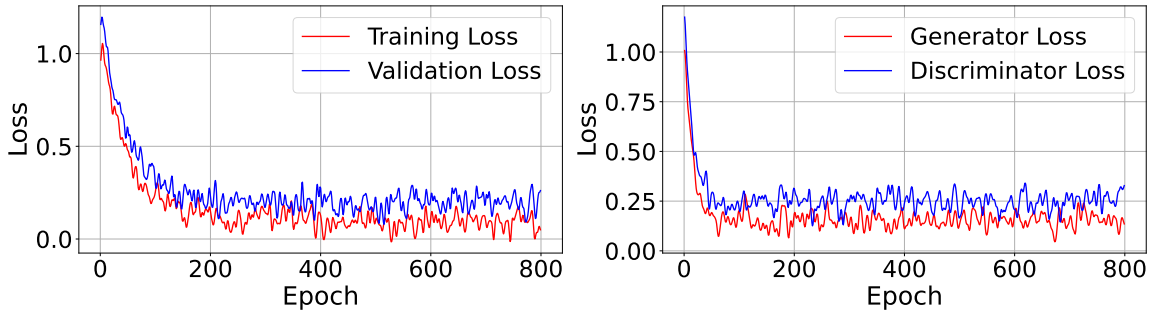


Figure 3.25: *soft-GAN* training and validation loss over epochs (left picture). Generator and discriminator loss over epochs (right picture).

the model's complexity without significantly improving performance. Having three hidden layers allows the model to capture more complex patterns in the data. Setting the hidden layer size to $2 \times \text{InputSize}$ ensures that the network has sufficient neurons to learn intricate features of I/Q samples without overcomplicating the model. A learning rate of 0.005 is a moderate choice that facilitates faster convergence while avoiding the pitfalls of overshooting the optimal point, which can occur with a higher learning rate. A batch size of 256 provides a good compromise between training stability and computational efficiency. We found that larger batch sizes require more memory and longer computation times per update, while smaller batch sizes lead to noisy gradient estimates.

As shown in Figure 3.25 (left), both training and validation losses start at a relatively high value, around 1.2. This is expected as the model begins learning the data patterns from scratch. As training progresses, both losses decrease significantly, stabilizing at lower values, around 0.2. The training loss declines more smoothly than the validation loss, which shows more fluctuations. However, these fluctuations are within a narrow range, and both losses remain close to each other throughout the training process. This behavior suggests that the model is learning effectively without overfitting. If the model were overfitting, we would observe the validation loss diverging from the training loss, with the validation loss increasing while the training loss continues to decrease. Conversely, underfitting would be indicated by both losses remaining high and not decreasing significantly. The close alignment between the training and validation losses in our model demonstrates a good balance, indicating that the *soft-GAN* generalizes well to unseen data.

Figure 3.25 (right) plot shows the generator and discriminator losses over the epochs. Initially, both losses start high, around 1.0, which is typical at the beginning of GAN training. As training proceeds, the generator loss decreases steadily, stabilizing around 0.1 to 0.2. The discriminator loss also decreases but at a slower rate and stabilizes around 0.2 to 0.3. This dynamic is crucial in GAN training. The generator aims to produce data that the discriminator cannot distinguish from real data, while the discriminator aims to correctly identify real and generated data. The observed balance between these losses indicates that the training process is stable. If the discriminator loss were to decrease too rapidly, it would suggest that the discriminator is too powerful, making it difficult for the generator to improve. On the other hand, if the generator loss were too low compared to the discriminator loss, it might indicate mode collapse, where the generator produces limited diversity in the generated data. The balance observed here suggests that both the generator and discriminator are improving in tandem, contributing to the overall performance of the model. The stability and

Table 3.6: NRMSE and Context FID-Scores (Lower values in these metrics indicate better model performance)

Models	NRMSE		Context FID-scores	
	128	256	128	256
TimeGAN	0.27 ± 0.06	0.26 ± 0.02	0.23 ± 0.04	0.63 ± 0.10
Autoencoder	0.45 ± 0.07	0.43 ± 0.01	0.58 ± 0.03	0.42 ± 0.10
BiLSTM	1.03 ± 0.055	0.97 ± 0.003	1.07 ± 0.20	0.92 ± 0.07
BiLSTMGAN	0.95 ± 0.06	1.13 ± 0.04	0.71 ± 0.01	0.23 ± 0.05
CnnGAN	1.87 ± 0.07	2.73 ± 0.02	1.87 ± 0.09	1.63 ± 0.06
soft-GAN (ours)	0.23 ± 0.02	0.21 ± 0.07	0.15 ± 0.01	0.09 ± 0.04

Table 3.7: Discriminative and Predictive Score Results (Lower values in these metrics indicate better model performance)

Models	Discriminative Score		Predictive Score	
	128	256	128	256
TimeGAN	0.028 ± 0.003	0.013 ± 0.01	0.019 ± 0.08	0.17 ± 0.03
Autoencoder	0.15 ± 0.03	0.17 ± 0.08	0.24 ± 0.09	0.23 ± 0.01
BiLSTM	0.04 ± 0.03	0.053 ± 0.002	0.18 ± 0.04	0.13 ± 0.04
BiLSTMGAN	0.113 ± 0.09	0.088 ± 0.02	0.27 ± 0.017	0.09 ± 0.03
CnnGAN	0.43 ± 0.08	0.39 ± 0.01	0.36 ± 0.008	0.33 ± 0.004
soft-GAN (ours)	0.017 ± 0.02	0.013 ± 0.06	0.016 ± 0.004	0.009 ± 0.006

convergence of these loss curves provide a numerical testament to the model’s performance. The training and validation losses stabilize around 0.2, and the generator and discriminator losses around 0.1 to 0.3, indicating that the model has learned the underlying data distribution effectively.

3.4.4.2 Performance Comparison with Baseline Models

This section provides a comprehensive evaluation of the proposed *soft-GAN* architecture against baseline models for time-series data augmentation, all trained on our dataset, including TimeGAN [108], Autoencoder [109], BiLSTM [110], BiLSTMGAN [111], and CNNGAN [112]. The performance

Table 3.8: Comparison of classification performance of baseline models

Models	Accuracy	Precision	Recall	F1-score
TimeGAN	0.83	0.68	0.84	0.87
Autoencoder	0.88	0.63	0.82	0.85
BiLSTM	0.78	0.70	0.80	0.81
BiLSTMGAN	0.83	0.73	0.81	0.83
CnnGAN	0.77	0.61	0.79	0.73
soft-GAN (ours)	0.93	0.78	0.91	0.89

metrics presented in Table 3.6 include Normalized Root Mean Squared Error (NRMSE) and Context Fréchet Inception Distance (FID)-scores, which are widely used in computer vision to evaluate the quality of synthetic data [113]. Table 3.7 includes Discriminative and Predictive Scores, derived as evaluation criterion from baseline work [108], where a post-hoc time-series classification model (2-Layer LSTM) is trained to distinguish between original and generated sequences, labeled as "real" and "generated," respectively. The classification error on a held-out test set is reported as a quantitative metric for similarity assessment. In Table 3.8, the results are presented using well-known classification metrics, including accuracy, precision, recall, and F1-score.

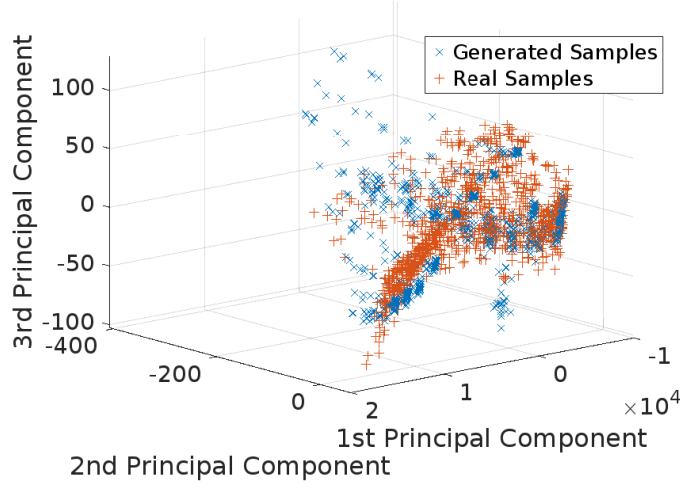


Figure 3.26: Components of real and generated samples in the PCA subspace; Generated samples (marked as “ \times ”) exhibit a substantial overlap with the real samples (marked as “ $+$ ”).

Performance results show that the use of a soft-attention mechanism allows the model to focus on the most relevant parts of the input sequence, enhancing its ability to capture long-range dependencies and intricate patterns in the time-series data. Table 3.6 shows how *soft*-GAN achieves an NRMSE of approximately 0.23 and 0.21, outperforming the best-performing baseline, TimeGAN, whose NRMSE ranges from 0.26 to 0.27. Statistically, this equates to about an 11–19% reduction in the NRMSE relative to strong baselines. Lower NRMSE signifies a tighter fit of the generated time series to the real data distribution, indicating that *soft*-GAN’s internal soft-attention and recurrent mechanisms effectively preserve key temporal dependencies. Decreasing the FID-score relative to leading baselines suggests that *soft*-GAN maintains more accurate local and global temporal structures. Table 3.7 shows that for 128-length sequences, *soft*-GAN achieves a Discriminative Score approximately 39% lower than TimeGAN (0.017 vs. 0.028) and significantly lower than all other baselines. This improvement at the 256-length scale is also notable, matching TimeGAN at approximately 0.013 but with a more stable variance. Such a low Discriminative Score suggests that the synthetic sequences from *soft*-GAN are statistically indistinguishable from real data, reinforcing that our generative model is not merely capturing coarse trends but rather the nuanced statistical behavior observed in authentic RAN measurements.

To further validate the utility of generated data, Table 3.8 presents results from a classification task

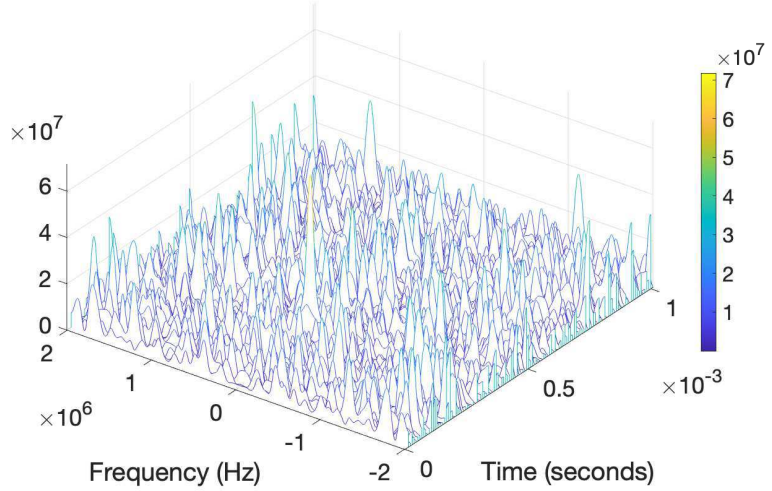


Figure 3.27: Spectrogram of *soft*-GAN generated synthetic RF (25 dB gain) Signals

trained on synthetic samples. *soft*-GAN achieves an accuracy of 0.93, outperforming all baselines by at least 5 percentage points. Its F1-score of 0.89 represents a $\sim 9\%$ improvement over the closest competitor. This higher classification metric confirms that *soft*-GAN does not just produce visually or statistically similar data, but also preserves class-discriminative features. Higher precision results of our model indicate that *soft*-GAN has a lower false positive rate. *Soft*-GAN improves accuracy by 5-11% over TimeGAN and 7-19% over BiLSTM.

The Principal Component Analysis (PCA) projection in Figure 3.26 offers a reduced dimensionality view of both real and *soft*-GAN generated samples. If we consider the distributions of points along each principal component axis, the generated samples do not form a distinctly separate cluster; rather, they integrate into the same regions occupied by the real samples. This suggests that the generative model has learned not only the mean and covariance structure of the underlying data but also the higher-order moments that define the geometry of the data manifold in a lower-dimensional space. The close spatial proximity and pattern similarity between real and synthetic points imply that *soft*-GAN captured complex temporal correlations, amplitude variations, and other spectral signatures pertinent to RAN signals. The spectrogram in Figure 3.27 provides a joint time-frequency representation of a *soft*-GAN generated RF signal at 25 dB signal power level. By applying a time-frequency decomposition—commonly via Short-Time Fourier Transform (STFT)—we visualize how signal energy is distributed across frequencies as a function of time. The generated spectrogram exhibits key spectral and temporal patterns that mirror realistic RF conditions.

3.4.5 Conclusions

This section introduced Gen-TWIN, a synthetic data generation DT platform, that fulfills the data-intensive demands of advanced DT-RAN operations. By producing high-fidelity RF signals through the proposed soft-GAN model, Gen-TWIN empowers AI-driven network management with

richer, more representative training sets. The experimental evaluation demonstrated that soft-GAN achieves up to 19% improvement in NRMSE compared to baseline models, with generated samples that are statistically indistinguishable from real data.

The data collection methodology presented in this section further demonstrates the potential connections and use cases between real-world testbeds (POWDER) and DT platforms (Colosseum). We demonstrated that the tools developed in this dissertation, such as *CaST*, are portable and can be used to collect I/Q samples across both environments. Additionally, it showed how digitized scenarios can complement physical measurements to create comprehensive datasets for training generative models. This approach also highlighted one of the key enablers of testbeds and platforms, high-volume data generation for ML training. It positions testbeds and DTs not only as environments for validation and experimentation, but also as critical data sources for developing and evaluating AI/ML solutions for next-generation wireless networks.

3.5 Summary and Discussion

This chapter demonstrated the *use case* dimension of DTs and emulation platforms, showing how they enable E2E pipelines for three specific applications: spectrum sharing, AI-driven channel modeling, and synthetic data generation. Each use case highlighted a different aspect and capability of the Colosseum emulation platform, the main experimental platform in this dissertation. First, we demonstrated how spectrum-sharing CBRS scenarios between 4G and 5G cellular and incumbent radar systems can be emulated safely on Colosseum using waveform twinning and dApp-based detection to study interference management in conditions that would be difficult, expensive, or unsafe to reproduce OTA in the real world. Then, we showed the AIRMap framework and how AI-driven propagation modeling can create ultra-fast radio maps using ray-tracing datasets, real-world measurements, and a simple elevation map, which can then be fed back into the emulator for real-time dynamic scenario adaptation. Finally, we introduced Gen-TWIN, in which Colosseum and other OTA testbeds serve not only as execution environments but also as data factories for training generative models, with the objective of augmenting RF data for AI-native and AI-RAN-related tasks.

These results highlight the broader impact that DT platforms, such as Colosseum, have on the research community. They provide a controlled, repeatable, and reproducible environment in which to prototype algorithms, collect large and diverse datasets, and test and validate these solutions safely in a realistic setting before committing to more expensive field trials. Additionally, the tools we developed, such as *CaST*, were used to create and validate scenarios and to collect data across various platforms, demonstrating their portability across different experimental environments. This is key to following the experimental workflow envisioned in this work for transitioning from emulation to the real world.

However, while DT platforms like Colosseum offer significant advantages thanks to their controlled environments, they also have inherent limitations. Channel emulation, regardless of its fidelity, remains an approximation of reality. DTs are derived from ray-tracing simulations or measurement campaigns, but they cannot capture the full complexity of dynamic environments and channel effects, such as scattering, unwanted interference, hardware impairments in actual deployments, and environmental imperfections. These limitations motivate the transition from emulated to OTA experi-

mentation. Once algorithms have been sufficiently validated in controlled emulation scenarios, the next step is to deploy these solutions on a physical testbed and test them under real RF propagation, hardware constraints, and environmental conditions. The following chapters address this next phase by designing, deploying, and experimenting with an OTA platform, namely X5G, to continue the experimental journey and move from DTs to physical wireless networks.

Chapter 4

Design and Deployment of an Open and Programmable Private 5G O-RAN Testbed

The DT platforms presented in Chapters 2 and 3 have shown how large-scale emulation, such as Colosseum, can provide a controlled, repeatable, and reproducible environment for wireless network experimentation. However, as discussed in Section 3.5, while these platforms provide control over channel conditions, topology, and traffic, they inherently approximate real-world effects and abstract away some important aspects of real deployments, including hardware impairments, dynamic wireless propagation, and unexpected real-world interference and situations. To complete the experimental journey outlined in Chapter 1 and validate the solutions under realistic conditions, an OTA testbed with physical, commercial-grade hardware and software components is an essential step.

This chapter addresses the *deployment* and *usability* dimensions of experimental wireless platforms through the design and implementation of X5G, an open, programmable, multi-vendor private 5G O-RAN-compliant testbed [20, 21, 22]. While DTs like Colosseum excel at providing repeatable experimentation at scale, OTA testbeds provide the necessary *realism* for final validation before moving to a large-scale production deployment.

4.1 Introduction

The evolution of the RAN in 5G networks has led to key performance improvements in cell and user data rates, now averaging hundreds of Mbps, and in air-interface latency [114], thanks to specifications developed within 3GPP. From an architectural point of view, 5G deployments are also becoming more open, intelligent, programmable, and software-based [1], through activities led by the O-RAN ALLIANCE, which is developing the network architecture for Open RAN. These elements have the potential to transform how we deploy and manage wireless mobile networks [115], leveraging intelligent control, with RAN optimization and automation exercised via closed-loop data-driven control; softwarization, with the components of the end-to-end protocol stack defined

through software rather than dedicated hardware; and disaggregation, with the 5G RAN layers distributed across different network functions, i.e., the CU, the DU, and the RU.

Open and programmable networks are often associated with lower capital and operational expenditures, facilitated by the increasing robustness and diversity of the telecom supply chain [116], now also including open-source projects [117, 65] and vendors focused on specific components of the disaggregated RAN. This, along with increased spectrum availability in dedicated or shared bands, has opened opportunities to deploy private 5G systems, complementing public 5G networks with more agile, dynamic deployments for site-specific use cases (e.g., events, warehouse automation, industrial control).

While the transition to disaggregated, software-based, and programmable networks offers significant benefits, several challenges must be addressed before Open RAN systems can match or exceed the performance of traditional cellular systems and translate the potential cost savings into actual deployments. First, the radio domain still exhibits a low degree of automation and zero-touch provisioning for the RAN configuration, complicating the successful *deployment* of end-to-end cellular systems. Second, the diverse vendor ecosystem poses challenges related to interoperability and end-to-end integration across multiple products, potentially from different vendors [118, 119, 120] (*usability* dimension). Third, the Digital Signal Processing (DSP) at the Physical (PHY) layer of the stack is a computationally complex element, using about 90% of the available compute when run on general-purpose CPUs, and thus introducing a burden on the software-based and virtualized 5G stack components. Finally, there are still open questions in terms of how the intelligent and data-driven control loops can be implemented with AI and ML solutions that generalize well across a multitude of cellular network scenarios [121]. These challenges call for a concerted effort across different communities (including hardware, DSP, software, DevOps, AI/ML) that aims to design and deploy open, programmable, multi-vendor cellular networks and testbeds that can support private 5G requirements and use cases with the stability and performance of production-level systems.

Beyond the challenges of deploying and integrating Open RAN systems, enabling real-time, AI-native applications on the RAN infrastructure presents additional requirements. Current RAN control and observability (e.g., with O-RAN interfaces) remain limited to near- or non-real-time scales (i.e., above 10 ms), and focused on the control plane. O-RAN programmable applications, xApps and rApps, are deployed in dedicated controllers that aggregate data from tens of gNBs. They typically operate with timescales of tens of milliseconds to seconds and observe the RAN through aggregated KPIs, per-device and per-cell statistics computed over many slots and subcarriers. This design is intentional, as sending granular control- or user-plane data—for example, I/Q samples or full CSI matrices—to a remote controller would incur prohibitive (Gbps-scale) data rates and raise security and privacy concerns. Today’s programmable RANs cannot thus leverage fine-grained PHY/Medium Access Control (MAC) telemetry for tasks that require per-slot accuracy, such as fast link adaptation, beam management, or ISAC.

This chapter presents the design, deployment, and experimental evaluation of X5G, a private 5G network testbed deployed at Northeastern University in Boston, MA, and based on multiple programmable and open-source components from the physical layer all the way up to the Core Network (CN), as shown in Figure 4.1. X5G integrates a PHY layer implemented on GPU (i.e., NVIDIA Aerial) with OAI for the higher layers of the 5G stack through the Small Cell Forum (SCF) Functional Application Platform Interface (FAPI), which regulates the interaction between the PHY and MAC layers. The testbed also connects to a near-real-time RIC from the O-RAN

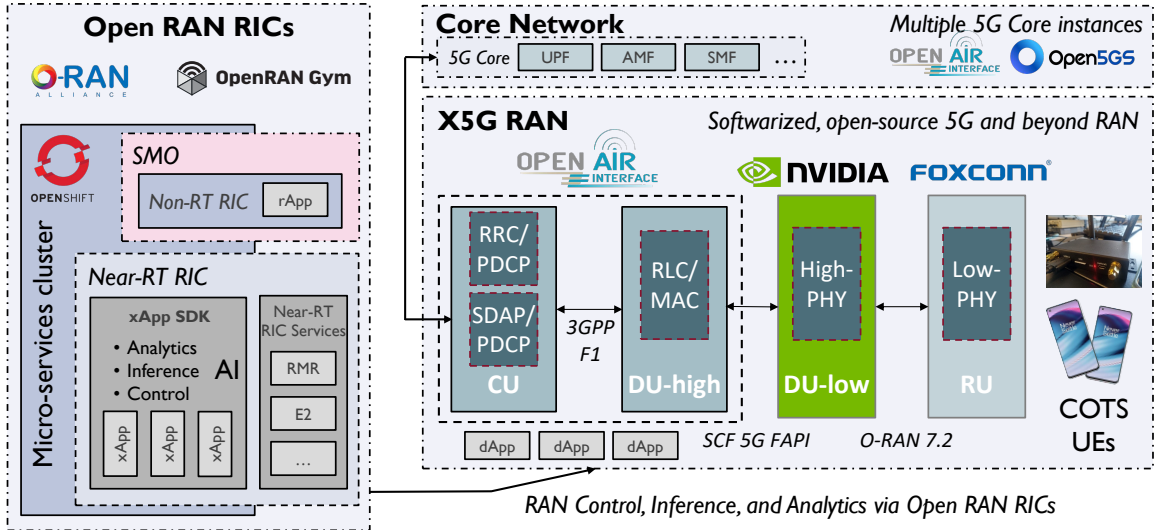


Figure 4.1: X5G end-to-end programmable testbed overview.

Software Community (OSC) running on an OpenShift-based cluster, and supports multiple 5G CN implementations, multiple RUs, and commercial smartphones and programmable devices.

Beyond the core platform infrastructure, a distinctive feature of X5G is its GPU-accelerated RAN architecture, which not only offloads the PHY processing to NVIDIA GPUs but also allows reuse of spare resources for AI/ML workloads co-located with the gNB, enabling the execution of distributed applications, or dApps [83], timescales in the real-time domain. In this model, these dApps can run on the same accelerator used for baseband processing, access low-level PHY measurements, and close control loops at timescales in the real-time domain, complementing xApps and rApps near-real-time and non-real-time cycles. Therefore, we also focus on the design and integration of this dApp framework within a GPU-accelerated gNB, such as X5G.

The key contributions of this chapter include:

- **Multi-vendor 5G O-RAN integration:** The integration of NVIDIA Aerial GPU-accelerated PHY with OAI higher layers through the SCF FAPI interface, demonstrating interoperability across open-source and commercial components.
- **End-to-end infrastructure deployment:** A comprehensive deployment including synchronization and networking infrastructure, multiple RUs, and integration with various CNs.
- **Digital twin-based RF planning:** A ray-tracing-based methodology using a DT framework to optimize RU placement in an indoor space, combining DT and OTA experimentation.
- **GPU-accelerated dApp framework:** A real-time framework for distributed applications that exposes PHY/MAC telemetry via shared memory and an E3-based interface, enabling E2E control loops with sub-millisecond latency.

- **Experimental validation:** Performance profiling with commercial smartphones and emulated UEs, demonstrating cell throughput up to 1.65 Gbps in downlink and system stability spanning multiple days.

The rest of the chapter is organized as follows. Section 4.2 introduces the X5G software architecture. Section 4.3 concerns the deployment and configuration of the X5G physical hardware infrastructure. Section 4.4 describes an RF planning study to determine an optimal location for deploying the RUs using a DT framework. System performance is evaluated in Section 4.5 through various use case scenarios with multiple COTS UEs and applications. Section 4.6 introduces the GPU-accelerated dApp framework for real-time AI applications on the RAN. Section 4.7 compares X5G with the state of the art. Section 4.8 summarizes the main takeaways and connects the X5G platform to the OTA use cases presented in Chapter 5.

4.2 X5G Software

This section describes the software components of X5G, also shown in Figure 4.1. These components can be divided into three main groups: (i) a full-stack programmable gNB (X5G RAN); (ii) the Open RAN RICs deployed on a micro-services cluster based on OpenShift; and (iii) various Core Networks (CNs) deployed in a micro-services-based architecture essential for the effective functioning of the 5G network.

4.2.1 Full-stack Programmable RAN with NVIDIA Aerial and OpenAirInterface

The right part of Figure 4.1 shows a detailed breakdown of the architecture of the X5G RAN, which follows the basic O-RAN architecture split into CU, DU, and RU. The DU is further split into a DU-low, implementing Layer 1 (PHY, or L1) functionalities, and into a DU-high, implementing Layer 2 (MAC and Radio Link Control (RLC), or L2) ones. As shown in Figure 4.2, DU-low and DU-high communicate over the 5G FAPI interface specified by the SCF [122]. The DU-low is implemented using the NVIDIA Aerial Software Development Kit (SDK) [123] on in-line GPU accelerator cards, whereas DU-high and CU are implemented by OAI on general-purpose Central Processing Units (CPUs). We deploy each function in separate Docker containers, sharing a dedicated memory space for the inter-process communication library that enables the FAPI interface. In our setup, we also combine the CU and the DU-high into a combined L2/L3 gNB Docker container, but the F1 split has also been deployed and tested.

The FAPI interface between the DU-high and DU-low defines two sets of procedures: configuration and slot procedures. Configuration procedures handle the management of the PHY layer and happen infrequently, e.g., when the gNB stack is bootstrapped or reconfigured. On the contrary, slot procedures happen in every slot (i.e., every 500 μ s for a 30 kHz subcarrier spacing) and determine the structure of each DL and Uplink (UL) slot. In our case, L1 serves as the primary and L2 as the subordinate. Upon the reception of a slot indication message from L1, L2 sends either an UL or DL request to dictate the required actions for the PHY layer in each slot. Additionally, L1 might transmit other indicators to L2, signaling the receipt of data related to Random Access Channel (RACH), Uplink Control Indication (UCI), Sounding Reference Signal (SRS), checksums, or user plane activities.

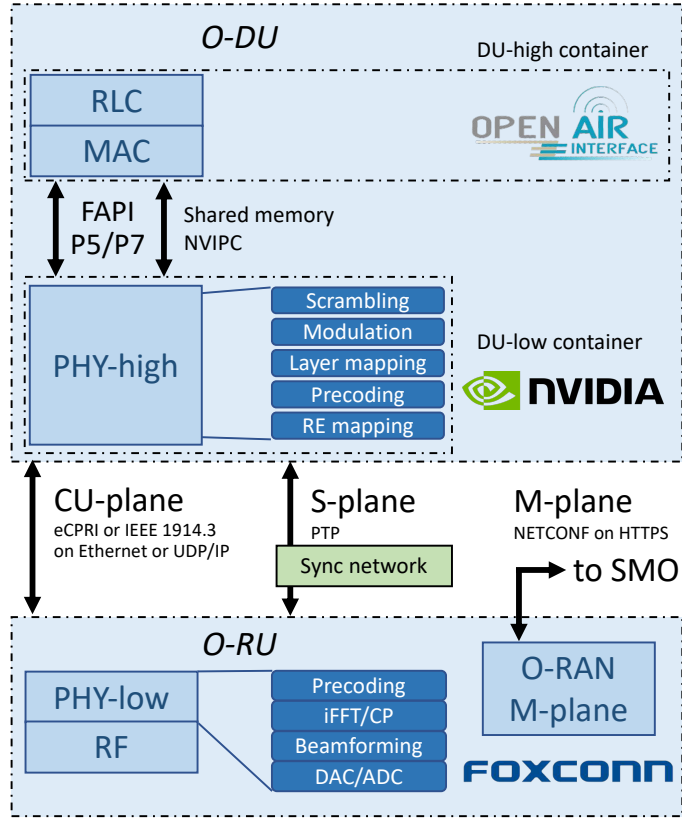


Figure 4.2: Architecture of the lower layers of the X5G RAN following O-RAN specifications and consisting of: (i) a Foxconn O-RU; (ii) an O-DU-low based on NVIDIA Aerial SDK; (iii) an O-DU-high based on OpenAirInterface with their corresponding interfaces.

In our implementation, we use FAPI version 222.10.02 with a few exceptions as outlined in the NVIDIA Aerial release notes [124]. The transport mechanism for FAPI messages is specified in the networked FAPI (nFAPI) specification [125], which assumes that messages are transported over a network. However, in our implementation, the L1 and L2 Docker containers communicate through the NVIDIA Inter-Process Communication (NVIPC) library. This tool provides a robust shared memory communication framework specifically designed to meet the real-time performance demand of the data exchanges between MAC and PHY layers. In our implementation, we choose to transport the messages using little-endian with zero padding to 32 bits. The NVIPC library is also capable of tracing the FAPI messages and exporting them to a pcap file that can be analyzed offline with tools such as Wireshark.

The NVIDIA physical layer in the DU-low implements the O-RAN Open Fronthaul interface, also known as the O-RAN 7.2 interface [126], to communicate directly with the O-RU, in our case manufactured by Foxconn. This interface transports frequency domain I/Q samples (with optional block floating point compression) over a switched network, allowing for flexible deployments. The interface includes synchronization, control, and user planes. The synchronization plane, or S-plane, is based on PTPv2. We use synchronization architecture option 3 [127], where the fronthaul switch

provides timing to both DU and RU. The interface also includes a management plane, although our system currently does not support it.

Table 4.1: X5G ARC deployment main features.

Feature	Description
3GPP Release	15
Frequency Band	n78 (FR1, TDD)
Carrier Frequency	3.75 GHz
Bandwidth (β)	100 MHz
Subcarrier spacing (Δf)	30 kHz
Resource Block size (χ)	12 subcarriers
Modulation order (Q_m)	8 (256-QAM)
TDD config	DDDSU, DDDDDDSUUU*
Number of antennas used	4 TX, 4 RX
MIMO config (L_{DL}, L_{UL})	4 layers DL, 1 layer UL
Max theoretical cell throughput** (T_{DL}, T_{UL})	1.64 Gbps DL, 204 Mbps UL

*Currently the special slot is unused due to limitations in Foxconn radios.

**The single-user maximum theoretical DL throughput can currently only be reached in the DDDDDDSUUU TDD configuration. In the DDDSU TDD configuration, it is limited to 350 Mbps since we can schedule a maximum of 2 DL slots per user in one TDD period, as only 2 ACK/NACK feedback bits are available per user.

Table 4.1 summarizes the main features and operational parameters of the Aerial RAN CoLab Over-the-Air (ARC-OTA) deployment in the X5G testbed. The protocol stack is aligned with 3GPP Release 15 and uses the 5G n78 Time Division Duplexing (TDD) band and numerology 1. The DDDSU TDD pattern, which repeats every 2.5 ms, includes three downlink slots, one special slot (which is not used due to limitations in the Foxconn RUs), and an uplink slot. The uplink slot format implemented in OAI carries only two feedback bits for ACK/NACK per UE, thus allowing only the scheduling of two downlink slots per UE, eventually limiting the single UE throughput. Alternative TDD patterns, including DDDDDDSUUU and DDDDDDDSUU, repeating every 5 ms, are also already in use to provide additional ACK/NACK bits for reporting from the UEs and mitigate this limitation.

To compute the maximum theoretical cell throughput in downlink (T_{DL}) and uplink (T_{UL}), we first derive a few additional parameters from Table 4.1. The number of resource blocks (N_{RB}) is computed using

$$N_{RB} = \frac{\beta}{\chi \cdot \Delta f} = 273. \quad (4.1)$$

By default, the number of OFDM symbols per slot (N_{sym}) is 14. The number of slots per second (N_{slot}) is inversely proportional to the slot duration, which for numerology $\mu = 1$ is 0.5 ms. Hence, $N_{slot} = 1s/0.5ms = 2000$ slots/second. The maximum theoretical cell throughput for downlink and uplink is given by

$$T_{DL,UL} = N_{RB} \cdot \chi \cdot N_{sym} \cdot N_{slot} \cdot Q_m \cdot R \cdot L_{DL,UL} \cdot \eta, \quad (4.2)$$

where R is the effective code rate, which can approach 0.93 (as specified in the 3GPP standard [128]), and η is the fraction of time allocated for downlink or uplink operations based on the chosen TDD

pattern. Considering the DDDDDDSUUU pattern to circumvent current OAI limitations on the ACK/NACK feedback bits, 60% of time is allocated for downlink and 30% for uplink since the special slot is unused due to Foxconn RU constraints. Consequently, the resulting theoretical peak cell throughput is 1.64 Gbps for downlink (T_{DL}) and 204 Mbps for uplink (T_{UL}). These values do not account for overheads typical of real networks—such as DeModulation Reference Signal (DMRS), Physical Uplink Control Channel (PUCCH), and Physical Downlink Control Channel (PDCCH)—which may further reduce net throughput. As shown by the experimental results in Section 4.5.5, X5G peak performance nearly reaches the theoretical downlink throughput, while the uplink is still under improvement.

Core Network. The X5G testbed facilitates the integration and testing of different CNs from various vendors and projects. We leverage virtualization to deploy all the necessary micro-services, e.g., Access and Mobility Management Function (AMF), Session Management Function (SMF), User Plane Function (UPF), in the OpenShift cluster that also supports the Near-RT RIC. We have successfully tested and integrated the X5G RAN with two open-source core network implementations, i.e., the 5G CNs from OAI [117] and Open5GS [129], as well as the CoreSIM software from Keysight [130]. As part of our ongoing efforts, we plan to incorporate additional cores, including the commercial core from A5G [131].

4.2.2 Integration with the OSC Near-RT RIC

One of the key components of an O-RAN deployment is the Near-Real-Time (or Near-RT) RIC, and the intelligent applications hosted therein, namely xApps. These can implement closed-control loops at timescales between 10 ms and 1 s to provide optimization and monitoring of the RAN [132, 133]. In the current X5G setup, we deploy the “E” release of the OSC Near-RT RIC on a RedHat OpenShift cluster [115], which manages the lifecycle of edge-computing workloads instantiated as containerized applications. The Near-RT RIC and the ARC-OTA RAN are connected through the O-RAN E2 interface (see Figure 4.3), based on Stream Control Transmission Protocol (SCTP) and an O-RAN-defined application protocol (E2AP) with multiple service models implementing the semantics of the interface (e.g., control, reporting, etc) [1]. On the gNB side, we integrate an E2 agent based on the *e2sim* software library [134, 135], which is used to transmit the metrics collected by the OAI gNB to the RIC via the KPM E2 service model. These metrics are then processed by xApps deployed on the RIC, and used to compute some control action (e.g., through AI/ML agents) that is sent to the RAN through the E2 interface and processed by the *e2sim* agent.

As an example, Figure 4.4 shows the architecture of a KPM xApp integrated with the X5G testbed. This xApp receives metrics from the E2 agent in the gNB, including throughput, number of UEs, and RSRP, and stores them in an InfluxDB database [136]. The database is then queried to display the RAN performance on a Grafana dashboard [137] (see Figure 4.4). This setup creates a user-friendly observation point for monitoring network performance and demonstrates the effective integration of the near-RT RIC in our configuration. A tutorial on how to deploy and run this xApp in X5G or on a similar testbed can be found on the OpenRAN Gym website [138], which hosts an open-source project and framework for collaborative research in the O-RAN ecosystem [46].

The metrics collected by a KPM xApp can then be leveraged by a second xApp or an rApp to perform smart closed-loop RAN controls at runtime, based on an arbitrary optimization strategy or specific requirements. ORANSlice—an open-source, network-slicing-enabled Open RAN system

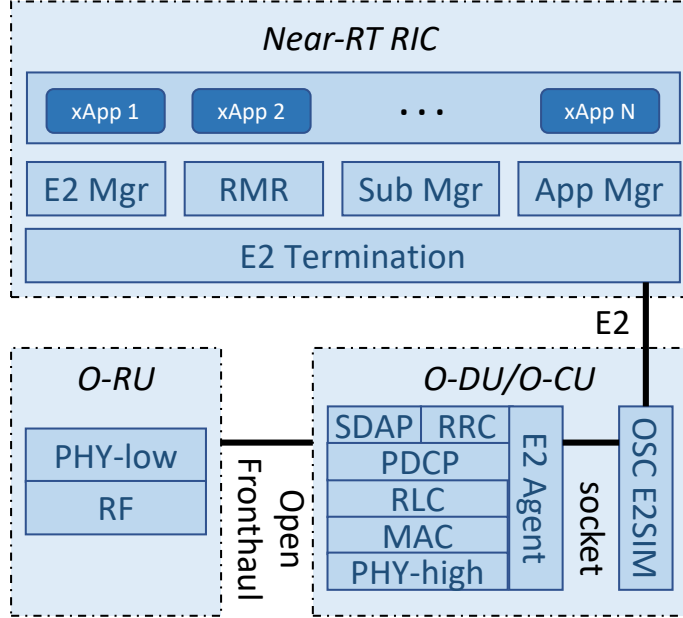


Figure 4.3: Integration of the OSC Near-RT RIC in the OpenShift cluster with the X5G RAN.

that leverages open-source RAN frameworks such as OAI [24]—was successfully integrated and tested in X5G, enabling near-real-time slicing control of the resources allocated by a gNB to multiple slices of the network, according to different policies set by the network manager. Figure 4.5 presents the effects of various network policies applied by an ORANSlice slicing xApp in a X5G gNB. Figure 4.5a shows the DL throughput results for the two slices (slice 1 in blue and slice 2 in orange), with a single UE per slice connected and transmitting 50 Mbps of DL UDP data, according to the policy shown in Figure 4.5b. The slicing xApp switches between three policies: (0) no-priority, where all slices share all resources, so both UEs achieve the target throughput of 50 Mbps; (1) prioritize slice 1: where 98% of resources are reserved for the first slice and 2% for the second one, causing the latter performance to drop to only 6 Mbps; (2) prioritize slice 2, where the opposite behavior of policy 1 is observed, with slice 1 now unable to achieve the target throughput. In this example, the policy is applied arbitrarily as a proof-of-concept for the network slicing control capabilities of X5G, while more intelligent strategies employing AI/ML components can be easily integrated into the decision process. Additional applications, including the emerging dApps [139], are currently being integrated into X5G to fully leverage its openness and programmability, further demonstrating the benefits of smart closed-loop control within the O-RAN ecosystem.

4.2.3 X5G Software Licensing and Tutorials

X5G, including the Aerial PHY, the OAI higher layers, as well as the OSC RIC, is open and can be extended with custom features and functionalities. The NVIDIA ARC-OTA framework is documented on the NVIDIA portal [124], which is accessible through NVIDIA’s 6G developer program. As mentioned in Section 4.2.2, the step-by-step integration between the OSC RIC and

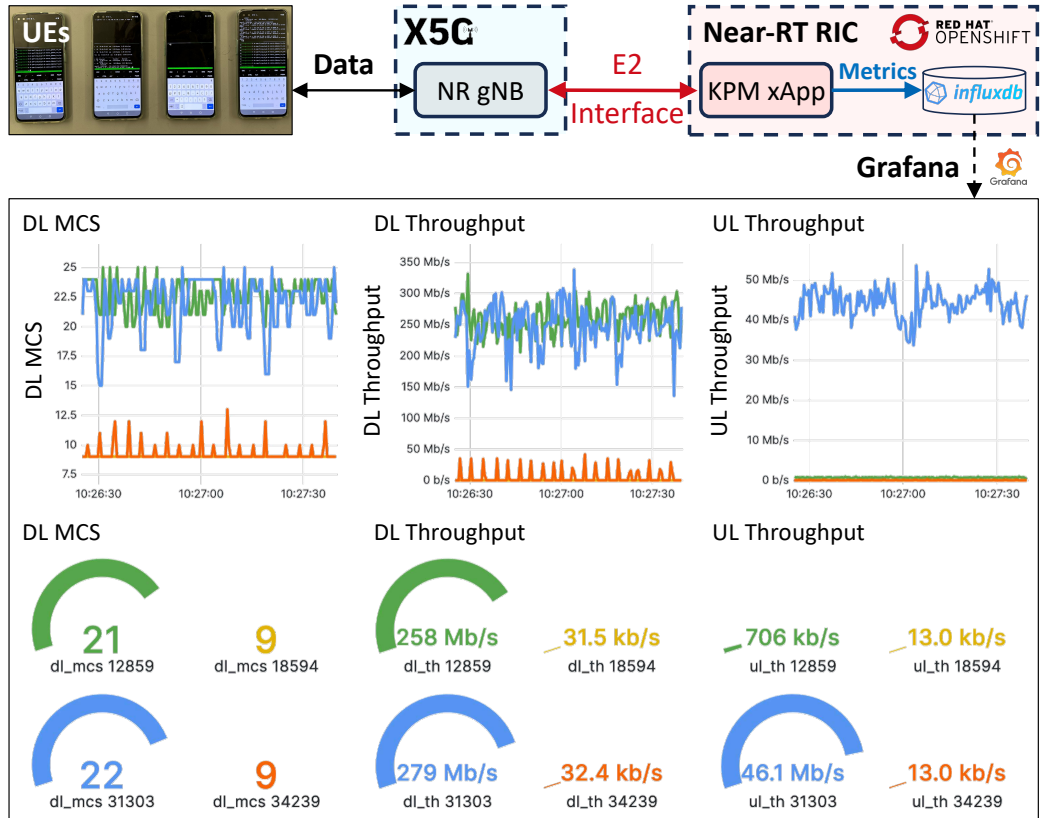


Figure 4.4: KPM xApp example architecture including an X5G gNB with four connected UEs, each performing a different operation (ping, video streaming, DL test, and DL/UL tests), and a KPM xApp that pushes UE metrics into an Influx database, which are then visualized in a Grafana dashboard.

the ARC-OTA stack through the X5G E2 agent is discussed in a tutorial on the OpenRAN Gym website [138, 46].

The components implemented by OAI are published under the OAI public license v1.1 created by the OAI Software Alliance (OSA) in 2017 [140]. This license is a modified Apache v2.0 License, with an additional clause that allows contributors to make patent licenses available to third parties under Fair, Reasonable, And Non-Discriminatory (FRAND) terms, similar to 3GPP for commercial exploitation, to allow contributions from companies holding intellectual property in related areas. The usage of OAI code is free for non-commercial/academic research purposes. The Aerial SDK is available through an early adopter program [124]. The OSC software is published under the Apache v2.0 License.

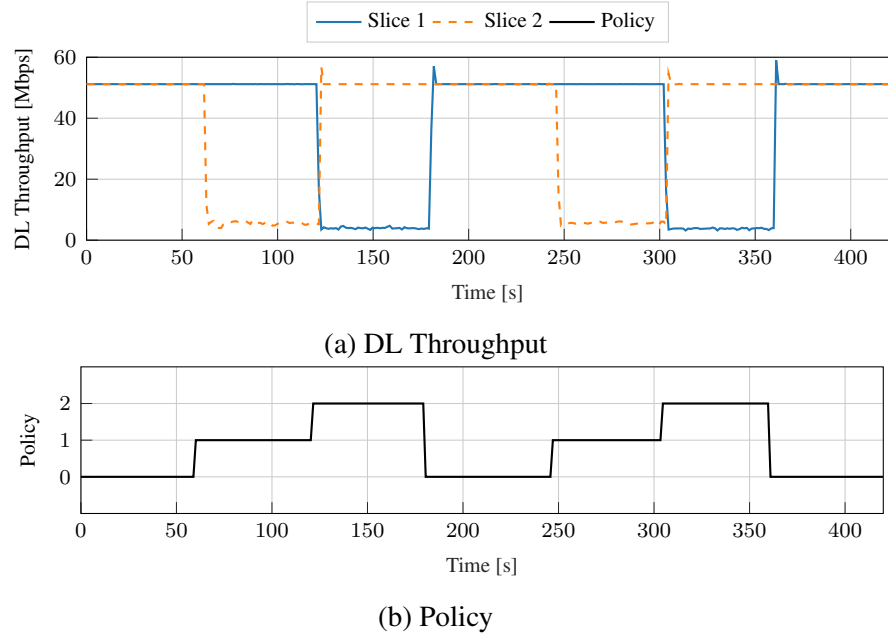


Figure 4.5: Slicing xApp example showing: (a) DL throughput for two different slices, each with a single UE connected and pushing 50 Mbps of UDP traffic; (b) the network policy applied by the slicing xApp, switching between no-priority (0), prioritize slice 1 (1), and prioritize slice 2 (2).

4.3 X5G Infrastructure

This section describes the X5G physical deployment that is currently located on the Northeastern University campus in Boston, MA.¹ The deployment includes a server room with a dedicated rack for the private 5G system and an indoor laboratory open space area with benches and experimental equipment that provide a realistic RF environment with rich scattering and obstacles. Figure 4.6 illustrates the hardware infrastructure that we deployed to support the X5G operations. This includes synchronization and networking infrastructures, radio nodes, eight ARC-OTA servers with integrated DU and CU, and additional compute infrastructure for the RIC and CN deployments. This infrastructure, which will be described next, has been leveraged to provide connectivity for up to eight concurrent COTS UEs, such as OnePlus smartphones (AC Nord 2003) and Sierra Wireless boards (EM9191) [141].

Synchronization Infrastructure. The synchronization infrastructure consists of a Qulsar (now VIAVI) QG-2 device acting as grandmaster clock. The QG-2 unit is connected to a GPS antenna for precise class-6 timing and generates both PTP and Synchronous Ethernet (SyncE) signals to provide frequency, phase, and time synchronization compliant with the ITU-T G.8265.1, G.8275.1, and G.8275.2 profiles. It sends the synchronization packets to the networking infrastructure through a 1 Gbps Ethernet connection. The networking infrastructure then offers full on-path support, which is necessary to distribute phase synchronization throughout the X5G platform.

¹X5G website: <https://x5g.org>.

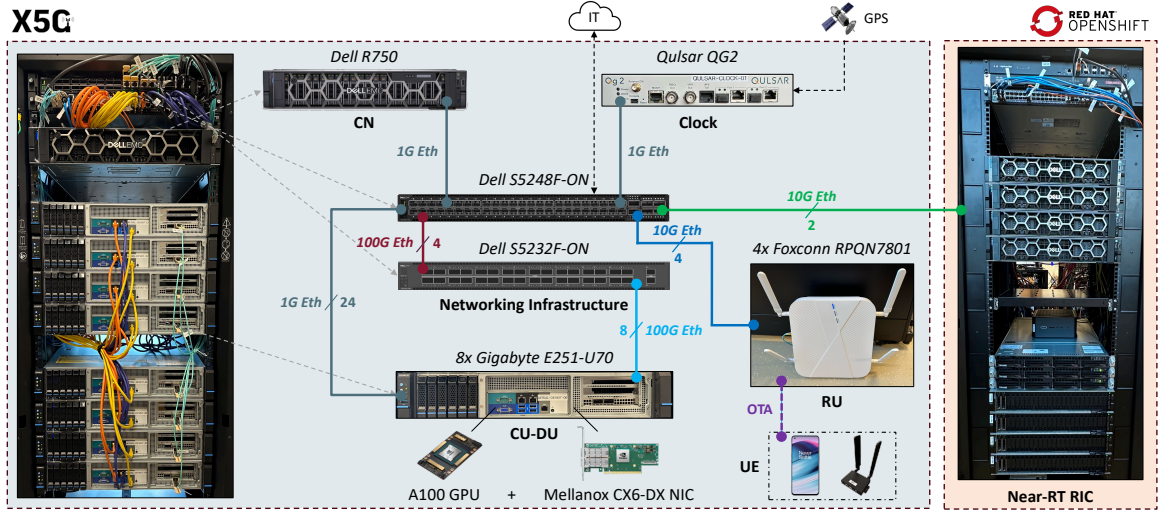


Figure 4.6: Hardware architecture infrastructure of the X5G deployment at Northeastern University.

Networking Infrastructure. The networking infrastructure provides connectivity between all the components of the X5G platform. It features fronthaul and backhaul capabilities through the use of two Dell switches (S5248F-ON and S5232F-ON) interconnected via four 100 Gbps cables in a port channel configuration. This configuration allows for the aggregation of multiple physical links into a single logical one to increase bandwidth and provide redundancy in case some of them fail. All switch ports are sliced into different Virtual Local Area Networks (VLANs) to allow the proper coexistence of the various types of traffic (i.e., fronthaul, backhaul, management). The Dell S5248F-ON switch primarily provides backhaul capabilities to the network and acts as a boundary clock in the synchronization plane, receiving PTP signals from the synchronization infrastructure. This switch includes 48 SFP+ ports: 12 ports are dedicated to the RUs and receive PTP synchronization packets, 10 are used to connect to the OpenShift cluster and service network, 10 are used for the out-of-band management network, and 16 connect to the CN and the Internet. Additionally, the switch includes 6 QSFP28 ports, 4 of which interconnect with the second switch. The Dell S5232F-ON switch mainly provides fronthaul connectivity to the gNBs. It includes 32 QSFP28 ports: 8 ports connect to the Mellanox cards of the ARC-OTA nodes via 100 Gbps fiber links, and 4 connect to the Dell S5248F-ON switch. The latter also acts as a boundary clock, receiving the synchronization messages from the S5232F-ON and delivering them to the gNBs.

RU. We deployed eight Foxconn RPQN 4T4R RUs, operating in the n78 band, with additional units being tested in the lab, and the Keysight RuSIM emulator. The Foxconn units have 4 externally mounted antennas, each antenna with a 5 dBi gain, and 24 dBm of transmit power. The OTA transmissions are regulated as part of the Northeastern University FCC Innovation Zone [142], with an additional transmit attenuation of 20 dB per port to comply with transmit power limits and guarantee the coexistence of multiple in-band RUs in the same environment. As we will discuss in Section 4.5, we leverage two of these RUs for the experimental analysis presented in this work. These RUs are deployed following RF planning procedures discussed in Section 4.4. Plans are in place to procure CBRS RUs and deploy them in outdoor locations. RUs from additional vendors are being

tested and integrated as part of our future works. Finally, we also tested and integrated the ARC-OTA stack with the Keysight RuSIM emulator, which supports the termination of the fronthaul interface on the RU side and exposes multiple RUs to the RAN stack, for troubleshooting, conformance testing, and performance testing [143].

CU and DU. The 8 ARC-OTA nodes that execute the containerized CU/DU workloads are deployed on Gigabyte E251-U70 servers with 24-core Intel Xeon Gold 6240R CPU and 96 GB of RAM. The servers—which come in a half rack chassis for deployment in RAN and edge scenarios—are equipped with a Broadcom PEX 8747 Peripheral Component Interconnect (PCI) switch that enables direct connectivity between cards installed in two dedicated PCI slots without the need for interactions with the CPU. Specifically, the two PCI slots host an NVIDIA A100 GPU, which supports the computational operations of the NVIDIA Aerial PHY layer, as well as a Mellanox ConnectX-6 Dx Network Interface Card (NIC). The latter, which is used for the fronthaul interface, connects to the fronthaul part of the networking infrastructure via a QSFP28 port and 100 Gbps fiber-optic cable. In this way, the NIC can offload or receive packets directly from the GPU, thus enabling low-latency packet processing. Finally, each server is connected to the backhaul part of the networking infrastructure through three 1 Gbps Ethernet links, which provide connectivity with the OpenShift cluster (and thus the Near-RT RIC and the core networks), the management infrastructure, and the Internet. In addition to the Gigabyte servers, seven Grace Hopper (GH) machines—one of the latest NVIDIA high-computing ARM-based devices—are currently being integrated into X5G to run the ARC-OTA CU/DU workloads. Each GH combines a 72-core NVIDIA Grace CPU Superchip and an NVIDIA H100 Tensor Core GPU, linked through NVIDIA NVLink-C2C technology, which ensures seamless data sharing with up to 900 GB/s of bandwidth. It also features 480 GB of RAM, two BlueField-3 Data Processing Units (DPUs), and ConnectX-7 NICs. This configuration provides significantly higher computational capabilities compared to the Gigabyte servers, enabling the efficient support of concurrent RAN and AI/ML workloads.

Additional Compute. We leverage additional servers that are part of the OpenShift cluster and are used to instantiate the various CNs and the Near-RT RIC. The OpenShift cluster includes three Dell R740 servers acting as control-plane nodes and two Microway Navion Dual servers as worker nodes. The OpenShift rack is linked to the X5G rack through two 10 Gbps connections, one dedicated to OpenShift operations, and the other for the out-of-band management. Additionally, a Dell R750 server with 56 cores and 256 GB RAM is available for the deployment and testing of additional core network elements. This server connects to the networking infrastructure via a 1 Gbps Ethernet link and has access to the Internet through the Northeastern University network.

4.4 RF Planning with Ray-tracing

In this section, we present RF planning procedures to identify suitable locations for the RU deployment. This approach leverages an exhaustive search within a ray-tracing-based digital twin framework, with the objective of maximizing the RUs coverage while minimizing the overall interference. The study is conducted only once during the system deployment phase and remains valid as long as no significant changes occur in the environment. We perform ray-tracing in a detailed digitized representation of our indoor laboratory space in the Northeastern University ISEC building in Boston, MA, to achieve high fidelity between the real-world environment and the digital one. We

carefully study how to deploy 2 RUs by considering the SINR between the RUs and the UEs as the objective function in the optimization problem. We limit the optimization space by using a grid of 24 possible RU locations and 52 UE test points, enabling an exhaustive search approach instead of a formal integer optimization problem, since these constraints keep the computation manageable.

First, we leverage the 3D representation of our laboratory space, created as part of the digital twin framework developed in [3] using the SketchUp modeling software. We then import the model in the MATLAB ray-tracing software and define the locations of RUs and UEs as shown in Figure 4.7a (from a top perspective) and in Figure 4.7b (from a side view). The 24 possible RUs locations (2 for each bench) are shown in red, while the 52 test points for the UEs (arranged in a 4×13 grid) are in blue. Tables 4.1 and 4.2 summarize the parameters used in our ray-tracing model. For the deployment planning purpose, we consider the RUs as transmitter nodes (TX) and the UEs as receiver ones (RX), i.e., we tailor our deployment to downlink transmissions.

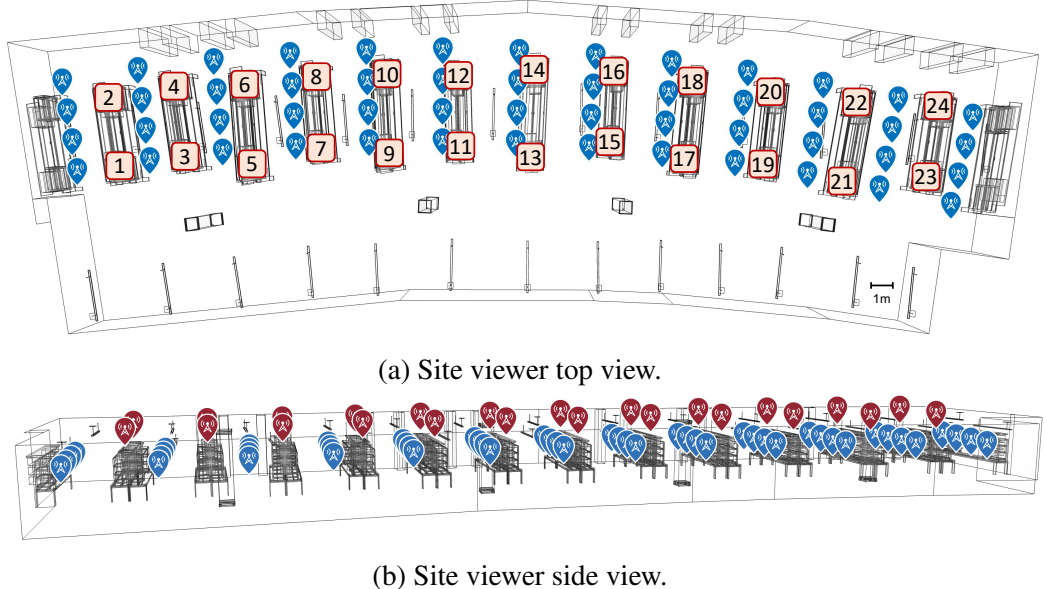


Figure 4.7: Site viewer with RU (red squares) and UE (blue icons) locations.

The ray-tracer generates a 24×52 matrix \mathbf{C} where each entry $c_{i,j}$ corresponds to the channel information between RU_i with $i \in \mathcal{R}$, $\mathcal{R} = 1, \dots, 24$, and UE_j with $j \in \mathcal{U}$, $\mathcal{U} = 1, \dots, 52$. We use this to derive relevant parameters such as the thermal noise (\mathcal{N}) and the path loss (\mathcal{L}) to compute the Received Signal Strength Indicator (RSSI) $\mathcal{S}_{i,j}$ for UE_j connected to RU_i , as follows:

$$\mathcal{S}_{i,j} = P_{RU,i} + G_{RU,i} - A_{RU,i} - \mathcal{L}_{i,j} + G_{UE,j}, \quad (4.3)$$

where $P_{RU,i}$, $G_{RU,i}$, and $A_{RU,i}$ are the antenna TX power, gain, and attenuation of RU_i , respectively. Then, considering the linear representation of $\hat{\mathcal{S}}_{i,j}$, the SINR $\Gamma_{i,j}$ is

$$\Gamma_{i,j} = \frac{\hat{\mathcal{S}}_{i,j}}{\mathcal{N}F_{UE,i} + \sum_{u=1, u \neq i}^M \hat{\mathcal{S}}_{u,j}}, \quad (4.4)$$

Table 4.2: Parameters of the MATLAB ray-tracing study to determine RU locations.

Parameter	Value
RU antenna spacing	0.25 m
RU antenna TX power (P_{RU})	24 dBm
RU antenna gain (G_{RU})	5 dBi
RU antenna pattern	Isotropic
RU TX attenuation (A_{RU})	[0 – 50] dB
Set of RU locations (\mathcal{R})	24 in a 2×12 grid
RU height	2.2 m
UE number of antennas	2
UE antenna spacing	0.07 m
UE antenna gain (G_{UE})	1.1 dBi
UE noise figure (F_{UE})	5 dB
Set of UEs locations (\mathcal{U})	52 in a 4×13 grid
UE height	0.8 m
Environment material	Wood
Max number of reflections	3
Max diffraction order	1
Ray-tracing method	Shooting and bouncing rays

where M is the number of RUs being deployed, \mathcal{N} is the thermal noise, and $F_{UE,i}$ is the noise figure of UE_i . The SINR $\Gamma_{i,j}$ considers the interference to the signal from RU_i to UE_j due to downlink transmissions of all other $M - 1$ RUs being deployed.

In our RF planning, we deploy two RUs (i.e., $M = 2$). In the following study, we consider scenarios where the first RU serves one UE from the test locations, while we assume that the second RU creates interference with the first, even without being assigned any UE from the list. We test all possible combinations of the 24 RU test locations, which, following the combinatorial equation of choosing 24 elements (n) in groups of 2 (r) as $C(n, r) = \frac{n!}{r!(n-r)!}$, results in a total of 276 pairs. The proposed approach for determining the optimal RU locations and the maximum average SINR ($\Phi_{\max}(\Gamma)$), called score, is presented in Algorithm 2. It takes as input the set of RU locations (\mathcal{R}), the set of UE test points (\mathcal{U}), and the SINR matrix Γ . Then, it performs an exhaustive search, testing all pairs of RU against all UEs to determine the optimal RU pair (p^*, q^*) with the best maximum average SINR $\Phi_{\max}(\Gamma)$.

We test this algorithm with different values of the attenuation A_{RU} , from 0 to 50 dB in 10 dB increments. Figure 4.8 visualizes the normalized values of the score $\Phi(\Gamma)$ for all possible combinations of RU pairs and different attenuation values. Additionally, Table 4.3 provides the best RU locations including the minimum and maximum values of $\Phi(\Gamma)$ for the corresponding combinations. As expected, locations with further RUs exhibit higher average SINR values, as they are less affected by interference. However, it is important to note that the score also considers coverage, as it is computed based on the SINR. Consequently, the optimal combination of locations identifies RUs that are further apart but not necessarily the furthestmost pair. Considering these results, for the experiments in Section 4.5, we select a TX attenuation of 20 dB, which exhibits a good trade-off between coverage and average SINR values. Moreover, during our real-world experiments, we observed that a 20 dB attenuation leads to increased system stability and reduced degradation compared to

Algorithm 2 Exhaustive Search Algorithm for RF Planning

Input: Set of RU locations (\mathcal{R}), set of UE test points (\mathcal{U}), precomputed SINR matrix Γ

Output: Optimal RU pair (p^*, q^*) and maximum average SINR $\Phi_{\max}(\Gamma)$

```

1: Initialize  $bestScore \leftarrow -\infty$  and  $bestPair \leftarrow \text{None}$ 
2: for all RU pairs  $(p, q) \in \binom{\mathcal{R}}{2}$  do
3:    $sumSINR \leftarrow 0$ 
4:   for all UE  $j \in \mathcal{U}$  do
5:     Compute  $\Gamma_{p,j}$  (RU  $p$  serving, RU  $q$  interfering)
6:     Compute  $\Gamma_{q,j}$  (RU  $q$  serving, RU  $p$  interfering)
7:      $sinrMax \leftarrow \max(\Gamma_{p,j}, \Gamma_{q,j})$ 
8:      $sumSINR \leftarrow sumSINR + sinrMax$ 
9:   end for
10:   $avgSINR \leftarrow sumSINR/|\mathcal{U}|$ 
11:  if  $avgSINR > bestScore$  then
12:     $bestScore \leftarrow avgSINR$ 
13:     $bestPair \leftarrow (p, q)$ 
14:  end if
15: end for
16: return  $bestPair, bestScore$ 

```

Table 4.3: Best RUs and average SINR $\Phi(\Gamma)$ range values.

A_{RU} [dB]	RU locations with best SINR	[Min, Max]	$\Phi(\Gamma)$ [dB]
0	[8, 23]	[6.08, 23.33]	
10	[6, 23]	[5.71, 22.66]	
20	[6, 23]	[5.00, 21.03]	
30	[8, 23]	[3.58, 17.82]	
40	[7, 24]	[0.19, 12.94]	
50	[8, 20]	[-6.23, 6.63]	

lower attenuation values, resulting in improved overall performance, as it reduces the likelihood of saturation at the UE antenna. Therefore, we select locations [6,23] for our RUs deployment.

4.5 Experiment Results

In this section, we describe the design and execution of a comprehensive set of experiments that illustrate the capabilities of the X5G infrastructure in a variety of operational scenarios. We assess the adaptability of the testbed through rigorous testing, utilizing iPerf to measure network throughput and MPEG-DASH to gauge video streaming quality. The experiments are mainly conducted in the same indoor laboratory area modeled in Section 4.4. They include static configurations with a single UE as well as more complex setups with multiple UEs and RUs, leveraging the Keysight RuSIM emulator, and scenarios with UE mobility.

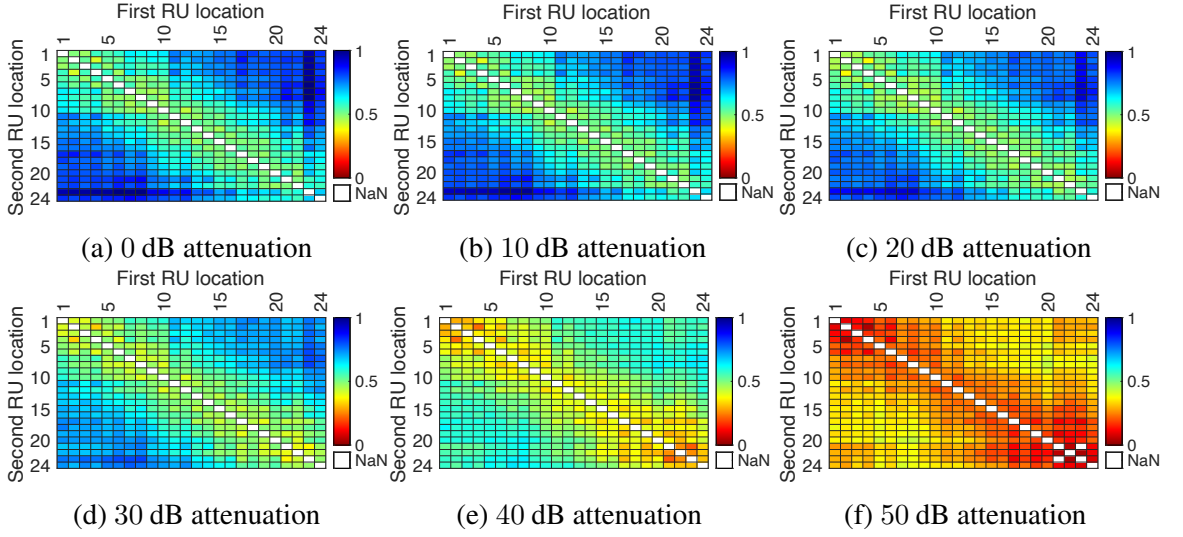


Figure 4.8: Heatmap results of the normalized average SINR $\Phi(\Gamma)$ with 2 RUs.

4.5.1 Setup Overview

We consider two different setups: (i) Gigabyte RAN servers with a 2×2 MIMO configuration (L_{DL}, L_{UL}), 2 layers DL, 1 layer UL, a DDDSU TDD pattern, and a modulation order (Q_m) up to 64-Quadrature Amplitude Modulation (QAM) (results for this setup are shown in Sections 4.5.2, 4.5.3, and 4.5.4); and (ii) GH RAN servers with a 4×4 MIMO configuration, 4 layers DL, 1 layer UL, a DDDDDDSUUU TDD pattern, and a Q_m up to 256-QAM (Sections 4.5.5 and 4.5.6). All experiments utilize a carrier frequency of 3.75 GHz with a bandwidth (β) of 100 MHz.

The experiments are mainly conducted in the laboratory area shown in Figure 4.9, which highlights the RU locations (outcome of the ray-tracing study discussed in Section 4.4), as well as the UE locations and the mobility pattern for the non-static experiments. All tests involving a single RU are conducted at location 6, as illustrated in Figure 4.9. An edge server, configured to support

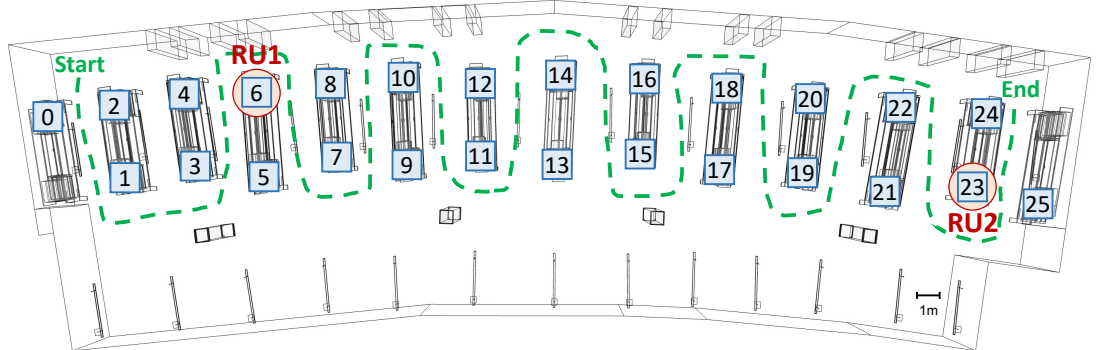


Figure 4.9: Node locations considered in our experiments: RUs (red circles in 6 and 23); possible static UEs (blue squares); and mobile UEs (green dashed line).

the iPerf and MPEG-DASH applications, is deployed within the campus network to ensure minimal

latency, ranging from 1 to 2 ms. During static throughput tests, TCP backlogged traffic is transmitted first in the downlink and then in the uplink directions for 40 seconds each across different UE configurations. For video streaming, the server employs FFmpeg [144] to deliver five distinct profiles simultaneously at various resolutions—ranging from 1080P at 250 Mbps to 540P at 10 Mbps—to the UEs. On the device side, we leverage a pre-compiled iPerf3 binary for Android to generate TCP traffic, and Google’s ExoPlayer for client-side video playback. Each set of experiments is replicated five times to ensure data reliability, with results including mean values and 95% confidence intervals of the metrics plotted. These metrics encompass application layer measurements such as throughput, bitrate, and rebuffer ratio, alongside MAC layer metrics like SINR, RSRP, and Modulation and Coding Scheme (MCS), collected at the OAI gNB level.

4.5.2 Static Experiments

1 UE, static, iPerf. In the initial series of tests, we analyze the performance of a single UE in ten static locations at varying distances from the RU, as shown in Figure 4.10, using the first configuration setup of 2x2 MIMO, 2 layers DL, 1 layer UL, a DDDSU TDD pattern, and a Q_m up to 64-QAM.

The iPerf throughput results in Figure 4.10a highlight the upper layer’s responsiveness, showing a significant reduction from an average downlink throughput of 300 Mbps and an uplink one of 38 Mbps at locations near the RU, to significantly lower rates of 177 Mbps in downlink and 1.5 Mbps in uplink at the most remote point, i.e., location 18. This high-level data throughput behavior is supported by corresponding shifts in the lower layers.

For example, this trend is clearly noticeable from the results of Figure 4.10b, which shows the RSRP values reported by the UE to the gNB during DL (blue bars) and UL (orange bars) data transmissions. As the distance from the RU initially decreases starting from location 0 to location 6, the RSRP values peak at around -80 dBm. Subsequently, as the distance starts to increase again, moving from location 6 towards location 18, the RSRP values begin to decrease, reaching as low as -100 dBm.

In the same way, the MCS values for both downlink and uplink initially mirror each other, then begin to diverge from around location 10, as shown in Figure 4.10c. In uplink, the MCS values tend to remain stable or slightly increase, whereas downlink MCS values experience a slight decline possibly due to power control strategies that better favor the uplink at more distant locations.

Similarly, the CQI (Figure 4.10d) for both downlink and uplink starts closely matched but begins to show variation past the midpoint of the locations. The downlink CQI experiences a modest decline, while the uplink CQI sustains higher values. This suggests better channel conditions or more effective adaptation mechanisms in the uplink, due to adaptive power adjustments in uplink transmissions that maintain signal quality over distance.

PH metrics, shown in Figure 4.10e, reveal that downlink power headroom remains relatively stable across all locations, indicating a consistent application of power levels for downlink transmissions. In contrast, the uplink displays greater variability and generally higher values in distant locations to compensate for potential path loss and ensure that the transmit power remains adequate to maintain quality of service as the UE moves further from the RU.

Finally, the BLER (Figure 4.10f) for downlink remains below 10% for most locations, pointing to good reliability and effective adaptation of the MCS. However, while the uplink BLER is generally

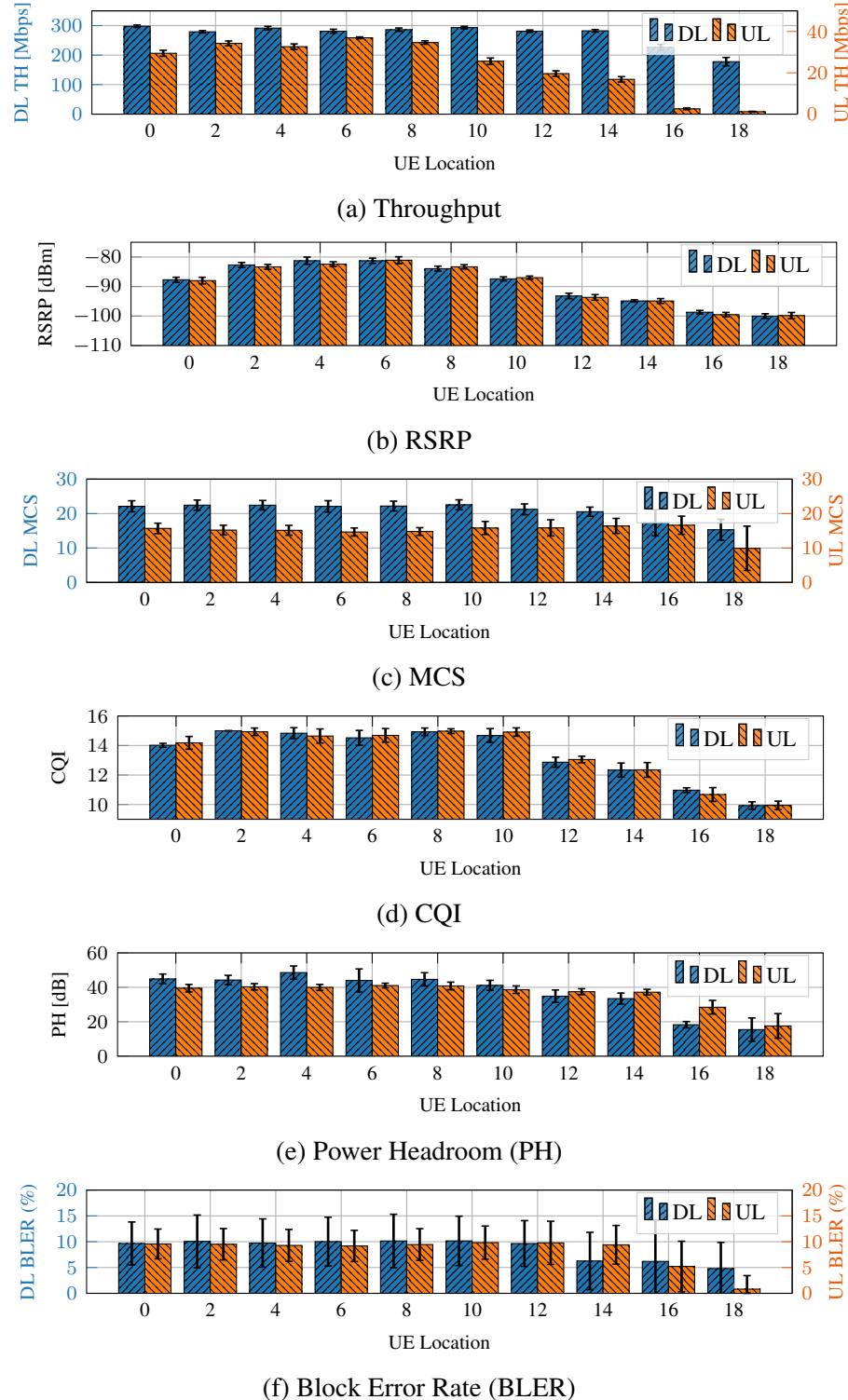


Figure 4.10: Performance profiling with one UE and single RU for the static iPerf use case during DL (blue bars) and UL (orange bars) data transmissions.

low, it exhibits some peaks, especially around mid-range locations which may be related to specific lab obstacles or multipath effects and slow adaptation loops.

2 UEs, static, iPerf. We test the performance of 2 UEs for a single RU. We position the UEs at the same static locations as in the previous single UE static case. The results are plotted in Figure 4.11 for both downlink and uplink transmissions. We observe that, in most cases, the UEs are able to share bandwidth fairly. The best achievable average aggregate throughput from both UEs is around 400 Mbps in DL and 44 Mbps in UL. This shows that the total cell throughput can be higher than the single UE throughput. As discussed in Table 4.1, this is due to a limitation in the number of transport blocks that can be acknowledged in a single slot for a single UE in the case of the DDDSU TDD pattern used in this first set of experiments. Therefore, scheduling multiple UEs improves the resource utilization of the system.

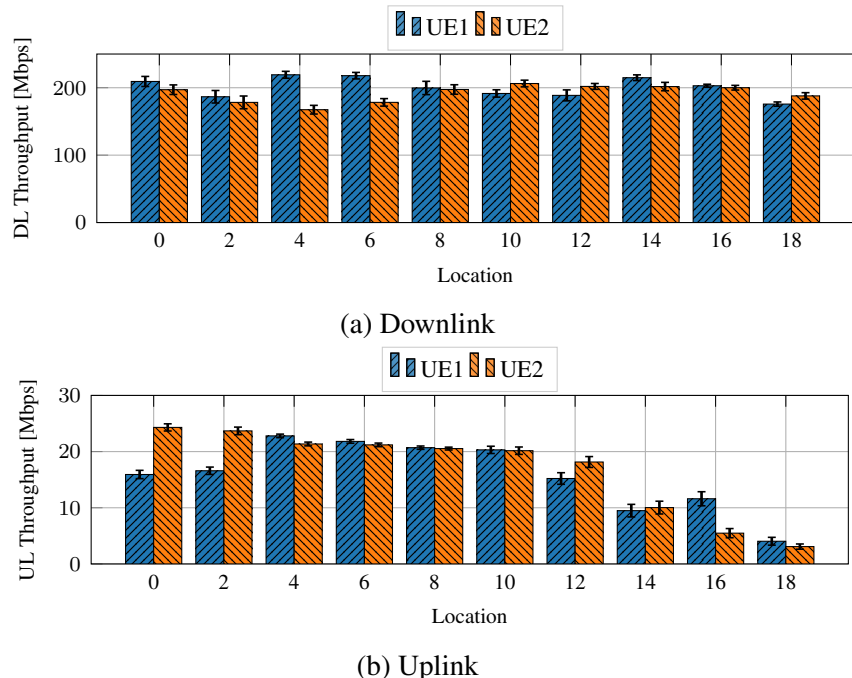


Figure 4.11: Performance profiling for one RU and two static UEs for the static iPerf use case.

1-4 UEs, static, iPerf. We further extend our evaluation to include additional tests with multiple UEs. At fixed location 4, we compare system performance with varying numbers of UEs (from 1 to 4) connected to our network. The average throughput and 95% confidence intervals are plotted in Figure 4.12. We observe that the UEs achieve steady throughput in all the cases, as indicated by the small confidence interval values. Additionally, the combined throughput increases with the number of UEs connected: with four UEs, the aggregate throughput reaches 512 Mbps in DL and 46 Mbps in UL. This scenario highlights the maximum throughput performance that X5G is able to achieve with the current 2x2 MIMO configuration, featuring 2 layers in DL and a DDDSU TDD pattern, ensuring a fair distribution of resources among all UEs. It is worth noting that the peak performance of X5G is detailed in Section 4.5.5.

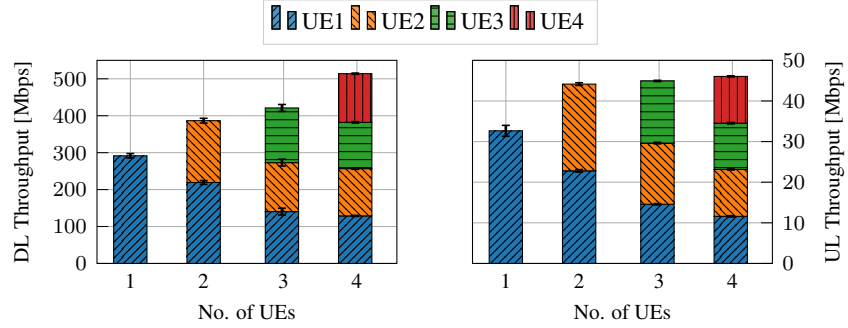


Figure 4.12: Performance profiling with multiple UEs at fixed location 4 for the static iPerf use case using a DDDSU TDD pattern, a 2x2 MIMO configuration, 2 layers DL and 1 layer UL.

2 RUs, 1 UE per RU, static, iPerf. Finally, we evaluate X5G performance with two RUs by connecting UE1 to RU1 and UE2 to RU2. RU1 is located at position 6, and RU2 is at position 23. We select six pairs of locations—(0,25), (2,23), (4,21), (6,19), (8,17), (10,15)—for the UEs to ensure different distances among them and the RU.

From Figure 4.13a, we observe that the DL throughput is significantly impacted by interference, particularly at cell edge locations. The throughput for UE1 shows a reduction of up to 90% as the UEs approach each other, while UE2 throughput decreases by up to 50%. These observations indicate that interference predominantly affects the DL direction. Conversely, as depicted in Figure 4.13b, UL throughput remains relatively stable across different location pairs, suggesting that UL is less susceptible to the types of interference affecting DL throughput.

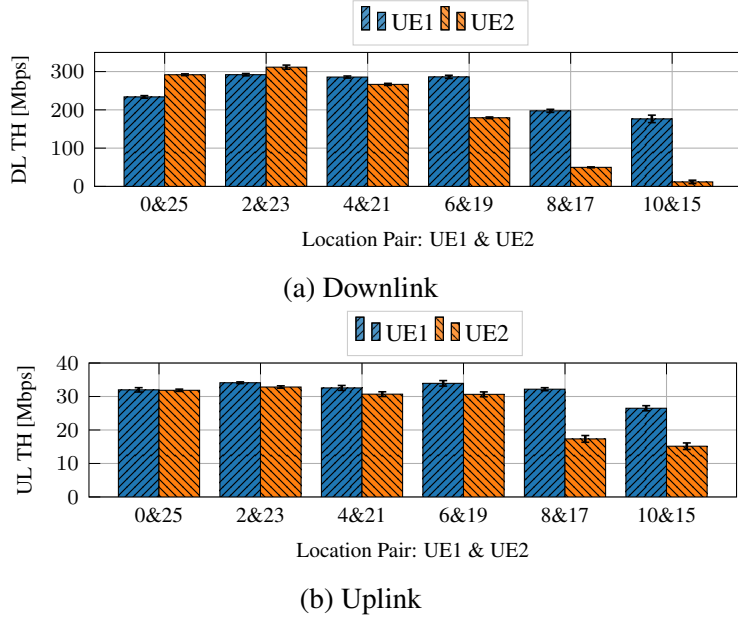


Figure 4.13: Performance profiling for two RUs in the static iPerf use case, each with one assigned UE: UE1 to RU1 and UE2 to RU2.

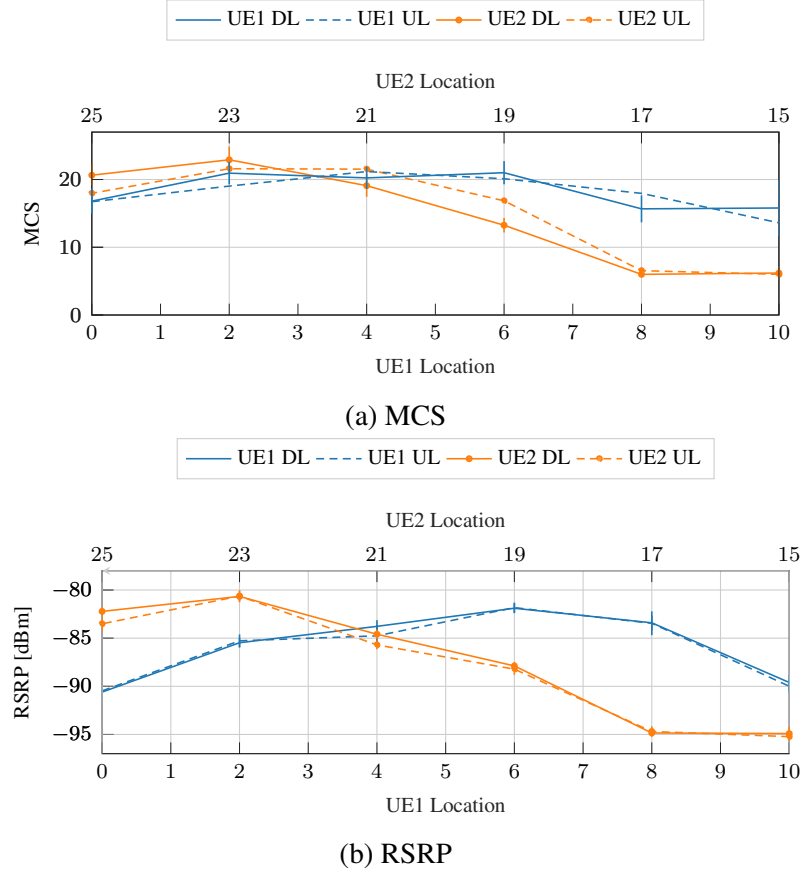


Figure 4.14: MAC KPIs in the two RUs iPerf use case, each with one static UE (UE1 assigned to RU1 and UE2 to RU2): (a) averages and confidence intervals for DL MCS (solid lines) during DL data transmissions, and UL MCS (dashed lines) during UL transmissions, for UE1 (blue) and UE2 (orange); (b) averages and confidence intervals of RSRP reported by UE1 (blue) and UE2 (orange) during DL (solid lines) and UL (dashed lines) transmissions.

Figure 4.14 further supports these observations by presenting additional KPIs from the MAC layer. Figure 4.14a shows that the MCS for both UEs decreases as the distance between the UEs diminishes, indicative of increasing interference levels. Figure 4.14b illustrates the RSRP, which varies in response to the UEs locations. Notably, despite adequate RSRP levels, the throughput remains low, highlighting the significant impact of interference, particularly in the DL direction.

4.5.3 Mobile Experiments

We assess the network performance by measuring throughput as the UE follows the walking pattern around the laboratory space depicted by the dashed green line in Figure 4.9. The entire walk from the start to the end point spans approximately 3 minutes at regular walking speed. The mobile use case results are illustrated in Figure 4.15. The application layer throughput is depicted by Cumulative Distribution Function (CDF) plots in Figure 4.15a, where solid lines represent the

averaged curve for all runs, while the shaded areas around these lines illustrate the variation across different runs, indicating the range of values within one SD above and below the mean. The MCS and RSRP results at the MAC layer are shown in Figure 4.15b and Figure 4.15c, respectively. Also here, the average values are depicted using solid lines, while the shaded areas indicate the SD.

The throughput results of Figure 4.15a highlight notable variability in network quality influenced by mobility. Throughout the test, the UE achieves peaks of up to 350 Mbps in DL and 50 Mbps in UL. However, significant fluctuations in performance are observed, particularly as the UE moves further from the initial RU position. Figure 4.15b illustrates a significant drop in UL MCS values around the 100-second mark, while averages initially above 10 drop sharply, while DL MCS fluctuate more gradually until they fall below 10. This sudden decline in UL MCS at this specific time is likely due

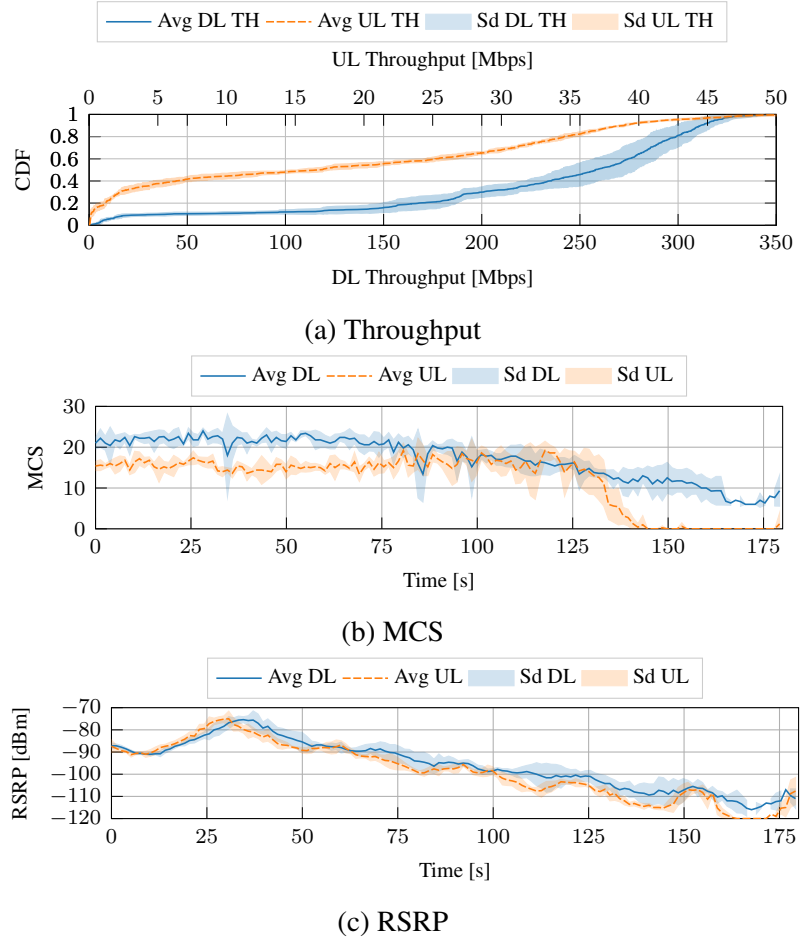


Figure 4.15: Performance profiling with one RU and one mobile UE in the iPerf use case: (a) CDF of DL and UL throughputs with averages (solid lines) and SD (shaded areas); (b) averages (solid lines) and SD (shaded areas) of the DL MCS during DL transmissions (blue) and of the UL MCS during UL transmissions (orange); (c) averages (solid lines) and SD (shaded areas) of the RSRP reported by the UE during DL (blue) and UL (orange) data transmissions.

to deteriorating signal conditions, as corroborated by the corresponding RSRP trends in Figure 4.15c. This is most probably due to increased distance from the base station or physical obstructions, leading to a necessary reduction in MCS to maintain connectivity under compromised signal strength.

The MCS results of Figure 4.15b show that both DL and UL MCS values start relatively high but decrease as the UE moves further from the RU. The DL MCS exhibits more variability and sharper declines compared to the UL, which maintains a more stable profile until the final part of the walk. This suggests that the uplink benefits from more aggressive modulation and coding strategies due to 5G adaptive power control mechanisms that mitigate the impact of increasing distance and obstacles more effectively. Additionally, the RSRP data, shown in Figure 4.15c, indicates a gradual decline in signal strength as the UE moves along its trajectory. RSRP values for both DL (blue) and UL (orange) cases decrease over time, with the most significant drops observed after 100 seconds. This reduction in signal quality corresponds with declines in throughput and MCS, highlighting the strong dependency of these metrics on signal strength.

4.5.4 Video Streaming Experiments

We place the UE at three static locations at different distances from the RU: location 8 (close); 12 (mid); and 16 (far). We run each video session for three minutes, streaming five distinct profiles simultaneously at various resolutions as described in Section 4.5.1. We then plot the mean bitrate over five runs, as well as the rebuffer ratio, in Figure 4.16. As expected, the average bitrate decreases and the rebuffer ratio increases as further distances between UE and RU are considered, transitioning from close to far static locations. We observe that the UE can achieve a steady mean bitrate of around 180 Mbps in all static cases. Note that, unlike test results achieved through iPerf backlogged traffic, the mean bitrate for video streaming is lower. The video client fetches segments in an intermittent fashion (causing flows to be short), which depends on parameters, e.g., video buffer and segment size. Because of this, throughput sometimes does not increase to the fullest during that short period of time, and the client algorithm Adaptive Bitrate Streaming (ABR) downgrades the bitrate based on the estimate it gets. This is due to a slow MCS selection loop in the OAI L2, which will be improved as part of our future work. However, this shows that our setup is capable of supporting up to 8K High Dynamic Range (HDR) videos that require 150 – 300 Mbps bitrates according to YouTube guidelines [145]. During mobility, the average bitrate is 120 Mbps, and the rebuffer ratio increases to

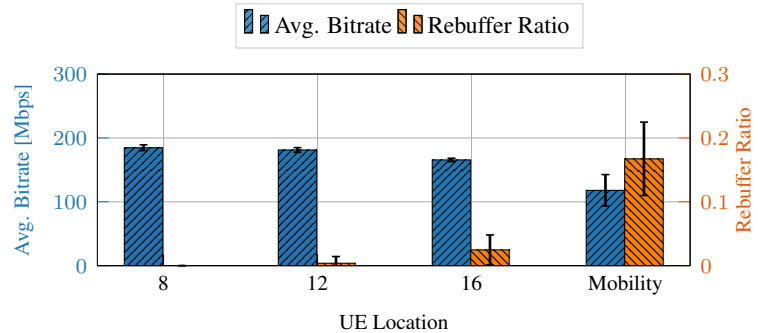


Figure 4.16: Video streaming performance with one UE and single RU across both static (8—close, 12—mid, 16—far) and mobile use cases.

15%. This is once again because the UE moves away from the RU, gradually entering low-coverage regions and eventually disconnecting.

4.5.5 Peak Performance Experiments

In this second set of experiments, we expand our evaluation to stress-test the system and attain peak performance results. To achieve these compared to previous tests, we leverage a GH RAN server with a DDDDDDSUUU TDD pattern, a 4x4 MIMO configuration, 4 layers DL, 1 layer UL and a Q_m up to 256-QAM. We compare system output with a single and double commercial OTA UEs connected to our network at a fixed location using Open5GS as CN and iPerf to generate traffic, as well as with the Keysight RuSIM emulator device, emulating both RU and up to 25 UEs, using Keysight CoreSIM to emulate the CN. The average throughput and 95% confidence intervals are plotted in Figure 4.17. We observe that in OTA at a fixed location, the UEs achieve steady throughput in all cases, as indicated by the small confidence interval values, with a peak of up to 1.05 Gbps in DL and 100 Mbps in UL for a single UE (*1-ota*). Furthermore, the combined throughput increases with the number of connected UEs (*2-ota*), reaching a maximum of 1.2 Gbps in DL, while remaining close to 100 Mbps in UL.

By using the Keysight RuSIM emulator with the same configuration as OTA, performance improves to over 1.26 Gbps with a single UE (*1-sim*) and 1.42 Gbps with two UEs in DL (*2-sim*), and close to 110 Mbps in UL for both one and two UEs. This performance increase can be attributed to the more controlled environment provided by RuSIM, which eliminates external interference and impairments. In this case, an *ExcellentRadioConditions* channel model—also used for BS conformance testing as specified in the 3GPP specifications [146]—is enabled to simulate ideal radio

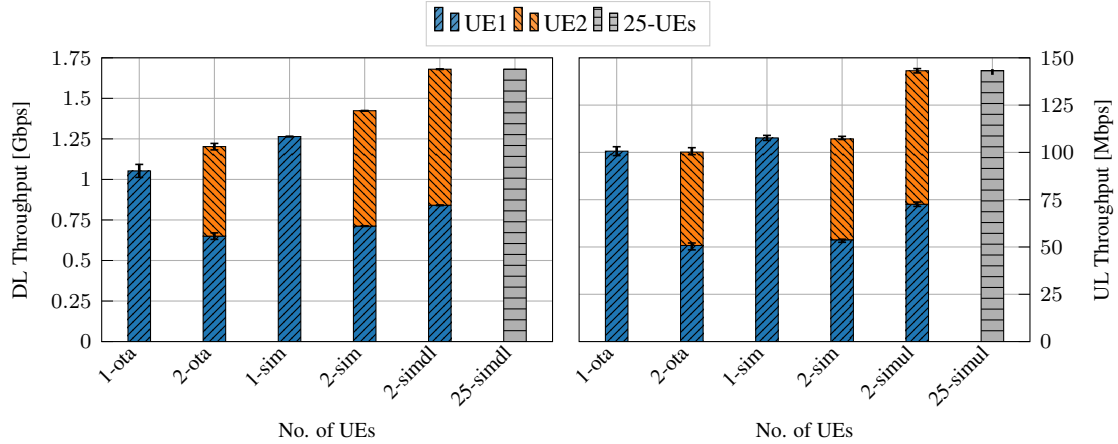


Figure 4.17: Performance profiling to achieve peak network throughput, leveraging: one (*1-ota*) and two (*2-ota*) OTA UEs at a fixed location using iPerf and a DDDDDDSUUU TDD pattern; one (*1-sim*) and two (*2-sim*) emulated UEs using Keysight RuSIM and CoreSIM with a DDDDDDSUUU TDD pattern; and two (*2-simdl*, *2-simul*) and twenty-five (*25-simdl*, *25-simul*) emulated UEs with Keysight RuSIM and CoreSIM, a reduced number of guard symbols, a DDDDDDDDSUU TDD pattern for DL cases, and a DDSU TDD pattern for UL cases.

conditions. To achieve the current peak cell throughput, we leverage a DDDDDDDDSUU TDD pattern in DL and a DDDSU pattern in UL, utilizing a reduced number of guard symbols (only one) enabled by RuSIM during two separate experiment runs with two emulated UEs. This approach results in an aggregate throughput of 1.68 Gbps in DL (*2-simdl*) and 143 Mbps in UL (*2-simul*). Moreover, we stress-test the system by simultaneously connecting up to 25 emulated UEs while exchanging traffic, achieving similar performance (*25-simdl*, *25-simul*). This demonstrates that the network can reliably sustain multiple UEs and reaches its peak with two UEs, while fairly distributing resources when more devices are connected. These results highlight the maximum performance currently achievable by X5G, showcasing values comparable to those of production-level systems.

4.5.6 Long-running Experiments

To validate stability and reliability, we evaluate X5G through long-running experiments with a single UE performing continuous operations. The cell configuration remains the same as in Section 4.5.5, utilizing the DDDDDDDSUUU TDD pattern, a 4x4 MIMO setup with 4 DL layers and 1 UL layer. The UE is a Samsung S23 phone, which cycles randomly every 10 minutes between three different operations:

- DL test, a 1-minute UDP downlink iPerf data test targeting 50 Mbps.
- UL test, a 1-minute UDP uplink iPerf data test targeting 10 Mbps.
- Disconnection, the UE disconnects from the network, remains disconnected for the remaining 10 minutes, and then reconnects.

Figure 4.18 shows the results of the long-running experiment, where the operations performed by the UE every 10 minutes are represented with colored bars. The system can sustain indefinite uptime, as highlighted in the figure with over 180 hours of operation before the cell was manually shut down to vacate the spectrum for other planned experiments in the area. Additionally, Figure 4.19 presents some of the metrics available on the RAN server side, showing the resource utilization

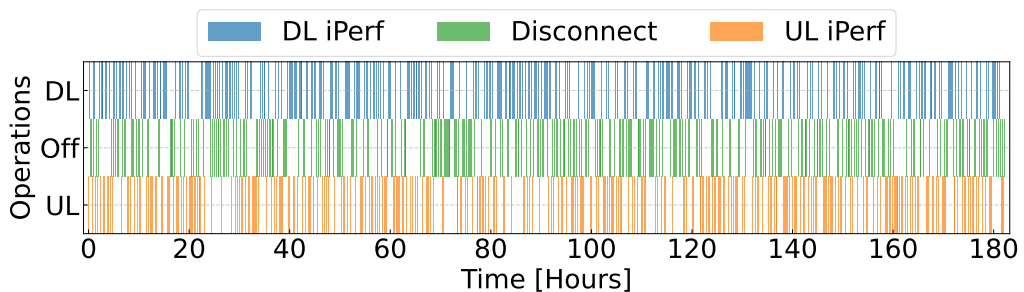


Figure 4.18: Long-running stability experiment involving one UE randomly cycling for over 180 hours among three operations, repeated every 10 minutes: (blue) DL iPerf for 1 minute; (orange) UL iPerf for 1 minute; and (green) disconnection from the network for the remainder of the 10-minute cycle window.

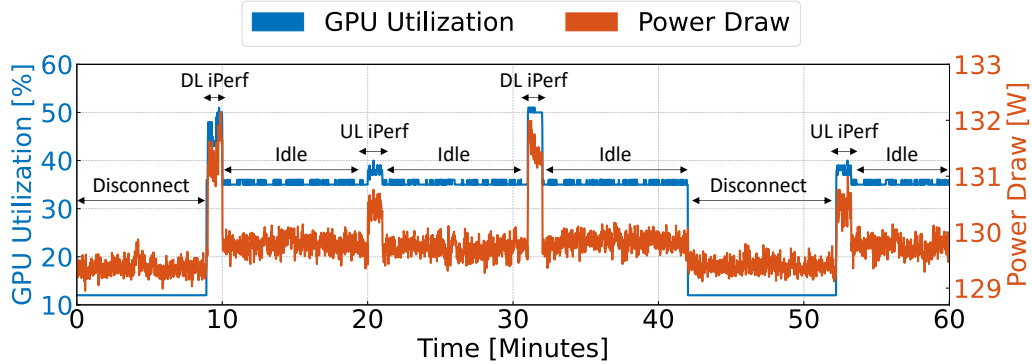


Figure 4.19: GPU utilization (blue) and power draw (orange) of the NVIDIA Grace Hopper server node during a one-hour window of the long-running stability experiment. The results show the behavior of the system when the UE cycles through three operations: disconnecting for 10 minutes, performing a DL iPerf test for 1 minute, followed by 10 minutes of idling, and performing a UL iPerf test for 1 minute, followed by 10 minutes of idling.

required to run the NVIDIA ARC-OTA gNB with a single cell on a GH200 GPU. Specifically, GPU utilization and power draw are depicted for a GH server during a one-hour window of the previous long-running stability experiment. We can see how the utilization (in blue) drops to nearly 10% when no UE is connected, and rises to approximately 50% during DL data traffic, reflecting the system's computation demand. On the other hand, during idle periods and UL communication, GPU utilization remains stable between 35% and 40%, respectively. The power draw (in orange) follows a similar trend, ranging from 129 to 132 W. It is important to note that these results apply to a single cell, but the resource requirements for multiple cells do not scale linearly. Each GH server can support up to 20 cells [147] while maintaining a high-level of energy efficiency for RAN communications [148]. Overall, these results highlight the high reliability of X5G in terms of both performance and stability, positioning it as a suitable candidate for Private 5G (P5G) deployments, as well as a valuable playground to develop, test, and evaluate novel AI/ML algorithms and solutions for the RAN.

4.6 GPU-Accelerated dApp Framework

This section presents a GPU-accelerated framework for real-time distributed Applications (dApps) on an NVIDIA ARC-OTA gNB, such as X5G. Section 4.6.1 provides background on AI-native RANs and dApps, and identifies key design challenges. Section 4.6.2 describes the framework architecture, including the real-time Aerial Data Lake (ADL), Shared Memory (SHM) design, and E3 interface integration. Section 4.6.4 evaluates the framework performance through E2E latency benchmarks.

4.6.1 dApp Background and Motivation

4.6.1.1 AI-Native RAN Vision.

Recent work in both standardization and industry is shifting towards an AI-native RAN vision, where gNBs are becoming programmable edge nodes that expose data and compute to AI workloads. The O-RAN ALLIANCE promotes this transition through a disaggregated architecture with open interfaces and RICs for data-driven control [1], while initiatives such as the AI-RAN Alliance further refine how AI workloads and services should be co-designed with the RAN [149].

4.6.1.2 dApps: Real-Time Distributed Applications.

dApps are lightweight applications, deployed directly on the gNB, capable of accessing PHY/MAC telemetry and executing control actions at sub-10 ms timescales [83]. The architecture in [139] defines a new E3 interface to allow real-time interactions between RAN (e.g., CU and DUs) and dApps, and an E3 Application Protocol (E3AP) to expose structured user-plane messages and control primitives, and demonstrates feasibility with use cases such as spectrum sharing and positioning on an OAI-based gNB. The O-RAN nGRG research report [150] further analyzes dApp use cases and requirements. [23] extends this line of work by embedding a GPU-accelerated dApp for UL interference detection directly into the NVIDIA Aerial pipeline. In contrast, our work introduces a generic and comprehensive GPU-driven framework that exposes a shared-memory telemetry plane and structured E3 interface to support multiple data types and models, with dApps running outside the RAN process and decoupled from custom embedded kernels.

4.6.1.3 NVIDIA Aerial Data Lake

The X5G ARC-OTA deployment described in Section 4.2 includes the NVIDIA ADL tool, a data capture platform that records OTA signals and associated L2 metadata from gNBs built on the Aerial stack, stores them in a database for offline post-processing [151]. pyAerial complements this by providing Python tools to query Data Lake, decode and process captured signals, and build datasets and AI pipelines. While ADL enables offline analysis, the dApp framework presented in this section extends it with a SHM data path to expose telemetry in real-time, as described in Section 4.6.2.

4.6.1.4 Key Challenges and Requirements

Enabling dApps on a GPU platform such as ARC-OTA poses several key challenges, motivating the design of our GPU-accelerated dApp framework presented in this section.

C1: Real-time data access. dApps require low-latency access to selected data (e.g., I/Q samples, channel estimates) without the overhead and latency of extra operations and remote RICs.

C2: Co-location with loose coupling. dApps should be co-located with the gNB to meet strict timing constraints, and also remain loosely coupled so they can be deployed and updated without modifying the production RAN.

C3: GPU-native AI tooling. The framework should be able to take advantage of the existing GPU infrastructure used by the RAN and support various AI toolchains, providing a simple path to develop and deploy new models.

C4: Isolation and scalability. Third-party dApps must be isolated from the RAN, with controlled access to shared-memory regions and compute resources, and the framework should support multiple concurrent dApps without degrading RAN performance.

C5: Alignment with standardization and existing frameworks. Interfaces and message formats should align with existing frameworks and build on E3 abstractions and serve as a reference for ongoing O-RAN, AI-RAN, and 3GPP standardization efforts on AI-native RANs and ISAC use cases.

4.6.2 GPU-accelerated dApp Framework Design

This section describes our GPU-accelerated dApp framework, including its main components and design choices.

4.6.3 High-Level Architecture

Figure 4.20 shows the architecture of an ARC-OTA gNB, extended to support our GPU-accelerated dApp framework, with three main components: (i) DU-Low running the NVIDIA Aerial CUDA L1 pipeline, ADL, and an E3 Agent component; (ii) DU-High and above running OAI open-source stack; and (iii) one or more dApps. The entire framework runs on the same physical host, requiring partitioning of host resources, such as CPU core pinning and GPU sharing mechanisms like NVIDIA Multi-Process Service (MPS) or Multi-Instance GPU (MIG), to avoid degradation of RAN performance, which remains the highest priority.

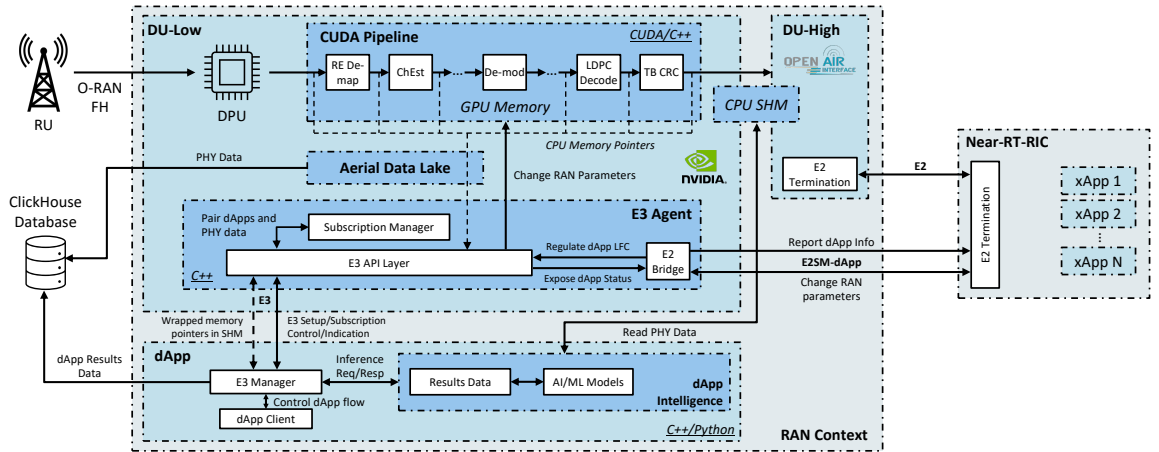


Figure 4.20: NVIDIA ARC-OTA dApp Integration Architecture.

4.6.3.1 Real-Time ADL and Shared Memory

Real-time Aerial Data Lake. To satisfy *C1* (real-time data access), we extend ADL, discussed in Section 4.6.1.3, to a real-time version which uses a double buffering mechanism to capture and manage incoming data efficiently. As shown in Figure 4.21, the main thread uses two pointers ($p1$ and $p2$) that point to two buffers ($ping$ and $pong$) and alternates writes between them. When one

buffer is full, the thread swaps the pointers, starts collecting into the other buffer, and triggers a database insertion thread to write the completed buffer to the ClickHouse DB. The database can be configured at start time to use in-memory RAM tables or SSD storage. Since insertion is slower than capture, this ping-pong pattern allows continuous data collection without interruptions, as long as the buffers are large enough.

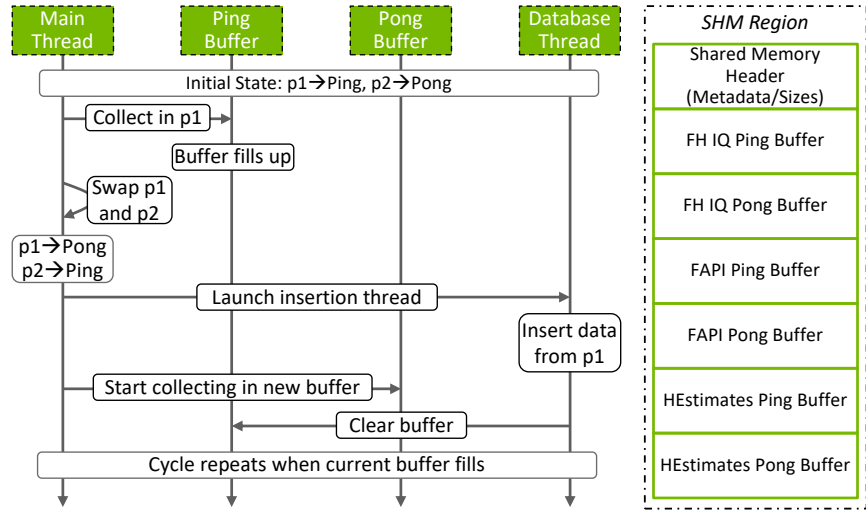


Figure 4.21: Aerial Data Lake ping-pong mechanism and shared memory structure.

E3 Agent Integration. We integrate an E3 Agent into the NVIDIA Aerial software, leveraging the same initial data path pipelines, triggering mechanisms (once per uplink Transmission Time Interval (TTI)), and double-buffering abstraction of ADL. We expose the ping-pong buffers as a POSIX shared-memory object in pinned host memory with the structure shown in Figure 4.21, enabling direct access by external dApps. As illustrated in Figure 4.22, when ADL and/or the E3 Agent are enabled, the Physical Uplink Shared Channel (PUSCH) pipeline is instructed to copy (Op. 1) selected UL data from device memory (GPU) into pinned host memory via an asynchronous CUDA memcpy. This allows the CPU to proceed with other work while the GPU performs the transfers, minimizing the impact on the critical real-time L1 PHY path. Currently, we export I/Q samples, Channel Estimates (\hat{H}), MAC Packet Data Units (PDUs), and a set of FAPI metadata, but additional data types can be added with minimal changes.

An atomic notification (Op. 2) from the PUSCH processing then triggers the ADL routines, which write (Op. 3.1) the data from pinned host memory into the next slot of the appropriate SHM ping-pong buffer. Although these memcpy routines are fast, an additional copy is currently required to decouple data ownership between cuPHY and ADL. We plan to optimize this path by removing this extra copy in future versions, for example, by allowing the PUSCH pipeline to copy directly into SHM. If the E3 Agent is enabled, it is notified (Op. 3.2) and then packs and sends the corresponding pointers and metadata to subscribed dApps via E3 Indication messages (Op. 4). In particular, for small scalar values or metadata (e.g., slot index, cell ID), the indication carries the value directly. For larger data structures stored in SHM, the indication includes: (i) the data type (e.g., I/Q, \hat{H}); (ii) the buffer index (ping or pong); (iii) the offset within the buffer, expressed in units of TTIs; and (iv)

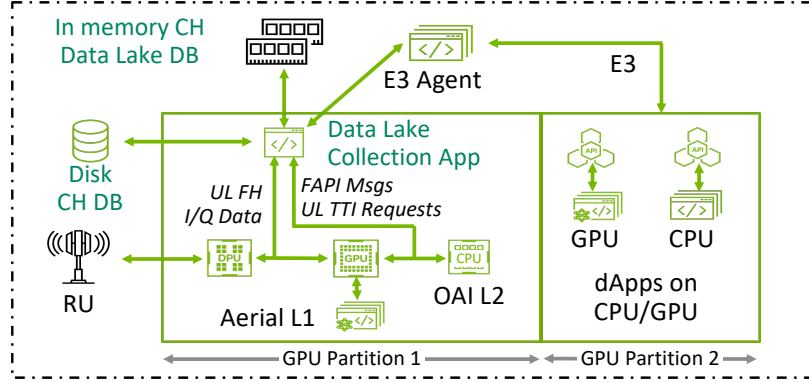


Figure 4.22: Data path integration between Aerial L1, Real-time ADL, shared-memory, and the E3 Agent. The steps (Op. 1–4) match the operations in Table 4.4.

optionally, the size of the written data. The dApp can then read the referenced memory while ADL and the E3 Agent prepare the next batch. Here, ADL and the E3 Agent act as read-write producers, while dApps act as read-only consumers.

Shared Memory. This pointer-based access pattern provides zero-copy data sharing between RAN and dApps, enabled by a copy path that decouples from critical GPU signal processing pipelines. Placing the buffers in host SHM also ensures portability across different deployment configurations. While NVIDIA provides direct GPU-to-GPU mechanisms, such as NVLink for peer-to-peer access and GPUDirect RDMA for inter-node communication, these require specific hardware topologies and do not support memory sharing across MIG partitions, which present isolated memory spaces even within the same physical GPU. By routing the data through pinned host memory and exposing it via SHM, our design provides a general access path for dApps regardless of whether they execute on a different MIG partition, a separate GPU, or the CPU. This also allows the same data to be accessed safely by multiple concurrent dApps while still meeting the low-latency requirements of ISAC and other sensitive applications. While the current implementation focuses on a specific set of data types, the SHM layout is generic and can be extended with additional structures by defining new regions, up to a practical limit beyond which further additions may incur performance penalties. Additionally, buffer sizes are configurable at startup, allowing for a trade-off between the amount of accessible history and memory usage. ADL and the E3 Agent share the same initial data paths and buffering mechanism, however, they can be enabled independently without changes to the RAN.

4.6.3.2 E3 Agent and E3 Manager

The E3 Agent and E3 Manager implement the communication over the recently proposed E3 interface between a RAN node and a dApp, respectively, following the E3AP procedures described in [139] of setup, subscription, indication, and control (*C5: Standardization*). As shown in Figure 4.23, our framework supports multiple E3 Agents running within a gNB, one for each RAN function (e.g., NVIDIA DU-Low, OAI DU-High). An E3 Manager can independently register with multiple E3 Agents and create multiple subscriptions, for example, at different sampling rates or telemetry streams. This design enables system scalability (*C4: Scalable*), allowing additional agents

to be added without modifying existing dApps and for multiple dApps to subscribe to the same telemetry at different rates. Figure 4.23 shows two dApp examples: a spectrum sharing dApp that subscribes to L1 telemetry and sends control messages to L2 for scheduling decisions, and an ISAC dApp like cuSense that only consumes channel estimates for inference without closing the control loop.

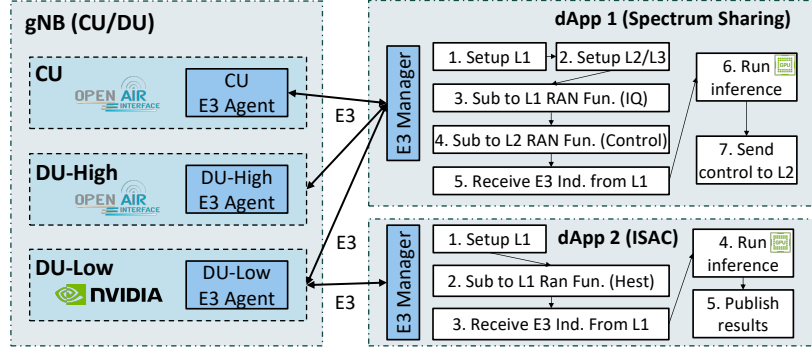


Figure 4.23: Support for multiple RAN nodes, E3 Agents, and dApps in the same gNB.

4.6.3.3 dApp Reference Architecture

To address *C3 (GPU-native AI tooling)* and *C4 (isolation and scalability)*, we design a reference dApp container architecture with three main components, as shown in Figure 4.24: (i) an E3 Manager, the required dApp orchestrator; (ii) an NVIDIA Triton Inference Server [152], our design choice for inference tasks; and (iii) a dApp Client, an optional application controller. This design serves as a concrete blueprint for deploying a GPU-accelerated dApp within a single container.

E3 Manager. The E3 Manager is a mandatory component that serves as the dApp orchestrator, interacting with the RAN nodes via the E3 interface. It manages all communication with the E3 Agent (e.g., E3 Setup and Subscription procedures) and with the dApp Client to implement the desired behavior, including application-specific Service Models (SMs). Additionally, it processes received E3 Indications by: (i) mapping the logical buffer information into the corresponding SHM locations; (ii) validating the presence and format of all inputs required by the selected AI model; (iii) preparing and sending the inference request to Triton; and (iv) post-processing the inference results for possible control actions or external reporting.

NVIDIA Triton Inference Server. In our reference design, each dApp container hosts an instance of Triton [152], an open-source inference serving software developed by NVIDIA and optimized for GPU-accelerated inference. Developers can replace it with alternative inference engines or even lightweight CPU-only scripts, while still using the same dApp architecture. It exposes a model repository with models packaged as standard Triton directories and supports different backends running on CPU or GPU, including Python, PyTorch (LibTorch), Open Neural Network Exchange (ONNX) Runtime, and Tensor RealTime (TRT). The E3 Manager and dApp client interact with Triton via its gRPC Remote Procedure Calls (gRPC)/HyperText Transfer Protocol (HTTP) or C Application Programming Interfaces (APIs) to handle model life cycles, consume memory pointers, schedule inference requests, and retrieve inference responses. Triton also allows combining different

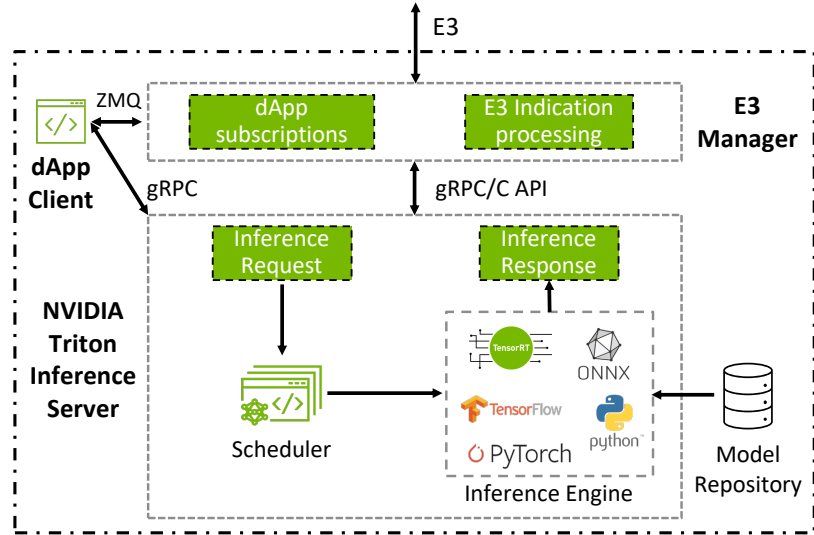


Figure 4.24: dApp container reference architecture with E3 Manager, NVIDIA Triton Inference Server, and dApp Client.

backends or running multiple models in parallel or in sequence, providing a flexible playground for benchmarking and experimentation.

dApp client. The dApp client is an optional user-level service that controls the overall dApp flow. It implements the application-specific logic by: (i) querying and managing Triton models via its gRPC APIs (e.g., selecting the model and backend to use); (ii) configuring the E3 Manager with subscription options, including the target RAN node, a list of RAN functions, Triton model to run, polling interval, duration, and SM; and (iii) performing additional post-processing of the results and triggering external events or control actions when needed. In some configurations, developers can choose to include all or part of the dApp client logic within the E3 Manager component.

This dApp design enables flexibility, as shown in Section 4.6.4, and simplifies the modular deployment of different inference pipelines, as demonstrated by the cuSense ISAC use case in Section 5.2. The source code will be released as open source, with documentation, guides, and inline code comments, providing developers with reference points for developing and deploying their own dApp use cases.

4.6.4 Profiling dApp Framework Performance

We now evaluate the performance of the proposed framework, integrated with NVIDIA ARC-OTA, in terms of E2E control-loop latency, overhead on the RAN pipeline, and model backend flexibility. All experiments share the same ARC-OTA setup and traffic configuration, and employ a simple reference dApp.

4.6.5 ARC-OTA Experimental Setup

We perform our integration and evaluation on a standard ARC-OTA node as described in the documentation [151]. It consists of: (i) a single NVIDIA GH200 GH server for the RAN workloads, featuring a 72-core Grace CPU, an NVIDIA H100 Tensor Core GPU, two BlueField-3 DPUs, and two ConnectX-7 NICs; (ii) a VIAVI Qulsar QG-2 device as grandmaster synchronization clock; (iii) an NVIDIA Spectrum-2 SN3750-SX as Fronthaul (FH) switch; (iv) a 4T4R Foxconn CBRS Frequency Range 1 (FR1) RU centered at 3.65 GHz with 100 MHz of bandwidth; and (v) a Samsung S23 acting as UE. The complete gNB stack, comprising NVIDIA Aerial L1, OAI L2 and above, the dApp framework, and OAI CN, runs within the GH200 node. The server used for the experiments presented here is not MIG-partitioned, but we have also validated the dApp framework on MIG-partitioned servers with other L2+ stacks like ORAN Development Company (ODC). CPU cores are pinned separately for L1/L2 and dApp workloads, and the GPU is shared using CUDA MPS.

4.6.6 Framework Benchmarks

To evaluate the performance characteristics of our framework, we conduct comprehensive benchmarking experiments measuring E2E control-loop latency and the impact of different model backends. These experiments use a simple dApp, `iq-processor`, a PHY-layer telemetry processing application that is representative of use cases such as interference detection, spectrum monitoring, and ISAC.

Reference dApp Model: `iq-processor`. Our benchmark model `iq-processor` accepts as input a tensor of I/Q samples with dimensions [4, 14, 273, 12, 2], corresponding to 4 antenna ports, 14 OFDM symbols, 273 Physical Resource Blocks (PRBs), 12 subcarriers per PRB, and 2 values (the I and Q components) in Float16 (FP16) format. This corresponds to one full UL slot of 100 MHz bandwidth data with numerology $\mu = 1$. The model computes the average power per PRB using

$$P_{\text{PRB}}(p) = \frac{1}{N_a N_s N_{sc}} \sum_{a=1}^{N_a} \sum_{s=1}^{N_s} \sum_{k=1}^{N_{sc}} (I_{a,s,p,k}^2 + Q_{a,s,p,k}^2), \quad (4.5)$$

where $P_{\text{PRB}}(p)$ is the average power for PRB $p \in \{1, \dots, 273\}$, $N_a = 4$ number of antennas, $N_s = 14$ the number of OFDM symbols, $N_{sc} = 12$ the number of subcarriers per PRB, and $I_{a,s,p,k}$ and $Q_{a,s,p,k}$ are the I/Q components. The output is a 273-element Float32 (FP32) vector containing the power measurements for each PRB.

End-to-end Complete Control Loop. Table 4.4 shows the complete control-loop data path, from the time an UL slot completes processing on the GPU pipeline, through the dApp routines, to the application of a control decision at the RAN. The communication between the E3 Agent and the E3 Manager is implemented with ZeroMQ (ZMQ), a high-performance asynchronous messaging library for distributed systems that provides efficient request/reply and publish/subscribe socket patterns. The framework currently contributes a fixed average overhead of approximately 495 μ s plus the model-dependent inference time δ (Operation 7). Operations 1–4 ($\approx 130 \mu$ s) represent the data collection phase involving the GPU→CPU→SHM transfers and atomic notifications. Operations 5–8 correspond to the inference pipeline, measured as *client latency* in our backend comparison analysis. This phase includes interactions with Triton, SHM access, and tensor preparation, and model inference time. For simplicity, we currently use gRPC as the communication protocol between

the E3 Manager and Triton. This choice simplifies integration but dominates the overall framework overhead. We plan to replace gRPC with Triton C-based APIs to further reduce latency. Finally, Operations 9-10 close the loop by sending an optional control message back to the E3 Agent and applying it. In this benchmark, the control logic is not implemented, so the additional processing beyond ZMQ messaging is excluded.

Table 4.4: Data messaging path and cumulative latency for a single dApp end-to-end control-loop iteration.

Operation	Protocol	Overhead [μs]	Total [μs]
1. cuPHY copies data from GPU to CPU	memcpy	35	35
2. cuBB notifies ADL data is ready	Atomic	30	65
3. ADL copies data from CPU to SHM	memcpy	50	115
4. E3 Agent sends pointers to E3 Manager	ZMQ	15	130
5. E3 Manager sends request to Triton	gRPC	150	280
6. Triton accesses and prepares input data	SHM	50	330
7. AI Model performs inference	CUDA	δ	$330 + \delta$
8. Triton sends results to E3 Manager	gRPC	150	$480 + \delta$
9. E3 Manager sends control to E3 Agent	ZMQ	15	$495 + \delta$
10. E3 Agent receives and applies control	API	~ 0	$495 + \delta$

Note: δ represents the model-dependent inference time, which varies with model complexity and backend as shown in Figure 4.25.

Model Backend Performance Comparison. To assess the flexibility of the Triton-based architecture, we deploy the same `iq_processor` model with five different backends: (i) Python/NumPy as CPU baseline; (ii) GPU-accelerated Python using torch tensor operations; (iii) PyTorch/LibTorch with TorchScript-compiled execution; (iv) ONNX Runtime for cross-platform deployment; and (v) TRT for NVIDIA-optimized inference with FP16 precision. We benchmark these models using Triton `perf_analyzer`, a tool that generates continuous inference requests and reports both the pure mode inference time (δ) and the E2E client latency (Operations 5-8 in Table 4.4). The results are shown in Figure 4.25. The measurements highlight a substantial reduction in inference latency from more than 1 ms for the CPU baseline to just 16 μ s with the optimized TRT backend, with all GPU-based backends achieving sub-millisecond latency. On the other hand, the difference between client and

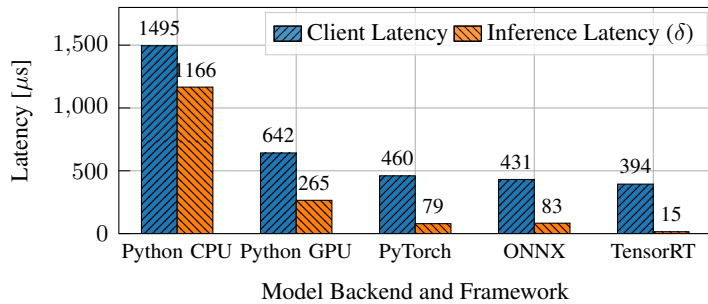


Figure 4.25: Client latency (Operations 5-8 of Table 4.4) and inference latency (δ) for the `iq_processor` model across different backends.

inference times remains roughly constant across backends (around 440–480 μ s), reflecting the framework overhead due to gRPC-based communication and Triton internal request handling. Combining these client latencies with the overheads of approximately 315 μ s (Operations 1-4 and 9-10) results in full E2E control-loop latencies ranging from approximately 1.8 ms for the CPU baseline down to around 710 μ s for TRT backend. While these values are obtained from our benchmarks and may vary slightly with different dApps and subscription configurations, they provide representative reference points.

Overall, these results validate the ability of our framework to meet real-time dApp requirements, with end-to-end control-loop latencies well below 10 ms and, for GPU-accelerated backends, even below 1 ms. At the same time, it provides a flexible and performant playground for developers to experiment, prototype, and deploy a variety of applications without any architectural change.

4.7 Related Work

This section compares the features and capabilities of the X5G testbed within the context of similar programmable open RAN and 5G, highlighting its unique features and contributions beyond 5G research and experimentation. Surveys of testbeds for open and programmable wireless networks can also be found in [7, 1].

The PAWR [26] offers a set of geographically and technically diverse testbeds designed to enhance specific wireless communication areas. These include POWDER, AERPAW, COSMOS, ARA, and Colosseum, each equipped with specialized technologies to address varied research needs.

The POWDER facility, located at the University of Utah in Salt Lake City, UT, supports a wide spectrum of research areas, including next-generation wireless networks and dynamic spectrum access [107]. Its 5G stack is based primarily on a combination of open-source stacks, combined with SDRs or RUs but not accelerated at the physical layer, and on a commercial Mavenir system, which does not support access to the source code from the PHY to the core network, differently from the X5G stack.

Similarly, AERPAW, deployed on the campus of North Carolina State University in Raleigh, NC, focuses on aerial and drone communications, diverging from our emphasis on private 5G network configurations [153]. The AERPAW facility hosts an Ericsson 5G deployment with similar limitations with respect to stack programmability for research use cases.

The COSMOS project [154] leverages an array of programmable and software-defined radios, including USRP and Xilinx RFSoC boards, to facilitate mmWave communication experiments across a city-scale environment. The outdoor facilities of COSMOS are deployed in the Harlem area, in New York City, while its indoor wireless facilities are on the Rutgers campus in North Brunswick, NJ. Unlike X5G, COSMOS is designed for broad academic and industry use and is more focused on mmWave deployments enabling diverse external contributions to its development without specific emphasis on any single network architecture.

The ARA testbed [155], deployed across Iowa State University (ISU), in the city of Ames, and surrounding rural areas in central Iowa, serves as a large-scale platform for advanced wireless research tailored to rural settings. ARA includes diverse wireless platforms ranging from low-UHF massive MIMO to mmWave access, long-distance backhaul, free-space optical, and Low Earth Orbit (LEO) satellite communications, utilizing both SDR and programmable COTS platforms and

CHAPTER 4. DESIGN AND DEPLOYMENT OF A PRIVATE 5G O-RAN TESTBED

leveraging open-source software like OAI, srsRAN, and SD-RAN [156]. However, unlike the X5G testbed, ARA focuses primarily on rural connectivity without focusing on specialized hardware for PHY layer optimization or digital twin frameworks for RF planning.

Colosseum is the world’s largest Open RAN digital twin [3, 35]. This testbed allows users to quickly instantiate softwarized cellular protocol stacks, e.g., the OAI one, on its 128 compute nodes. These nodes control 128 SDRs that are used as RF front-ends and are connected to a massive channel emulator, which enables experimentation in a variety of emulated RF environments. However, the Colosseum servers are not equipped to offload lower-layer cellular operations on GPUs, and the available SDRs are USRP X310 from NI, instead of commercial RUS.

The OSC is also involved in the creation of laboratory facilities [157] that comply with O-RAN standards and support the testing and integration of O-RAN-compliant components. These testing facilities, distributed across multiple laboratories, foster a diverse ecosystem through their commitment to open standards and collaborative development. However, unlike X5G, they do not explicitly focus on the deployment complexities of private networks, nor do they provide any PHY layer acceleration technology or utilize a digital twin for RF planning. Instead, they aim to promote multi-vendor interoperability within an open collaborative framework.

6G-SANDBOX [158] is a versatile facility that includes four geographically displaced platforms in Europe, each equipped to support a variety of advanced wireless technologies and experimental setups. It uses a mix of commercial solutions (for example, Nokia microcells, Ericsson Base Band Unit (BBU), and the Amarisoft stack) and open source solutions (for example, OAI and srsRAN) in diverse environments ranging from urban to rural settings. Unlike X5G, 6G-SANDBOX primarily facilitates wide-ranging 6G research through its extensive, multi-location infrastructure. Its predecessor, 5GENESIS [159], featured a modular and flexible experimentation methodology, supporting both per-component and E2E validation of 5G technologies and KPI across five European locations. This testbed emphasizes a comprehensive approach to 5G performance assessment, integrating diverse technologies such as SDN, Network Function Virtualization (NFV), and network slicing to enable rigorous testing of vertical applications but not including O-RAN architectures.

The Open AI Cellular (OAIC) testbed [160], developed at Virginia Tech, is an open-source 5G O-RAN-based platform designed to facilitate AI-based RAN management algorithms. It includes the OAIC-Control framework for designing AI-based RAN controllers and the OAIC-Testing framework for automated testing of these controllers. The OAIC testbed introduces a new real-time RIC, zApps, and a Z1 interface to support use cases requiring latency under 10 ms, integrated with the CORNET infrastructure for remote accessibility.

The CCI xG Testbed provides a comprehensive platform for advanced wireless research, particularly in the realm of 5G and beyond. It features a disaggregated architecture with multiple servers distributed across geographically disparate cloud sites, leveraging a combination of central and edge cloud infrastructures to optimize resource allocation and latency. The testbed includes several SDR-based CBRS Base Station Device (CBSD) integrated with an open-source Spectrum Access System (SAS) for dynamic spectrum sharing in the CBRS band [161]. Additionally, the testbed supports a full O-RAN stack using srsRAN and Open5GS and features both non-RT RIC and near-RT RIC for real-time and non-real-time radio resource management [162, 163].

The testbed in [164] provides a prototypical environment designed to experiment with vRAN deployments and evaluate resource allocation and orchestration algorithms. It focuses on the decoupling of radio software components from hardware to facilitate efficient and cost-effective RAN

deployments. This testbed includes datasets that characterize computing usage, energy consumption, and application performance, which are made publicly available to foster further research. Unlike the X5G testbed, the O-RAN platform primarily addresses the flexibility and cost efficiency of virtualized RANs without incorporating specialized hardware for PHY layer tasks.

The disaggregated 5G testbed for live audio production [165] emphasizes ultra-reliable low-latency communication for media applications. Its scope is narrower than X5G, which supports a broader range of experimental scenarios and computationally intensive network configurations.

The data usage control framework [166] addresses privacy challenges in hybrid private-public 5G networks. While it highlights the importance of secure orchestration and policy management, its focus on analytics differs from X5G capabilities in physical layer acceleration and network performance experimentation.

Finally, the Microsoft enterprise-scale Open RAN testbed [119] highlights the potential of virtualized RAN functions on commodity servers, employing disaggregated architectures to demonstrate scalability and flexibility. By integrating Kubernetes for dynamic orchestration and using Intel FlexRAN with ACC100 accelerators for Low Density Parity-Check (LDPC) look-aside offloading, this testbed achieves functional disaggregation of RAN workloads.

Regarding real-time programmability, recent work extends O-RAN toward real-time and user-plane control, building on initial visions and implementations [83, 150, 139]. Follow-up work demonstrates dApps for CPU power management and interference detection on GPU-accelerated 5G PHYs [167, 23]. Janus takes a complementary approach, embedding eBPF-based “codelets” directly into vRAN functions to enable flexible telemetry and real-time control with strict safety guarantees [168], while [160] zApps target similar real-time functionality below the 10 ms timescale at the RIC level. Compared to these systems, the dApp framework presented in Section 4.6 focuses on PHY telemetry on GPU on a production-grade ARC-OTA deployment and uses dApps to implement intelligent GPU-accelerated applications by creating complete E2E pipelines for generic real-time data access and consumption, while keeping dApps outside the gNB process and decoupled from vendor-specific PHY kernels.

While state-of-the-art software stacks such as srsRAN already offer similar performance in terms of core 5G functionalities, including handovers, X5G distinguishes itself through its integration of GPU acceleration, enabling enhanced flexibility and computational power for future innovations. Unlike traditional platforms that rely on CPU-based architectures, which achieve performance parity for standard RAN tasks, it leverages GPUs not only for optimized PHY processing but also as a unified platform for AI/ML workloads. Indeed, the GPU architecture of X5G supports the development and deployment of dApps [139] that utilize AI/ML models for real-time network optimization. This capability aligns directly with the vision outlined by the AI-RAN Alliance [149], which emphasizes the integration of AI-driven decision-making processes across three key development areas: (i) AI-for-RAN, (ii) AI-and-RAN, and (iii) AI-on-RAN, making our platform an ideal candidate for advancing these areas. Moreover, the modular design of X5G guarantees compatibility with both open-source and commercial cores, facilitating future experiments with advanced technologies like massive MIMO, mmWave, and beamforming that are currently under development.

4.8 Conclusions and Discussion

This chapter introduced X5G, an open, programmable, and multi-vendor private 5G O-RAN testbed deployed at Northeastern University in Boston, MA. We demonstrated the integration of NVIDIA Aerial, a PHY layer implementation on GPUs, with higher layers based on OAI, resulting in the NVIDIA ARC-OTA platform. We provided an overview of the ARC-OTA software and hardware implementations, designed for a multi-node deployment, including a Red Hat OpenShift cluster for the OSC RIC deployment, as well as examples of a KPM xApp and a slicing xApp. Additionally, we conducted a ray-tracing study using our DT framework to determine the optimal placement of X5G RUs in an indoor space. Finally, we discussed platform performance with varying numbers of COTS and emulated UEs and applications, such as iPerf and video streaming, as well as through long-running and stress-test experiments to evaluate its stability.

Beyond the core infrastructure, we designed, implemented, and evaluated a GPU-accelerated framework for real-time O-RAN dApps on NVIDIA ARC-OTA that exposes PHY/MAC telemetry via shared memory and an E3-based interface. Coupled with NVIDIA Triton-based inference pipelines running on the same GPU as the gNB, the framework enables complete end-to-end control loops with less than $500\ \mu\text{s}$ overhead. This design addresses the key challenges of real-time data access, co-location with loose coupling, GPU-native AI tooling, isolation and scalability, and alignment with ongoing O-RAN and AI-RAN standardization efforts.

Similar to Colosseum explained in Chapter 2, X5G and the dApp framework address the key research challenges outlined in Chapter 1 for experimental wireless platforms. From a *deployment* perspective, we designed and deployed a multi-vendor platform following disaggregated O-RAN architectures, achieving production-level stability, with the testbed operating continuously for extended periods. The platform provides *realism* by validating an E2E, 3GPP-compliant private 5G network with commercial UEs, capturing hardware impairments and RF propagation effects that emulation cannot fully reproduce. In terms of *usability*, X5G provides reference design architectures and experimental pipelines for data collection and testing, including the dApp framework with its E3 interface and Triton-based inference integration. Finally, the platform supports a broad range of *use cases*, including interference mitigation, network slicing, security, ISAC, and a wide range of 5G/6G research applications—some of which are demonstrated in Chapter 5. Together with the digital twin platforms presented in Chapters 2 and 3, X5G takes the experimental idea journey one step further by providing a comprehensive methodology from controlled emulation to real-world validation.

Chapter 5

Intelligent RAN Control and Security on Physical Platforms

5.1 Introduction

Chapters 2 and 3 demonstrated how large-scale emulation and DT platforms such as Colosseum, combined with *CaST*, can be used to prototype spectrum sharing, AI-driven propagation modeling, and synthetic RF data generation in a controlled environment, while Chapter 4 introduced X5G as a production-grade private 5G O-RAN testbed that brings these ideas into the physical world. With X5G, we now have a stable, GPU-accelerated, end-to-end 5G platform with commercial UEs, multi-vendor RUs, and integrated O-RAN control, capable of supporting long-running experiments under realistic propagation and hardware conditions. This chapter leverages X5G and its dApp framework to explore how intelligent control and security mechanisms can be realized and validated OTA on a physical platform.

X5G provides an open and programmable platform that spans both the data and the control plane. On one hand, the GPU-accelerated dApp framework introduced in Section 4.6 allows AI-native applications to run co-located with the gNB, operating directly on PHY/MAC telemetry with sub-millisecond latency. On the other hand, the OSC near-real-time RIC deployed on X5G enables xApps to control RAN behavior at timescales of tens to hundreds of milliseconds. Additionally, the platform is also leveraged to study the security of open interfaces in realistic a deployment. Together, these capabilities enable X5G to expand the research possibilities from intelligent RAN control to security fields, where solutions can be evaluated under real RF propagation, hardware constraints, and dynamic environmental conditions.

Within the four key research challenges introduced in Chapter 1, this chapter primarily targets the *use case* dimension on physical platforms, building on the *deployment*, *realism*, and *usability* foundations established with Colosseum and X5G. It focuses on completed studies on ISAC, interference detection, resource management, and security, while additional works, both completed and ongoing, address mobility, handover, automation, and energy saving, among other topics.

This chapter is organized as follows. Section 5.2 presents cuSense, an uplink DMRS CSI-based ISAC dApp for real-time person detection using the GPU-accelerated framework. Section 5.3 describes InterfO-RAN, a dApp for in-band uplink interference detection that leverages a custom im-

lementation to monitor and identify anomalous transmissions. Section 5.4 turns to the control plane and discusses ORANSlice, an xApp-based platform for dynamic resource management and network slicing integrated with the OSC RIC. Section 5.5 focuses on security, introducing TIMESAFE and its ML-based detection of timing attacks on the fronthaul. Finally, Section 5.6 summarizes the main findings, and concludes the chapter with discussions and lessons learned.

5.2 cuSense: Uplink CSI-based ISAC dApp for Person Detection

Building upon the dApp framework presented in Section 4.6, this section introduces cuSense, an ISAC dApp for indoor person localization using uplink CSI. This case study validates the framework’s ability to support intensive AI workloads while showcasing the potential of ISAC applications in 5G networks.

5.2.1 Overview and Goals

cuSense targets indoor location estimation in a single-cell CBRS deployment using CSI derived from UL PUSCH transmissions. In particular, it leverages DMRS signals transmitted by a UE and exposed by the E3 Agent, in what is known as UL-collaborative ISAC [169]. Following the reference dApp container architecture of Section 4.6.2, the cuSense dApp processes these DMRSs through a lightweight signal-processing pipeline deployed in Triton, and runs a Neural Network (NN) model to capture the variations in the channel given by the moving object, as shown in Figure 5.1. The goal is to estimate the 2D position (x_t, y_t) of a person walking in the space through a probability map over the area of interest. The system addresses the following key challenges in UL-CSI-based sensing: (i) extracting real-time channel perturbations from static multipath; (ii) learning spatial mapping from high-dimensional CSI data; and (iii) achieving real-time inference.

Finally, cuSense is designed as a reference ISAC dApp to showcase our framework’s ability to support real-time, slot-level inference, and provide a reusable dataset and base pipelines for future ISAC experiments. In the current prototype, we focus on single-user localization, but the same design can be extended without modifying the RAN to other tasks, such as occupancy monitoring and Unmanned Aerial Vehicle (UAV) or ground vehicles detection.

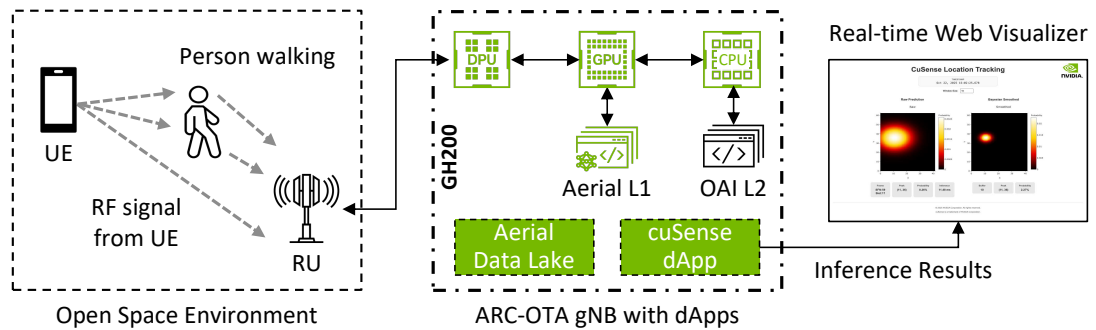


Figure 5.1: Overview of the cuSense UL DMRS-based ISAC dApp for person localization.

5.2.2 Uplink CSI Processing Pipeline

cuSense processes raw UL DMRS CSI measurements to estimate spatial locations of targets within an indoor environment through a three-stage pipeline: (i) background environment characterization (computed offline); (ii) temporal noise reduction and feature normalization (online in the cuSense dApp pipeline); and (iii) NN-based location estimation (online in Triton), as shown in Figure 5.2.

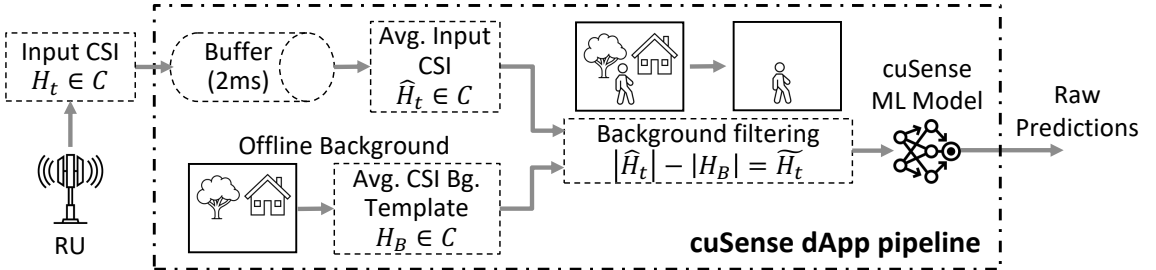


Figure 5.2: cuSense dApp processing pipeline overview.

Stage 1: Background Environment Characterization. The objective of this first stage is to establish a baseline characterization of the wireless channel in the absence of dynamic targets. This background template captures an averaged *snapshot* of multi-path reflections from static objects in a deployment location, such as walls, furniture, and other stationary objects, which can then be removed from live measurements to isolate target-induced perturbations.

Let $H_i[a, k, s] \in \mathbb{C}$ denote the complex CSI for measurement i at antenna a , subcarrier k , and DMRS symbol s , obtained after frequency-domain interpolation over all active subcarriers and before time-domain interpolation to all OFDM symbols. To handle variable-length subcarrier allocations with zero-padding, we define a validity set for each (a, k, s) position:

$$\mathcal{V}_{a,k,s} = \{i : |H_i[a, k, s]| > \tau\} \quad (5.1)$$

where $\tau = 10^{-10}$ is a tolerance power threshold, and $\mathcal{V}_{a,k,s}$ contains the indices of non-zero measurements. This ensures that statistics are computed exclusively from active subcarriers, avoiding contamination from zero-padded frequency bins that may vary across different channel allocations.

We compute a complex-valued background template by averaging over the $N_{a,k,s} = |\mathcal{V}_{a,k,s}|$ valid background measurements:

$$H_B[a, k, s] = \frac{1}{N_{a,k,s}} \sum_{i \in \mathcal{V}_{a,k,s}} H_i[a, k, s]. \quad (5.2)$$

The output of this stage is a complex background template H_B over active subcarriers, which is reused at inference time to remove static multi-path components.

Stage 2: Temporal Noise Reduction and Feature Normalization. This stage applies temporal averaging to mitigate measurement noise, subtracts the static background to isolate dynamic components, and normalizes features to enable stable gradient-based optimization. For each time t in a target run, we construct a causal temporal window

$$W(t) = \{H_i \mid t - \Delta t \leq t_i \leq t\}, \quad (5.3)$$

containing all CSI samples whose timestamp t_i falls within a window of length Δt ending at t . Based on empirical hyper-parameter tuning, we set $\Delta t = 2$ ms, which provided the best trade-off between noise reduction and temporal resolution in our experiments. We then compute the phase-coherent average element-wise in the complex domain for each $W(t)$:

$$\hat{H}_t[a, k, s] = \frac{1}{|W(t)|} \sum_{i \in W(t)} H_i[a, k, s], \quad (5.4)$$

excluding zero-valued samples on inactive subcarriers. Temporal averaging reduces noise variance by approximately a factor of $1/|W(t)|$ under an Additive White Gaussian Noise (AWGN) assumption, improving the effective SNR while preserving the slowly varying channel characteristics associated with target motion.

To isolate dynamic components from static environment reflections, we subtract the background template in the magnitude domain from the averaged measurements,

$$\tilde{H}_t[a, k, s] = |\hat{H}_t[a, k, s]| - |H_B[a, k, s]|, \quad (5.5)$$

and then average across the S DMRS symbols in the UL slot,

$$\tilde{H}_t^D[a, k] = \frac{1}{S} \sum_{s=1}^S \tilde{H}_t[a, k, s]. \quad (5.6)$$

This produces a real-valued tensor $\tilde{H}_t^D \in \mathbb{R}^{A \times K_v}$, where A is the total number of receive antennas and K_v the number of active (or valid) subcarriers. This step further reduces noise through intra-slot averaging under the assumption that the channel remains approximately constant within a single OFDM slot.

Finally, we apply global z -score normalization,

$$X_t[a, k] = \frac{\tilde{H}_t^D[a, k] - \mu_{\text{global}}}{\sigma_{\text{global}} + \epsilon}, \quad (5.7)$$

where μ_{global} and σ_{global} are computed over all available samples, antennas, and valid subcarriers, and are then applied identically to all splits, and $\epsilon = 10^{-8}$ is a small constant to prevent division by zero. This produces standardized input features $X_t[a, k]$ for our NN model with approximately zero mean and unit variance, preserving relative power relationships between samples, which facilitates stable training and inference. In a deployed system, Stage 1 runs offline once per environment, while Stage 2 executes online inside the cuSense dApp, using the CSI data delivered by the E3 Agent via SHM.

Stage 3: Neural Network Architecture and Training. In the last stage, we use a ResNet-inspired CNN optimized for frequency-domain, multi-antenna CSI magnitude data to predict a 2D probability grid representing the likelihood of target presence at each location within the environment. In order to account for the relatively shallow architecture and to keep the parameter count low and allow fast inference, we consider only *plain* blocks without residual connections for our architecture design (see [170] for the original model). The normalized features $X_t \in \mathbb{R}^{A \times K_v}$ are fed to our proposed architecture, as shown in Figure 5.3. The network consists of: (i) an initial 1D convolution

and max-pooling layer; (ii) three sequential blocks with progressive channel expansion ($64 \rightarrow 128 \rightarrow 256 \rightarrow 512$); (iii) an adaptive global average pooling layer, to allow inputs of different shapes in case not all RBs are utilized in the UL transmission; (iv) a three-layer Multilayer Perceptron (MLP) stack that outputs an $H \times W$ (grid height and width) spatial probability map; and (v) a final softmax to ensure $\sum_{i,j} P_t(i,j) = 1$ for each (i,j) grid cell probability value P_t .

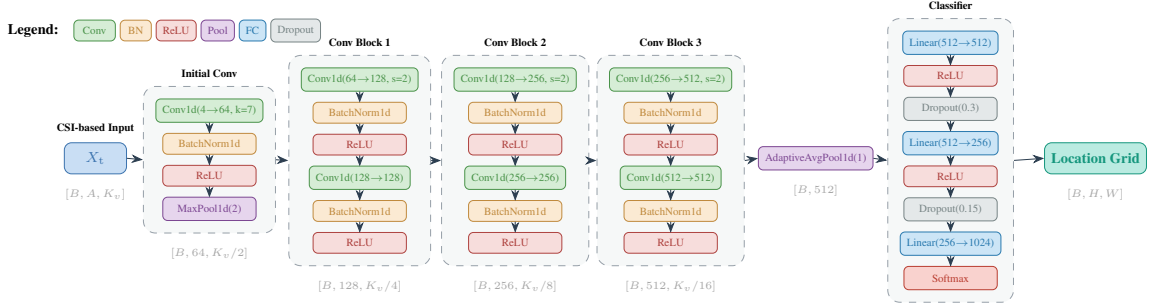


Figure 5.3: Proposed NN architecture of cuSense dApp for CSI-based location estimation.

Training uses the Kullback–Leibler (KL) divergence between the predicted distribution P_X and a smoothed target distribution P_Y as loss:

$$\mathcal{L}_{\text{KL}} = \sum_{i=0}^{H-1} \sum_{j=0}^{W-1} P_Y(i,j) \log \frac{P_Y(i,j)}{P_X(i,j)}. \quad (5.8)$$

This formulation encourages learning the entire spatial distribution rather than only peak locations, improving robustness to measurement noise. The target distribution is obtained by convolving a one-hot probability grid¹ with a 2D Gaussian kernel G_σ (label smoothing):

$$P_Y = \frac{(G_\sigma * P_{\text{one-hot}})(i,j)}{\sum_{i,j} (G_\sigma * P_{\text{one-hot}})(i,j)}, \quad (5.9)$$

with $\sigma = 8.0$ in our experiments. Spatial smoothing encodes the intuition that nearby locations should receive similar probabilities, reflecting uncertainty in ground-truth annotations and measurement noise. We train the model using Adam optimizer, mini-batches of size $B = 256$, and a learning rate $l_r = 10^{-3}$ for 100 epochs. At inference time, cuSense runs Stage 2 pre-processing and the NN inside the dApp container (via Triton), receiving CSI for each UL slot t , and outputting a 2D probability map $P_t(i,j)$ over the $H \times W$ grid. From this distribution, we can derive a maximum-likelihood estimate $(\hat{i}_t, \hat{j}_t) = \arg \max_{i,j} P_t(i,j)$ to obtain the grid coordinates of highest target location probability, which can be then mapped to the relative world-coordinates. In order to reduce output predictions errors, we average the output probability for the last 10 predictions and apply Kalman filtering before returning the final estimated tracked 2D location, as detailed in Section 5.2.3.2.

¹All grid probability values are 0, except for the target location with value equal to 1.

5.2.3 Experimental Evaluation

To assess the feasibility and performance of cuSense, we perform an extensive OTA data-collection campaign, develop labeling pipelines to obtain ground truth and build datasets, and train and test the cuSense NN under realistic environmental conditions.

5.2.3.1 Data Collection and Labeling Methods

Measurement Campaigns. All cuSense experiments are conducted on the same ARC-OTA setup described in Chapter 4 and illustrated in Figure 5.4. The CBRS Foxconn RU is mounted on a custom stand [123] facing an open indoor space in NVIDIA Lab. The Samsung UE, together with a laptop used for remote access and traffic generation, is placed at the opposite end of a rectangular target area of approximately 6.78×10.06 m. We collect multiple runs under two conditions: (i) *background runs*, with no moving target present, to characterize the static channel; and (ii) *target runs*, in which a person walks along various trajectories (e.g., lawnmower, spiral, random) at normal walking speed. Each run follows the same procedure: (i) start camera recording at 30 or 60 Frames per second (FPS) (for target runs); (ii) start the ARC-OTA gNB with ADL enabled; (iii) connect the UE; (iv) start uplink UDP traffic through *iperf* with a target rate of 100 Mbps; (v) perform the walking trajectory within the target area (for target runs); and (vi) stop the run after approximately 2–3 minutes. Across all runs, we collect more than 400.000 CSI records together with more than 30.000 video frames, which we use in the next step for labeling and dataset construction.

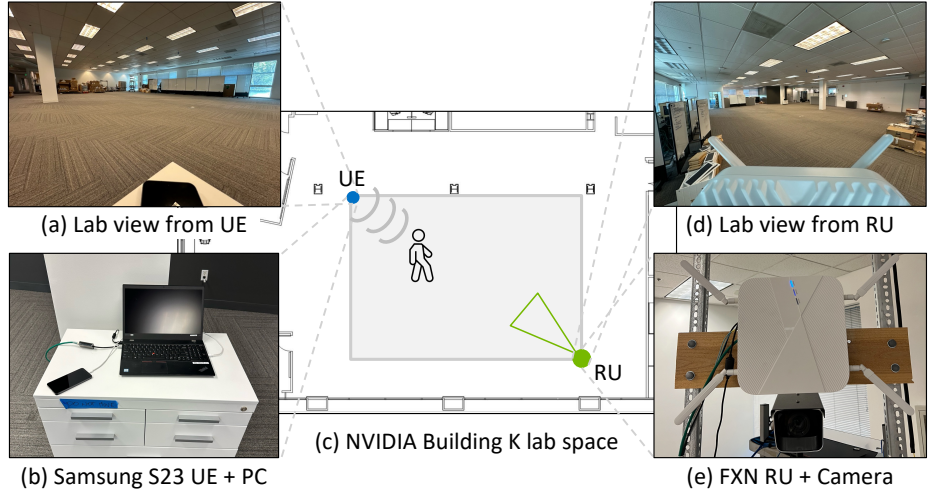


Figure 5.4: cuSense experimental environment.

Temporal Video and Sensing Synchronization. To build the complete dataset for training and testing, we collect UL CSI data (i.e., DMRS $\hat{\mathbf{H}}$) together with a camera video recording the scene at a fixed frame rate, used to generate ground-truth 2D trajectories of the person walking. Synchronizing CSI data and video frames requires handling both time-reference differences and clock skew between devices. CSI records from ADL use International Atomic Time (TAI) timestamps, while video frames from the camera (an iPhone in our experiments, though any commercial 5G

camera could be used) employ standard Coordinated Universal Time (UTC) UNIX timestamps. TAI is a continuous atomic time scale that differs from UTC by a constant offset Δ_{leap} (37 s at the time of our experiments), such that $t_{\text{TAI}} = t_{\text{UTC}} + \Delta_{\text{leap}}$ due to the leap seconds introduced since 1972 to account for Earth’s rotation variations. In addition to this systematic offset, we compensate for residual clock skew between the camera and the gNB server with respect to a common Network Time Protocol (NTP) server. The gNB maintains microsecond-level timing accuracy through PTP synchronization with the grandmaster clock, making its contribution to skew negligible, while the camera achieves millisecond-level precision, which we estimate during the measurement campaigns. In a second step, we run an offline pipeline that parses the video file, extracts per-frame timestamps and images, and aligns them with the CSI after compensating for the 37 s TAI offset and the measured server–camera clock skew. We assign each CSI record to the closest video frame within a threshold of half the frame period, generating tightly synchronized CSI–video pairs, where a single frame may correspond to multiple CSI records.

Ground-Truth Extraction. To extract the ground-truth locations, we derive the 2D person coordinates from the camera stream using an offline computer-vision pipeline based on YOLOv8 [171]. For each video frame, we run a person detector and retain the bounding box with the highest confidence (our experiments are limited to a single walking subject). The box centroid (u, v) in image coordinates is then projected onto the floor plane using a planar homography H estimated from the manually annotated image corners of the rectangular area of interest in the environment. This generates a continuous trajectory $\{(x_t, y_t)\}$ in meters, sampled at the camera frame rate. Each CSI record then inherits a physical position (x_t, y_t) , since it is associated with the closest video frame in time. For training, we discretize the floor plan into an $H \times W$ grid and quantize each position to the corresponding cell (i, j) , producing a one-hot label $P_{\text{one-hot}}(i, j)$ for that CSI sample. These one-hot labels are then converted into smoothed target distributions P_{target} using the Gaussian label-smoothing procedure described in Stage 3.

5.2.3.2 Performance Results

We now evaluate cuSense on the dataset described in Section 5.2.3.1, focusing on three aspects: (i) localization accuracy against the ground-truth; (ii) comparison with 3GPP sensing service categories; and (iii) real-time inference capability within our dApp framework.

Dataset and Evaluation Setup. The cuSense model is trained on CSI data from 5 runs with a moving target, for a total of 362,318 slot samples each with 4 antennas and 3 DMRS symbols. We use a temporal-random split strategy of 80% training, 10% validation, 10% test as shown in the examples of Figure 5.5. Validation and test sets are two contiguous temporal blocks randomly positioned within each run’s timeline, rather than randomly sampling individual points. This design choice is critical because consecutive CSI values may be highly correlated, leading to overfitting and poor generalization to unseen trajectories. The background template H_B is computed from a single dedicated run of 54,400 samples in a static environment with no moving target. We also evaluate cuSense generalization across two independent unseen runs (Unseen-Run 1 and Unseen-Run 2) collected separately from all training, testing, or validation data. We measure localization performance using standard RMSE, median, and success rate within different thresholds over all unseen CSI records. Additionally, the inference pipeline applies a temporal arithmetic mean over 10 consecutive predictions from stage 3 processing output for noise reduction, followed by a Kalman

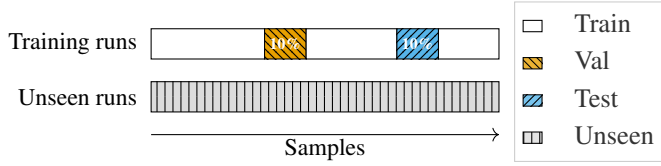


Figure 5.5: Temporal-random split strategy with example of contiguous validation/test blocks within training runs and fully unseen runs.

filter tracking with process noise $Q = 10^{-5}$ and measurement noise base $R_{\text{base}} = 750$ to produce temporally coherent trajectory estimates.

Localization Accuracy. Table 5.1 summarizes the localization performance on the unseen runs. cuSense achieves a mean localization error of 77.4 cm with a median of 58.7 cm, demonstrating sub-meter accuracy for the majority of predictions. The RMSE of 103 cm reflects occasional outliers in challenging multipath conditions. Notably, performance is consistent across both test campaigns (75.1 and 79.7 cm), indicating robust generalization to unseen measurement campaigns in the same environment.

Table 5.1: cuSense localization accuracy on unseen runs.

Metric	Unseen-Run 1	Unseen-Run 2	Average
Samples	47,211	47,404	-
Mean Error [cm]	75.1	79.7	77.4
Median Error [cm]	54.9	62.6	58.7
Std. Dev. [cm]	67.6	68.3	68.0
RMSE [cm]	101.0	105.0	103.0

3GPP Sensing Service Categories. We benchmark these results against the 3GPP Release 19 sensing accuracy categories defined for 5G wireless sensing applications [172]. Figures 5.6a and 5.6b show the cumulative accuracy at each category threshold, and the error CDF for the test set (approximately 35k samples from the temporal-random split of training), while Figures 5.6c and 5.6d present the same metrics for the two completely unseen runs (over 94k samples). On the test set, around 42% of predictions achieve Category 4 accuracy (≤ 50 cm), with cumulative sub-meter accuracy of 75% (Categories 4 and 3). We note that performance on unseen runs remains consistent with 43% of predictions falling within Category 4 and over 74% within Category 3, despite these runs being entirely excluded from training. This indicates that the model generalizes well to new trajectories within the same environment rather than overfitting to training data. Over 93% of predictions meet Category 2 requirements (≤ 2 m) for the unseen runs, with the remaining predictions within Category 1 (2–10 m). These results demonstrate that cuSense meets 3GPP sensing requirements for indoor localization applications such as asset tracking, occupancy monitoring, and intelligent building automation.

Trajectory Tracking. Figure 5.7 visualizes the X and Y position estimates over time for a representative test segment (downsampled to 10 for clarity), comparing raw model predictions, temporally averaged predictions, Kalman-filtered output, and ground truth. The raw predictions

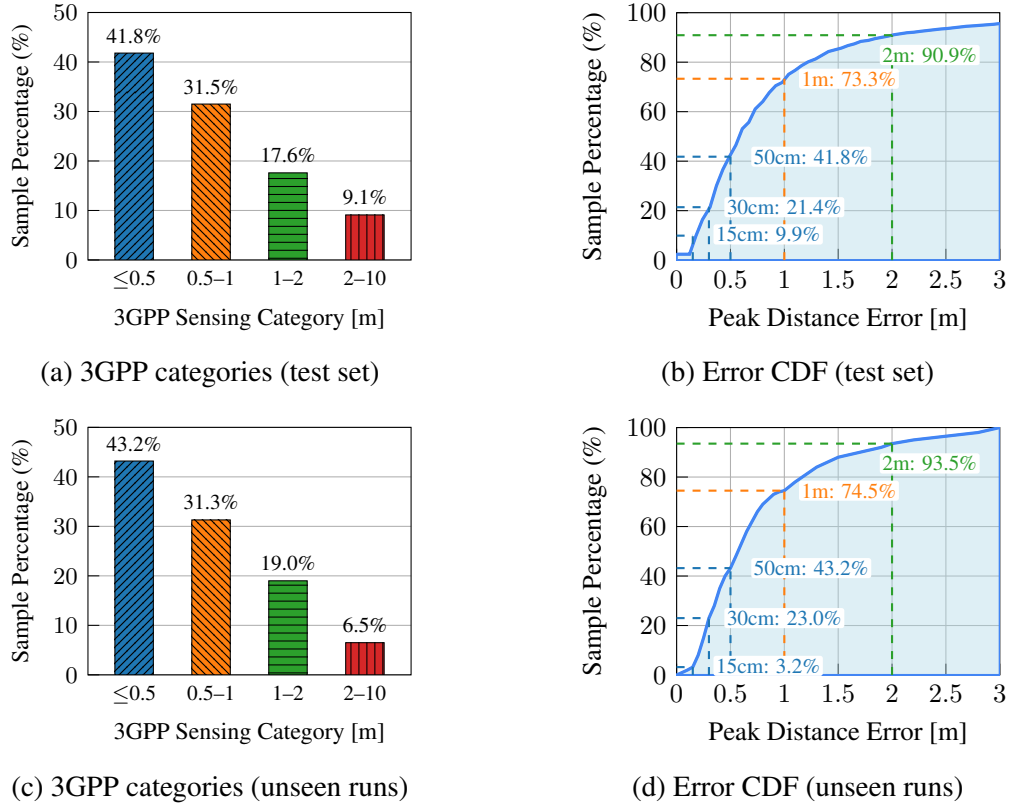


Figure 5.6: cuSense localization accuracy on test set (a, b) and unseen runs (c, d): 3GPP wireless sensing service category distributions and CDF of peak distance error.

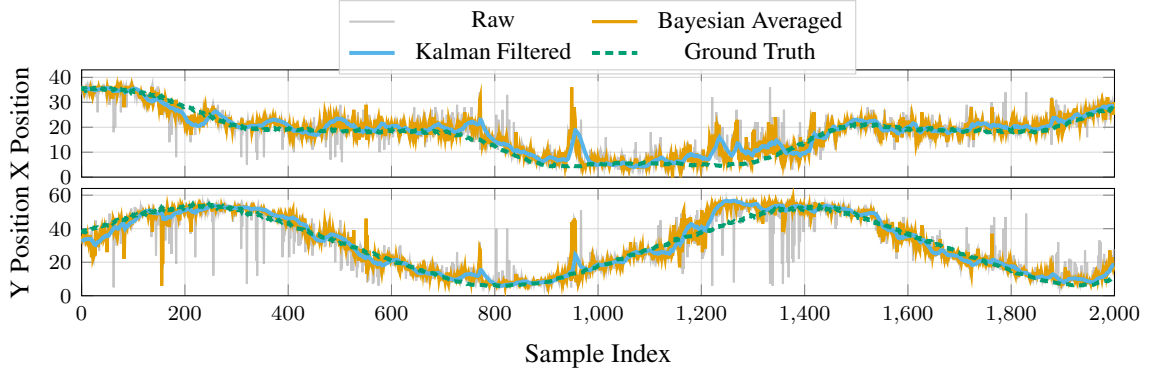


Figure 5.7: Trajectory tracking comparison of an unseen run segment for the X and Y axis.

exhibit significant frame-to-frame jitter from measurement noise. Temporal averaging reduces this variability, while the Kalman filter produces smooth, physically plausible trajectories that closely track the ground truth. The multi-stage refinement provides cumulative error reduction of 30–40% compared to raw predictions, with the Kalman filter successfully handling both slow movements and

rapid direction changes.

Real-Time dApp Inference Performance. Table 5.2 shows the computational performance of the cuSense dApp inference pipeline. The complete pipeline—including CSI preprocessing (background removal and temporal averaging), NN inference via Triton, prediction averaging, and Kalman filtering—achieves a mean E2E latency of 1.36 ms per sample with PyTorch, and 0.65 ms with TRT acceleration. Combined with the dApp framework overhead of 495 μ s (Table 4.4), the total cuSense control-loop latency is approximately 1.85 ms (or 1.15 ms with TRT), well within real-time requirements for tracking applications.

Table 5.2: cuSense inference latency breakdown.

Operation	Overhead [ms]
CSI preprocessing	0.3
Neural network inference	0.8 (PyTorch) - 0.1 (TRT)
Bayesian temporal averaging	0.1
Kalman filter tracking	0.15
Total inference Latency	1.35 (PyTorch) - 0.65 (TRT)

5.2.4 Related Work

ISAC has been widely studied as a key enabler for beyond-5G and 6G networks, with recent surveys reviewing system architectures, performance limits, and open challenges [173, 174]. In the context of 5G, recent work has explored communication-centric ISAC schemes for cooperative target localization and UL-collaborative sensing using OFDM/New Radio (NR) signals [175, 176], as well as passive radar sensing and CSI-based localization using NR reference signals [177, 178, 179]. Earlier Wi-Fi sensing systems [180, 181, 182] have demonstrated that commodity Wi-Fi signals and CSI can enable fine-grained localization and person perception. cuSense is complementary to this literature: rather than using Wi-Fi or standalone receivers, it implements CSI-based indoor localization as an uplink-collaborative ISAC service directly on a 3GPP-compliant, GPU-accelerated 5G gNB, exposing it as a programmable dApp within an O-RAN/AI-RAN framework without dedicated sensing hardware or changes to the RAN stack.

5.2.5 Summary

This section presented cuSense, an uplink DMRS CSI-based indoor localization dApp operating in real time on a production-grade 5G network without dedicated sensing hardware or RAN modifications. Building on the GPU-accelerated dApp framework introduced in Section 4.6, cuSense processes channel estimates through a three-stage pipeline (background characterization, temporal noise reduction, and neural network inference) to achieve sub-meter localization accuracy with over 74% of predictions within the 3GPP Category 3 threshold (≤ 1 m).

The experimental evaluation on X5G validates both the *realism* and *use-case* dimensions of this dissertation. On one hand, real OTA channels with commercial UEs provide ground-truth validation that would be difficult to achieve in emulation. On the other hand, the complete data-

collection, training, and inference pipelines demonstrate the feasibility of ISAC deployment on physical platforms, particularly on a production-grade 5G RAN testbed.

The current UL-collaborative bistatic architecture with a transmitting UE offers a practical deployment model but limits spatial diversity and relies on environment-specific calibration. These constraints motivate future work on dynamic environments, multi-cell configurations, and sensing modes that reduce the need for explicit device collaboration. The dApp framework and cuSense pipelines are planned for open-source release to enable further research on GPU-accelerated real-time applications for AI-native RAN.

5.3 InterfO-RAN: In-band Uplink Interference Detection

This section explores another real-time dApp use case focusing on interference detection: InterfO-RAN. InterfO-RAN is a custom GPU-accelerated dApp implementation embedded within the NVIDIA Aerial CUDA pipeline of X5G, which targets in-band UL interference that degrades network performance in dense deployments. This work further validates the flexibility of the X5G physical platform and its dApp architecture, demonstrating how the same infrastructure can support diverse AI-driven applications operating at sub-millisecond timescales.

5.3.1 Introduction

The evolution of wireless communication networks has been driven by the increasing demand for high-speed, low-latency, and ultra-reliable connectivity to support emerging applications such as autonomous systems, industrial automation, and immersive experiences. To meet these demands, 5G-and-beyond networks leverage massive densification to improve throughput and latency within the limited spectrum allocated to mobile communications [183]. In ultra-dense networks, multiple neighboring small cells are configured to reuse the same frequency bands to increase frequency reuse [184]. Directional millimeter wave systems further push this concept, with commercial deployments often leveraging the same 400 MHz or 800 MHz bands at 28 GHz and 39 GHz for all base stations [114]. Finally, private network deployments (e.g., for enterprise scenarios) use limited portions of shared spectrum, with all deployments constrained in the same 100 MHz (e.g., Germany, Brazil, Netherlands) or 150 MHz (e.g., U.S., with CBRS) [185].

However, densification, sharing, and spectrum reuse also increase inter-cell interference. Although significant research has focused on coordination mechanisms to reduce interference in downlink [186, 187, 188, 189], in-band UL interference remains a challenging problem, especially considering the unpredictability of user mobility and configurations and thus of the source of interference. This occurs when unwanted transmissions from UEs, operating within the same frequency band but connected to different gNBs, interfere with the UL reception of a serving gNB, as shown in Figure 5.8. Such an overlap can significantly degrade the UL SINR at the affected gNB, potentially leading to unrecoverable packets and thus reduced network performance [190]. This is particularly significant when UEs are located at the cell edge, where overlapping regions between two neighboring cells force the devices to increase their transmit power to overcome the link budget constraints. In such cases, the unpredictability of potential in-band UL interference is closely associated with UE power control. Similarly, UEs may transmit at excessive power levels to compensate for signal

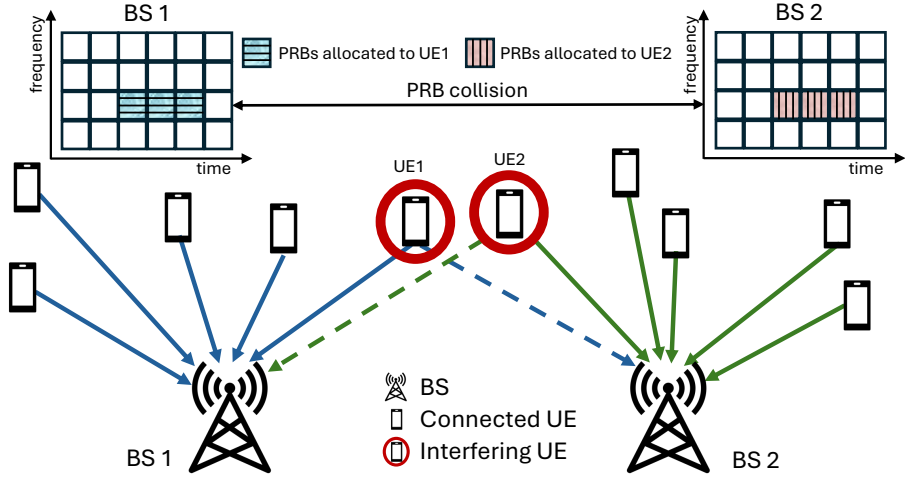


Figure 5.8: In-band UL interference overview (dashed lines).

degradation when experiencing Non-Line-of-Sight (NLOS) conditions with respect to their serving node. While this adjustment helps maintain reliable links, it can also lead to unintended interference in adjacent cells. Moreover, in scenarios involving directional UE transmissions, as in millimeter wave links, beamforming introduces an additional source of unpredictability. It can impact adjacent cells through strong sidelobes or, under highly dynamic conditions, even affect them with the main lobe. These conditions are often unknown a priori (e.g., at scheduling time), and can vary on timescales faster than a subframe (i.e., sub-ms). This calls for real-time interference detection to enable a prompt reaction across the protocol stack.

The impact of in-band UL interference extends beyond immediate signal degradation, and can disrupt protocol operations like scheduling and resource allocation at the gNB. To execute these operations, the gNB relies on quality indicators like RSRP and RSSI. However, interference distorts the gNB's assessment of UE channel conditions, introducing errors that propagate across multiple slots and affect both UL and DL transmissions. This disruption becomes particularly critical when interference affects control signaling (e.g., UCI) or DMRS used for channel estimation. Because of the inherently lower power of UL signals compared to DL transmissions, even interference at low power levels can significantly impair communication quality. This forces the gNB to allocate additional resources through retransmissions and more robust coding schemes, thereby reducing spectral efficiency and limiting overall user capacity. In scenarios with severe interference, connection drops can occur, underscoring the importance of developing and implementing robust interference detection and mitigation methods in practical deployments.

To address this challenge, this section presents InterfO-RAN, a real-time programmable solution that integrates a CNN within the gNB physical layer to process and analyze I/Q samples. The solution achieves interference detection with accuracy exceeding 91% in less than 650 μ s, enabling practical implementation in production cellular networks. Designed as a pluggable, programmable component, InterfO-RAN extends GPU acceleration to dApps for real-time CNN-based interference detection. It is integrated with the NVIDIA Aerial 5G NR PHY layer, following the emerging O-RAN dApp

paradigm [139] and aligning with AI-for-RAN use cases within the AI-RAN Alliance [149]. InterfO-RAN is implemented as a custom application embedded in the Aerial CUDA pipeline to access the necessary KPMs, including I/Q samples and channel quality data, and to allocate the computational resources required for proper execution. Comparable performance can also be achieved by deploying its intelligence within the dApp framework presented in Section 4.6.

We design, develop, and test InterfO-RAN on the X5G testbed, leveraging this real-world setup to collect data with and without interference from a deployment spanning two different buildings. More than seven million NR UL slots, together with artificially generated data in MATLAB, are used to train and test eight configurations of the CNN, employing Transfer Learning (TL) techniques as well. The selected solution is then evaluated OTA across various scenarios with different pairs of interfering RUs. Our results demonstrate the robustness of InterfO-RAN in detecting interference, achieving over 91% accuracy in less than 650 μ s, while imposing minimal strain on PHY operations.

The remainder of this section is organized as follows. Section 5.3.2 presents the system architecture overview. Section 5.3.3 provides some background on the Aerial framework. Section 5.3.4 describes the system design and implementation of the InterfO-RAN dApp, including details on the CNN and data pipelines. Section 5.3.5 outlines the experimental setup and data collection operations, while Section 5.3.6 discusses the results. Related work is reviewed in Section 5.3.7. Finally, Section 5.3.8 summarizes the main findings and outlines directions for future research.

5.3.2 System Architecture

Figure 5.9 illustrates our system architecture, where InterfO-RAN is integrated as a programmable dApp into the high-PHY of a 5G NR protocol stack. Specifically, we design the system to harness GPU resources available as part of the NVIDIA Aerial GPU-accelerated platform. Aerial already uses GPU to offload computationally intensive and time-sensitive high-PHY layer workloads, contributing approximately 85% of the overall computational complexity and processing demands in gNBs [191]. This architecture enables efficient resource sharing, allowing the dApp to perform inference with minimal computational overhead while preserving real-time processing capabilities. As explained in Section 5.3.4, InterfO-RAN is implemented through customized functions utilizing a CNN architecture, executed on a GPU for real-time interference detection. The output of InterfO-RAN is a binary indicator that denotes the presence of interference. Once interference is detected, different strategies can be put in place for mitigation (e.g., coordinated resource allocation), which are left for future work.

The system processes input features comprising a combination of raw I/Q samples within a slot carrying PUSCH data, along with RSSI, RSRP, the number of Code Block (CB) errors, the total count of CBs, SINR, MCS index, and MCS table index. The I/Q samples are extracted from the PUSCH physical channel, without any processing such as equalization, demodulation, or decoding. InterfO-RAN does not interfere with ongoing UL/DL processes, let alone PUSCH channel processes, while determining whether transmissions are affected by unwanted signals within the same frequency band.

Figure 5.9 further illustrates the UL interaction between gNB and UE, providing a comprehensive view of the data flow and the PUSCH channel engaged by InterfO-RAN. The PUSCH carries data, control information, and DMRS for channel estimation. The figure also highlights the other uplink channels, i.e., PUCCH, SRS, and Physical Random Access Channel (PRACH).

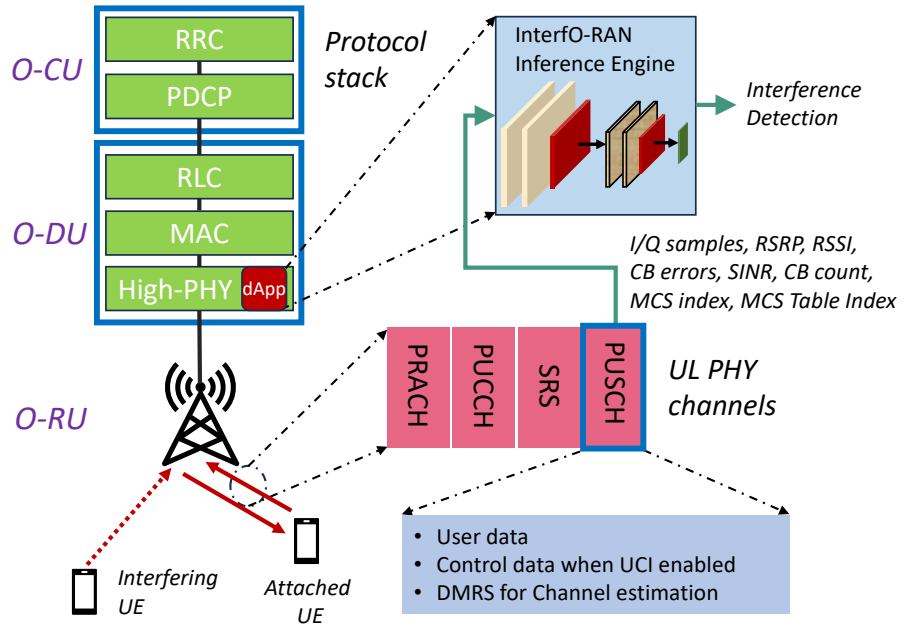


Figure 5.9: System Architecture.

In the next sections, we provide a preliminary overview of the GPU-accelerated framework for physical layer processing, and then detail how InterfO-RAN is designed and implemented in detail.

5.3.3 GPU-Accelerated Physical Layer Processing

This section provides a detailed overview of the framework we leverage as the basis for the InterfO-RAN implementation, as well as notions on the physical layer PUSCH.

5.3.3.1 NVIDIA Aerial Physical Layer

InterfO-RAN is embedded as a functional plugin in NVIDIA Aerial CUDA Baseband (cuBB), a SDK developed by NVIDIA that provides a 5G signal processing pipeline for GPUs, implemented in Compute Unified Device Architecture (CUDA) and C++ [151]. cuBB operates with slot-level granularity, with each slot lasting 500 μ s, aligned with a 30 kHz subcarrier spacing. InterfO-RAN complements cuBB with real-time, high-performance inference. NVIDIA Aerial uses a GPU for inline acceleration of resource-intensive tasks such as channel estimation, LDPC encoding/decoding, and channel equalization, among others.

From an implementation standpoint, cuBB combines several software components, which we extend to design and implement InterfO-RAN. The CUDA Physical layer (cuPHY) controller serves as the primary coordinator, initializing GPU resources and creating the initial context for RU connections. During OTA UL/DL transmissions, the L2 adapter within the cuPHY controller translates control plane messages from the SCF FAPI interface into slot commands for PHY-layer data traffic. These commands are processed by the cuPHY controller, converted into tasks, and assigned

to specific UL and DL channel worker threads. Mapped to appropriate CPU cores, these threads delegate computational tasks to the GPU. Each thread represents a physical channel implemented as a pipeline, with operations executed on CUDA kernels. CUDA kernels are functions executed in parallel on a GPU. The pipeline is supported by APIs provided by the cuPHY library, invoked by the cuPHY driver to manage creation, configuration, and execution.

5.3.3.2 PUSCH Operations

InterfO-RAN focuses on the UL receive path, particularly the PUSCH, to detect interference. UL processing starts with slot configuration from the L2 layer and ends with UL signal processing. Among UL channels (PUSCH, PUCCH, PRACH, SRS), InterfO-RAN analyzes the PUSCH, the primary UL channel for data transmission, to detect interference from other UEs sharing the same radio resources.

PUSCH transmissions are dynamically scheduled by the gNB, which allocates frequency and time resources based on real-time network conditions. The resource allocation is signaled to the UE through Downlink Control Information (DCI) messages, specifying parameters such as MCS, resource block allocation, and transmission power [192]. The PUSCH channel in cuBB is implemented as a pipeline, for operations such as Resource Element (RE) demapping, channel estimation, channel equalization, de-rate matching, de-layer mapping, de-scrambling, LDPC decoding, and Cyclic Redundancy Check (CRC) checks for both CBs and Transport Blocks (TBs). Additionally, it includes processing for UCI on PUSCH and transform precoding, if enabled, executed through individual CUDA kernels. Specialized kernels also manage Timing Advance (TA) and Carrier Frequency Offset (CFO).

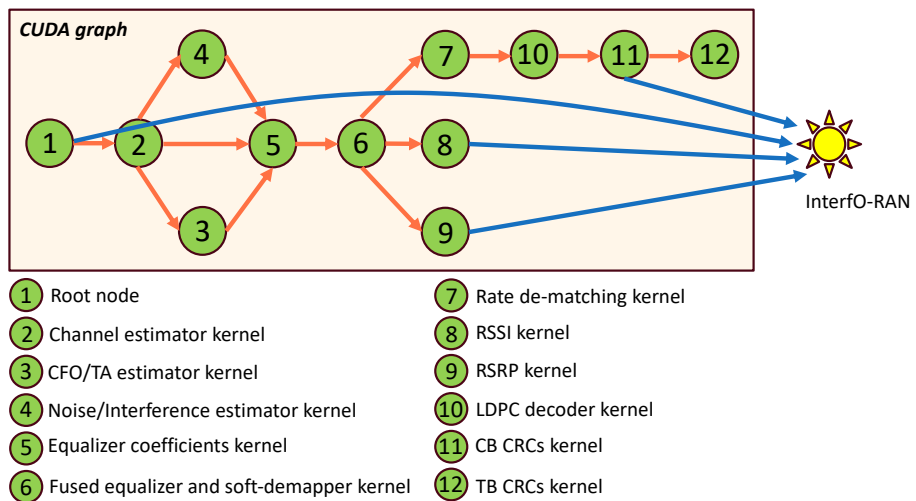


Figure 5.10: InterfO-RAN as a post-processing component following the PUSCH CUDA graph, where each node represents a CUDA kernel.

This pipeline is further optimized and structured using an advanced feature known as CUDA graph, which represents an acyclic graph where nodes correspond to kernels, and edges define

their inter-dependencies, as illustrated in Figure 5.10. This graph-based architecture effectively delineates the intricate workflow of kernel operations, enabling the management of dependencies within the graph itself. By facilitating the concurrent launch of all kernels as a unified entity, the GPU autonomously oversees the execution process, thereby reducing the necessity for continuous CPU intervention. This method significantly enhances temporal efficiency by minimizing launch overhead, which is the latency associated with initiating CUDA kernels.

5.3.4 InterfO-RAN Design and Implementation

We design and implement InterfO-RAN on top of the NVIDIA Aerial SDK, leveraging the spare capacity of the GPU to execute the CNN-based dApp. As discussed in detail in the results analysis in Section 5.3.6, the typical execution of the PHY layer in cuBB utilizes at most 50% of the GPU resources, leaving substantial computational capacity available for additional tasks. This excess capacity enables InterfO-RAN to take advantage of the remaining GPU resources for interference detection. In doing this, however, it becomes necessary to design the dApp to efficiently access the available resources and to avoid interfering with real-time processing constraints of the gNB physical layer.

5.3.4.1 dApp Design and PHY Integration

Design and Implementation Challenges. To design and integrate InterfO-RAN within the 5G NR GPU-accelerated PHY, we addressed the following challenges. First, the dApp needs to access information available across different processing steps of the PUSCH pipeline (i.e., I/Q samples, RSRP, RSSI, the sum of CB CRC errors, count of CBs derived from CB CRCs, SINR, MCS Index and MCS table index). This can amount to 183,484 bytes for each UL transport block, thus requiring an efficient mechanism to expose such information. Second, the CNN needs to return results in less than a millisecond (i.e., a 5G NR subframe) to make sure that the output is relevant to take further decisions across the stack. Therefore, the GPU-based implementation needs to be efficient in running inference with the provided input. In addition, there may be a need to support different models or configurations for the AI processing, thus managing the lifecycle of the overall model. For these reasons, we select ONNX Runtime (ORT) as the provider, making it possible to efficiently deploy trained models on the GPU-based dApp. At the same time, ORT requires a significant loading and configuration time the first time it is executed. In general, as part of our design, it is important to avoid disrupting operations of the rest of the physical layer, thus guaranteeing that the timing of any operation within the dApp does not affect physical layer processing. Finally, for development purposes, the InterfO-RAN implementation needs to enable automated data collection and labeling, to streamline the gathering of samples for the training of AI models.

InterfO-RAN System Structure. As the core component of InterfO-RAN, the inference module functions as a post-processing unit following the execution of the PUSCH pipeline, ensuring that ongoing UL/DL pipeline processes remain unaffected, as illustrated in Figure 5.10. This functionality is efficiently implemented through the function `CuPhyInferCuDnn()`—a customized API hosted by cuPHY and managed by the cuPHY driver, as indicated in Figure 5.11. This API further employs the `Session.Run()` method from the ORT framework to execute the actual inference process. To prevent InterfO-RAN from interfering with the tightly time-coupled operations of the PUSCH or

other channels, the cuPHY driver delegates the processing to a newly instantiated and independent CPU thread. This thread is assigned to a dedicated CPU core—isolated from other operations—to improve stability.

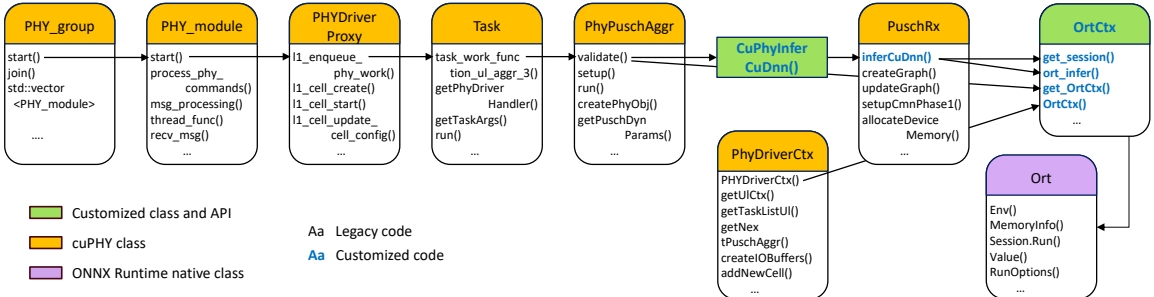


Figure 5.11: The workflow diagram for the OrtCtx class for performing inference.

ORT Integration and Tuning. ORT is built to execute models in the ONNX format, which is an open standard for representing ML models. AI operations using ORT can be executed on either the CPU, utilizing the CPU execution provider, or on the GPU, utilizing CUDA or TRT execution providers. Our implementation supports all three options, with processing latency shown in Table 5.3, for inference using standalone ORT (i.e., independently of the dApp implementation) and the model discussed in Section 5.3.4.2. CPU-based inference takes approximately 30.354 ms for a 24-core Intel Xeon Gold CPU, while GPU-based inference using TRT and CUDA takes 0.524 ms and 3.675 ms using an NVIDIA A100, respectively.

Table 5.3: Inference time between different execution providers for standalone ORT.

ORT Execution Provider	CPU	CUDA	TensorRT
Inference Time [ms]	30.354	3.675	0.524

Although both CUDA and TRT utilize the GPU for inference tasks, TRT is specifically optimized for high performance. NVIDIA TRT is an SDK for deep learning model optimization, featuring an inference optimization engine and runtime environment. As evidenced in Table 5.3, it achieves lower execution times than both CPU and CUDA providers. The framework parses the ONNX model, applies optimizations such as layer fusion, and selects efficient CUDA kernels by leveraging libraries like CUDA Deep Neural Network library (cuDNN) and CUDA Basic Linear Algebra Subroutines (cuBLAS). Consequently, TRT is used exclusively in our experiments to maximize performance.

Based on our measurements, however, the GPU-based ORT mode comes with a significant delay during initial execution—1.25 s and 9.65 s with CUDA and TRT, respectively—for the model described in Section 5.3.4.2. These findings identify the root cause of the timing issue as the long GPU warm-up phase. This is because ORT requires several seconds to initialize and allocate GPU resources essential for inference. In particular, during the first call to `Session.Run()`, ORT performs several critical setup steps: (i) Memory allocation for the model tensors; (ii) Graph optimization and compilation to ensure efficient runtime execution; (iii) Execution provider setup, such as configuring CUDA for GPU inference; and (iv) Caching mechanisms for future executions.

This warm-up latency conflicts with the strict timing constraints of the UL slot in 5G NR systems, making it a challenge for real-time execution. However, once initialized, these setup steps are cached, allowing subsequent invocations to bypass the preparatory steps and run significantly faster.

PHY Layer and dApp Setup. Therefore, we design the InterfO-RAN dApp so that it performs an initial warm-up inference before the base station becomes operational. Particularly, during the initialization of cuBB, a preliminary inference step is performed on dummy data encompassing all input features. Then a pointer to the ORT run session (already initialized) is passed to InterfO-RAN. To support this, InterfO-RAN is encapsulated within a customized ORT context class, `OrtCtx`, which is instantiated within the cuPHY driver context class, `PhyDriverCtx`, as illustrated in Figure 5.11. This manages instances of transmit and receive processing pipelines for UL and DL slots, as well as individual classes corresponding to each PHY channel, among others. Additionally, it handles the allocation of GPU resources and manages the GPU footprint for all UL and DL executions. `PhyDriverCtx` is instantiated as the whole physical layer instance starts, making it possible to execute the warm-up phase for ORT.

As part of this process, the `OrtCtx` class constructor initializes and configures the dynamically allocated instance of an ORT inference session as a smart pointer, using the native ORT API and leveraging its comprehensive classes and methods, as shown in Figure 5.11. The process starts with creating an `Ort::Env()` object for logging and runtime management, followed by configuring session options for optimization, including graph processing, threading, memory allocation, and GPU-specific settings for CUDA and TRT. The dummy input data for warm-up inference is allocated in CPU memory and transferred to the GPU for execution, encapsulated as `Ort::Value()` tensors. `Session.Run()` processes the data through the pre-trained ONNX model and generates output tensors containing class probabilities, selecting the highest probability as the final prediction.

Runtime Inference. Upon initialization, the `OrtCtx` object is passed to the PUSCH channel via the physical PUSCH aggregate class, `PhyPuschAggr`, and invoked during the validation phase as a callable function, `get_OrtCtx()`. This validation phase is a post-processing step always executed after the PUSCH pipeline. Inference in the PUSCH pipeline is orchestrated by `inferCuDnn()`, a member of `PuschRx` class, and invoked by `CuPhyInferCuDnn()` API, as illustrated in Figure 5.11. It retrieves the inference session from the `OrtCtx` object via `get_session()`, reusing the session configuration and runtime environment. We encapsulate input features into ONNX-compatible tensors using `ort_infer()`, using GPU memory for CUDA/TRT or CPU memory otherwise. When performing inference on the GPU, the input features are transferred directly within GPU memory without overhead. Tensors follow predefined shapes and types, with input/output names built dynamically for runtime flexibility.

dApp-based Automated Data Collection. We also designed the InterfO-RAN dApp to perform automated data collection to create datasets for offline model training. This leverages a `CuPhyInferCuDnn()` API to stream data into an Hierarchical Data Format version 5 (HDF5) file at a frequency of one every 10 UL slots. Different from what happens for online inference, the API asynchronously transfers features to be stored from GPU to CPU and writes to disk thereafter. This avoids many GPU operations, including data conversion to tensors and subsequent GPU memory deallocation. Besides, to avoid interference with the tightly coupled operations of PUSCH or other channels, the cuPHY driver delegates data logging to a newly instantiated CPU thread operating in detached mode, ensuring uninterrupted processing.

5.3.4.2 AI-Based Interference Detection

InterfO-RAN leverages a CNN for real-time interference classification, using a data-driven methodology that allows the network to identify complex patterns in incoming UL data.

Input Features. As discussed above, the input features include I/Q samples for the PUSCH, as well as additional KPMs representing RSSI, RSRP, SINR, MCS index, MCS table index, total count of CB errors, and number of CBs derived from CB-CRCs. As part of the dApp design, one challenge was ensuring the compatibility of heterogeneous numerical formats, such as *float16* (for I/Q), *float32* (for RSSI, RSRP, SINR), and *int32* (for MCS and CB inputs), across frameworks such as Tensorflow (TF) (offline training) and cuBB.

Unlike traditional approaches that rely on heatmaps of I/Q samples for interference detection [193, 194], InterfO-RAN processes raw I/Q data directly and incorporates additional features to improve classification accuracy. I/Q samples are extracted prior to the Minimum Mean Square Error (MMSE)-Interference Rejection Combining (IRC) equalizer, which is designed to mitigate channel distortion and interference. This pre-equalization extraction provides an unaltered view of interference effects, allowing for more accurate analysis. In cuBB, the PUSCH channel I/Q samples are stored as 32-bit words (with two 16 bits floats for each component), in blocks of $14 \times 273 \times 12$ contiguous words, where 14 is the number of symbols per slot, 273 is the maximum number of PRBs with 12 subcarriers each. ORT converts the I/Q samples into a matrix with dimensions 14, 3276, 2, to align with TF's expected format for inference, interpreting the third dimension as the real and imaginary components of the I/Qs.

Additionally, specific input features are transformed to ensure data compatibility. In the native CB-CRC CUDA kernel, the CB errors for each PUSCH channel are output as an array, where each non-zero value represents a corrupted CB within the TB, resulting in a dynamic size. To meet the fixed-size input requirements of the learning model, two additional variables are added to the GPU: one to determine the number of corrupted CBs in a TB and another to find the total number of CBs. These operations are seamlessly integrated into the kernel 11 in Figure 5.10.

CNN Architecture. We choose CNNs for their ability to extract complex patterns from OFDM-based IQ samples and their consistent outperformance of alternatives like LSTMs and ResNets. Figure 5.12 illustrates the selected architecture. The network features seven layers. Two convolutional blocks perform feature extraction on PUSCH I/Q samples, each containing two Conv2D layers (128 and 256 filters, 3×3 kernel, ReLU activation) and one 2×2 MaxPooling layer. Then, the extracted features are flattened and concatenated with the additional normalized structured inputs (i.e., RSSI, RSRP, SINR, MCS index, MCS table index, total count of CB errors, and number of CBs). This final representation is processed through a fully connected Dense layer with softmax activation, which performs the final interference detection. The starting point of our proposed CNN is the VGG16 model, a widely recognized architecture in image processing. We systematically reduced its depth and identified a two-block variant that provided the best trade-off between computational efficiency and classification performance.

To enhance generalization and mitigate overfitting, we integrate dropout layers and an L2 regularizer. Dropout layers randomly deactivate neurons during training, encouraging the model to learn underlying patterns rather than memorizing the training data, while the L2 regularizer penalizes large weights, promoting simpler, more generalized models. Additionally, to address class imbalances (e.g., in case of data collections with different number of samples for different radios,

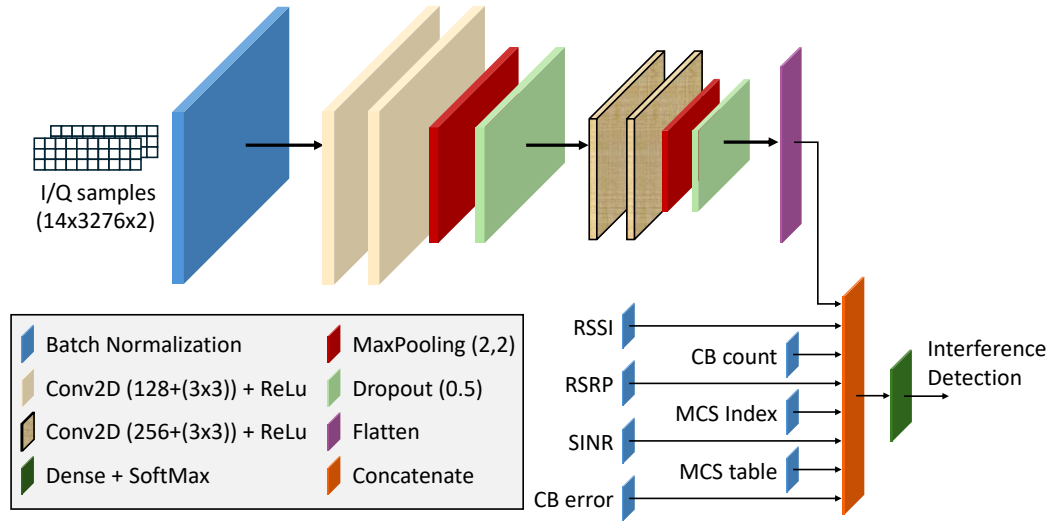


Figure 5.12: InterfO-RAN’s CNN architecture showing inputs (I/Q and scalar features), layer specifications, and the binary interference detection output.

or interference conditions), we use a weighted loss function instead of a standard one, which tends to favor the majority class. By assigning a greater weight to the minority class, the loss function ensures that its contributions have a stronger influence on the overall loss computation.

Transfer Learning. We employ TL using heterogeneous datasets from diverse RF environments, detailed in Section 5.3.5.1, to enhance model generalization capabilities. TL is a machine learning technique wherein knowledge acquired from a source domain is leveraged to improve performance on a target domain through model adaptation. In our implementation, we partially fine-tune the foundational CNN model (Figure 5.12), trained on data from multiple deployment locations (see Figure 5.13), and then tune to specific deployments by freezing the first block and fine-tuning the remaining layers with site-specific data. Thus, we allow the model to learn from a broader range of conditions and fine-tune it for a specific deployment, retaining knowledge of diverse scenarios by preserving foundational feature representations and enhancing performance.

5.3.5 Data and Evaluation Framework

This section presents the setup for the training, testing, and evaluation of InterfO-RAN, from the generation of synthetic data with simulations to experimental OTA data collection and evaluation. We also discuss preprocessing and offline training procedures. Real-world data collection, experiments, and validation of InterfO-RAN are all performed using the X5G platform.

5.3.5.1 Empirical OTA Data Collection, Automated Labeling, and Preprocessing

All experiments involving interference are conducted in a controlled indoor environment within the Northeastern University EXP building in Boston, MA, as depicted in the indoor experiment map shown in Figure 5.13a. The layout includes: two cell sites (shown in light blue and pink regions), where the corresponding UEs can be located; the RU locations for each cell site, with only one

active at a time per site (represented by blue and red icons); and the two primary UE locations for the two cell sites, where most of the data is collected (violet and green icons). Each experiment involves both cell sites and one UE per cell at a time, tested under Line-of-Sight (LOS) and NLOS channel conditions. Similarly, we collected additional data in a second indoor environment within the Northeastern University ISEC building in Boston, MA, (Figure 5.13b).

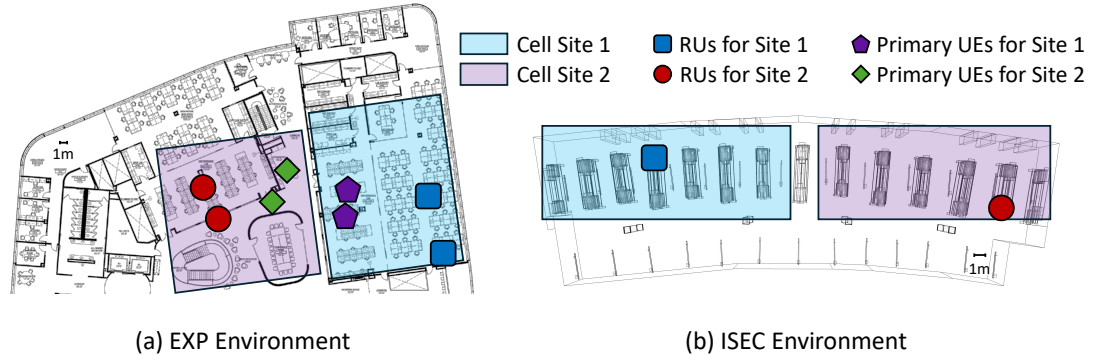


Figure 5.13: Indoor experiment layout maps of Northeastern University EXP (a) and ISEC (b) buildings, showing: the designated regions for the two cell sites, where the corresponding UEs can be located; RU locations for each respective cell site; and primary UE locations, where most of the data is collected.

During each data collection session, the UE connects to its RU and generates UL traffic using iPerf. We categorize the gNBs traffic levels into two distinct classes—High Traffic and No Traffic—based on the TB size, to improve interference identification accuracy. In the No Traffic scenario, the UE remains connected to the gNB while exchanging minimal control information necessary for maintaining the connection stability. In this case, we observe that the TB size is typically around 185 bytes and does not exceed 1056 bytes, with the number of CBs limited to one. The CBs from a TB are segmented and LDPC-encoded using base graphs defined by the 3GPP for error correction. LDPC base graph 2 is used for smaller CBs, with each CB sized at 480 bytes, while base graph 1 is used for larger ones, with each CB sized at 1056 bytes. In contrast, High Traffic UL transmissions produce sufficiently strong signals that can interfere with neighboring cells. In this scenario, the TB size typically exceeds 1056 bytes, and the number of CBs is greater than one.

As depicted in Figure 5.14, there is a strong correlation between the TB size and the number of CBs (Figure 5.14a), as well as between the UL throughput and the CB count (Figure 5.14b), reinforcing the decision to use the CB count as the primary criterion for traffic classification. Building upon this, we create a systematic labeling methodology based on the UL traffic levels to classify the UL transmissions as either affected by interference ('INTERF') or unaffected ('CLEAN'). The labeling rules, shown in Table 5.4, are defined as follows:

- No Traffic/High Traffic: if one UE transmits with 'High Traffic' while the other has 'No Traffic', the 'High Traffic' time windows on one side are used to label the other side as being affected by interference, designated as 'INTERF', while the transmitting side is labeled as 'CLEAN'.

- High Traffic on both sides: if both UEs transmit simultaneously to different RUs with 'High Traffic', the corresponding samples are labeled as 'INTERF'.
- No Traffic on both sides: if both UEs are transmitting with 'No Traffic', the samples are labeled as 'CLEAN', i.e., no interference.
- Single-active Transmission: if only one UE transmits while the other remains in airplane mode (i.e., not connected to the base station), the samples are labeled as 'CLEAN'.

A threshold of 1 is set for the CB count in an UL slot to identify high-traffic windows on one gNB, which are subsequently used to mark instances of interference on the other gNB. Notably, the exact thresholding mechanism is utilized to evaluate inference performance in OTA data scenarios by identifying high-traffic time windows, which are then used to assign ground truth labels of 'CLEAN' or 'INTERF' to each input example, thereby enabling the effective monitoring of spectrum sensing capabilities.

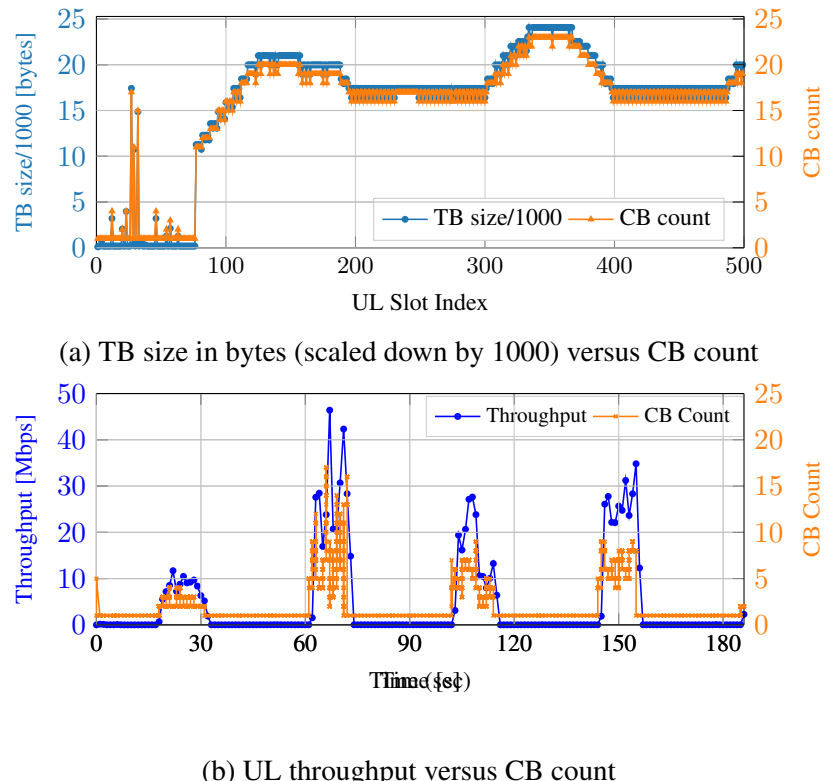


Figure 5.14: UL throughput, TB size, and CB count across different scenarios, demonstrating their close correlation.

To efficiently manage GPU memory during offline training—particularly given the relatively large input feature consisting of 3D I/Q samples of size $14 \times 3276 \times 2$ —we use TF's Sequence class to implement a custom data generator. The data generator dynamically loads small batches into

Table 5.4: Lookup Table for gNB UL Traffic and Labels

gNB1 Traffic	gNB2 Traffic	gNB1 UL Label	gNB2 UL Label
High Traffic	No Traffic	CLEAN	INTERF
No Traffic	High Traffic	INTERF	CLEAN
High Traffic	High Traffic	INTERF	INTERF
No Traffic	No Traffic	CLEAN	CLEAN
No UE	No/High Traffic	NA	CLEAN
No/High Traffic	No UE	CLEAN	NA

GPU memory, rather than loading the entire dataset at once, thereby optimizing memory usage and avoiding excessive memory strain.

5.3.5.2 Synthetic Data

We also perform an extensive data collection campaign using the NVIDIA Aerial simulator `nr_sim`, which complements the cuBB framework by extending the 5G MATLAB Toolbox. Through this, we collect data and evaluate the model in a larger variety of configurations compared to those supported in our experimental setup. The parameters that we sweep include SNR, Signal to Interference Ratio (SIR), MCS index, channel type, delay profile, interference channel delay profile, numerology, and carrier frequency. In addition, we simulate up to 5 interfering UEs, so that the classification can be extended to include additional UEs.

To simulate interference, an in-band interference signal is artificially generated by transmitting OFDM signals from each antenna independently through a Tapped Delay Line (TDL) channel characterized by high delay spread and Doppler shift. These conditions emulate a dynamic and realistic environment affected by multipath propagation and high mobility, thus creating a robust testbed for interference mitigation. The processed signal is then multiplied by a modified all-zero matrix with randomly distributed contiguous ones, introducing localized and burst interference in the REs of the OFDM slot. This process ensures random patterns for contiguous ones across antenna streams while maintaining the average power of the interference signal. The resulting combination of randomized interfering signals, thermal noise, and received OFDM signal at the gNB closely mimics real-world interference effects.

5.3.6 Performance Evaluation and Experimental Results

This section presents experimental results to benchmark the performance of InterfO-RAN across various model configurations, using the simulation setup described in Section 5.3.5.2 as well as over OTA tests.

We test the model, shown in Figure 5.12, on synthetic data with scenarios involving 0 to 5 interferers, totaling 13800 samples per class, to ensure consistent performance across different parameters described in Section 5.3.5.2 before OTA deployment in InterfO-RAN. The resulting confusion matrix in Figure 5.15 indicates that the model achieves high accuracy (above 96%) for scenarios with no interferer and 2 or more interferers. For scenarios with a single interferer, accuracy remains solid at 93.87%, with the slight drop likely due to the lower impact of a single interferer on

the signal. Thus, the model becomes a strong candidate for OTA deployment, along with several other models with minor modifications explained in Section 5.3.6.1.

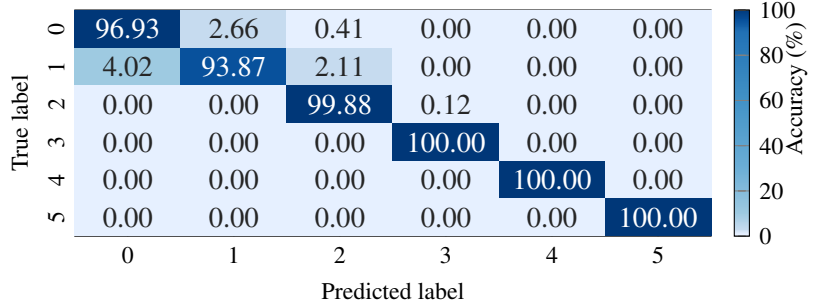


Figure 5.15: Confusion matrix of the model tested on synthetic data with 13800 samples per class.

5.3.6.1 OTA Evaluation

To select the best generalized model suitable for diverse RF environments, we conduct a series of OTA experiments evaluating eight configurations of the underlying CNN architecture shown in Figure 5.12. We represent each model as $\{[\alpha, \beta], \gamma\}$, where α and β denote the number of filters in the convolutional layers of the first and second blocks, and γ represents the batch size. We select two configurations for $[\alpha, \beta]$: [64, 128] and [128, 256], inspired by VGG16’s first blocks for a lightweight model, with γ ranging over 16, 32, 64, and 128.

We carry out experiments at various RU locations and UE positions across the map, as shown in Figure 5.13. For fair comparability, we evaluate different models using the same dataset with data logging. The data collected from one side is labeled with ground truth based on the traffic level on the other side, as detailed in Table 5.4. We then compute metrics such as accuracy, measuring the ratio of correctly predicted samples to the total number of samples, specificity, evaluating the identification of ‘CLEAN’ examples, and recall, assessing the detection of ‘INTERF’ examples.

Figure 5.16 compares accuracy, specificity, and recall for TL models, described in Section 5.3.6.2, tested in a familiar RF environment (Figure 5.16a), and an unseen RF environment (Figure 5.16b), to evaluate generalization capabilities. We select the $\{[128, 256], 32\}$ model as the best-performing configuration, based on its strong results in familiar settings (96.12% accuracy, 94.92% specificity, and 99.31% recall) and its superior generalization in the unseen RF environment (91.33% accuracy, 90.97% specificity, and 91.40% recall), outperforming the other model configurations.

5.3.6.2 Impact of Transfer Learning

We evaluate InterfO-RAN performance across various RF configurations to assess the impact of the TL method on the model. We use ISEC dataset (Figure 5.13b), dominated by High Traffic instances on both sides, as the foundational model for TL, then fine-tuned on the EXP dataset (Figure 5.13a), detailed in Section 5.3.4.2, which contains sufficient data for all traffic instances, as described in Table 5.4. Additionally, we train a baseline model using only the EXP dataset, and compare both performances to assess the benefits of TL.

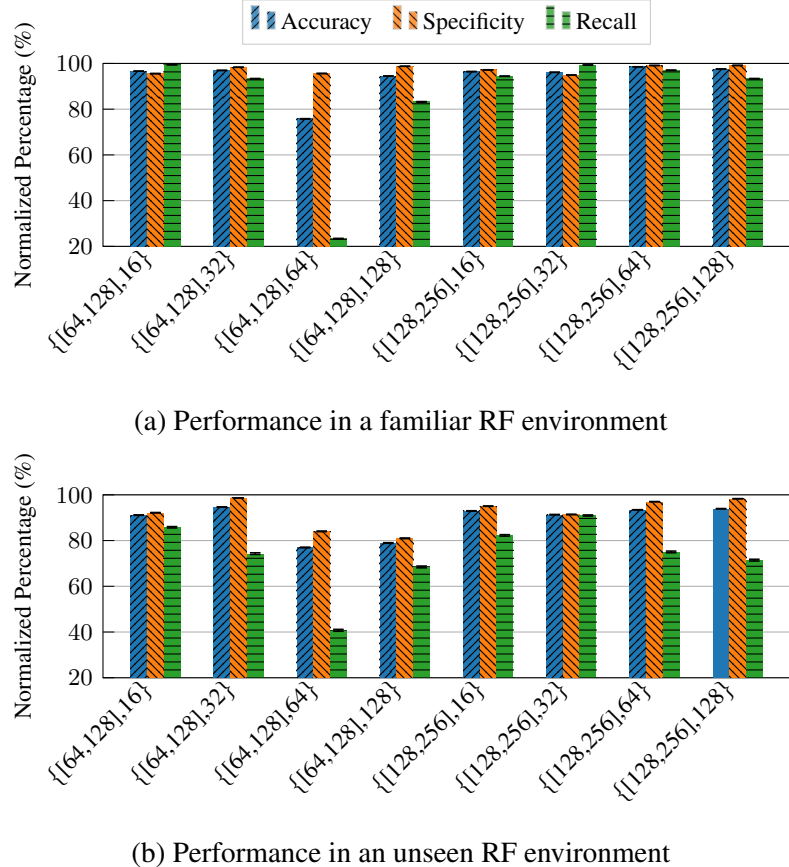


Figure 5.16: Model performance (accuracy, specificity, and recall) for Transfer Learning: (a) familiar RF environment and (b) unseen RF environment to evaluate generalization.

Figure 5.17a shows the confusion matrix of the baseline model without TL, tested in a familiar RF environment using the same pair of RUs locations as in the training. In contrast, Figure 5.17b and Figure 5.17c present the performance of the TL model, evaluated both in the same familiar RF setting as the non-TL model, and in a new set of RU locations, i.e., an unseen environment. The TL model achieves overall better performance in detecting interference when tested in both a familiar (+10.52%) and unseen (+2.24%) RF. However, it is outperformed by the non-TL model in No Traffic scenarios, with performance drops of -2.11% in the familiar and -5.63% in the unseen one, likely due to the influence of the foundational model.

5.3.6.3 Timing and Power Benchmarking

We assess InterfO-RAN's robustness by analyzing its inference time, GPU utilization, and power consumption, both with and without it.

Analysis of Inference Time. Figure 5.18a shows the temporal variation of the inference time using a 5-instance moving average between No (before 24 s) and High Traffic (after 24 s), while Figure 5.18b presents the corresponding CDF. We observe fluctuations during high-traffic scenarios,

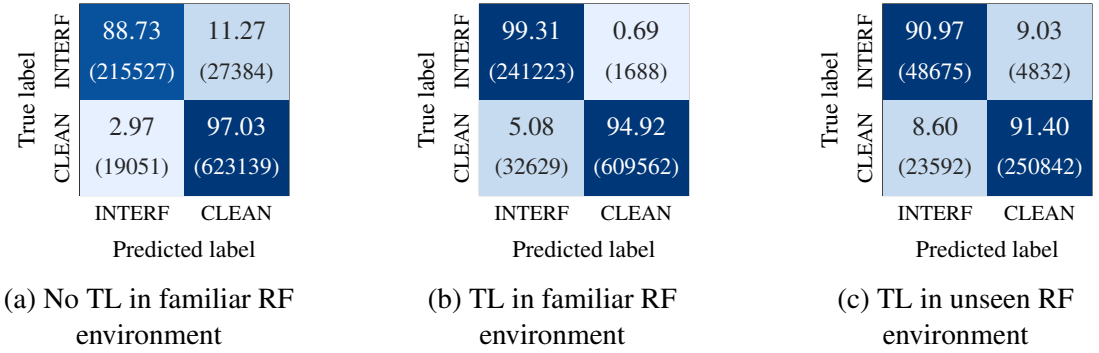


Figure 5.17: Classification accuracy (percentage, sample count) with and without TL across different RF environments: (a) no TL in a familiar environment, (b) TL tested in a familiar environment, and (c) TL tested in an unseen environment, using the same color bar as Figure 5.15.

when InterfO-RAN performs more frequent inferences, likely due to the increased number of operations and contention for GPU resources. However, the system maintains overall stability, effectively managing workload distribution. Additionally, Table 5.5 shows the average inference time for different model configurations, varying with filter counts. We notice a $220\ \mu\text{s}$ improvement in the smaller configuration due to the reduced computational complexity.

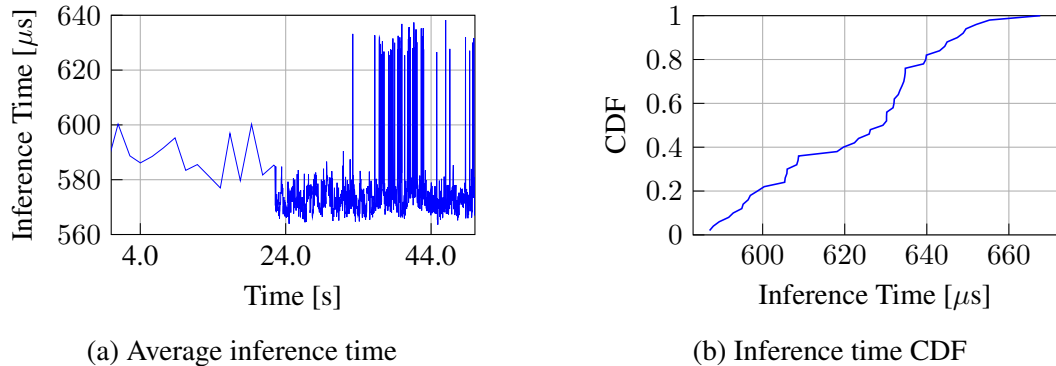


Figure 5.18: Inference time from first iteration: (a) temporal variation with a 5-instance moving average with No (before 24 s) and High Traffic (after 24 s), (b) inference time CDF.

Analysis of GPU Utilization and Power. Figure 5.19a and Figure 5.19b compare A100 GPU utilization and power draw with and without InterfO-RAN in the same end-to-end scenario. During the warm-up phase (see Section 5.3.4), GPU usage spikes to 21.2% (vs. 3.3% without InterfO-RAN), and the power rises to 82.73 W (vs. 61.79 W). In other phases, power remains similar, except in High Traffic conditions, where it increases from 63.83 W to 66.13 W and a higher standard deviation (1.77 vs. 0.67) when using InterfO-RAN. We conclude that InterfO-RAN effectively balances the workload without straining RAN operations, while leveraging TRT optimizations.

Table 5.5: Average inference times across different models.

Model Configuration	$\{[64,128],\text{any}\}$	$\{[128,256],\text{any}\}$
Inference Time [μs]	401.8	621.6

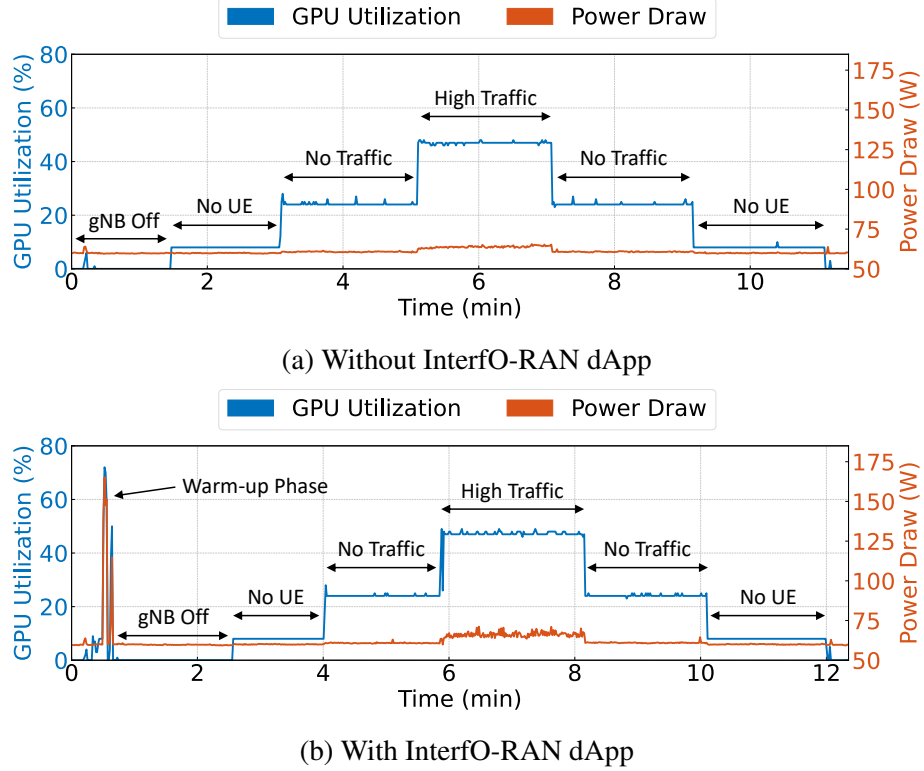


Figure 5.19: GPU utilization (blue) and power draw (orange) comparison with and without InterfO-RAN dApp.

5.3.7 Related Work

Limited research has been conducted on UL interference in 5G NR within real-time timescales and tested on real-world testbed environments. Existing literature predominantly relies on simulations to predict the presence of interference. For instance, [195] and [196] detect intermodulation interference in 5G NR using linear regression and CNNs, respectively. Similarly, [193] and [194] detect LTE UL interference using a novel approach that preprocesses time-domain signals into spectral waterfall representations and addresses the problem using an image classification CNN. Additionally, authors in [197] identify interference among IEEE 802.11b/g, IEEE 802.15.4, and IEEE 802.15.1 using a deep CNN.

In the context of spectrum monitoring, [198] develops a CNN for wireless signal identification, while [199] applies logistic regression to detect co-channel interference between LTE and WiFi users, though both approaches still lack validation beyond simulations. The authors of [200] propose a

framework based on CNNs to sense and classify wideband spectrum portions, supported by real-world data collection and testing. Several studies are conducted to characterize interference signals in various scenarios, such as [201], which addresses downlink interference in massive MIMO 5G macro-cells using geometric channel models, and [202], which focuses on modeling interference at higher frequencies for 6G networks. Furthermore, [203] and [204] discuss interference mitigation mechanisms. The former focuses on angular-based exclusion zones and spatial power control in mmWave frequency ranges, while the latter employs supervised learning-based Interference Whitening (IW) selection methods. InterfO-RAN differs from these approaches by implementing end-to-end interference detection on a GPU-based RAN node, tested in real time on a production-ready testbed, processing raw I/Q samples directly within the physical-layer pipeline.

5.3.8 Summary

This section presented InterfO-RAN, a GPU-accelerated O-RAN dApp that detects in-band UL interference with over 91% accuracy at sub-millisecond speeds (650 μ s). This solution leverages a CNN to analyze I/Q samples directly within the gNB physical layer, demonstrating seamless integration with both NVIDIA Aerial’s 5G NR stack and OAI on the X5G platform.

From the perspective of the research dimensions introduced in Chapter 1, InterfO-RAN validates the *use case* one by demonstrating interference detection on the X5G physical platform. Additionally, *realism* is shown through extensive OTA data collection and testing across multiple indoor environments under realistic interference conditions, while *usability* is demonstrated through the data-collection and labeling pipelines that enable rapid model development and deployment.

Future work on InterfO-RAN includes exploring scalability to higher UE densities and mobility scenarios, repurposing it for Angle of Arrival (AoA) estimation/5G positioning, implementing interference mitigation via resource allocation tuning to enhance performance, and developing online training capabilities allowing the CNN to adapt continuously to specific RF environments and scenarios.

5.4 ORANSlice: Dynamic Resource Management

The previous sections demonstrated real-time dApp use cases operating at sub-millisecond timescales for ISAC and interference detection. This section explores a complementary capability of the X5G platform: near-real-time control via the O-RAN near-real-time RIC. ORANSlice is an open-source network slicing framework that extends OAI to support 3GPP-compliant RAN slicing with xApp-based control. In this work, we integrate ORANSlice with the OSC near-real-time RIC deployed on X5G and validate slice-aware resource management with commercial UEs and realistic traffic patterns, showcasing a complete, standards-compliant slicing solution that integrates with the broader O-RAN ecosystem and operates on a production-ready OTA testbed.

5.4.1 Introduction

Network slicing has been identified as a key technology to deliver bespoke services and superior performance in 5G networks. Specifically, RAN slicing makes it possible to dynamically allocate a

certain amount of RAN resources, e.g., PRBs, to each slice based on their Quality of Service (QoS), current network conditions, and traffic load.

The importance of network slicing is emphasized by the O-RAN ALLIANCE, which has defined it as a critical use case and technology in the context of Open RAN systems [205]. The O-RAN architecture foresees network slicing in the RAN, controlled through an xApp deployed on the Near-RT RIC. The latter is connected to the RAN through the E2 interface, whose functionalities can be specified through SMs. For slicing, the E2 Service Model (E2SM) Cell Configuration and Control (E2SM-CCC) [206] allows for near-real-time adaptation of slicing parameters via xApps [207].

Despite the potential of network slicing, which has generated tremendous momentum and technological advancements, practical deployment of RAN slicing in commercial 5G networks remains largely unrealized. Numerous studies and research have demonstrated the benefits of RAN slicing, exploring various aspects, including the use of optimization [188] and AI-based solutions [208]. However, most existing RAN slicing implementations are confined to research environments and bench setups.

Contributions. With ORANSlice, we advance the state of the art by developing and implementing network slicing models compliant with both 3GPP and O-RAN specifications. First, we extend the OAI 5G protocol stack to support RAN slicing, redesigning the original proportional-fair scheduler into a two-tier radio resource scheduler that operates at both slice and UE level. We also develop multi-PDU support for the OAI softwarized 5G UE (nrUE), enabling multiple concurrent slices on the same device. Second, we implement an E2SM-CCC-based service model and RAN slicing xApp for closed-loop control via the Near-RT RIC. Third, we conduct extensive testing and validation on Arena [29] and X5G [20], demonstrating that ORANSlice can enforce and control slicing policies with both COTS 5G modules and softwarized UEs, and across different radio devices and Near-RT RICs. By releasing ORANSlice as open source, we provide the community with a 3GPP- and O-RAN-compliant RAN slicing framework that can serve as a reference design for future research and experimentation.²

Organization. The remainder of this section is organized as follows. The overview of network slicing is given in Section 5.4.2. The details of the developed software components in ORANSlice are elaborated in Section 5.4.3. The testbeds and experiment results are presented in Section 5.4.4. Finally, Section 5.4.5 discusses related work, and we conclude in Section 5.4.6.

5.4.2 Network Slicing Background

A network slice is an end-to-end logical network spanning both RAN and CN. It can be dynamically created and configured to provide bespoke services to serve a diverse set of applications and use cases. In a cellular network, each network slice is uniquely identified by a Single Network Slice Selection Assistance Information (S-NSSAI), which consists of a Slice/Service Type (SST) and a SD. SST is an 8-bit mandatory field identifying the slice type. SD is a 24-bit optional field that differentiates among slices with the same SST. It is worth noting that the same UE can be subscribed to up to 8 slices, which benefits applications with varying network requirements.

RAN Slicing. Radio resources are organized in a time and frequency grid (Figure 5.20). Each grid element, referred to as a PRB, is used to schedule UE transmissions and to broadcast control

²<https://github.com/wineslab/ORANSlice>

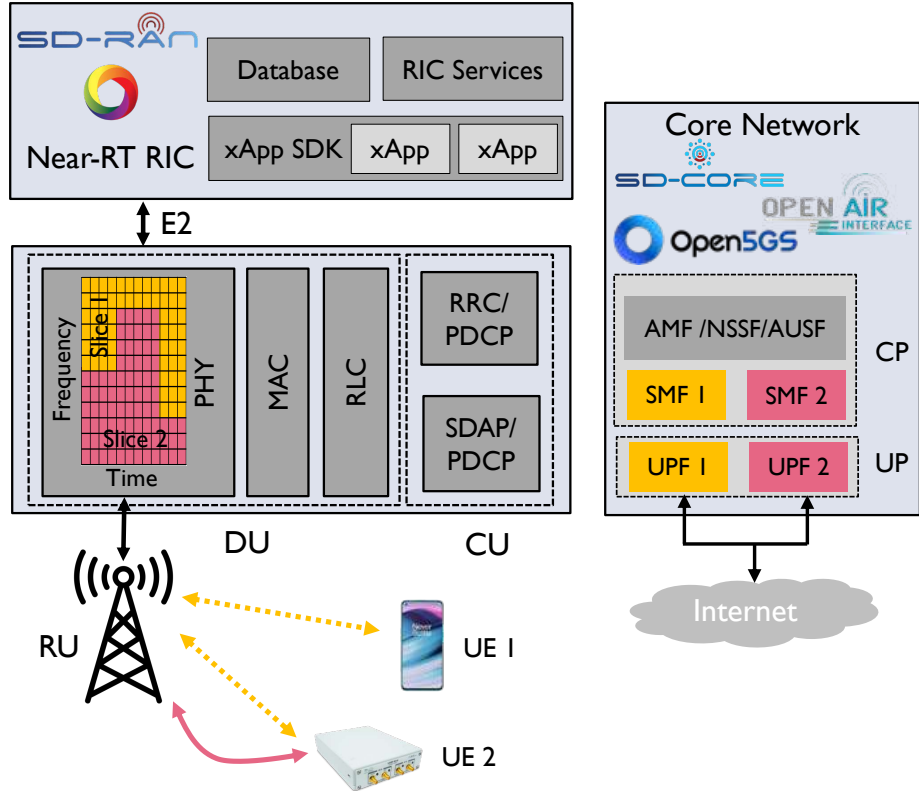


Figure 5.20: End-to-end network slicing in O-RAN.

messages, among other uses. Network slicing in the RAN (i.e., RAN slicing) refers to the problem of allocating (and dedicating) such radio resources (i.e., PRBs) to different slices according to certain slicing policies.

Core Network Slicing. The 5G CN enables secure and reliable connectivity between the UE and the Internet. As shown in Figure 5.20, the 5G CN is decoupled into User Plane (UP) and Control Plane (CP). To enable network slicing in the CN (i.e., core slicing), dedicated Network Functions (NFs) in both CP and UP need to be created for each slice. For example, a dedicated SMF and UPF pair can be created for each slice (Figure 5.20). The other NFs in the CN, such as the AMF, can be shared instead.

Multi-slice Support. 3GPP specifies a set of procedures to link UE traffic to a certain network slice. Specifically, during the PDU session establishment phase, the UE can specify the S-NSSAI of the target network slice. Upon establishment, the PDU session is assigned an IP address, allowing applications in the UE to access the network service of the network slice by binding to that IP. This procedure enables multiple PDU sessions on the same UE, and each PDU can be bound to a dedicated network slice tailored to the use case or application executed by the UE.

RAN Slicing in O-RAN. The O-RAN WG3 has identified RAN slicing as a key use case in the context of the Near-RT RIC specifications [209]. It has also released the O-RAN service model E2SM-CCC [206] which details the structure and procedures necessary to enable RAN slicing in

O-RAN following the 3GPP specifications described above. This is performed via xApps executing at the Near-RT RIC, where limited radio resources are managed in near-real-time to meet QoS requirements and to accommodate highly varying RAN load and conditions.

5.4.3 ORANSlice Implementation

This section details the design and implementation of the missing blocks required to support the RAN slicing use cases based on the O-RAN specifications. From a software point of view, the open-source ecosystem already offers all architectural blocks necessary to instantiate and operate a 5G network. For example, disaggregated 5G base stations can be instantiated via OAI [210] and srsRAN [211], which also offer O-RAN integration and functionalities. A 5G core network can be instantiated via OAI, Open5GS [212], or SD-Core [213], all of which support core slicing. Similarly, the OSC and Aether offer open-source implementations of Near-RT RICs. OpenRAN Gym, an open-source project for collaborative research in the O-RAN ecosystem, provides components to connect across RAN and RICs [46].

What has been missing is an open-source, 3GPP- and O-RAN-compliant implementation of RAN slicing functionalities and the support for multi-slice applications at the same UE.

5.4.3.1 RAN Slicing Enabled Protocol Stacks

The protocol stack of ORANSlice is based on OAI [210]. To enable RAN slicing, ORANSlice advances and extends the functionalities of the MAC layer, including slice information of PDU sessions of each UE and a re-designed two-tier radio resource scheduler. Moreover, we extend the OAI nrUE to support the instantiation and management of multiple PDU sessions for different slices.

Slice-Aware MAC. In OAI, the MAC layer implements a *proportional-fair* scheduling algorithm to allocate radio resources between different UEs. However, to realize RAN slicing, the MAC scheduler needs to be aware of PDU-slice associations so as to properly allocate resources among users.

There are two basic types of RAN slicing schemes. The first one implements *slice-isolation*, where a fixed amount of resources is exclusively dedicated to each slice to guarantee resource availability [64]. This method completely prevents resource sharing, resulting in low resource utilization efficiency because unused PRBs are not reallocated to other slices. However, it offers a low-complexity implementation. The second one is the *slice-aware* scheme, in which resources can be exclusively allocated to each slice or shared among slices via a priority-based access mechanism. The slice-aware scheme increases resource utilization efficiency by allowing PRBs allocated to a slice but unused to be distributed across other slices on demand.

Since the second approach is more efficient, it has been selected by the 3GPP [214] and the O-RAN ALLIANCE [205] as a reference implementation for RAN slicing, and for this reason, we consider it in ORANSlice. In the context of RAN slicing, the 3GPP introduces the concept of Radio Resource Management (RRM) RAN slicing policy [214], as illustrated in Figure 5.21. The `rRMPolicyDedicatedRatio` represents the dedicated percentage of PRBs allocated to the network slice and is exclusively allocated to the slice even if the slice has no active traffic demand. The 3GPP also defines the concept of prioritized PRB access via two parameters: `rRMPolicyMinRatio` and `rRMPolicyMaxRatio`. The former represents the minimum per-

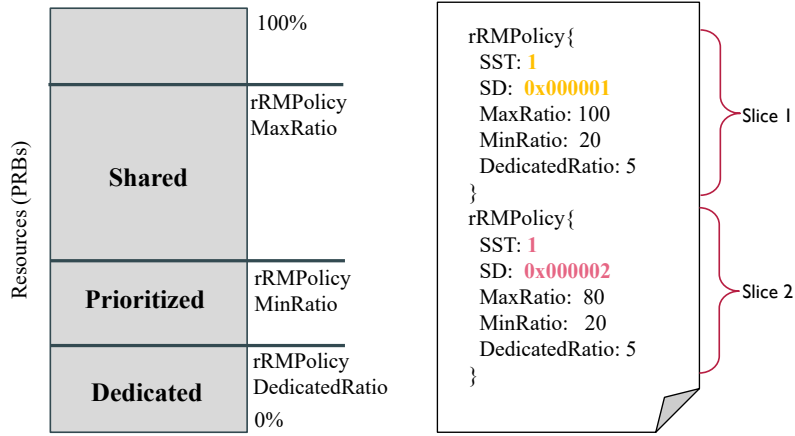


Figure 5.21: Illustration of RRM Policy Ratio Message

centage of PRBs that would be prioritized for allocation to the network slice. The latter represents the maximum percentage of PRBs that can be allocated to the slice. At a high level, the percentage of PRBs that falls within the prioritized range (i.e., defined as the difference between the maximum ratio and the dedicated ratio) is guaranteed to be allocated to the slice, but only if the slice has active users requesting PRBs.

ORANSlice extends the *proportional-fair* scheduler of OAI to integrate the slice-aware scheme described above. As we will describe later, this is achieved by implementing a two-tier resource allocation mechanism that considers: (i) inter-slice resource allocation and sharing according to RAN slicing policies, which will be elaborated in Section 5.4.3.2; and (ii) intra-slice resource allocation to schedule transmissions for all UEs that belong to the same slices.³

UE Slicing Support in OAI nrUE. The other important contribution of ORANSlice is the introduction of support for multiple slices on the same UE. Prior to ORANSlice, OAI softwarized 5G UE, i.e., OAI nrUE, supported only one PDU session per UE, limiting each UE to a single active slice at any time. To enable multi-slice support, we have extended nrUE functionalities to: (i) enable the coexistence of multiple PDU sessions on each UE; (ii) instantiate/delete new PDUs on-demand; and (iii) assign each PDU to a slice. We already contributed these functionalities to OAI nrUE repository, and they are available to the community as open-source components. It is worth mentioning that currently available 5G smartphones do not support these features, and we hope that this will help the community to investigate and explore RAN slicing topics that go beyond single UE-slice associations.

5.4.3.2 Implementing the E2SM-CCC

To enable the O-RAN RAN slicing use case, we also developed the corresponding E2SM to realize the O-RAN E2SM-CCC service model. We developed two versions of the E2SM-CCC. One

³We would like to mention that support for the dedicated ratio defined by the RRM policy in Figure 5.21 will be added in the future.

has been integrated with the Linux Foundation’s Aether SD-RAN Near-RT RIC [213] and already made public,⁴ while a simplified version has been integrated with the OSC Near-RT RIC.

E2SM-CCC Service Model. The E2SM describes how a specific RAN function (the *service*) within an E2 node interacts with the Near-RT RIC and its xApps. It consists of an E2 Application Protocol (E2AP) and a data schema accepted by both the RAN function and Near-RT RIC. The flexible, programmable E2SM-CCC is critical to the autonomous, intelligent RAN control loop in O-RAN.

To support RAN slicing reconfiguration via xApps, we have implemented a simplified version of the E2SM-CCC service model integrated with the OSC Near-RT RIC to support 3GPP-compliant RAN slicing reconfiguration via xApps.

Only the *O-RRMPolicyRatio* configuration of E2SM-CCC is supported in the implemented service model. Other configurations defined in E2SM-CCC are omitted as they are beyond the scope of this work. Protobuf is used to send control messages that include the RRM policy necessary to update RAN slicing strategies enforced by the RAN.

5.4.3.3 RAN Slicing xApp and Data-driven Control Automation

We developed a RAN Slicing xApp to compute RRM policies necessary to update RAN slicing strategies. Specifically, the RAN Slicing xApp periodically reads the RAN KPIs from an InfluxDB database, processes them, and generates the slicing policies that are sent to the gNB through the E2 interface via a RIC Control message. Control messages from the xApp are serialized into Protobuf objects and sent via the SMs described above. The data from the gNB is periodically sent to a dedicated OSC KPM xApp, which reads KPMs received over the E2 termination via a RIC Indication message. The KPM xApp, which is also running on the Near-RT RIC and subscribes to the gNB reporting through a RIC Subscription message, inserts the received RAN KPMs into the InfluxDB database that is leveraged by the RAN Slicing xApp. Similar to the RIC Control messages, the payload of the RIC Indication messages is serialized into Protobuf objects.

5.4.4 Testbeds and Experiment Results

In this section, we demonstrate the effectiveness and portability of ORANSlice by deploying an end-to-end O-RAN cellular network on two physical testbeds: Arena, the SDR-based OTA platform described in Section 2.3.2 [29], and X5G, described in Chapter 4 [21]. We demonstrate the functionality of ORANSlice by performing two experiments. In the first experiment (Section 5.4.4.1), we show an end-to-end network slicing deployment with KPM and RAN slicing xApp running in the OSC Near-RT RIC. The goal of the first experiment is to demonstrate the RAN slicing functionalities enabled by ORANSlice. In the second experiment (Section 5.4.4.2), we show a simple, yet illustrative, example of how to guarantee access to a minimum amount of radio resources via tailored RAN slicing policies in ORANSlice. In this latter experiment, we also demonstrate the multi-slice support offered by ORANSlice. In addition to the OTA transmission experiments on two testbeds, we also replicate the two experiments in OAI RFSim mode to show the ability of ORANSlice working without physical UE or radio devices.

5G UE. We test both COTS and softwarized UEs. The COTS Sierra Wireless EM9191 5G module is selected for flexible experiments, as it supports multiple PDU sessions and customized S-NSSAI for

⁴<https://github.com/onosproject/onos-e2-sm/pull/392>

each PDU session. We also tested ORANSlice with the OAI nrUE, a softwarized UE that we have extended to enable multi-PDU sessions support and thus UE multi-slicing.

5G Core Network. To validate slicing operations, we tested ORANSlice with OAI CN, Open5GS, and SD-Core. These are modular CNs and support network slicing natively. With consistent slicing configuration at UE, gNB, and the core network, ORANSlice can achieve an end-to-end 5G network slicing.

Near-RT RIC. The Near-RT RIC and the xApps of Figure 5.20 are deployed via Red Hat OpenShift. Specifically, we deployed the “E” release of the OSC Near-RT RIC together with the OSC KPM xApp and the RAN Slicing xApp.

5.4.4.1 Testing RAN Slicing Control

In the Near-RT RIC, the deployed KPM xApp and RAN Slicing xApp work together to enable RAN slicing control. Every 0.5 seconds, the KPM xApp acquires KPIs for all connected UEs from the E2 interface. This includes user information (e.g., Radio Network Temporary Identifier (RNTI) and S-NSSAI) and KPMs such as BLER, MCS, and throughput. This data is stored in an InfluxDB database in the form of time series data.

The RAN Slicing xApp reads the KPMs from the database and calculates the average downlink throughput for each slice for the previous 5 seconds. Then, it identifies the slice with the lowest and highest reported throughput and sets their `rRMPolicyMaxRatio` to 90% and 10%, respectively. The goal of this experiment is to demonstrate the correctness of the RRM policy update. How to use ORANSlice to satisfy a target QoS will be shown in Section 5.4.4.2.

We consider two slices and two UEs, each associated with one slice. The control logic computes a new RRM policy every 10 seconds. As shown in Figure 5.22, the averaged PRBs per frame for UE 1 and UE 2 changes every 10 seconds. For the Arena testbed (which can allocate up to 106 PRBs), the PRBs of each UE varies between 10 and 90. For the X5G testbed, the PRBs of each UE range from 27 to 230 (the gNB in this testbed can allocate up to 273 PRBs). RFSim has the same 5G numerology as Arena, and the average number of allocated PRBs follows the same pattern. In all cases, the number of PRBs allocated to each slice is approximately equal to 10% and 90% of the number of available PRBs in each testbed, which proves that the RRM policy is applied correctly. In Figure 5.23, we also show the impact that the slicing policy has on the downlink throughput of each slice, which depends on the amount of PRBs available to the slice. We see the downlink throughput for the two UEs varies following the number of PRBs in Figure 5.22. The difference between the throughput values of UEs is related to the differences in the hardware and RF channel peculiar to each testbed.

5.4.4.2 Multi-Slice with Guaranteed PRBs

In this experiment, we show how ORANSlice handles multi-slice applications and guarantees minimum PRB allocation by fine-tuning `rRMPolicyMinRatio` in the RRM policy. We consider two slices and 2 UEs, and UE 1 activates two PDUs each with a different S-NSSAI. This means that UE 1 has active PDUs on both slices. We set `rRMPolicyMinRatio` = 0 and `rRMPolicyMaxRatio` = 100 for all slices, i.e., no minimum PRB guarantee.

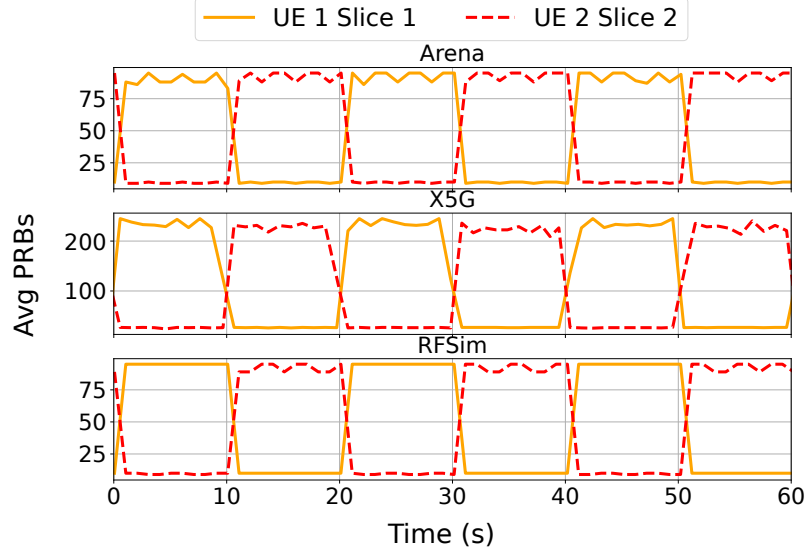


Figure 5.22: Average number of DL PRBs allocated to each slice in the first experiment.

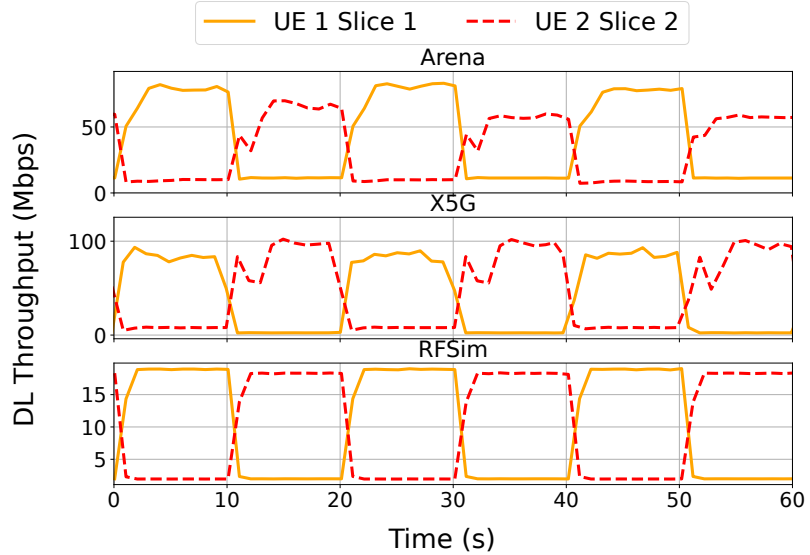


Figure 5.23: DL Throughput for each slice in the first experiment.

The experiment evolution is illustrated in Figure 5.24. In step 1 (0 ~ 20s), UE 1 establishes two PDU sessions, with one PDU session associated with each slice. For each PDU, UE 1 generates TCP downlink data via *iPerf3*, while UE 2 is inactive. We observe that the throughput achieved by the two PDUs of UE 1 is comparable, thanks to the proportional-fair scheduler. In step 2 (20 ~ 40s), UE 2 establishes a PDU session associated to slice 1, and starts an *iPerf3* TCP downlink data transmission. The throughput of UE 1's PDU associated with slice 2 decreases to

about 1 Mbps, due to the resource competition caused by the new establishment of UE 2's PDU on slice 1. Moreover, since `rRMPolicyMinRatio` = 0 for all slices, the gNB does not attempt to improve the throughput of UE 1's PDU associated with slice 2 as the RRM policy does not specify any guaranteed PRB provisioning for slice 2. In step 3 (40 ~ 60s), the `rRMPolicyMinRatio` of slice 2 is set to 80, which makes the throughput of UE 1's PDU associated to slice 2 increase thanks to the minimum PRBs guarantee. Similarly, in step 4 (60 ~ 80s), the `rRMPolicyMinRatio` of slice 2 is decreased from 80 to 40 and the throughput of UE 1 on slice 2 decreases. In step 5 (80 to 100 seconds), UE 1 stops the `iPerf3` transmission at the beginning of this step, while UE 2 stops it at the end. This experiment demonstrates how fine-tuning the `rRMPolicyMinRatio` parameter for each slice can guarantee a minimum PRB level for individual slices.

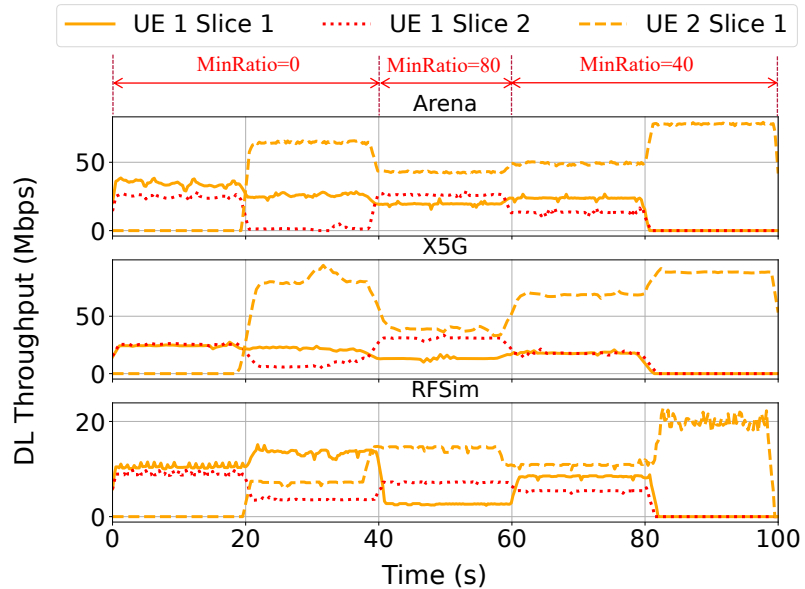


Figure 5.24: DL throughput for each slice and UE in the second experiment.

5.4.5 Related Work

RAN software stacks, such as OAI [210] and srsRAN [211], have been instrumental in advancing the field by welcoming contributions from the open-source community, for example, to integrate and release network slicing technologies for both 5G [215] and 4G [64] systems. Examples of this are provided by SCOPE [64] and FlexSlice [215]. The former is a network slicing framework based on srsRAN 4G, which, however, uses custom SMs to communicate with the xApps. The latter is a RAN slicing framework with a recursive radio resource scheduler based on OAI 5G. However, only a single slice can be associated with each UE, and it lacks integration with the O-RAN E2SM.

Efforts similar to ours have been documented in the literature. ProSlice in [216] developed a customized E2SM and xApp to support RAN slicing. However, ProSlice does not follow the 3GPP RAN slicing model, and the E2SM is not O-RAN-compliant. Besides, ProSlice is not open-source. RadioSaber [217] is a channel-aware RAN slicing framework implemented in a RAN simulator.

Finally, Zipper [218] is a RAN slicing framework based on closed-source commercial protocol stacks. The closest works to ours are [216] and [215]. Compared to these works, ORANSlice advances the state-of-the-art by introducing support for multi-PDU and thus multi-slice management on the same UE. This enhancement enables more efficient, flexible handling of different types of traffic, catering to the diverse needs of modern applications where multiple classes of traffic with different QoS requirements coexist on the same device and must be satisfied simultaneously.

5.4.6 Conclusions

This section presented ORANSlice, an open-source 5G framework for network slicing in O-RAN. ORANSlice extends OAI to deliver 3GPP-compliant RAN slicing and support for multi-slice applications, integrating an E2 service model based on E2SM-CCC and a RAN Slicing xApp working with the OSC Near-RT RIC. The RAN slicing functionalities were demonstrated on multiple OTA O-RAN testbeds, including X5G and Arena, and on the OAI RF simulator for different use cases.

The release of ORANSlice as open-source software aims to bridge the gap between research and practice, providing the community with a valuable resource for further exploration and development of RAN slicing technologies in the O-RAN ecosystem.

5.5 TIMESAFE: Security of Open Interfaces

The previous use cases focused on leveraging the X5G physical platform for AI-driven applications and intelligent control, such as sensing, interference detection, and resource management. This section explores a different capability, security assessment, through the development of TIMESAFE. TIMESAFE investigates vulnerabilities in the O-RAN FH synchronization plane, demonstrating how attacks against PTP can cause catastrophic failures in production 5G networks. This work highlights the unique value of physical platforms like X5G for security research, enabling the validation of attack impact on real hardware with commercial RUs and UEs, and providing insights that cannot be obtained through simulation alone.

5.5.1 Introduction

Recent advancements in 5G and beyond have focused on disaggregating the gNB and core networks, leading to the evolution of more open and modular systems. As a result, the FH has emerged as a critical component, enabling the separation of radio elements from baseband processing. Disaggregated FH deployments were initially based on the Common Public Radio Interface (CPRI). While CPRI facilitated high-speed, centralized processing of radio signals, it lacked built-in security measures due to its design for single-vendor, co-located deployments [219]. The subsequent enhanced CPRI (eCPRI) introduced some security improvements, but significant gaps remain, particularly in synchronization [220]. The eCPRI-based O-RAN ALLIANCE's open FH now connects disaggregated components from multiple vendors, often using switched Ethernet topologies [126, 221]. While Ethernet's flexibility supports diverse traffic types, it also exposes the FH to threats, as demonstrated by potential attacks on interconnected devices [222, 132, 223, 224, 225]. These attacks can disrupt synchronization and cause outages. For example, as shown in Figure 5.25, an attacker that gains access to the FH network can carry out spoofing attacks that cause synchronization drift, resulting in

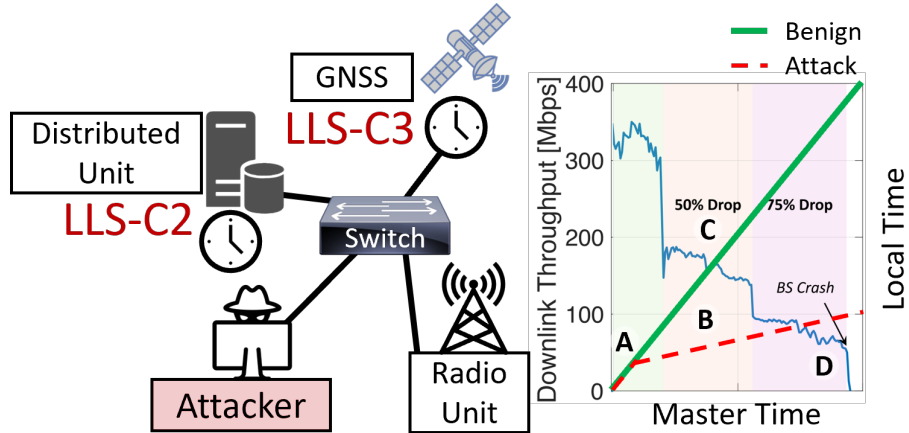


Figure 5.25: The Open Fronthaul employs PTP to synchronize the master clock with distributed base station components over a switched network. In this scenario, an attacker compromises a device on the network and, at time **A**, initiates a Spoofing Attack. This leads to gradual synchronization drift (**B**), first degrading performance (**C**) and then causing the base station to crash at time **D**.

a reduction in throughput and eventually a complete crash of the base station. Although industry, government, and academia are working to address these security gaps [219, 226, 227, 228, 132, 229], no comprehensive standards for securing the FH have yet been established.

The open FH relies on precise timing through the Synchronization Plane (S-plane) to perform critical operations like OFDM synchronization, carrier aggregation, and handovers, which require time accuracy within tight margins [230, 231]. This synchronization depends on the PTP, which, like the FH, was initially developed without any security mechanisms [232]. While recent updates to the PTP standard include additional security features [233, Annex P], these have not been widely implemented in Open RAN (RAN) environments, leaving vulnerabilities that attackers could exploit.

Security is critical for the success and widespread adoption of any system, and Open RAN has been criticized for lacking robust security mechanisms. In response, the O-RAN ALLIANCE established WG11 [227] to define a security framework, including zero-trust architectures [234], procedures, and defense mechanisms essential for Open RAN's success [229]. While WG11 acknowledges that attacks on the S-plane can have a high impact, they consider the likelihood low due to the perceived sophistication required by an attacker [235]. However, a significant gap remains in analyzing security risks and proposing solutions for the open FH S-plane in production-grade Open RAN environments.

This section presents TIMESAFE (Timing Interruption Monitoring and Security Assessment for Fronthaul Environments), a framework for assessing the impact and likelihood of attacks against PTP in the FH of O-RAN and 5G networks. The key contributions relevant to this dissertation include: (i) the first experimental analysis of timing attack impact on a production-ready private cellular network, following O-RAN ALLIANCE testing procedures [236], revealing that such attacks can cause catastrophic gNB outages; and (ii) demonstration that timing attacks on PTP in the FH S-plane are straightforward and require minimal sophistication, countering the assumption that such attacks are highly complex. The broader TIMESAFE framework also includes a transformer-based ML

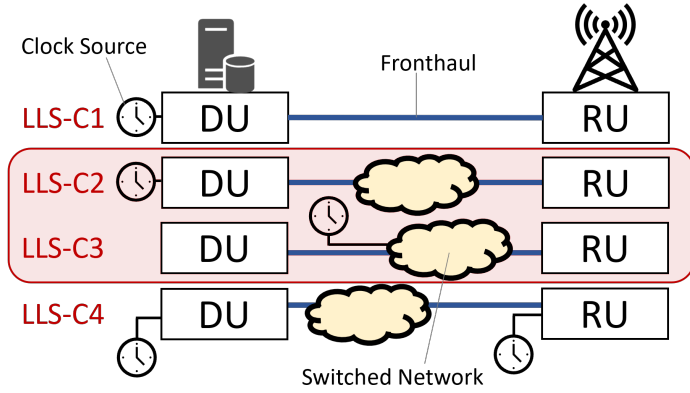


Figure 5.26: The Fronthaul connects the Distributed Unit (DU) to the Radio Unit (RU). There are four Synchronization Plane topologies based on the location of the clock source and switched network. LLS-C2 and LLS-C3 present the greatest risk to PTP because the switched network is used to transport the timing messages.

detection mechanism achieving over 97.5% accuracy. However, the focus in this dissertation is on the experimental security assessment enabled by the X5G platform [25].

The remainder of this section is organized as follows. Section 5.5.2 provides background on FH synchronization and PTP. Section 5.5.3 describes the threat model and attack methods. Section 5.5.4 presents the experimental setup on X5G, and Section 5.5.5 demonstrates the production network impact. Section 5.5.6 describes an ML-based attack detector. Finally, Section 5.5.7 surveys related work and Section 5.5.8 concludes.

5.5.2 Background

5.5.2.1 Fronthaul Synchronization Plane

The FH S-plane standards define four clock models and synchronization topologies based on the Lower Layer Split Control Plane (LLS-C): LLS-C1, LLS-C2, LLS-C3, and LLS-C4 [126], as illustrated in Figure 5.26. LLS-C1, where the DU and RU are directly connected without a switched network, poses the least security risk due to the absence of intermediate attack vectors. LLS-C4 provides timing directly to the DU and RU using local GNSS receivers, reducing PTP attack opportunities, except for potential GNSS jamming.

In contrast, LLS-C2 and LLS-C3 are more vulnerable due to their reliance on the switched network for PTP message transport. In these scenarios, every device in the switched network represents a potential attack vector. In LLS-C2, the DU is part of the synchronization chain to the RU with one or more Ethernet switches in between. LLS-C3 differs in that the DU is not in the synchronization chain; instead, timing is distributed from the Primary Reference Time Clocks (PRTC) to the DU and RU(s) through the network. The increased complexity and multiple entities involved in securing the network infrastructure expand the risk surface, making LLS-C2 and LLS-C3 the most susceptible to attacks [237, 235].

5.5.2.2 Precision Time Protocol Overview

The PTP standard (IEEE 1588 [233]) ensures precise network clock synchronization in the nanosecond range. It achieves this through hardware time stamping, which minimizes delays from the networking stack [238]. The process involves electing a master clock that synchronizes all slave clocks in the network through a series of exchanges and messages.

The initial step involves leader election through the Best Master Clock Algorithm (BMCA). Each clock periodically broadcasts *Announce* messages containing attributes such as: *Priority1*, a configurable priority setting used as the first comparison feature; *ClockClass*, indicating the clock's traceability and suitability as a time source; *ClockAccuracy*, reflecting the clock's precision; and *ClockIdentity*, a unique identifier used to resolve ties. Each clock evaluates the *Announce* messages based on the available attributes, selecting the clock with the highest quality as the master. This process is dynamic, allowing for continuous re-evaluation and re-selection if higher-quality clocks are introduced or current attributes change.

After election, the master clock begins synchronization with slave clocks through three critical aspects, illustrated in Figure 5.27. *Frequency* refers to the rate at which a clock oscillates; the master sends *Sync* messages and takes a timestamp (T_1), with TwoStep clocks sending a separate *FollowUp* message containing this timestamp. The slave records the receive timestamp (T_2), and by comparing successive *Sync* messages, calculates the drift to adjust its oscillation rate. *Delay* refers to the propagation time through the network; the slave sends a *DelayReq* message and records timestamp (T_3), while the master records the receive timestamp (T_4) and returns it in a *DelayResp* message, allowing the slave to compute the one-way delay as $Delay = \frac{(T_4 - T_1) - (T_3 - T_2)}{2}$. *Phase* refers to the relative alignment between clocks; after calculating delay, slaves compute the offset as $Offset = (T_2 - T_1) - Delay$ to minimize phase difference with the master. This message exchange process is repeated at defined intervals to maintain synchronization.

5.5.3 Threat model

The threat model of this work assumes an attacker has gained access to a device within the FH network. The complexity of the O-RAN architecture, with its many interconnected components, heightens security risks through several vectors. *Increased remote access*: O-RAN's multi-vendor architecture involves diverse suppliers and service providers with varying levels of access control, increasing the risk of misconfigured authentication or compromised credentials [239, 240]. *Increased physical access*: the distributed nature of gNB edge servers, often located in accessible public spaces, makes on-site physical access an increasingly viable entry point, where adversaries can insert rogue devices to intercept or replay traffic [241]. *Supply chain vulnerabilities*: software-based network functions are susceptible to supply chain attacks, with recent studies uncovering high-risk dependencies, misconfigurations, and weak security practices across multiple O-RAN components [225, 223, 224].

Once an attacker gains access to the switched network, they can observe, replay, or inject PTP broadcast packets. Within the TIMESAFE framework, we focus on two specific attacks targeting PTP synchronization and chosen for their direct impact on PTP synchronization mechanisms: *Spoofing Attack* and *Replay Attack*.

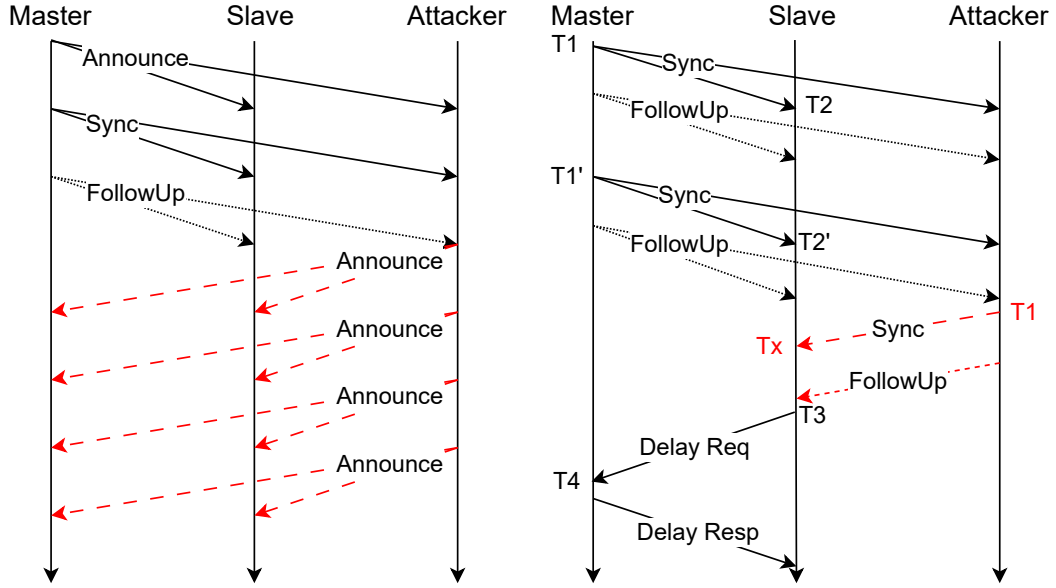


Figure 5.27: The black (solid/dotted) lines represent normal traffic, while the red (dashed) lines on the left side illustrate the flow of messages during a Spoofing Attack, where an attacker manipulates the BMCA to become the master. The red (dashed) on the right side illustrates the flow of messages during a Replay Attack, showing the re-transmission of Sync and FollowUp messages.

5.5.3.1 Spoofing Attack

The TIMESAFE framework spoofing attack targets PTP nodes by sending counterfeit *Announce* messages to manipulate the BMCA leader election and assume the role of the master clock. Initially, the attacker monitors benign traffic to gather critical information about the protocol configuration and node attributes. With this data, the attacker crafts *Announce* packets designed to have superior attributes crucial for master clock selection. The BMCA relies on up to nine features to determine the master clock, starting with *Priority1* (Section 5.5.2.2). The attacker manipulates this value by setting it to 1. Similarly, the attacker sets the values for *ClockClass* to 1. The *ClockIdentity* field is created by inserting priority values between the manufacturer ID and device ID portions of the MAC address. The attacker inserts `fffff` ensuring it has higher priority values than the legitimate Master. Other values are copied from the legitimate master.

These crafted messages are sent periodically to maintain the attacker's role as master. Apart from *Announce* messages, no synchronization packets are sent, and *DelayReq* messages from slaves remain unanswered. By disrupting the synchronization process, all clocks operate independently, leading to a gradual drift. Consequently, the attacker introduces synchronization errors among all nodes in the network, causing a complete outage for the gNB, as we will show in Section 5.5.5 and illustrated in Figure 5.25.

5.5.3.2 Replay Attack

The Replay Attack involves sniffing time synchronization messages (*Sync* and *FollowUp*) from the Master clock, storing, and retransmitting them after a delay. When the Slave clock receives the retransmitted messages, it uses the outdated timestamp T_1 and a new timestamp T_x to compute drift, delay, and offset (see Figure 5.27). The formulas in Section 5.5.2.2 become: $Drift = \frac{(T'_2 - T_x) - (T'_1 - T_1)}{T'_1 - T_1}$, $Delay = \frac{(T_4 - T_1) - (T_3 - T_x)}{2}$, and $Offset = (T_x - T_1) - Delay$. The actual difference between when T_1 is generated and received in the malicious PTP message significantly exceeds the calculated difference, causing offset to increase by orders of magnitude and severely disrupting network synchronization.

5.5.4 Experimental Setup

The experimental analysis is performed on the X5G platform described in Section 4. The platform comprises multiple NVIDIA ARC nodes with dedicated CN and FH infrastructure. NVIDIA ARC combines OAI for the higher layers of the protocol stack with NVIDIA Aerial, a physical layer implementation accelerated on GPU (NVIDIA A100) with a 7.2 split implementation using NVIDIA Mellanox smart NICs. The GPU is coupled with the programmable NIC (Mellanox ConnectX-6 Dx) via Remote Direct Memory Access (RDMA), bypassing the CPU for direct packet transfer. The FH infrastructure uses a Dell S5248F-ON switch and a Qulsar QG-2 as the grandmaster clock, distributing PTP and SyncE synchronization to the DU and RU with an O-RAN LLS-C3 configuration. For PTP synchronization, *ptp4l* is used, an IEEE 1588 compliant implementation for Linux. The RU is a Foxconn 4T4R unit operating in the 3.7–3.8 GHz band, with COTS 5G smartphones from OnePlus as UEs. Based on the threat model, one of the DUs is assumed to be the compromised machine from which the attacker can send malicious PTP packets. The experimental validation focuses on the spoofing attack, as proper switch port configuration in the production environment prevented the replay attack from reaching other nodes.

5.5.5 Impact of the Attacks

The spoofing attack is tested in the production-ready private 5G network to assess their impact following the recently published guidelines in the O-RAN ALLIANCE testing specifications [236]. According to NIST's National Vulnerability Database [242], impact levels are categorized as none, low, or high. Low impact attacks cause performance degradation or intermittent availability without fully denying service. High impact attacks result in complete outages, denying service to all UEs.

5.5.5.1 Switch Configuration Effects

In our initial tests, we found that switch configurations can provide protection against attacks. Malicious packets are not always received by other nodes, as verified through Wireshark captures on both the malicious machine and other nodes. This protection is tied to the switch port's PTP role settings. On the Dell S5248F-ON switch, ports set to master only send PTP packets, slave mode only receives, and dynamic mode allows both. Additionally, switch configurations can block duplicate MAC addresses. While a properly configured switch prevented our replay attack, assuming correct configurations is risky, especially when DU and RU vendors lack control over network settings,

and the complexity and diversity of equipment and configurations in the FH path exacerbate this risk [240, 239, 243]. The spoofing attack, which does not rely on MAC address duplication, remained effective under various switch configurations.

5.5.2 Attack Results

In our first successful attack, we configure the port of our malicious machine with a PTP master role. We start our private 5G network, connect the UE, and begin sending around 300 Mbps downlink iPerf traffic. After approximately 60 seconds, we launch the spoofing attack, as shown in Figure 5.28. Monitoring the PTP service logs at the DU reveals that the attack causes the DU to lose synchronization with the grandmaster clock, leading to a drift in network synchronization as the DU uses its internal clock. This drift degrades UE performance, eventually causing disconnection from the network. About 380 seconds after the beginning of the attack, there is a sudden 50% drop in throughput. From this point, the throughput continues to drop roughly linearly as the clock drift increases. Finally, the DU loses synchronization with the RU, the throughput drops to 0, and the UE disconnects. When this attack stops, the DU resynchronizes with the grandmaster clock, and the network returns to a healthy state.

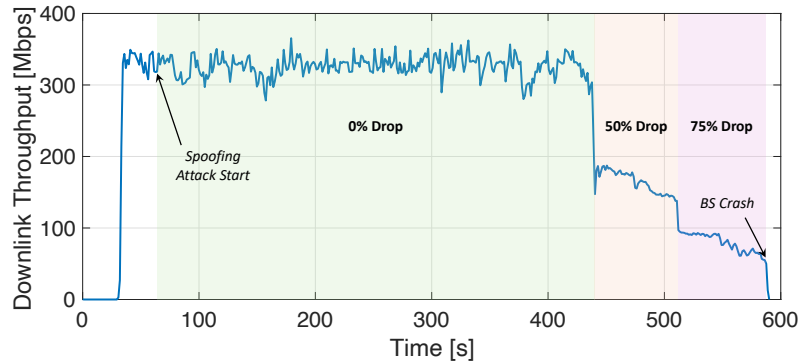


Figure 5.28: Downlink throughput to a UE during a spoofing attack with the switch port set to PTP master. Approximately 60 seconds into the experiment, the spoofing attack is initiated. Around second 440 there is a 50% drop in throughput, progressing to a 75% drop by second 510, and ultimately causing the base station to crash at around second 580.

Next, we configure all ports as PTP dynamic so that malicious packets can be received by the other nodes and repeat the experiment. This time, the malicious PTP packets reach all the machines in the network. Approximately 2 seconds after the attack begins, the RU crashes, stopping its operations, causing the 5G cell to drop and the UE to lose connection, as shown in Figure 5.29. While the DU was able to recover on its own after the first attack, the RU required a manual reboot to regain functionality after the second attack. This behavior might be device specific, in our case the Foxconn RU. Regardless of any potential vendor-specific variations, these attacks proved to be very powerful, causing significant disruption and necessitating manual intervention to restore full network operations. These tests demonstrate the impact to the Open RAN gNB is *high*. Failing to secure the S-plane against spoofing attacks results in a complete outage of the gNB.

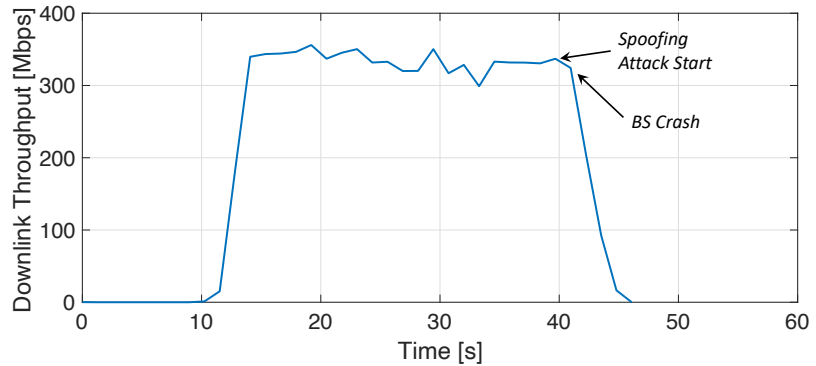


Figure 5.29: Downlink throughput to a UE during a spoofing attack with switch ports set to PTP dynamic role. Throughput remains stable at around 350 Mbps initially. About 40 seconds in, the spoofing attack begins, causing the 5G cell to drop and the UE to lose connectivity.

5.5.6 ML-Based Attack Detection

Given the demonstrated impact of synchronization attacks, a detection mechanism is essential. Traditional rule-based solutions require extensive expert knowledge and fixed thresholds that struggle to adapt to evolving threats. In contrast, ML offers a more adaptive approach: models can learn complex patterns in PTP traffic to distinguish between benign fluctuations and actual attacks, without requiring manually specified rules for each attack type.

5.5.6.1 Detection Pipeline

The TIMESAFE detection pipeline consists of three parallel components deployed on the DU. The *packet acquisition* stage captures Ethernet frames, filters for PTP packets, and extracts six features from each packet: Ethernet source and destination addresses (to identify flows and packet direction), packet length (to detect malformed packets), PTP sequence ID and message type (to understand the nature and order of messages), and inter-arrival time (a key indicator since O-RAN specifies fixed intervals for announce and sync messages). The *pre-processing* stage maps observed MAC addresses to integers, enabling the model to learn traffic patterns rather than specific addresses. The *decision-making* stage uses a sliding window approach to classify each sequence as benign or malicious. With a stride of two, at most two malicious packets are sent before the model detects an attack.

5.5.6.2 Model Architecture

Several ML architectures were evaluated, including Random Forest, LSTM, CNN, and Transformer models. The task of classifying packet sequences as malicious or benign parallels sentiment analysis and image classification, where context and sequential features are key. CNNs excel at extracting spatial features from packet patterns, while Transformers are superior at capturing contextual dependencies in sequential data. Both significantly outperformed other approaches.

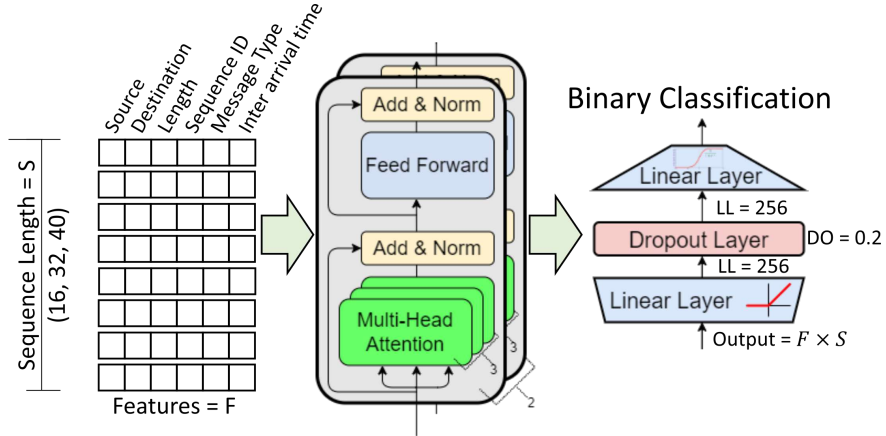


Figure 5.30: The final TIMESAFE transformer model uses 2 transformer layers, a fully connected linear layer with ReLU activation function, a dropout layer, and a second linear layer with a sigmoid activation function. The output is a single binary classification for the entire sequence.

The selected Transformer model (Figure 5.30) uses only the encoder portion of the full transformer architecture. It processes input sequences of fixed length $S = 32$ packets with $F = 6$ features. The transformer encoder outputs a feature matrix fed into a fully connected linear layer with ReLU activation, followed by a dropout layer (probability 0.2) and a final linear layer with sigmoid activation for binary classification. The model uses 2 attention heads and comprises 115,609 parameters (463 KB)—small enough for deployment on production DU hardware.

5.5.6.3 Training and Evaluation

Training data was generated by capturing PTP traffic during attack and normal operation periods using the DT environment described fully in [25]. The data was split into equal-sized chunks (1000 messages each) without overlaps, with 80% for training, 10% for validation, and 10% for testing. Training employed weighted binary cross-entropy loss to address class imbalance, the Adam optimizer with initial learning rate of 0.001, and a StepLR scheduler reducing the learning rate by 0.1 every 10 epochs. Early stopping monitored validation loss with patience of 20 epochs.

Given that the impact of false negatives (missing an attack) is catastrophic while false positives have lower impact, both accuracy and recall were considered in model selection. The Transformer achieved the best balance with accuracy exceeding 97.5% and low false negative rate on offline evaluation.

5.5.6.4 Production Detection Results

The detection pipeline was evaluated using packet traces (.pcap files) captured during successful attacks on the X5G production network. As shown in Figure 5.31, the Transformer model achieves accuracy exceeding 99%, demonstrating strong ability to distinguish between malicious and benign traffic in a real-world setting. This result validates that ML-based monitoring provides a cost-

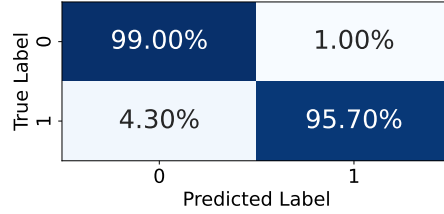


Figure 5.31: Confusion matrix for production environment attack detection. The Transformer model achieves over 99% accuracy in detecting PTP attacks on the X5G platform.

effective approach to detecting synchronization attacks without the latency and complexity overhead of cryptographic solutions.

5.5.7 Related Work

There is a growing awareness of the need to secure PTP. Several attacks are demonstrated in a data center context by DeCusatis *et al.* [244]. Itkin and Wool developed a detailed analysis of threats against PTP and proposed using an efficient elliptic-curve public-key signature for Prong A [245]. Shereen *et al.* [246] experimentally evaluated implementing Prong A, finding that software-based authentication adds at least an additional $70\mu\text{s}$ of delay. Similarly, Rezabek *et al.* [238] evaluated software-based authentication and concluded that there is visible degradation of clock synchronization for each hop in the network with standard deviations between 118 and 571 ns.

There are several works that investigate security threats and propose related defense mechanisms for PTP in smart grids. Moussa *et al.* [247] proposed adding a new type of PTP clock and modifying the PTP slave functionality. Then in subsequent work, Moussa *et al.* proposed adding further message types to aid in detection and mitigation [248], and adding feedback from both slaves and master clocks to a reference entity [249]. A method targeting Prong C, where clock and network path redundancy are added, is proposed by Shi *et al.* [232]. Likewise, the approach by Finkenzeller *et al.* [250] uses redundant, or cyclic paths, to detect and mitigate time delay attacks. Maamary *et al.* give an overview of several threats to the FH S-plane and discuss possible countermeasures [231], though they do not implement either attacks or countermeasures. FH security considerations are further described and MACsec is proposed as a solution by Dik *et al.* [222, 251, 252, 253]. While these works are the most similar to ours, they primarily address Prong B and could be implemented in parallel to our work. In contrast to the above works, TIMESAFE demonstrates successful attacks against PTP used for the S-plane causing the gNB to fail and demonstrating how O-RAN-connected devices can be leveraged as attack vectors. Additionally, we propose a ML-based method to monitor PTP in accordance with Prong D, successfully discriminating between benign and malicious traffic with over 97.5% accuracy.

5.5.8 Conclusion

This section presented TIMESAFE, a security assessment framework that demonstrates the vulnerability of O-RAN FH synchronization to PTP attacks. Experimental validation on the X5G platform showed that spoofing attacks can cause production-ready 5G base stations to fail within

2 seconds, with the RU requiring manual reboot to restore operations. While proper switch configuration prevented replay attacks in the production environment, the spoofing attack remained effective, showing that network configuration alone cannot guarantee security. To counter these threats, TIMESAFE employs an ML-based detection pipeline that achieves over 99% accuracy in identifying malicious PTP traffic on the production network.

Addressing synchronization security involves balancing security costs against performance implications. While robust measures like cryptographic authentication introduce latency and computational overhead—particularly challenging for FPGA-based RUs—TIMESAFE’s monitoring approach offers a cost-efficient alternative. By enabling real-time detection, higher-cost security measures can be applied only when necessary, optimizing both security and performance. Future work should investigate additional attack vectors such as GNSS jamming (affecting LLS-C4), packet removal, and selective delay manipulation, as well as multi-class classification to distinguish between different attack types.

This work highlights a unique capability of physical, production-grade testbeds for security research. Unlike simulation-based studies, attacks validated on real hardware with commercial RUs and UEs provide evidence of vulnerability effects. The results show the importance of securing the S-plane in O-RAN deployments through proactive security measures and demonstrate how platforms like X5G enable security research that would be difficult on emulated or simulated systems.

5.6 Summary and Discussion

This chapter demonstrated the *use case* dimension of physical platforms, moving one step further in the experimental journey from DTs and emulation environments to real-world OTA experimentation. Building on the X5G platform architecture and dApp framework presented in Chapter 4, we showcased four representative use cases highlighting the unique capabilities of production-grade systems and demonstrating how an open and programmable 5G RAN can support advanced AI-native functionalities under realistic propagation and hardware conditions for advancing 5G and 6G research.

First, cuSense demonstrated ISAC capabilities by leveraging CSI from existing 5G uplink signals for real-time person localization, achieving sub-millisecond inference latency while operating as a sensing overlay on the GPU-accelerated RAN. Second, InterfO-RAN showcased real-time interference detection using a CNN-based classifier on IQ samples, achieving over 91% accuracy with latency under 650 μ s. Third, ORANSlice provided an open-source, 3GPP-compliant RAN slicing platform with E2SM-CCC integration and Near-RT RIC xApp control, validated on X5G with commercial hardware. Finally, TIMESAFE exposed FH synchronization vulnerabilities, demonstrating that PTP spoofing attacks can crash production base stations within 2 seconds, while an ML-based detector achieves over 99% accuracy.

These results demonstrate the complementary role of physical platforms compared to DTs and emulation environments discussed in Chapters 2 and 3. While emulation provides controlled, repeatable conditions for initial design and large-scale data generation, physical testbeds such as X5G are necessary to capture hardware impairments, synchronization issues, environmental dynamics, and implementation details for a proper full end-to-end behavior.

From the perspective of the four key research challenges introduced in Chapter 1, this chapter mainly addressed the *use case* dimension on physical platforms, building on the *deployment*, *realism*, and *usability* foundations established in Chapter 4. The design, development, deployment, and validation of the presented applications (cuSense, InterFO-RAN, ORANSlice, and TIMESAFE) on X5G confirm that the software and hardware infrastructure enable the execution of AI-native workloads and security experiments through the use of commercial UEs, multi-vendor RUs, and realistic traffic patterns. Additionally, the open-source components and pipelines developed and released by these works contribute reusable tools that can be leveraged by the whole research community.

Finally, the four case studies presented in this chapter represent only a subset of the research that physical platforms like X5G can enable. Several additional studies are ongoing or already published, including: mobility and handover optimization, e.g., via traffic-aware F1 handover strategies using data-driven controllers; AI-based channel estimation, such as [254], which combines DT-based training with OTA validation; network automation and zero-touch provisioning [255]; energy-efficient RAN operation; multi-vendor integration testing [256]; agentic AI for scheduling and autonomous control [257, 258].

Chapter 6

Conclusions

This dissertation has explored the design, development, deployment, and evaluation of next-generation cellular networks through open and programmable platforms, moving from digital twins and emulation environments to production-grade physical OTA testbeds. Starting from the observation that modern RANs are becoming more complex, are being realized as software running on general-purpose and accelerated hardware, and that the Open RAN paradigm with its open interfaces, such as those defined by O-RAN, is making the network programmable and observable at multiple timescales, this work has focused on two complementary goals: building realistic platforms to enable the development and testing of novel ideas in a safe and reproducible environment; and using those platforms to realize intelligent applications for monitoring, control, sensing, and security.

On the digital side, we demonstrated the use of Colosseum, the world’s largest wireless network emulator with hardware-in-the-loop, as a digital twin for experimental wireless research at scale. Through the development of the Channel Emulation Scenario generator and Sounder Toolchain (CaST), we enabled the automated creation of emulated environments that faithfully replicate real-world deployments. CaST combines 3D modeling, ray-tracing-based channel generation, and channel sounding validation to bridge physical and digital domains. On top of this toolchain, we realized end-to-end emulation pipelines for spectrum sharing, AI-driven propagation modeling, and synthetic RF data generation, demonstrating how digital platforms can serve both as safe experimentation environments and as data factories for AI-native RAN solutions.

On the physical side, we designed, deployed, and evaluated X5G, an open, programmable, and multi-vendor private 5G O-RAN testbed. X5G integrates GPU-accelerated physical layer processing through NVIDIA Aerial with open-source higher layers from OpenAirInterface, connected via O-RAN fronthaul to commercial and programmable RUs and multiple CNs, and connects to a Near-RT RIC running xApps on an OpenShift cluster. Beyond the core infrastructure, we developed a GPU-accelerated dApp framework that exposes real-time PHY/MAC telemetry through shared memory and E3-based interfaces and couples it with Triton-based inference pipelines on the same accelerator as the gNB, enabling AI-native distributed applications to close control loops at sub-millisecond timescales.

We leveraged these platforms through a set of representative intelligent RAN applications. In emulation, Colosseum and CaST have been used to study spectrum sharing between cellular and incumbent systems, AI-assisted radio map generation, and generative models for synthetic RF

CHAPTER 6. CONCLUSIONS

datasets. On X5G, we realized cuSense for uplink-CSI-based ISAC, InterfO-RAN for real-time uplink interference detection, ORANSlice for dynamic resource management and network slicing via xApps, and TIMESAFE for security assessment of fronthaul synchronization. Colosseum and X5G play complementary roles. Colosseum offers a controlled, reproducible environment where solutions can be safely prototyped and validated at scale, while X5G provides a production-grade OTA network with commercial devices and real-world RF conditions. Together, they form a pipeline from emulation to real deployment, allowing researchers to refine ideas while gradually increasing experimental fidelity without risking commercial infrastructure.

Throughout this dissertation, we can now fully revisit the four key research dimensions from Chapter 1 that guided our work. In terms of *deployment*, we developed CaST for automating DT scenario creation and validation on Colosseum and we designed and deployed a multi-vendor O-RAN-compliant platform with GPU-acceleration, namely X5G. For *realism*, we proved that Colosseum digital twins can closely reproduce real setups, and we validated X5G as an end-to-end, 3GPP-compliant private 5G network with commercial smartphones. Regarding *usability*, we released open-source tools, DT scenarios, reference design architectures, experimental pipelines, and comprehensive documentation that lower the barrier for researchers to develop and test their own solutions. Finally, the *use case* dimension has been demonstrated through an extensive set of applications across both platforms, showcasing the capabilities and how these systems can help address key challenges and advance research.

Beyond these specific contributions, this work highlights how modern wireless networks are evolving into more open, programmable systems that require realistic and controlled infrastructures to test bold ideas and collect data at scale. By combining digital twins on Colosseum with a private 5G cell like X5G, we obtain an end-to-end pipeline from emulation to over-the-air validation. The resulting tools, platforms, and use cases form a reusable blueprint where a new idea can follow the experimental journey from concept through simulation and emulation on Colosseum, to OTA validation on X5G, and finally to deployment as an AI-native dApp or xApp, lowering the barrier to designing and testing the next generation of intelligent, open, and secure wireless networks.

Bibliography

- [1] M. Polese, L. Bonati, S. D’Oro, S. Basagni, and T. Melodia, “Understanding O-RAN: Architecture, Interfaces, Algorithms, Security, and Research Challenges,” *IEEE Communications Surveys & Tutorials*, vol. 25, no. 2, pp. 1376–1411, Second quarter 2023.
- [2] L. Bonati, P. Johari, M. Polese, S. D’Oro, S. Mohanti, M. Tehrani-Moayyed, D. Villa, S. Shrivastava, C. Tassie, K. Yoder, A. Bagga, P. Patel, V. Petkov, M. Seltzer, F. Restuccia, M. Gosain, K. R. Chowdhury, S. Basagni, and T. Melodia, “Colosseum: Large-Scale Wireless Experimentation Through Hardware-in-the-Loop Network Emulation,” in *Proceedings of IEEE DySPAN 2021*, Virtual Conference, December 13–15 2021, pp. 1–9.
- [3] D. Villa, M. Tehrani-Moayyed, C. P. Robinson, L. Bonati, P. Johari, M. Polese, and T. Melodia, “Colosseum as a Digital Twin: Bridging Real-World Experimentation and Wireless Network Emulation,” *IEEE Transactions on Mobile Computing*, vol. 23, no. 10, pp. 9150–9166, October 2024.
- [4] J.-H. Lee and A. F. Molisch, “A Scalable and Generalizable Pathloss Map Prediction,” *IEEE Transactions on Wireless Communications*, vol. 23, no. 11, pp. 17 793–17 806, 2024.
- [5] International Telecommunication Union Radiocommunication Sector (ITU-R), “IMT-2030 Framework Recommendation: Vision, Framework and Overall Objectives of the Future Development of IMT for 2030 and Beyond,” ITU Radiocommunication Sector (ITU-R), Tech. Rep., August 2024. [Online]. Available: https://www.5gamericas.org/wp-content/uploads/2024/08/ITUs-IMT-2030-Vision_Id.pdf
- [6] A. Shahraki, M. Abbasi, M. J. Piran, M. Chen, and S. Cui, “A Comprehensive Survey on 6G Networks: Applications, Core Services, Enabling Technologies, and Future Challenges,” *arXiv:2101.12475 [cs.NI]*, 2021.
- [7] L. Bonati, M. Polese, S. D’Oro, S. Basagni, and T. Melodia, “Open, Programmable, and Virtualized 5G Networks: State-of-the-Art and the Road Ahead,” *Computer Networks*, vol. 182, pp. 1–28, December 2020.
- [8] L. Atzori, A. Iera, and G. Morabito, “The Internet of Things: A survey,” *Computer Networks*, vol. 54, no. 15, pp. 2787–2805, 2010.
- [9] D. Villa, X. Song, M. Heim, and L. Li, “Internet of Robotic Things: Current Technologies, Applications, Challenges and Future Directions,” *arXiv:2101.06256 [cs.RO]*, 2021.

BIBLIOGRAPHY

- [10] M. Giordani, M. Polese, M. Mezzavilla, S. Rangan, and M. Zorzi, “Toward 6G Networks: Use Cases and Technologies,” *IEEE Communications Magazine*, vol. 58, no. 3, pp. 55–61, March 2020.
- [11] Z. Zhang, Y. Xiao, Z. Ma, M. Xiao, Z. Ding, X. Lei, G. K. Karagiannidis, and P. Fan, “6G Wireless Networks: Vision, Requirements, Architecture, and Key Technologies,” *IEEE Vehicular Technology Magazine*, vol. 14, no. 3, pp. 28–41, 2019.
- [12] L. Bonati, S. D’Oro, M. Polese, S. Basagni, and T. Melodia, “Intelligence and Learning in O-RAN for Data-driven NextG Cellular Networks,” *IEEE Communications Magazine*, vol. 59, no. 10, pp. 21–27, October 2021.
- [13] A. V. Sheshashayee, M. Bordin, P. B. del Prever, D. Villa, H. Cheng, C. Petrioli, T. Melodia, and S. Basagni, “Experimental Evaluation of the Performance of UAV-assisted Data Collection for Wake-up Radio-enabled Wireless Networks,” in *2024 IEEE 99th Vehicular Technology Conference (VTC2024-Spring)*, June 2024, pp. 1–6.
- [14] D. Villa, M. Tehrani-Moayyed, P. Johari, S. Basagni, and T. Melodia, “CaST: A Toolchain for Creating and Characterizing Realistic Wireless Network Emulation Scenarios,” in *Proceedings of the ACM Workshop on Wireless Network Testbeds, Experimental Evaluation & Characterization (WiNTECH)*, Sydney, Australia, October 2022.
- [15] P. Johari, T. Melodia, M. Polese, L. Bonati, and D. Villa, “Smart and Real-time Digital Twins for Open, Programmable and Virtualized Wireless Network Systems,” May 2025, US Patent Application US20250139324A1.
- [16] D. Villa, D. Uvaydov, L. Bonati, P. Johari, J. M. Jornet, and T. Melodia, “Twinning Commercial Radio Waveforms in the Colosseum Wireless Network Emulator,” in *Proc. of ACM WiNTECH*, Madrid, Spain, October 2023.
- [17] A. Saeizadeh, M. Tehrani-Moayyed, D. Villa, J. G. Beattie, I. C. Wong, P. Johari, E. W. Anderson, S. Basagni, and T. Melodia, “AI-assisted Agile Propagation Modeling for Real-time Digital Twin Wireless Networks,” in *2024 IEEE 29th International Workshop on Computer Aided Modeling and Design of Communication Links and Networks (CAMAD)*, 2024, pp. 1–6.
- [18] A. Saeizadeh, M. Tehrani-Moayyed, D. Villa, J. G. B. Jr., P. Johari, S. Basagni, and T. Melodia, “AIRMap – AI-Generated Radio Maps for Wireless Digital Twins,” *arXiv:2511.05522 [eess.SP]*, 2025.
- [19] O. T. Basaran, D. Villa, P. Johari, M. Polese, C. Fiandrino, F. Dressler, and T. Melodia, “Gen-TWIN: Generative-AI-Enabled Digital Twin for Open Radio Access Networks,” in *Proceedings of IEEE Digital Twins over NextG Wireless Networks (DTWin)*, London, UK, May 2025.
- [20] D. Villa, I. Khan, F. Kaltenberger, N. Hedberg, R. S. da Silva, A. Kelkar, C. Dick, S. Basagni, J. M. Jornet, T. Melodia, M. Polese, and D. Koutsonikolas, “An Open, Programmable, Multi-vendor 5G O-RAN Testbed with NVIDIA ARC and OpenAirInterface,” in *Proceedings of*

BIBLIOGRAPHY

the 2nd Workshop on Next-generation Open and Programmable Radio Access Networks (NG-OPERA), May 2024.

- [21] D. Villa, I. Khan, F. Kaltenberger, N. Hedberg, R. S. da Silva, S. Maxenti, L. Bonati, A. Kelkar, C. Dick, E. Baena, J. M. Jornet, T. Melodia, M. Polese, and D. Koutsonikolas, “X5G: An Open, Programmable, Multi-Vendor, End-to-End, Private 5G O-RAN Testbed With NVIDIA ARC and OpenAirInterface,” *IEEE Transactions on Mobile Computing*, vol. 24, no. 11, pp. 11 305–11 322, 2025.
- [22] D. Villa, M. Belgiovine, N. Hedberg, M. Polese, C. Dick, and T. Melodia, “Programmable and GPU-Accelerated Edge Inference for Real-Time ISAC on NVIDIA ARC-OTA,” *arXiv:2512.06493 [cs.NI]*, 2025.
- [23] N. Neasamoni Santhi, D. Villa, M. Polese, and T. Melodia, “InterfO-RAN: Real-Time In-band Cellular Uplink Interference Detection with GPU-Accelerated dApps,” *Proc. of ACM International Symposium on Theory, Algorithmic Foundations, and Protocol Design for Mobile Networks and Mobile Computing (MobiHoc)*, October 2025.
- [24] H. Cheng, S. D’Oro, R. Gangula, S. Velumani, D. Villa, L. Bonati, M. Polese, T. Melodia, G. Arrobo, and C. Maciocco, “ORANSlice: An Open Source 5G Network Slicing Platform for O-RAN,” in *Proceedings of ACM Workshop on Open and AI RAN*, Washington, DC, USA, November 2024.
- [25] J. Groen, S. DiValerio, I. Karim, D. Villa, Y. Zhang, L. Bonati, M. Polese, S. D’Oro, T. Melodia, E. Bertino, F. Cuomo, and K. Chowdhury, “TIMESAFE: Timing Interruption Monitoring and Security Assessment for Fronthaul Environments,” *ACM Transactions on Privacy and Security*, November 2025.
- [26] Platforms for Advanced Wireless Research (PAWR). <https://www.advancedwireless.org>. Accessed March 2023.
- [27] K. R. Dandekar, S. Begashaw, M. Jacovic, A. Lackpour, I. Rasheed, X. R. Rey, C. Sahin, S. Shaher, and G. Mainland, “Grid Software Defined Radio Network Testbed for Hybrid Measurement and Emulation,” in *Proceedings of IEEE SECON*, Boston, MA, USA, June 2019.
- [28] M. Kohli, T. Chen, M. B. Dastjerdi, J. Welles, I. Seskar, H. Krishnaswamy, and G. Zussman, “Open-Access Full-Duplex Wireless in the ORBIT and COSMOS Testbeds,” *Computer Networks*, 2021.
- [29] L. Bertizzolo, L. Bonati, E. Demirors, A. Al-shawabka, S. D’Oro, F. Restuccia, and T. Melodia, “Arena: A 64-antenna SDR-based Ceiling Grid Testing Platform for Sub-6 GHz 5G-and-Beyond Radio Spectrum Research,” *Computer Networks*, vol. 181, p. 107436, 2020.
- [30] M. L. Sichitiu, I. Güvenç, R. Dutta, V. Marojevic, and B. Floyd, “AERPAW Emulation Overview,” in *Proceedings of ACM WiNTECH 2020*, London, UK, September 25 2020, pp. 1–8.

BIBLIOGRAPHY

- [31] B. R. Barricelli, E. Casiraghi, and D. Fogli, “A Survey on Digital Twin: Definitions, Characteristics, Applications, and Design Implications,” *IEEE Access*, vol. 7, pp. 167 653–167 671, 2 December 2019.
- [32] R. Saracco. (2022, June 12) 5G network digital twin(s). IEEE Future Directions: <https://www.advancedwireless.org>. Accessed March 2023.
- [33] P. Öhlén. (2021, July) The future of digital twins: what will they mean for mobile networks? <https://www.ericsson.com/en/blog/2021/7/future-digital-twins-in-mobile-networks>. Accessed March 2023.
- [34] Spirent, “Simplifying 5G with the Network Digital Twin,” *White paper*, 2019.
- [35] M. Polese, L. Bonati, S. D’Oro, P. Johari, D. Villa, S. Velumani, R. Gangula, M. Tsampazi, C. P. Robinson, G. Gemmi, A. Lacava, S. Maxenti, H. Cheng, and T. Melodia, “Colosseum: The Open RAN Digital Twin,” *IEEE Open Journal of the Communications Society*, vol. 5, pp. 5452–5466, 2024.
- [36] D. Jones, C. Snider, A. Nassehi, J. Yon, and B. Hicks, “Characterising the Digital Twin: A systematic literature review,” *CIRP Journal of Manufacturing Science and Technology*, vol. 29, pp. 36–52, May 2020.
- [37] M. Grieves, “Digital Twin: Manufacturing Excellence through Virtual Factory Replication,” *White paper*, March 2015.
- [38] R. Rolle, V. Martucci, and E. Godoy, “Architecture for Digital Twin implementation focusing on Industry 4.0,” *IEEE Latin America Transactions*, vol. 18, no. 05, pp. 889–898, April 2020.
- [39] F. Tao, H. Zhang, A. Liu, and A. Y. C. Nee, “Digital Twin in Industry: State-of-the-Art,” *IEEE Transactions on Industrial Informatics*, vol. 15, no. 4, pp. 2405–2415, September 2019.
- [40] Y. Wu, K. Zhang, and Y. Zhang, “Digital Twin Networks: A Survey,” *IEEE Internet of Things Journal*, vol. 8, no. 18, pp. 13 789–13 804, May 2021.
- [41] M. Polese, L. Bonati, S. D’Oro, S. Basagni, and T. Melodia, “ColO-RAN: Developing Machine Learning-based xApps for Open RAN Closed-loop Control on Programmable Experimental Platforms,” *IEEE Transactions on Mobile Computing*, pp. 1–14, 2022.
- [42] S. D’Oro, L. Bonati, M. Polese, and T. Melodia, “OrchestRAN: Network Automation through Orchestrated Intelligence in the Open RAN,” in *Proc. of IEEE INFOCOM*, Virtual Conference, May 2022.
- [43] A. Pinto, A. Ashdown, T. Hassan, H. Cheng, F. Esposito, L. Bonati, S. D’Oro, T. Melodia, and F. Restuccia, “An Emulation-Based Framework for Transport Layer Measurements over 5G Wireless Networks,” in *Proc. of ACM WiTECH*, Madrid, Spain, October 2023.
- [44] L. Baldesi, F. Restuccia, and T. Melodia, “ChARM: NextG Spectrum Sharing Through Data-Driven Real-Time O-RAN Dynamic Control,” in *Proceedings of IEEE INFOCOM*, May 2022.

BIBLIOGRAPHY

- [45] C. P. Robinson, L. Bonati, T. Van Nieuwstadt, P. Johari, M. Polese, H. Nguyen, C. Watson, and T. Melodia, “eSWORD: Implementation of Wireless Jamming Attacks in a Real-World Emulated Network,” in *Proc. of IEEE Wireless Communications and Networking Conf. (WCNC)*, Glasgow, UK, March 2023.
- [46] L. Bonati, M. Polese, S. D’Oro, S. Basagni, and T. Melodia, “OpenRAN Gym: AI/ML Development, Data Collection, and Testing for O-RAN on PAWR Platforms,” *Computer Networks*, vol. 220, p. 109502, 2023.
- [47] F. Kaltenberger, A. P. Silva, A. Gosain, L. Wang, and T.-T. Nguyen, “OpenAirInterface: Democratizing innovation in the 5G Era,” *Computer Networks*, vol. 176, p. 107284, 2020.
- [48] A. Chaudhari and M. Braun, “A Scalable FPGA Architecture for Flexible, Large-Scale, Real-Time RF Channel Emulation,” in *Proceedings of IEEE ReCoSoC*, Lille, France, July 2018.
- [49] U.S. Naval Research Laboratory. MGEN Traffic Emulator. <https://www.nrl.navy.mil/Our-Work/Areas-of-Research/Information-Technology/NCS/MGEN>. Accessed March 2023.
- [50] Remcom, *Wireless InSite Reference Manual, version 3.3.3*, June 2019.
- [51] ETSI, “5G Study on channel model for frequencies from 0.5 to 100 GHz,” 3GPP TR 38.901 version 14.3.0 Release 14, 2018.
- [52] M. Tehrani Moayyed, L. Bonati, P. Johari, T. Melodia, and S. Basagni, “Creating RF Scenarios for Large-scale, Real-time Wireless Channel Emulators,” in *Proceedings of IEEE MedComNet 2021*, Virtual Conference, June 2021, pp. 1–8.
- [53] Eric Blossom and GNU Radio Project. GNU Radio. <https://www.gnuradio.org>. Accessed November 2022.
- [54] J. R. Buck, M. M. Daniel, and A. C. Singer, *Computer Explorations in Signals and Systems Using MATLAB®*, 2nd ed. Prentice Hall, 2002.
- [55] R. Defosseux, B. Djalal, R. Hardy, M. Ismail, and R. Schmidt, “OAI continuous integration home,” 2023. [Online]. Available: <https://gitlab.eurecom.fr/oai/openairinterface5g/-/wikis/ci/continuous-integration-home>
- [56] J. M. Velazquez-Gutierrez and C. Vargas-Rosales, “Sequence Sets in Wireless Communication Systems: A Survey,” *IEEE Communications Surveys & Tutorials*, vol. 19, pp. 1225–1248, December 2016.
- [57] S. Stanczak, H. Boche, and M. Haardt, “Are LAS-codes a Miracle?” in *Proceedings of IEEE GLOBECOM 2001*, San Antonio, TX, November 25–29 2001, pp. 589–593.
- [58] Z. Xinyu, “Analysis of M-sequence and Gold-sequence in CDMA System,” in *Proceedings of IEEE ICCSN 2011*, Xián, China, May 27–29 2011, pp. 466–468.

BIBLIOGRAPHY

- [59] M. Golay, “Complementary series,” *IRE Transactions on Information Theory*, vol. 7, no. 2, pp. 82–87, April 1961.
- [60] IEEE 802.11 Wireless LAN Working Group, “IEEE Standard for Information Technology – Part 11 - Amendment 3,” *IEEE Std 802.11ad-2012 (Amendment to IEEE Std 802.11-2012)*, pp. 1–598, December 2012.
- [61] E. García Núñez, J. García, J. Ureña, C. Pérez-Rubio, and A. Hernández, “Generation Algorithm for Multilevel LS Codes,” *Electronics Letters*, vol. 46, pp. 1465–1467, November 2010.
- [62] D. K. Pradhan and M. Chatterjee, “GLFSR–A New Test Pattern Generator for Built-in-self-test,” *IEEE Transactions on Computer-Aided Design of Integrated Circuits and Systems*, vol. 18, pp. 238–247, February 1999.
- [63] Last Software and Google. SketchUp. <https://www.sketchup.com>. Accessed November 2022.
- [64] L. Bonati, S. D’Oro, S. Basagni, and T. Melodia, “SCOPE: An Open and Softwarized Prototyping Platform for NextG Systems,” in *Proc. of ACM Intl. Conf. on Mobile Systems, Applications, and Services (MobiSys)*, Virtual Conference, June 2021, pp. 415–426.
- [65] I. Gomez-Miguel, A. Garcia-Saavedra, P. Sutton, P. Serrano, C. Cano, and D. Leith, “srsLTE: An Open-source Platform for LTE Evolution and Experimentation,” in *Proceedings of ACM WiNTECH*, New York City, NY, USA, October 2016.
- [66] R. McMahon, B. Kaushik, and T. Auckland. iPerf. <https://iperf.fr/>. Accessed November 2022.
- [67] “Jammer Enforcement,” Mar. 2011. [Online]. Available: <https://www.fcc.gov/general/jammer-enforcement>
- [68] B. Bloessl, “IEEE 802.11 a/g/p Transceiver,” November 2022, original-date: 2013-03-24T16:26:18Z. [Online]. Available: <https://github.com/bastibl/gr-ieee802-11>
- [69] W. Kritzinger, M. Karner, G. Traar, J. Henjes, and W. Sihn, “Digital Twin in manufacturing: A categorical literature review and classification,” *IFAC-PapersOnLine*, vol. 51, no. 11, pp. 1016–1022, June 2018, 16th IFAC Symposium on Information Control Problems in Manufacturing INCOM 2018.
- [70] S. Zeb, A. Mahmood, S. A. Hassan, M. J. Piran, M. Gidlund, and M. Guizani, “Industrial digital twins at the nexus of NextG wireless networks and computational intelligence: A survey,” *Journal of Network and Computer Applications*, vol. 200, p. 103309, April 2022.
- [71] H. X. Nguyen, R. Trestian, D. To, and M. Tatipamula, “Digital Twin for 5G and Beyond,” *IEEE Communications Magazine*, vol. 59, no. 2, pp. 10–15, February 2021.
- [72] L. U. Khan, W. Saad, D. Niyato, Z. Han, and C. S. Hong, “Digital-Twin-Enabled 6G: Vision, Architectural Trends, and Future Directions,” *IEEE Communications Magazine*, vol. 60, no. 1, pp. 74–80, January 2022.

BIBLIOGRAPHY

- [73] Y. He, M. Yang, Z. He, and M. Guizani, “Resource Allocation Based on Digital Twin-enabled Federated Learning Framework in Heterogeneous Cellular Network,” *IEEE Transactions on Vehicular Technology*, pp. 1–10, September 2022.
- [74] Y. Lu, X. Huang, K. Zhang, S. Maharjan, and Y. Zhang, “Low-Latency Federated Learning and Blockchain for Edge Association in Digital Twin Empowered 6G Networks,” *IEEE Transactions on Industrial Informatics*, vol. 17, no. 7, pp. 5098–5107, August 2021.
- [75] L. Zhao, G. Han, Z. Li, and L. Shu, “Intelligent Digital Twin-Based Software-Defined Vehicular Networks,” *IEEE Network*, vol. 34, no. 5, pp. 178–184, June 2020.
- [76] A. Patnaik, A. Talebzadeh, M. Tsiklauri, D. Pommerenke, C. Ding, D. White, S. Scearce, and Y. Yang, “Implementation of a 18 GHz Bandwidth Channel Emulator Using an FIR Filter,” in *Proceeding of IEEE EMC 2014*, Raleigh, NC, August 4–8 2014, pp. 950–955.
- [77] S. Ju and T. S. Rappaport, “Simulating Motion-incorporating Spatial Consistency into NYUSIM Channel Model,” in *Proceedings of IEEE VTC 2018–Fall*, Chicago, IL, August 27–30 2018, pp. 1–6.
- [78] D. Bilibashi, E. M. Vitucci, and V. Degli-Esposti, “Dynamic Ray Tracing: Introduction and Concept,” in *Proceedings of EuCAP 2020*, Copenhagen, Denmark, March 15–20 2020, pp. 1–5.
- [79] A. Oliveira, I. Trindade, M. Dias, and A. Klautau, “Ray-tracing 5G Channels from Scenarios with Mobility Control of Vehicles and Pedestrians,” in *Proceedings of SBrT 2019*, Petrópolis, RJ, Brasil, September 2019.
- [80] D. Villa, D. Uvaydov, L. Bonati, P. Johari, J. M. Jornet, and T. Melodia, “Demo: Intelligent Radar Detection in CBRS Band in the Colosseum Wireless Network Emulator,” *arXiv:2309.08861 [cs.NI]*, 2023.
- [81] G. Luo, Q. Yuan, J. Li, S. Wang, and F. Yang, “Artificial intelligence powered mobile networks: From cognition to decision,” *IEEE Network*, vol. 36, no. 3, pp. 136–144, July 2022.
- [82] R. Caromi, M. Souryal, and W. Yang, “Detection of Incumbent Radar in the 3.5 GHz CBRS Band,” in *Proceedings of IEEE GlobalSIP*, November 2018, pp. 241–245.
- [83] S. D’Oro, M. Polese, L. Bonati, H. Cheng, and T. Melodia, “dApps: Distributed Applications for Real-time Inference and Control in O-RAN,” *IEEE Communications Magazine*, 2022.
- [84] J. Gao, X. Yi, C. Zhong, X. Chen, and Z. Zhang, “Deep Learning for Spectrum Sensing,” *IEEE Wireless Communications Letters*, vol. 8, no. 6, pp. 1727–1730, September 2019.
- [85] Y. Wang, M. Liu, J. Yang, and G. Gui, “Data-Driven Deep Learning for Automatic Modulation Recognition in Cognitive Radios,” *IEEE Transactions on Vehicular Technology*, vol. 68, no. 4, pp. 4074–4077, February 2019.

BIBLIOGRAPHY

- [86] S. Zheng, S. Chen, P. Qi, H. Zhou, and X. Yang, “Spectrum Sensing Based on Deep Learning Classification for Cognitive Radios,” *China Communications*, vol. 17, no. 2, pp. 138–148, February 2020.
- [87] O. Goldreich, “Requirements for Commercial Operation in the U.S. 3550-3700 MHz Citizens Broadband Radio Service Band,” in *Wireless Innovation Forum*, 2016.
- [88] B. R. Mahafza, *Introduction to Radar Analysis*. CRC press, 2017.
- [89] R. J. Doviak and D. Zrnić, *Doppler Radar and Weather Observations*. Courier Corporation, 2006.
- [90] O. of the Federal Register (United States), *Citizens Broadband Radio Service*. Code of Federal Regulations, 2016, vol. 96.
- [91] Unwired Labs. (Accessed June 2023) OpenCellID. <https://opencellid.org>.
- [92] OpenStreetMap Foundation. (Accessed June 2023) OpenStreetMap. <https://www.openstreetmap.org>.
- [93] D. W. Taylor, *The Speed and Power of Ships*. Books on Demand, 2013.
- [94] K. Simonyan and A. Zisserman, “Very deep convolutional networks for large-scale image recognition,” *arXiv preprint arXiv:1409.1556 [cs.CV]*, September 2014.
- [95] X. Wang, R. Girshick, A. Gupta, and K. He, “Non-local neural networks,” in *Proceedings of the IEEE/CVF Conference on Computer Vision and Pattern Recognition*, Salt Lake City, UT, USA, June 2018.
- [96] X. Zhao, F. Du, S. Geng, Z. Fu, Z. Wang, Y. Zhang, Z. Zhou, L. Zhang, and L. Yang, “Playback of 5G and Beyond Measured MIMO Channels by an ANN-Based Modeling and Simulation Framework,” *IEEE journal on selected areas in communications*, vol. 38, no. 9, pp. 1945–1954, 2020.
- [97] 3GPP, “Study on channel model for frequencies from 0.5 to 100 GHz,” 3rd Generation Partnership Project (3GPP), Technical Report 38.901, 2020, version 16.1.0.
- [98] T. Zemen, J. Gomez-Ponce, A. Chandra, M. Walter, E. Aksoy, R. He, D. Matolak, M. Kim, J.-I. Takada, S. Salous, R. Valenzuela, and A. F. Molisch, “Site-Specific Radio Channel Representation for 5G and 6G,” *IEEE Communications Magazine*, vol. 63, no. 6, pp. 106–113, June 2025.
- [99] F. Fuschini, E. M. Vitucci, M. Barbiroli, G. Falciasecca, and V. Degli-Esposti, “Ray tracing propagation modeling for future small-cell and indoor applications: A review of current techniques: RAY TRACING RADIO PROPAGATION MODELING,” *Radio Science*, vol. 50, no. 6, pp. 469–485, June 2015.
- [100] Z. El-friakh, A. M. Voicu, S. Shabani, L. Simić, and P. Mähönen, “Crowdsourced Indoor Wi-Fi REMs: Does the Spatial Interpolation Method Matter?” in *2018 IEEE International Symposium on Dynamic Spectrum Access Networks (DySPAN)*, October 2018, pp. 1–10.

BIBLIOGRAPHY

- [101] REMCOM, “Wireless Insite,” <https://www.remcom.com/wireless-insite-em-propagation-software>.
- [102] Boston Planning and Development Agency, “3D Data and Maps,” 2024, accessed: 2024-06-30. [Online]. Available: <https://www.bostonplans.org/3d-data-maps/>
- [103] G. Gemmi, P. Johari, P. Casari, M. Polese, T. Melodia, and M. Segata, “ColosSUMO: Evaluating Cooperative Driving Applications with Colosseum,” in *2024 IEEE Vehicular Networking Conference (VNC)*, May 2024, pp. 97–100. [Online]. Available: <https://ieeexplore.ieee.org/document/10576000/>
- [104] T. Miyato, T. Kataoka, M. Koyama, and Y. Yoshida, “Spectral Normalization for Generative Adversarial Networks,” arXiv, cs.NI 1802.05957, Feb. 2018.
- [105] B. Xu, N. Wang, T. Chen, and M. Li, “Empirical Evaluation of Rectified Activations in Convolutional Network,” arXiv, cs.NI 1505.00853, Nov. 2015.
- [106] H. Zhang, I. Goodfellow, D. Metaxas, and A. Odena, “Self-Attention Generative Adversarial Networks,” arXiv, cs.NI 1805.08318, Jun. 2019.
- [107] J. Breen, A. Buffmire, J. Duerig, K. Dutt, E. Eide, M. Hibler, D. Johnson, S. K. Kasera, E. Lewis, D. Maas, A. Orange, N. Patwari, D. Reading, R. Ricci, D. Schurig, L. B. Stoller, J. Van der Merwe, K. Webb, and G. Wong, “POWDER: Platform for Open Wireless Data-driven Experimental Research,” in *Proceedings of ACM WiNTECH*, New York, NY, USA, 2020.
- [108] J. Yoon, D. Jarrett, and M. van der Schaar, “Time-series generative adversarial networks,” in *NeurIPS 2019*. Vancouver, Canada: Curran Associates Inc., Dec. 2019.
- [109] D. Bank, N. Koenigstein, and R. Giryes, “Autoencoders,” arXiv, cs.NI 2003.05991, Apr. 2021.
- [110] Z. Huang, W. Xu, and K. Yu, “Bidirectional LSTM-CRF Models for Sequence Tagging,” arXiv, cs.NI 1508.01991, Aug. 2015.
- [111] A. Benchama and K. Zebbar, “Novel Approach to Intrusion Detection: Introducing GAN-MSCNN-BILSTM with LIME Predictions,” arXiv, cs.NI 2406.05443, Jun. 2024.
- [112] A. Radford, L. Metz, and S. Chintala, “Unsupervised Representation Learning with Deep Convolutional Generative Adversarial Networks,” arXiv, cs.NI 1511.06434, Jan. 2016.
- [113] M. Heusel, H. Ramsauer, T. Unterthiner, B. Nessler, and S. Hochreiter, “GANs Trained by a Two Time-Scale Update Rule Converge to a Local Nash Equilibrium,” arXiv, cs.NI 1706.08500, Jan. 2018.
- [114] A. Narayanan, M. I. Rochman, A. Hassan, B. S. Firmansyah, V. Sathya, M. Ghosh, F. Qian, and Z.-L. Zhang, “A Comparative Measurement Study of Commercial 5G mmWave Deployments,” in *IEEE Conference on Computer Communications*, May 2022.

BIBLIOGRAPHY

- [115] L. Bonati, M. Polese, S. D’Oro, S. Basagni, and T. Melodia, “NeutRAN: An Open RAN Neutral Host Architecture for Zero-Touch RAN and Spectrum Sharing,” *IEEE Transactions on Mobile Computing*, vol. 23, no. 5, pp. 5786–5798, 2024.
- [116] S. Pongratz, “Open RAN Market Opportunity and Risks,” Dell’Oro Group report, November 2021.
- [117] F. Kaltenberger, T. Melodia, I. Ghauri, M. Polese, R. Knopp, T. T. Nguyen, S. Velumani, D. Villa, L. Bonati, R. Schmidt, S. Arora, M. Irazabal, and N. Nikaein, “Driving Innovation in 6G Wireless Technologies: The OpenAirInterface Approach,” *Computer Networks*, vol. 269, p. 111410, September 2025.
- [118] Meticulous Research. 5G Testing Market. [Online]. Available: <https://www.meticulousresearch.com/product/5g-testing-market-5482>
- [119] P. Bahl, M. Balkwill, X. Foukas, A. Kalia, D. Kim, M. Kotaru, Z. Lai, S. Mehrotra, B. Radunovic, S. Saroiu, C. Settle, A. Verma, A. Wolman, F. Y. Yan, and Y. Zhang, “Accelerating Open RAN Research Through an Enterprise-Scale 5G Testbed,” in *Proceedings of ACM MobiCom ’23*, Madrid, Spain, October 2023.
- [120] B. Tang, V. K. Shah, V. Marojevic, and J. H. Reed, “AI Testing Framework for Next-G O-RAN Networks: Requirements, Design, and Research Opportunities,” *IEEE Wireless Communications*, vol. 30, no. 1, pp. 70–77, February 2023.
- [121] C. Fiandrino, L. Bonati, S. D’Oro, M. Polese, T. Melodia, and J. Widmer, “EXPLORA: AI/ML EXPLAINability for the Open RAN,” in *Proceedings of ACM CoNEXT*, vol. 1, Paris, France, December 2023, pp. 1–26.
- [122] Small Cell Forum, “5G FAPI: PHY API Specification,” SCF, Techreport 222.10.02, March 2020.
- [123] A. Kelkar and C. Dick, “NVIDIA Aerial GPU Hosted AI-on-5G,” in *IEEE 4th 5G World Forum (5GWF)*, October 2021, pp. 64–69.
- [124] NVIDIA Corporation. Aerial CUDA-Accelerated RAN. Accessed June 2024. [Online]. Available: <https://docs.nvidia.com/aerial/cuda-accelerated-ran/index.html>
- [125] Small Cell Forum, “5G nFAPI specifications,” SCF, Techreport 225.2.1, November 2021.
- [126] O-RAN Working Group 4, “O-RAN Working Group 4 (Open Fronthaul Interfaces WG) Control, User and Synchronization Plane Specification,” O-RAN Alliance, Techreport O-RAN.WG4.CUS.0-R003-v12.00, June 2023.
- [127] O-RAN Working Group 4. (2021, July) O-RAN Fronthaul Control, User and Synchronization Plane Specification 7.0. ORAN-WG4.CUS.0-v07.00 Technical Specification.
- [128] ETSI, “5G; NR; User Equipment (UE) radio access capabilities,” 3GPP TR 38.306 version 17.0.0 Release 17, 2022.

BIBLIOGRAPHY

- [129] Open5GS. <https://open5gs.org>. Accessed May 2024.
- [130] Keysight. P8850S CoreSIM — Core Simulation RAN Solutions. Accessed June 2024. [Online]. Available: <https://www.keysight.com/it/en/product/P8850S/coresim-core-simulation-ran-solutions.html>
- [131] A5G Networks. <https://a5gnet.com>. Accessed May 2024.
- [132] A. S. Abdalla, P. S. Upadhyaya, V. K. Shah, and V. Marojevic, “Toward Next Generation Open Radio Access Networks: What O-RAN Can and Cannot Do!” *IEEE Network*, vol. 36, no. 6, pp. 206–213, November 2022.
- [133] F. Mungari, “An RL Approach for Radio Resource Management in the O-RAN Architecture,” in *18th Annual IEEE International Conference on Sensing, Communication, and Networking (SECON)*, July 2021.
- [134] E. Moro, M. Polese, A. Capone, and T. Melodia, “An Open RAN Framework for the Dynamic Control of 5G Service Level Agreements,” in *IEEE Conference on Network Function Virtualization and Software Defined Networks (NFV-SDN)*, Dresden, Germany, November 2023.
- [135] O-RAN Software Community. (2022) sim-e2-interface repository. <https://github.com/o-ran-sc/sim-e2-interface>.
- [136] InfluxData. InfluxDB. <https://www.influxdata.com>. Accessed May 2024.
- [137] Grafana Labs. Grafana Dashboard. <https://grafana.com>. Accessed May 2024.
- [138] OpenRAN Gym. OpenRAN Gym Website. <https://openrangym.com/>. Accessed May 2024.
- [139] A. Lacava, L. Bonati, N. Mohamadi, R. Gangula, F. Kaltenberger, P. Johari, S. D’Oro, F. Cuomo, M. Polese, and T. Melodia, “dApps: Enabling Real-Time AI-Based Open RAN Control,” *Computer Networks*, vol. 269, p. 111342, September 2025.
- [140] OpenAirInterface Software Alliance. Accessed June 2024. [Online]. Available: <https://openairinterface.org>
- [141] Sierra Wireless. EM9191 5G NR Sub-6 GHz Module. <https://www.sierrawireless.com/iot-modules/5g-modules/em9191/>.
- [142] FCC: Engineering & Technology Bureau. (2021, August) FCC Designates New Innovation Zones For Advanced Wireless Technology Research And Innovation. Public Notice: FCC-21-92.
- [143] Keysight. P8822S RuSIM – UE / O-RU Emulation Over the O-RAN Fronthaul. Accessed June 2024. [Online]. Available: <https://www.keysight.com/it/en/product/P8822S/rusim-over-o-ran-fronthaul.html>
- [144] F. Bellard and B. Bingham, “FFMPEG.” [Online]. Available: <https://ffmpeg.org/ffmpeg.html>

BIBLIOGRAPHY

- [145] A. Inc., “Guidelines for Video Bitrates.” [Online]. Available: <https://support.google.com/youtube/answer/1722171?hl=en#zippy=%2Cbitrate>
- [146] ETSI, “NR, Base Station (BS) conformance testing, Part 2: Radiated conformance testing,” 3GPP TS 38.141-2 version 16.10.0 Release 16, December 2021.
- [147] Fujitsu. Fujitsu Press Release. Accessed December 2024. [Online]. Available: <https://www.fujitsu.com/global/about/resources/news/press-releases/2024/1113-01.html>
- [148] L. Kundu, X. Lin, and R. Gadiyar, “Towards Energy Efficient RAN: From Industry Standards to Trending Practice,” 2024. [Online]. Available: <https://arxiv.org/abs/2402.11993>
- [149] AI-RAN Alliance, “AI-RAN Alliance: Vision and Mission White Paper,” 2024. [Online]. Available: https://ai-ran.org/wp-content/uploads/2024/12/AI-RAN_Alliance_Whitepaper.pdf
- [150] Northeastern University, NVIDIA, Mavenir, MITRE, and Qualcomm, “dApps for Real-Time RAN Control: Use Cases and Requirement,” October 2024. [Online]. Available: <https://mediastorage.o-ran.org/ngrg-rr/nGRG-RR-2024-10-dApp%20use%20cases%20and%20requirements.pdf>
- [151] NVIDIA, “Aerial RAN co-lab over-the-air (ARC-OTA),” 2025. [Online]. Available: <https://docs.nvidia.com/aerial/aerial-ran-colab-ota/current/index.html>
- [152] NVIDIA Corporation, “Triton Inference Server: An Optimized Cloud and Edge Inferencing Solution,” 2018, accessed December 2025. [Online]. Available: <https://docs.nvidia.com/deeplearning/triton-inference-server/user-guide/docs/index.html>
- [153] A. Panicker, O. Ozdemir, M. L. Sichitiu, I. Guvenc, R. Dutta, V. Marojevic, and B. Floyd, “AERPAW Emulation Overview and Preliminary Performance Evaluation,” *Computer Networks*, vol. 194, pp. 1–11, July 2021.
- [154] T. Chen, P. Maddala, P. Skrimponis, J. Kolodziejski, A. Adhikari, H. Hu, Z. Gao, A. Paidimari, A. Valdes-Garcia, M. Lee, S. Rangan, G. Zussman, and I. Seskar, “Open-access millimeter-wave software-defined radios in the PAWR COSMOS testbed: Design, deployment, and experimentation,” *Computer Networks*, vol. 234, p. 109922, October 2023.
- [155] H. Zhang, Y. Guan, A. Kamal, D. Qiao, M. Zheng, A. Arora, O. Boyraz, B. Cox, T. Daniels, M. Darr, D. Jacobson, A. Khokhar, S. Kim, J. Koltes, J. Liu, M. Luby, L. Nadolny, J. Peschel, P. Schnable, A. Sharma, A. Somani, and L. Tang, “ARA: A Wireless Living Lab Vision for Smart and Connected Rural Communities,” in *Proceedings of ACM WiNTECH*, New Orleans, LA, USA, October 2021.
- [156] J. O. Boateng, T. Zhang, G. Zu, T. U. Islam, S. Babu, H. Zhang, and D. Qiao, “AraSDR: End-to-End, Fully-Programmable Living Lab for 5G and Beyond,” in *IEEE International Conference on Communications (ICC)*, Denver, CO, USA, June 2024.
- [157] F. Bimo, F. Feliana, S. Liao, C. Lin, D. F. Kinsey, J. Li, R. Jana, R. Wright, and R. Cheng, “OSC Community Lab: The Integration Test Bed for O-RAN Software Community,” in *IEEE Future Networks World Forum (FNWF)*, Los Alamitos, CA, USA, October 2022.

BIBLIOGRAPHY

- [158] 6G-SANDBOX. 6G-SANDBOX: The Experimental Facility for Advanced Wireless Research. <https://6g-sandbox.eu/>. Accessed May 2024.
- [159] A. Diaz Zayas, G. Caso, Ö. Alay, P. Merino, A. Brunstrom, D. Tsolkas, and H. Koumaras, “A Modular Experimentation Methodology for 5G Deployments: The 5GENESIS Approach,” *Sensors*, vol. 20, no. 22, 2020.
- [160] P. S. Upadhyaya, N. Tripathi, J. Gaeddert, and J. H. Reed, “Open AI Cellular (OAIC): An Open Source 5G O-RAN Testbed for Design and Testing of AI-Based RAN Management Algorithms,” *IEEE Network*, vol. 37, no. 5, pp. 7–15, September 2023.
- [161] A. Tripathi, J. S. Mallu, M. H. Rahman, A. Sultana, A. Sathish, A. Huff, M. R. Chowdhury, and A. P. Da Silva, “End-to-End O-RAN Control-Loop For Radio Resource Allocation in SDR-Based 5G Network,” in *IEEE Military Communications Conference (MILCOM)*, December 2023.
- [162] O. R. Collaco, M. R. Chowdhury, A. P. da Silva, and L. DaSilva, “Enabling CBRS Experimentation through an OpenSAS and SDR-based CBSD,” in *IEEE Conference on Computer Communications Workshops (INFOCOM WKSHPS)*, August 2023.
- [163] G. Z. Bruno, G. M. Almeida, A. Sathish, A. P. da Silva, L. A. D. A. Huff, K. V. Cardoso, and C. B. Both, “Evaluating the Deployment of a Disaggregated Open RAN Controller On a Distributed Cloud Infrastructure,” *IEEE Transactions on Network and Service Management*, pp. 1–13, April 2024.
- [164] J. X. Salvat, J. A. Ayala-Romero, L. Zanzi, A. Garcia-Saavedra, and X. Costa-Perez, “Open Radio Access Networks (O-RAN) Experimentation Platform: Design and Datasets,” *IEEE Communications Magazine*, vol. 61, no. 9, pp. 138–144, June 2023.
- [165] J. Dürre, N. Werner, P. Matzakos, R. Knopp, A. Garcia, and C. Avellan, “A Disaggregated 5G Testbed for Professional Live Audio Production,” in *2022 IEEE International Symposium on Broadband Multimedia Systems and Broadcasting (BMSB)*, 2022, pp. 1–6.
- [166] H. Zafar, U. Fattore, F. Cirillo, and C. J. Bernardos, “Data Usage Control for Privacy-Enhanced Network Analytics in Private 5G Networks,” *IEEE Open Journal of the Communications Society*, pp. 1–1, 2024.
- [167] F. Crespo, J. Villegas, C. Baena, E. Baena, S. Fortes, and R. Barco, “Energy-Aware CPU Orchestration in O-RAN: A dApp-Driven Lightweight Approach,” *arXiv:2508.00629 [cs.NI]*, 2025.
- [168] X. Foukas, B. Radunovic, M. Balkwill, and Z. Lai, “Taking 5G RAN Analytics and Control to a New Level,” in *Proceedings of ACM MobiCom '23*. New York, NY, USA: ACM, October 2023.
- [169] K. Meng, C. Masouros, A. P. Petropulu, and L. Hanzo, “Cooperative ISAC Networks: Opportunities and Challenges,” *IEEE Wireless Communications*, vol. 32, no. 3, pp. 212–219, June 2025.

BIBLIOGRAPHY

- [170] K. He, X. Zhang, S. Ren, and J. Sun, “Deep Residual Learning for Image Recognition,” in *Proceedings of the IEEE Conference on Computer Vision and Pattern Recognition (CVPR)*, June 2016.
- [171] G. Jocher, J. Qiu, and A. Chaurasia, “Ultralytics YOLO,” January 2023. [Online]. Available: <https://github.com/ultralytics/ultralytics>
- [172] 3GPP, “Study on Integrated Sensing and Communication,” 3rd Generation Partnership Project (3GPP), Technical Specification 22.137, June 2024. [Online]. Available: https://www.3gpp.org/ftp/Specs/archive/22_series/22.137/
- [173] S. Lu, F. Liu, Y. Li, K. Zhang, H. Huang, J. Zou, X. Li, Y. Dong, F. Dong, J. Zhu, Y. Xiong, W. Yuan, Y. Cui, and L. Hanzo, “Integrated sensing and communications: Recent advances and ten open challenges,” *IEEE Internet of Things Journal*, vol. 11, no. 11, pp. 19 094–19 120, June 2024.
- [174] A. Liu, Z. Huang, M. Li, Y. Wan, W. Li, T. X. Han, C. Liu, R. Du, D. K. P. Tan, J. Lu, Y. Shen, F. Colone, and K. Chetty, “A survey on fundamental limits of integrated sensing and communication,” *IEEE Communications Surveys & Tutorials*, vol. 24, no. 2, pp. 994–1034, February 2022.
- [175] Z. Zhang, H. Ren, C. Pan, S. Hong, D. Wang, J. Wang, and X. You, “Target Localization in Cooperative ISAC Systems: A Scheme Based on 5G NR OFDM Signals,” *IEEE Transactions on Communications*, vol. 73, no. 5, pp. 3562–3578, May 2025.
- [176] P. Huang, F. Liu, F. Dong, and Z. Wang, “Uplink Collaborative Sensing with OFDM Communication Signals,” in *ICC 2025 - IEEE International Conference on Communications*, June 2025, pp. 1–6.
- [177] M. Dwivedi, I. E. L. Hulede, O. Venegas, J. Ashdown, and A. Mukherjee, “5G-Based Passive Radar Sensing for Human Activity Recognition Using Deep Learning,” in *2024 IEEE Radar Conference (RadarConf24)*, May 2024, pp. 1–6.
- [178] Y. Ruan, L. Chen, X. Zhou, G. Guo, and R. Chen, “Hi-Loc: Hybrid Indoor Localization via Enhanced 5G NR CSI,” *IEEE Transactions on Instrumentation and Measurement*, vol. 71, pp. 1–15, August 2022.
- [179] N. Bouknana, M. Ahadi, F. Kaltenberger, and R. Schmidt, “An O-RAN Framework for AI/ML-Based Localization with OpenAirInterface and FlexRIC,” *arXiv:2511.19233 [cs.NI]*, 2025.
- [180] F. Adib, Z. Kabelac, D. Katabi, and R. C. Miller, “3D Tracking via Body Radio Reflections,” in *11th USENIX Symposium on Networked Systems Design and Implementation (NSDI 14)*. Seattle, WA: USENIX Association, April 2014, pp. 317–329.
- [181] F. Adib and D. Katabi, “See through walls with WiFi!” *SIGCOMM Comput. Commun. Rev.*, vol. 43, no. 4, p. 75–86, August 2013.

BIBLIOGRAPHY

- [182] F. Wang, S. Zhou, S. Paney, J. Han, and D. Huang, “Person-in-WiFi: Fine-Grained Person Perception Using WiFi,” in *Proceedings of the IEEE/CVF International Conference on Computer Vision (ICCV)*, October 2019.
- [183] M. Kamel, W. Hamouda, and A. Youssef, “Ultra-Dense Networks: A Survey,” *IEEE Communications Surveys & Tutorials*, vol. 18, no. 4, pp. 2522–2545, 2016.
- [184] X. Ge, S. Tu, G. Mao, C.-X. Wang, and T. Han, “5G Ultra-Dense Cellular Networks,” *IEEE Wireless Communications*, vol. 23, no. 1, pp. 72–79, 2016.
- [185] E. Eren, “Spectrum for private networks: Recent advancements by countries,” 2025. [Online]. Available: <https://tinyurl.com/as3cndjd>
- [186] F. B. Mismar, B. L. Evans, and A. Alkhateeb, “Deep Reinforcement Learning for 5G Networks: Joint Beamforming, Power Control, and Interference Coordination,” *IEEE Transactions on Communications*, vol. 68, no. 3, pp. 1581–1592, 2020.
- [187] M. U. A. Siddiqui, F. Qamar, F. Ahmed, Q. N. Nguyen, and R. Hassan, “Interference Management in 5G and Beyond Network: Requirements, Challenges and Future Directions,” *IEEE Access*, vol. 9, 2021.
- [188] S. D’Oro, L. Bonati, F. Restuccia, and T. Melodia, “Coordinated 5G Network Slicing: How Constructive Interference Can Boost Network Throughput,” *IEEE/ACM Transactions on Networking*, vol. 29, no. 4, pp. 1881–1894, 2021.
- [189] C.-Y. Chen, Y.-Y. Chen, and H.-Y. Wei, “Multi-cell interference coordinated scheduling in mmWave 5G cellular systems,” in *Eighth International Conference on Ubiquitous and Future Networks (ICUFN)*, 2016, pp. 912–917.
- [190] W.-B. Yang, M. Souryal, and D. Griffith, “LTE Uplink Performance with Interference from In-Band Device-to-Device (D2D) Communications,” in *2015 IEEE Wireless Communications and Networking Conference (WCNC)*, 2015, pp. 669–674.
- [191] L. Kundu, X. Lin, E. Agostini, V. Ditya, and T. Martin, “Hardware Acceleration for Open Radio Access Networks: A Contemporary Overview,” *IEEE Communications Magazine*, vol. 62, no. 9, pp. 160–167, 2024.
- [192] E. Dahlman, S. Parkvall, and J. Skold, *5G NR: The Next Generation Wireless Access Technology*, 1st ed. Academic Press, 2018.
- [193] J. Ren, X. Zhang, and Y. Xin, “Using Deep Convolutional Neural Network to Recognize LTE Uplink Interference,” in *2019 IEEE Wireless Communications and Networking Conference (WCNC)*, 2019, pp. 1–6.
- [194] A. Medhat, M. Elattar, and O. M. Fahmy, “LTE Uplink Interference Inspection Using Convolutional Neural Networks,” in *2021 3rd Novel Intelligent and Leading Emerging Sciences Conference (NILES)*, 2021, pp. 318–322.

BIBLIOGRAPHY

- [195] F. B. Mismar, “Intermodulation Interference Detection in 6G Networks: A Machine Learning Approach,” in *IEEE Vehicular Technology Conference: (VTC-Spring)*, 2022.
- [196] F. Wu, R. Tan, C. Zhang, W. Fan, X. Chen, D. Niyato, and Y. Liu, “Mixed Numerology Interference Recognition Approach for 5G NR,” *IEEE Wireless Communications Letters*, vol. 10, no. 10, pp. 2135–2139, 2021.
- [197] M. Schmidt, D. Block, and U. Meier, “Wireless interference identification with convolutional neural networks,” in *2017 IEEE 15th International Conference on Industrial Informatics (INDIN)*, 2017, pp. 180–185.
- [198] M. Kulin, T. Kazaz, I. Moerman, and E. De Poorter, “End-to-End Learning From Spectrum Data: A Deep Learning Approach for Wireless Signal Identification in Spectrum Monitoring Applications,” *IEEE Access*, vol. 6, pp. 18 484–18 501, 2018.
- [199] L. Lai, D. Feng, and F.-C. Zheng, “Interference Detection and Resource Allocation in LTE Unlicensed Systems,” in *2020 IEEE Wireless Communications and Networking Conference (WCNC)*, 2020.
- [200] D. Uvaydov, S. D’Oro, F. Restuccia, and T. Melodia, “DeepSense: Fast wideband spectrum sensing through real-time in-the-loop deep learning,” in *IEEE Intl. Conf. on Computer Communications (INFOCOM)*, Vancouver, BC, Canada, May 2021.
- [201] K. Bechta, C. Ziolkowski, J. M. Kelner, and L. Nowosielski, “Modeling of Downlink Interference in Massive MIMO 5G Macro-Cell,” *Sensors*, vol. 21, no. 2, 2021.
- [202] P. Testolina, M. Polese, J. Jornet, T. Melodia, and M. Zorzi, “Modeling Interference for the Coexistence of 6G and Passive Sensing Systems,” *IEEE Transactions on Wireless Communications*, 2024.
- [203] G. Hattab, E. Visotsky, M. C. Cudak, and A. Ghosh, “Uplink Interference Mitigation Techniques for Coexistence of 5G Millimeter Wave Users With Incumbents at 70 and 80 GHz,” *IEEE Transactions on Wireless Communications*, vol. 18, no. 1, 2019.
- [204] S. Chaudhari and H. Kwon, “Machine Learning based Interference Whitening in 5G NR MIMO Receiver,” in *IEEE 95th Vehicular Technology Conference*, 2022.
- [205] O-RAN WG1, “O-RAN Slicing Architecture 13.0,” O-RAN.WG1.Slicing-Architecture-R003-v13.00 TS, June 2024.
- [206] O-RAN WG3, “O-RAN E2 Service Model (E2SM) Cell Configuration and Control 4.0,” O-RAN.WG3.E2SM-CCC-R003-v04.00 TS, June 2024.
- [207] ——, “O-RAN Near-RT RAN Intelligent Controller Near-RT RIC Architecture,” O-RAN.WG3.RICARCH-v06.00 TS, June 2024.
- [208] H. Zhang, H. Zhou, and M. Erol-Kantarci, “Federated Deep Reinforcement Learning for Resource Allocation in O-RAN Slicing,” in *IEEE Global Communications Conference (GLOBECOM)*, Dec 2022, pp. 958–963.

BIBLIOGRAPHY

- [209] O-RAN WG3, “Near-Real-time RAN Intelligent Controller Use Cases and Requirements 6.0,” O-RAN.WG3.0CR-R003-v6.00 TS, June 2024.
- [210] EURECOM, “OpenAirInterface5G,” 2024. [Online]. Available: <https://openairinterface.org/>
- [211] srsRAN Project, “srsRAN,” 2024. [Online]. Available: <https://www.srslte.com/>
- [212] Open5GS team, “Open5GS,” 2024. [Online]. Available: <https://github.com/open5gs/open5gs>
- [213] Linux Foundation, “Aether Project,” 2024. [Online]. Available: <https://aetherproject.org>
- [214] 3GPP, “5g network resource model (nrm),” 3rd Generation Partnership Project (3GPP), TS 28.541, 2021, version 16.4.0.
- [215] C.-C. Chen, C.-Y. Chang, and N. Nikaein, “FlexSlice: Flexible and Real-Time Programmable RAN Slicing Framework,” in *IEEE Global Communications Conference (GLOBECOM)*, 2023, pp. 3807–3812.
- [216] A. Kak, V.-Q. Pham, H.-T. Thieu, and N. Choi, “ProSLICE: An Open RAN-Based Approach to Programmable RAN Slicing,” in *IEEE Global Communications Conference (GLOBECOM)*, 2022, pp. 197–202.
- [217] Y. Chen, R. Yao, H. Hassanieh, and R. Mittal, “Channel-Aware 5G RAN Slicing with Customizable Schedulers,” in *20th USENIX Symposium on Networked Systems Design and Implementation (NSDI 23)*. Boston, MA: USENIX Association, Apr. 2023, pp. 1767–1782.
- [218] A. Balasingam, M. Kotaru, and P. Bahl, “Application-Level Service Assurance with 5G RAN Slicing,” in *USENIX Symposium on Networked Systems Design and Implementation (NSDI)*. Santa Clara, CA: USENIX Association, Apr. 2024, pp. 841–857.
- [219] M. Wong, A. Prasad, and A. C. Soong, “The Security Aspect of 5G Fronthaul,” *IEEE Wireless Communications*, vol. 29, no. 2, pp. 116–122, 2022.
- [220] Common Public Radio Interface, “Common Public Radio Interface: eCPRI Interface Specification V2.0,” Common Public Radio Interface, Tech. Rep., May 2019. [Online]. Available: http://www.cpri.info/downloads/eCPRI_v_2.0_2019_05_10c.pdf
- [221] ETSI, “Publicly Available Specification (PAS); O-RAN Fronthaul Control, User and Synchronization Plane Specification v07.02; (O-RAN-WG4.CUS.0-v07.02),” ETSI TS 103 859 V7.0.2 (2022-09), Tech. Rep., 2022.
- [222] D. Dik and M. S. Berger, “Transport Security Considerations for the O-RAN Fronthaul,” in *2021 IEEE 4th 5G World Forum (5GWF)*. IEEE, 2021, pp. 253–258.
- [223] C.-F. Hung, Y.-R. Chen, C.-H. Tseng, and S.-M. Cheng, “Security Threats to xApps Access Control and E2 Interface in O-RAN,” *IEEE Open Journal of the Communications Society*, vol. 5, pp. 1197–1203, 2024.

BIBLIOGRAPHY

- [224] T. O. Atalay, S. Maitra, D. Stojadinovic, A. Stavrou, and H. Wang, “Securing 5G OpenRAN with a Scalable Authorization Framework for xApps,” in *IEEE INFOCOM 2023 - IEEE Conference on Computer Communications*, 2023, pp. 1–10.
- [225] K. Thimmaraju, A. Shaik, S. Flück, P. J. F. Mora, C. Werling, and J.-P. Seifert, “Security Testing The O-RAN Near-Real Time RIC & A1 Interface,” in *Proceedings of the 17th ACM Conference on Security and Privacy in Wireless and Mobile Networks*, ser. WiSec ’24. New York, NY, USA: Association for Computing Machinery, 2024, p. 277–287. [Online]. Available: <https://doi.org/10.1145/3643833.3656118>
- [226] J. Boswell and S. Poretsky, “Security considerations of Open RAN,” *Stockholm: Ericsson*, 2020.
- [227] O-RAN Working Group 11, “Security Requirements Specifications,” O-RAN.WG11.Security-Requirements-Specification.O-R003-v06.00, Tech. Rep., June 2023.
- [228] D. of Defense, “5G Strategy Implementation Plan,” Department of Defense, Tech. Rep., December 2020, accessed: 2024-02-15. [Online]. Available: <https://apps.dtic.mil/sti/pdfs/AD1118833.pdf>
- [229] J. Groen, S. D’Oro, U. Demir, L. Bonati, D. Villa, M. Polese, T. Melodia, and K. Chowdhury, “Securing O-RAN Open Interfaces,” *IEEE Transactions on Mobile Computing*, vol. 23, pp. 1–13, December 2024.
- [230] E. Municio, G. Garcia-Aviles, A. Garcia-Saavedra, and X. Costa-Pérez, “O-RAN: Analysis of Latency-Critical Interfaces and Overview of Time Sensitive Networking Solutions,” *IEEE Communications Standards Magazine*, vol. 7, no. 3, pp. 82–89, 2023.
- [231] A. Maamary, H. A. Alameddine, M. Debbabi, and C. Assi, “Synchronization Plane in O-RAN: Overview, Security and Research Directions,” *IEEE Communications Magazine*, pp. 1–7, 2024.
- [232] S. Shi, Y. Xiao, C. Du, M. H. Shahriar, A. Li, N. Zhang, Y. T. Hou, and W. Lou, “MS-PTP: Protecting Network Timing from Byzantine Attacks,” in *Proceedings of the 16th ACM Conference on Security and Privacy in Wireless and Mobile Networks*, 2023, pp. 61–71.
- [233] IEEE, “IEEE Standard for a Precision Clock Synchronization Protocol for Networked Measurement and Control Systems,” *IEEE Std 1588-2019 (Revision of IEEE Std 1588-2008)*, pp. 1–499, 2020.
- [234] “NIST Special Publication 800-207: Zero Trust Architecture,” 2020.
- [235] O-RAN Working Group 11, “O-RAN Security Threat Modeling and Risk Assessment,” O-RAN.WG11.Threat-Modeling.O-R003-v03.0, Tech. Rep., 2024.
- [236] ——, “O-RAN Security Test Specifications,” O-RAN.WG11.SecTestSpecs.O-R003-v07.00, Tech. Rep., 2024.

BIBLIOGRAPHY

- [237] J. Groen, S. D’Oro, U. Demir, L. Bonati, M. Polese, T. Melodia, and K. Chowdhury, “Implementing and evaluating security in O-RAN: Interfaces, Intelligence, and Platforms,” *IEEE Network*, 2024.
- [238] F. Rezabek, M. Helm, T. Leonhardt, and G. Carle, “PTP security measures and their impact on synchronization accuracy,” in *2022 18th International Conference on Network and Service Management (CNSM)*. IEEE, 2022, pp. 109–117.
- [239] IBM, “IBM X-Force Cloud Threat Landscape Report 2023,” IBM Corporation, Tech. Rep., 2023. [Online]. Available: <https://www.ibm.com/downloads/cas/QWBXVAPL>
- [240] C. D. Hylander, P. Langlois, A. Pinto, and S. Widup, “2024 Data Breach Investigations Report,” Verizon Business, Tech. Rep., 2024. [Online]. Available: <https://www.verizon.com/business/resources/Tce6/reports/2024-dbir-data-breach-investigations-report.pdf>
- [241] J. Xing, S. Yoo, X. Foukas, D. Kim, and M. K. Reiter, “On the Criticality of Integrity Protection in 5G Fronthaul Networks,” in *33rd USENIX Security Symposium (USENIX Security 24)*, 2024, pp. 4463–4479.
- [242] National Institute of Standards and Technology (NIST). (2024) Common Vulnerability Scoring System (CVSS) v3 Calculator. <https://nvd.nist.gov/vuln-metrics/cvss/v3-calculator>. Accessed: 2024.
- [243] Rapid7 Global Consulting, “Under the hoodie, lessons from a season of penetration testing,” Rapid7, Tech. Rep., 2018. [Online]. Available: https://www.rapid7.com/globalassets/_pdfs/research/rapid7-under-the-hoodie-2018-research-report.pdf
- [244] C. DeCusatis, R. M. Lynch, W. Kluge, J. Houston, P. A. Wojciak, and S. Guendert, “Impact of cyberattacks on precision time protocol,” *IEEE Transactions on Instrumentation and Measurement*, vol. 69, no. 5, pp. 2172–2181, 2019.
- [245] E. Itkin and A. Wool, “A security analysis and revised security extension for the precision time protocol,” *IEEE Transactions on Dependable and Secure Computing*, vol. 17, no. 1, pp. 22–34, 2017.
- [246] E. Shereen, F. Bitard, G. Dán, T. Sel, and S. Fries, “Next steps in security for time synchronization: Experiences from implementing IEEE 1588 v2. 1,” in *2019 IEEE International Symposium on Precision Clock Synchronization for Measurement, Control, and Communication (ISPCS)*. IEEE, 2019, pp. 1–6.
- [247] B. Moussa, M. Debbabi, and C. Assi, “A detection and mitigation model for PTP delay attack in an IEC 61850 substation,” *IEEE Transactions on Smart Grid*, vol. 9, no. 5, pp. 3954–3965, 2016.
- [248] B. Moussa, M. Kassouf, R. Hadjidj, M. Debbabi, and C. Assi, “An extension to the precision time protocol (PTP) to enable the detection of cyber attacks,” *IEEE Transactions on Industrial Informatics*, vol. 16, no. 1, pp. 18–27, 2019.

BIBLIOGRAPHY

- [249] B. Moussa, C. Robillard, A. Zugenmaier, M. Kassouf, M. Debbabi, and C. Assi, “Securing the precision time protocol (PTP) against fake timestamps,” *IEEE Communications Letters*, vol. 23, no. 2, pp. 278–281, 2018.
- [250] A. Finkenzeller, O. Butowski, E. Regnath, M. Hamad, and S. Steinhorst, “PTPsec: Securing the Precision Time Protocol Against Time Delay Attacks Using Cyclic Path Asymmetry Analysis,” *arXiv preprint arXiv:2401.10664*, 2024.
- [251] D. Dik, R. Oliveira, E. Arabul, C. Vrontos, M. Berger, R. Nejabati, and D. Simeonidou, “100 Gbps Multi-Tenant FPGA-Based MACsec Aggregation to Secure the O-RAN Fronthaul,” in *49th European Conference on Optical Communications (ECOC 2023)*, vol. 2023. IET, 2023, pp. 870–873.
- [252] D. Dik, I. Larsen, and M. S. Berger, “MACsec and AES-GCM Hardware Architecture with Frame Preemption Support for Transport Security in Time Sensitive Networking,” in *2023 International Conference on Computer, Information and Telecommunication Systems (CITS)*. IEEE, 2023, pp. 01–07.
- [253] D. Dik and M. S. Berger, “O-RAN Fronthaul Transport Security Architecture and Implementation,” *IEEE Access*, 2023.
- [254] R. Ford, H. Chen, P. Madadi, M. Kulkarni, X. Ma, D. Burghal, G. Chen, Y. Hu, C. Tarver, P. Skrimponis, V. Loseu, Y. Zhang, Y. Xin, Y. Li, J. Zhang, S. Khunteta, Y. G. Reddy, A. K. R. Chavva, M. Kothiwale, and D. Villa, “Sim2Field: End-to-End Development of AI RANs for 6G,” in *Proceedings of ACM Workshop on Open and AI RAN*, Hong Kong, China, November 2025.
- [255] S. Maxenti, R. Shirkhani, M. Elkael, L. Bonati, S. D’Oro, T. Melodia, and M. Polese, “AutoRAN: Automated and Zero-Touch Open RAN Systems,” *arXiv:2504.11233 [cs.NI]*, 2025.
- [256] G. Gemmi, M. Polese, P. Johari, S. Maxenti, M. Seltser, and T. Melodia, “Open6G OTIC: A Blueprint for Programmable O-RAN and 3GPP Testing Infrastructure,” in *2024 IEEE 100th Vehicular Technology Conference (VTC2024-Fall)*, 2024, pp. 1–5.
- [257] M. Elkael, M. Polese, R. Prasad, S. Maxenti, and T. Melodia, “ALLSTaR: Automated LLM-Driven Scheduler Generation and Testing for Intent-Based RAN,” *arXiv:2505.18389 [cs.NI]*, 2025.
- [258] M. Elkael, S. D’Oro, L. Bonati, M. Polese, Y. Lee, K. Furueda, and T. Melodia, “Agen-tRAN: An Agentic AI Architecture for Autonomous Control of Open 6G Networks,” *arXiv:2508.17778 [cs.NI]*, 2025.

Acknowledgments

The Ph.D. journey is a path that everyone who decides to take it experiences in their own way. I have met many other students over these years, and most of the time they would tell me that they could not wait to graduate and move on. In my case, I truly enjoyed the journey, and even when it was not always easy, all the days spent in the lab—and all the effort to complete that last experiment late at night—were surely worth it in the end.

But none of this would have been possible without my advisor, Tommaso Melodia. He believed in me and welcomed me into this journey. He is the first person I would like to thank, and I will always be grateful for his immense guidance and support. I am also grateful to my Ph.D. committee members, Stefano Basagni and Josep Jornet, for their valuable insights and discussions over all these years. I owe special thanks to Michele Polese and Leonardo Bonati, who patiently guided me from the very beginning and from whom I learned so much. I could not have done this without them. In addition, I would like to recognize my co-authors, who provided valuable discussions, advice, and collaboration across all these projects, including: Salvatore D’Oro, Pedram Johari, Dimitrios Koutsonikolas, Hai Cheng, Neagin Neasamoni Santhi, Chris Dick, Mauro Belgiovine, Florian Kaltenberger, Ali Saeizadeh, Joshua Groen, Miead Tehrani-Moayyed, Nicholas Hedberg, Stefano Maxenti, Daniel Uvaydov, Simone Di Valerio, Osman Basaran, Russell Ford, Hao Chen, Imran Khan, Kurt Yoder, Paresh Patel, Ventz Petkov, Michael Seltser, Abhimanyu Sheshashayee, Clifton Robinson, Matteo Bordin, Pietro Brach del Prever, Gabriele Gemmi, Maria Tsampazi, Andrea Lacava, Ruben Soares da Silva, Anupa Kelkar, Abhimanyu Gosain, Kaushik Chowdhury, J. Gordon Beattie Jr., Ian Wong, Eric Anderson, Rajeev Gangula, Sakthivel Velumani, Claudio Fiandrino, Falko Dressler, Utku Demir, Eduardo Baena, Subhramoy Mohanti, Elisa Bertino, Francesca Cuomo, Chiara Petrioli, Robert Schmidt, Sagar Arora, Mikel Irazabal, Irfan Ghauri.

I also extend my acknowledgment to all other colleagues at the Wireless Networks and Embedded Systems (WiNES) Lab and, more broadly, at the Institute for the Wireless Internet of Things. Since I started in ISEC and now that we have moved to EXP, the group has grown a lot, and many people have passed through—some for just a few months, others for longer, and some who decided to stay—and they made the environment the dynamic and fun place that I enjoyed going to every day. So, if not already mentioned, I would like to thank: Ravis, Maxime, Paolo, MJ, Angelo, Eugenio, Mattia, Sergi, Ergest, Chris, Niloofar, Reena, Evgeniia, Fiona, Noah, Neko, Sandra, Bill, Kuntheary, Rosy, Ed, Deniz, Amani, Emreccan, Kerem, Luca, Kengo, Haruki, Nicoló, Filippo, Noemi, Nicole, Riccardo, Alessio, Manuel, Rawlings, Luca, Cleverson, Pierluigi, Tommaso, Matteo, Francesca, Raoul, Ivan, Leonardo, Antonio, Simone, Pietro, Luis, Rafael, Armando, Andrea, Hithesh, Madhukar, Reshma, Tamerlan, Dat, Francesco, Antonio, Daniele, Alessandro, Lorenzo, Raffaele, Francesco, Sofia, Alessandro, Aditya, Alberto, Moinak, Stella, Vitaly, Amin, Duschia, Samar, Xavi, Phuc, Andrew, Fabio, Sara.

ACKNOWLEDGMENTS

Boston has been my home for the past few years, and I have had the pleasure of meeting many good friends who made this time truly special. In particular, I would like to express my gratitude to, among others: Francesca, Maria, Gabriel, Farah, Sasha, Aldo, Marianna, Matteo, Federica, Davide, Valentina, Sandro, Francesca, Elisa, Farnoush, Justin, Luca, Pietro, Aurelio, Yvonne, Samuel, Teresa, Walter, Alessio, Nicolas, Zamora, Tommaso, Niccolò, Mariasilvia, Bernard, Lorenzo, Gaia, Kayland, Aruna, Benedetta, Amedeo, Sen, Filippo, Raffaela, Leonardo, Chiara, Maria, Matteo, Marco, Bianca, Michela, Simone, Andrea, Alessandro, Cristina, Pasquale, Helena, Francesco.

Moreover, I also had the chance to travel around, doing internships outside of Boston and experiencing different environments, and I always felt lucky to meet great people and make meaningful connections. I sincerely appreciated all the conversations and experiences we shared, and so I would like to thank, among others: Junho, Ana, Gavin, Humza, Nelson, Jing, JF, Fredrik, Kuntal, Lopa, Chason, Mingjun, Reinhard, Jacob, Caitriona, Ragav, Xiaowen, Jiayu, Andrew, Yirong, Longfei, Vitali, Debashri, Pranav, Sebastian, Carlo, Brighton, TK, Josh, Francesco, Chieh, Bimo, Neel, Manu.

In addition, I want to express my appreciation to my old friends from overseas who, even across this long distance, were able to maintain a great connection with me, including: Giancarlo, Francesco, Carlo, Francesco, Lorenzo, Willy, Giulio, Serena, Manuel, Mirko, Roberto, Marco, Marcello, Silvia, Giovanni, Giulia, Nacho, Erica, Federico, Simone.

Lastly, but certainly not least, I want to acknowledge all of my family for their constant support. Most of all, I would like to thank my parents, Mirella and Franco, to whom I was, am, and always will be immensely grateful for everything they give me every day from so far away, and who continue to make me the person I am today.